Searches for the New Resonant Production of $ZH/ZW/ZZ$ Pairs in the $\ell\ell qq$ Final State in Proton-Proton Collisions at $\sqrt{s} = 13\,\text{TeV}$ with the ATLAS Detector

by

Zhaoxu Xi

A dissertation submitted in partial fulfillment
of the requirements for the degree of
Doctor of Philosophy
(Physics)
in The University of Michigan
2018

Doctoral Committee:

Professor Jianming Qian, Chair
Professor Aaron T. Pierce
Assistant Professor Thomas A. Schwarz
Assistant Professor Gongjun Xu
Professor Bing Zhou

Zhaoxu Xi

xzhaoxu@umich.edu

ORCID iD: 0000-0002-6257-6203

© Copyright by Zhaoxu Xi 2018

All Rights Reserved

ACKNOWLEDGEMENTS

I have been fortunate to have come across so many wonderful people both at the University of Michigan and at CERN. This thesis would never have been possible without all the support and guidance I have received over the course of my graduate career. I want to sincerely thank all of you who have assisted me on this incredible journey.

First and foremost, I would like to thank my advisor Jianming Qian, who has been an invaluable source of knowledge and advice, and offered a steady hand to lead me through this challenging endeavor. Thank you for positioning me to succeed in a large collaboration, and for trusting me and giving me the freedom to work autonomously.

Thanks to Aaron Pierce, Tom Schwarz, Gongjun Xu, and Bing Zhou for serving on my committee. Your insights and suggestions have been extremely helpful for improving this work. Also thanks to Dante Amidei for being on my preliminary dissertation committee.

I further extend my gratitude to the entire group of ATLAS faculty at Michigan. The Michigan ATLAS group supported me throughout my time at Michigan and at CERN, and I'm especially grateful for having the opportunity to be stationed at CERN for an extended period. I would also like to thank Bob Ball, Benjeman Meekhof, and Shawn McKee for the upkeep of the great computing resources that we have at Michigan. Thanks to Tiesheng Dai for his guidance on muon spectrometer service work. To Tom Cheng, Matthew Klein, Hao Liu, Lulu Liu, Haonan Lu, Wen Guo, Yicheng Guo, Ismet Siral, Rongkun Wang, Zirui Wang, Yusheng Wu, Dongliang Zhang, Zhi Zheng, and the rest, thank you for making the transition to CERN easier and the long days well spent. Thanks to Aaron Armbruster, Magda Chelstowska, and Jonathon Long for the selfless help when I first joined the group.

I'm grateful for all the help and support I received from colleagues and friends from DBL, the best analysis group in ATLAS. Thanks to Flavia De Almeida Dias, Nikolaos Rompotis, Francesco Lo Sterzo, Xiaohu Sun, and Lailin Xu for organizing and coordinating the analysis efforts. Thanks to all the team members for churning out results for every conference and for making the publications possible. You all shaped my experience over the past few years into a memorable one, and I absolutely enjoyed working with everybody.

I would also like to thank all of the staff who helped me at the University of Michigan, all the professors who instructed me in and outside the classroom, and my fellow classmates for being there with me to survive coursework and quals. My friends at Michigan have made my graduate school experience an enjoyable and incredible one. To Anthony Charles, Yina Geng, Tanvi Gujarati, Peter Kordell, Anthony Kremin, Yina Liu, Glen Leung, Lu Ma, Joe Paki, Vimal Rathee, Natasha Sachdeva, Stephanie Su, Leyou Zhang, and Xiao Zhang, thank you all for the many shared experiences and adventures. Thank the Physics House for hosting movie nights and board games. I especially want to thank Glen Leung, who has been a great friend, for the countless discussions and beers when I was at Michigan.

Finally, I want to express my warmest thanks to my family, in particular my wife, Ruohan Wang, who has always been there for me. Of all people, you understand me the best. I could not imagine what it would be like to get through graduate school on my own.

A million thanks to everyone for being with me on this incredible journey. For today goodbye, for tomorrow good luck, and forever GO BLUE!

TABLE OF CONTENTS

ACKNOWLEDGEMENTS ii

LIST OF FIGURES vii

LIST OF TABLES xix

LIST OF ABBREVIATIONS xxii

ABSTRACT xxiv

CHAPTER

1. Introduction 1

2. Looking Beyond the Standard Model 3

- 2.1 The Standard Model of Particle Physics 3
  - 2.1.1 Brief Overview 3
- 2.2 Looking Beyond 9
  - 2.2.1 Two-Higgs-Doublet Model 9
  - 2.2.2 Heavy Vector Triplets 11
  - 2.2.3 Bulk Randall-Sundrum Graviton 13
- 2.3 Benchmark Models 15
  - 2.3.1 Models Considered in the ZW/ZZ Resonance Searches 15
  - 2.3.2 Models Considered in the ZH Resonance Search . . 16
- 2.4 Proton-Proton Collisions 18

3. The LHC and the ATLAS Detector 19

- 3.1 The Large Hadron Collider 19
- 3.2 The ATLAS Detector 22
  - 3.2.1 Inner Detector 24
  - 3.2.2 The Calorimetry System 27
  - 3.2.3 The Muon Spectrometer 29

3.2.4 Trigger and Data Acquisition 32

4. Particle Reconstruction and Identification 35

4.1 Electrons 35
4.2 Muons 38
4.3 Jets 39
  4.3.1 Small-R Jets 40
  4.3.2 Large-R Jets 41
4.4 Missing Transverse Momentum 51
4.5 Overlap Removal 51

5. Searches for ZW and ZZ Resonances 53

5.1 Analysis Overview and Strategy 53
  5.1.1 Main Background Processes 55
  5.1.2 Background and Signal Modeling 56
  5.1.3 Dataset 59
5.2 Object Selection 60
  5.2.1 Electron Selection 60
  5.2.2 Muon Selection 61
  5.2.3 Small-R Jet Selection 62
  5.2.4 Large-R Jet Selection 63
5.3 Event Selection and Categorization 64
  5.3.1 Trigger 64
  5.3.2 Preselection of Dilepton Events 66
  5.3.3 VBF and ggF/DY Categories 69
  5.3.4 Selection of $ZV \to \ell\ell qq$ 71
  5.3.5 Signal Acceptance 76
  5.3.6 Signal Resolution 77
5.4 Systematic Uncertainties 81
  5.4.1 Experimental Uncertainties 81
  5.4.2 Background Uncertainties 86
  5.4.3 Signal Uncertainties 89
5.5 Statistical Analysis 90
  5.5.1 Likelihood Function 90
  5.5.2 Test Statistics 92
  5.5.3 Fit inputs 94
5.6 Results 98
  5.6.1 Background-Only Fit 98
  5.6.2 Upper Limits on $\sigma \times \mathcal{B}(X \to ZV)$ 108
  5.6.3 Effects of Systematic Uncertainties 108

6. Search for ZH Resonances 112

6.1 Analysis Overview and Strategy 112
6.2 Object Selection 116
6.3 Event Selection and Categorization 117
    6.3.1 Signal Resolution and Acceptance 121
6.4 Signal Modeling 123
    6.4.1 Signal Shape Interpolation 123
    6.4.2 Signal Yield Interpolation 129
    6.4.3 Parameterization of the Large-Width Signals 131
6.5 Systematic Uncertainties 139
6.6 Statistical Analysis 142
6.7 Results 144

7. Conclusion 151

BIBLIOGRAPHY 153

LIST OF FIGURES

Figure

2.1 A schematic drawing of the particle content of the Standard Model Physics. The particles are classified into three broad categories: the three generations of matter particles (fermions), gauge bosons, and the Higgs boson. 4

2.2 Feynman diagrams for W' produced via Drell-Yan (left) and vector-boson fusion (right) processes. 12

2.3 Branching Ratios for the two body decays of the neutral vector V^0 for the benchmarks $A_{g_V} = 1$ (left) and $B_{g_V} = 3$ (right) [20]. Note that the left plot is in linear scale, whereas the plot on the right-hand side uses a semi-logarithmic scale on the y-axis. 13

2.4 In the bulk RS model, the Planck brane is separated from the weak brane by a warped extra dimension. The generation of an exponential hierarchy is shown. 14

2.5 A Feynman diagram showing the gluon-gluon fusion production mode for G_{KK}. 15

2.6 Heat-maps for the physical region (*left*) and region with a strongly first-order EWPT (*right*). *Top*: $(m_H, \alpha{-}\beta)$-plane. *Bottom*: (m_H, m_A)-plane. The dotted-black line corresponds to $m_A = m_H + m_Z$. Note that the $\alpha - \beta$ differs from the one defined in Section 2.2.1 by $\pi/2$ [18]. 16

2.7 *Left*: main Branching Ratios of the CP-odd scalar A as a function of m_H for $m_A = m_{H^\pm} = 400$ GeV, $\tan\beta = 2$, $\mu = 100$ GeV, $\alpha{-}\beta = 0.001\pi$ (solid lines) and $\alpha - \beta = 0.1\pi$ (dotted lines). *Right*: main Branching Ratios of H as a function of m_H (same benchmark parameters as in *left*). These branching ratios are for the Type-I 2HDM. Note that the $\alpha - \beta$ differs from the one defined in Section 2.2.1 by $\pi/2$ [18]. 17

2.8 Fraction of energy x carried by the parton times the parton distribution function $f(x, \mu^2)$ for protons at scales $\mu^2(Q^2) = 10\,\mathrm{GeV}^2$ and $10^4\,\mathrm{GeV}^2$ [26]. 18

3.1 The schematic layout of the accelerator complex at CERN. The protons are accelerated through Linac 2, PSB, PS and SPS before being injected into the LHC. Several other experiments not associated with the LHC are also depicted. 21

3.2 (a) The luminosity-weighted distribution of the average number of interactions per crossing for the combined 2015 and 2016 *pp* collision data at 13 TeV center-of-mass energy; (b) cumulative luminosity versus time delivered to (green) and recorded by ATLAS (yellow) during stable beams for *pp* collisions at 13 TeV center-of-mass energy in 2015. (c) same as (b) but for 2016. 22
3.3 Cut-away view of the ATLAS detector. The dimensions of the detector are 25 m in height and 44 m in length. The overall weight of the detector is approximately 7000 tonnes [6]. 23
3.4 Diagram of the ATLAS Inner Detector [6]. 24
3.5 A schematic drawing of the inner detector showing the sensors and structural elements traversed by a charged track of 10 GeV p_T in the barrel inner detector ($\eta = 0.3$) [6]. 25
3.6 Cut-away view of the ATLAS calorimeter system [6]. 28
3.7 Schematic illustration of the muon spectrometer system composed of the detector panels and the toroid magnets [6]. 30
3.8 *Left*: Cross-section of the barrel muon system perpendicular to the beam axis (non-bending plane), showing three concentric cylindrical layers of eight large and eight small chambers. The outer diameter is about 20m. *Right*: Cross-section of the muon system in a plane containing the beam axis (bending plane). Infinite-momentum muons would propagate along straight trajectories which are illustrated by the dashed lines and typically traverse three muon stations [6]. 31
3.9 Schematic layout of the ATLAS trigger and data acquisition system in Run-II [6]. 33
4.1 Electron reconstruction and identification efficiencies in $Z \rightarrow ee$ events as a function of transverse energy E_{T}, integrated over the full pseudo-rapidity range. The efficiencies are shown in data and MC for three operating points that are based on a likelihood approach, Loose, Medium and Tight [45]. 37
4.2 MV2c10 BDT output for b- (solid blue), c- (dashed green) and light-flavor (dotted red) jets evaluated with $t\bar{t}$ events [53]. 42
4.3 (a) The angular separation between the W boson and b-quark in top decays, $t \rightarrow Wb$, as a function of the top-quark transverse momentum (p_{T}^{t}) in simulated Pythia $Z' \rightarrow t\bar{t}$ ($m_{Z'} = 1.6\,\mathrm{TeV}$) events. (b) The angular distance between the light quark and anti-quark from $W \rightarrow q\bar{q}'$ decays as a function of the p_{T} of the W boson (p_{T}^{W}). Both distributions are at the generator level and do not include effects due to initial and final-state radiation, or the underlying event [54]. . . . 43
4.4 A schematic diagram depicting the trimming procedure for the large-R jets [54]. 44
4.5 Distributions of the combined track-assisted and calorimeter large-R jet mass for low p_{T} [200, 500] GeV (left) and high p_{T} [1000, 1500] GeV (right) W, top and QCD jets [55]. 45

4.6 The large-R jet mass resolution as a function of jet p_{T} for jets produced from boosted W bosons (left) and from boosted top quarks (right) [55]. m^{TAS} is the track-assisted subjet mass, which is the invariant mass of the sum of all track-assisted subjet four-vectors. The 68% interquartile range (IQnR) is defined as $q_{84\%} - q_{16\%}$, where $q_{16\%}$ and $q_{84\%}$ denote the 16th and the 84th percentiles of a given distribution. The resolution is shown as the ratio of $0.5 \cdot (q_{84\%} - q_{16\%})$ to the median location of the peak. 46
4.7 Distributions of the $D_2^{\beta=1}$ variable for the background di-jet samples and the signal W boson jets for different p_{T} bins of the truth-matched jets [55]. 47
4.8 Smoothed cut functions fitted to optimized fixed cuts for W-boson tagging using the substructure variable combination: combined mass + $D_2^{\beta=1}$. These cut functions are shown at $\epsilon_{\mathrm{sig}} = 50\%$ (a, b) and $\epsilon_{\mathrm{sig}} = 80\%$ (c, d) [58]. 48
4.9 Smoothed cut functions fitted to optimized fixed cuts for Z-boson tagging using the substructure variable combination: combined mass + $D_2^{\beta=1}$. These cut functions are shown at $\epsilon_{\mathrm{sig}} = 50\%$ (a, b) and $\epsilon_{\mathrm{sig}} = 80\%$ (c, d) [58]. 49
4.10 Recommended W-boson and Z-boson tagger performance (both signal efficiency and background rejection) as a function of combined mass corrected jet p_{T}. The performance is presented for W-boson tagging at $\epsilon_{\mathrm{sig}} = 50\%$ (a) and $\epsilon_{\mathrm{sig}} = 80\%$ (b), and for Z-boson tagging at $\epsilon_{\mathrm{sig}} = 50\%$ (c) and $\epsilon_{\mathrm{sig}} = 80\%$ (d) [58]. 50
5.1 Representative Feynman diagrams for the production of heavy resonances X with their decays into a pair of vector bosons [60]. 55
5.2 Efficiencies of the HLT_e26_lhtight_nod0_ivarloose trigger as a function of the offline electron candidate's (a) transverse energy, and (b) pseudo-rapidity, which are obtained from $Z \to ee$ events [91]. 65
5.3 Efficiencies of the logical OR between HLT_e26_lhtight_nod0_ivarloose, HLT_e60_lhmedium_nod0 and HLT_e140_lhloose_nod0 triggers as a function of the offline electron candidate's (a) transverse energy, and (b) pseudo-rapidity , which are obtained from $Z \to ee$ events [91]. . 66
5.4 Absolute efficiency of Level 1 (L1) MU20 trigger, and absolute and relative (with respect to the L1 trigger) efficiencies of the union of mu26_ivarmedium and mu50 high-level triggers as a function of p_{T} of offline muon candidates in the (a) barrel, and (b) end-cap regions [92]. 67

5.5 Observed and expected distributions of dilepton invariant mass and transverse momentum in the (a, c) di-electron channel and the (b, d) di-muon channel after preselection of the $Z \to \ell\ell$ candidates. For illustration, expected distributions from the ggF production of a 1 TeV Higgs boson with $\sigma \times \mathcal{B}(H \to ZZ) = 2\,\mathrm{pb}$ are also shown. Background contributions are obtained from a combined likelihood fit to the data. The ratio of the observed data to the background prediction is shown at the bottom, along with the uncertainty on the total background prediction after combining the statistical and systematic contributions. 68

5.6 Observed data and expected background distributions of dijet (a) invariant mass and (b) pseudo-rapidity separation of the two tag-jets of the VBF $H \to ZZ \to \ell\ell qq$ search, combining all signal regions [60]. For illustration, expected distributions from the VBF production of a 1 TeV Higgs boson with $\sigma \times \mathcal{B}(H \to ZZ) = 20$ fb are also shown. The middle panes show the ratio of the observed data to the background predictions. The uncertainty in the total background prediction, shown as bands, combines statistical and systematic contributions. The blue triangles in the middle panes indicate bins where the ratio is nonzero and outside the vertical range of the plot. The bottom panes are the ratios of the post-fit and pre-fit background predictions. 70

5.7 Observed and expected distributions of (a) $\min(p_{\mathrm{T}}^{\ell\ell}, p_{\mathrm{T}}^{J})/m_{\ell\ell J}$ before boson tagging and (b) $\sqrt{\left(p_{\mathrm{T}}^{\ell\ell}\right)^2 + \left(p_{\mathrm{T}}^{jj}\right)^2}/m_{\ell\ell jj}$ after preselection of the $Z \to \ell\ell$ candidates. For illustration, expected distributions from the ggF production of a 1 TeV Higgs boson with $\sigma \times \mathcal{B}(H \to ZZ) = 2\,\mathrm{pb}$ are also shown. Background contributions are obtained from a combined likelihood fit to the data. The ratio of the observed data to the background prediction is shown at the bottom, along with the uncertainty on the total background prediction after combining the statistical and systematic contributions. 71

5.8 Observed and expected distributions of (a) $p_{\mathrm{T}}(J)$ before boson tagging and (b) $p_{\mathrm{T}}(jj)$ before the $V \to qq$ mass window cut. For illustration, expected distributions from the ggF production of a 1 TeV Higgs boson with $\sigma \times \mathcal{B}(H \to ZZ) = 2\,\mathrm{pb}$ are also shown. Background contributions are obtained from a combined likelihood fit to the data. The ratio of the observed data to the background prediction is shown at the bottom, along with the uncertainty on the total background prediction after combining the statistical and systematic contributions. 72

5.9 Observed and expected distributions of $D_2(J)$ before boson tagging. For illustration, expected distributions from the ggF production of a 1 TeV Higgs boson with $\sigma \times \mathcal{B}(H \rightarrow ZZ) = 2\,\text{pb}$ are also shown. Background contributions are obtained from a combined likelihood fit to the data. The ratio of the observed data to the background prediction is shown at the bottom, along with the uncertainty on the total background prediction after combining the statistical and systematic contributions. 73
5.10 Observed and expected distributions of (a) the large-R jet mass m_J of the $ZV \rightarrow \ell\ell J$ candidate and (b) the dijet mass m_{jj} of the $ZV \rightarrow \ell\ell jj$ candidate [60]. These distributions are for the $H \rightarrow ZZ$ search before the identification of the $V \rightarrow qq$ decay, combining VBF and ggF/DY categories. Background contributions are obtained from a combined likelihood fit to the data. For illustration, expected distributions from the ggF production of a 1 TeV Higgs boson with $\sigma \times \mathcal{B}(H \rightarrow ZZ) = 2\,\text{pb}$ are also shown. The middle panes show the ratios of the observed data to the background predictions. The uncertainty on the total background prediction, shown as bands, combines statistical and systematic contributions. The bottom panes are the ratios of the post-fit and pre-fit background predictions. 74
5.11 Illustration of the selection flow and seven signal regions of the $X \rightarrow ZV \rightarrow \ell\ell qq$ search [60]. The VBF category is targeted for VBF production. The selected VBF tag-jets are removed from the subsequent selection for the VBF category. However, if an event fails to be selected for the VBF category, these jets are kept for the ggF/DY category selection. The $H \rightarrow ZZ$ search utilizes all seven signal regions and the $W' \rightarrow ZW$ search uses six signal regions by combining the b-tagged and untagged regions of the ggF/DY category. The $G_{\text{KK}} \rightarrow ZZ$ search bypasses the VBF selection, so it has only four signal regions. 75
5.12 Background compositions in the (a) signal regions and (b) control regions of the $H \rightarrow ZZ \rightarrow \ell\ell qq$ search. For simplicity, VBF and ggF categories are combined as similar compositions are expected. 77
5.13 Selection acceptance times efficiency for the $H \rightarrow ZZ \rightarrow \ell\ell qq$ events from MC simulations as a function of the Higgs boson mass for (a) ggF and (b) VBF production, combining the high- and low-purity signal regions of the $ZV \rightarrow \ell\ell J$ selection and the b-tagged and untagged regions of the $ZV \rightarrow \ell\ell jj$ selection [60]. The hatched band represents the total statistical and systematic uncertainties. 78

5.14 Selection efficiencies of $W' \to ZW \to \ell\ell qq$ events from MC simulations as functions of the W' mass for (a) DY and (b) VBF production, combining the high- and low-purity signal regions of the merged $ZV \to \ell\ell J$ selection and the b-tagged and untagged regions of the resolved $ZV \to \ell\ell jj$ selection [60]. The decrease in the $\ell\ell qq$ selection efficiency above approximately 2.5 TeV of the HVT W' boson mass is mainly due to the merging of electrons from the $Z \to ee$ decay. . 78
5.15 Selection efficiencies of $G_{\text{KK}} \to ZZ \to \ell\ell qq$ events from MC simulations as functions of the G_{KK} mass for (a) $k/\overline{M}_{\text{Pl}} = 0.5$ and (b) $k/\overline{M}_{\text{Pl}} = 1.0$ productions, combining the high- and low-signal regions of the $ZV \to \ell\ell J$ selection and the b-tagged and untagged regions of the $ZV \to \ell\ell jj$ selection [60]. The decrease in the $\ell\ell qq$ selection efficiency above approximately 2.5 TeV of the G_{KK} boson mass is mainly due to the merging of electrons from the $Z \to ee$ decay. . . . 79
5.16 The simulated (a) $m_{\ell\ell J}$ and (b) $m_{\ell\ell jj}$ distributions obtained from directly using the mass of the $\ell\ell J/\ell\ell jj$ system (filled histogram) and after scaling the $\mu\mu$ and jj systems (empty histogram). 79
5.17 Signal mass resolutions for the (a) merged and (b) resolved regimes. 80
5.18 Combined fractional JES uncertainty associated with fully calibrated small-R jets as a function of (a) jet p_{T} at $\eta = 0$ and (b) η at $p_{\text{T}} = 80\,\text{GeV}$ [51]. 82
5.19 The fractional scale uncertainties associated with large-R jets [96]. "ICHEP2018" refers to superseded results. 84
5.20 Distributions of mass and D_2 responses of the large-R jets in different p_{T} bins. 85
5.21 Resolutions of the large-R jet (a) mass and (b) D_2 responses as a function of reconstructed jet p_T for W/Z boson jets and QCD jets. IQnR (inter-quartile range) is defined as $q_{84\%} - q_{16\%}$, whereby $q_{16\%}$ and $q_{84\%}$ are the 16^{th} and 84^{th} percentiles of a given distribution. . . 86
5.22 Modeling uncertainties of the Z+jets background estimated using the α-ratio method. The uncertainties shown are for the spin-0 signal regions. 88
5.23 Comparisons of the observed data and expected background distributions of the final discriminants of the VBF category for the $H \to ZZ \to \ell\ell qq$ search: $m_{\ell\ell J}$ of (a) high-purity and (b) low-purity signal regions; (c) $m_{\ell\ell jj}$ of the resolved signal region [60]. For illustration, expected distributions from the VBF production of a 1 TeV Higgs boson with $\sigma \times \mathcal{B}(H \to ZZ) = 20$ fb are also shown. The middle panes show the ratios of the observed data to the background predictions. The uncertainty in the total background prediction, shown as bands, combines statistical and systematic contributions. The blue triangles in the middle panes indicate bins where the ratio is nonzero and outside the vertical range of the plot. The bottom panes show the ratios of the post-fit and pre-fit background predictions. 102

5.24 Comparisons of the observed data and expected background distributions of the final discriminants of the ggF category for the $H \to ZZ \to \ell\ell qq$ search: $m_{\ell\ell J}$ of (a) high-purity and (b) low-purity signal regions; $m_{\ell\ell jj}$ of (c) b-tagged and (d) untagged signal regions [60]. For illustration, expected distributions from the ggF production of a 1 TeV Higgs boson with $\sigma \times \mathcal{B}(H \to ZZ) = 20$ fb are also shown. The middle panes show the ratios of the observed data to the background predictions. The uncertainty in the total background prediction, shown as bands, combines statistical and systematic contributions. The blue triangles in the middle panes indicate bins where the ratio is nonzero and outside the vertical range of the plot. The bottom panes show the ratios of the post-fit and pre-fit background predictions. 103
5.25 Comparisons of the observed data and expected background event yields in each control region [60]. The middle pane shows the ratios of the observed data to the post-fit background predictions. The uncertainty in the total background prediction, shown as bands, combines statistical and systematic contributions. The bottom pane shows the ratios of the post-fit and pre-fit background predictions. 104
5.26 Comparisons of the observed data and expected background distributions of the final discriminants of the VBF category for the HVT $W' \to ZW \to \ell\ell qq$ search: $m_{\ell\ell J}$ of (a) high-purity and (b) low-purity signal regions; (c) $m_{\ell\ell jj}$ of the resolved signal region [60]. For illustration, expected distributions from the VBF production of a 1 TeV W' with $\sigma \times \mathcal{B}(W' \to ZW) = 20$ fb are also shown. The middle panes show the ratios of the observed data to the background predictions. The uncertainty in the total background prediction, shown as bands, combines statistical and systematic contributions. The blue triangles in the middle panes indicate bins where the ratio is nonzero and outside the vertical range of the plot. The bottom panes are the ratios of the post-fit and pre-fit background predictions. 105
5.27 Comparisons of the observed data and expected background distributions of the final discriminants of the DY category for the HVT $W' \to ZW \to \ell\ell qq$ search: $m_{\ell\ell J}$ of (a) high-purity and (b) low-purity signal regions; $m_{\ell\ell jj}$ of (c) resolved signal region [60]. For illustration, expected distributions from the DY production of a 1 TeV W' with $\sigma \times \mathcal{B}(W' \to ZW) = 20$ fb are also shown. The middle panes show the ratios of the observed data to the background predictions. The uncertainty in the total background prediction, shown as bands, combines statistical and systematic contributions. The blue triangles in the middle panes indicate bins where the ratio is nonzero and outside the vertical range of the plot. The bottom panes are the ratios of the post-fit and pre-fit background predictions. 106

5.28 Comparisons of the observed data and expected background distributions of the final discriminants for the $G_{\text{KK}} \to ZZ \to \ell\ell qq$ search: $m_{\ell\ell J}$ of (a) high-purity and (b) low-purity signal regions; $m_{\ell\ell jj}$ of (c) b-tagged and (d) untagged signal regions [60]. For illustration, expected distributions from a 1 TeV G_{KK} with $k/\overline{M}_{\text{Pl}} = 1$ and $\sigma \times \mathcal{B}(G_{\text{KK}} \to ZZ) = 20$ fb are also shown. The middle panes show the ratios of the observed data to the background predictions. The uncertainty in the total background prediction, shown as bands, combines statistical and systematic contributions. The blue triangles in the middle panes indicate bins where the ratio is nonzero and outside the vertical range of the plot. The bottom panes are the ratios of the post-fit and pre-fit background predictions. 107

5.29 Observed (black solid curve) and expected (black dashed curve) 95% CL upper limits on $\sigma \times \mathcal{B}(H \to ZZ)$ at $\sqrt{s} = 13$ TeV for the (a) ggF and (b) VBF production of a heavy Higgs boson as a function of its mass, combining $\ell\ell qq$ and $\nu\nu qq$ searches [60]. Limits expected from individual searches (dashed curves in blue and magenta) are also shown for comparison. Limits are calculated in the asymptotic approximation below 2 TeV and are obtained from pseudo-experiments above that. The green (inner) and yellow (outer) bands represent the $\pm 1\sigma$ and $\pm 2\sigma$ uncertainty in the expected limits. 109

5.30 Observed (black solid curve) and expected (black dashed curve) 95% CL upper limits on $\sigma \times \mathcal{B}(W' \to ZW)$ at $\sqrt{s} = 13$ TeV for the (a) DY and (b) VBF production of a W' boson in the HVT model as a function of its mass, combining $\ell\ell qq$ and $\nu\nu qq$ searches [60]. Limits expected from individual searches (dashed curves in blue and magenta) are also shown for comparison. Limits are calculated in the asymptotic approximation below 2 TeV and are obtained from pseudo-experiments above that. Theoretical predictions are overlaid in (a) for HVT *Model A* and *Model B* and in (b) for HVT *VBF Model*. The green (inner) and yellow (outer) bands represent the $\pm 1\sigma$ and $\pm 2\sigma$ uncertainty in the expected limits. 109

5.31 Observed (black solid curve) and expected (black dashed curve) 95% CL upper limits on $\sigma \times \mathcal{B}(G_{\text{KK}} \to ZZ)$ at $\sqrt{s} = 13$ TeV for the production of a G_{KK} in the bulk RS model with couplings of (a) $k/\overline{M}_{\text{Pl}} = 0.5$ and (b) $k/\overline{M}_{\text{Pl}} = 1.0$ as a function of the graviton mass, combining $\ell\ell qq$ and $\nu\nu qq$ searches [60]. Limits expected from individual searches (dashed curves in blue and magenta) are also shown for comparison. Limits are calculated in the asymptotic approximation below 2 TeV and are obtained from pseudo-experiments above that. The theoretical predictions for $\sigma \times \mathcal{B}(G_{\text{KK}} \to ZZ)$ as a function of resonance mass for a bulk RS graviton are also shown. The green (inner) and yellow (outer) bands represent the $\pm 1\sigma$ and $\pm 2\sigma$ uncertainty in the expected limits. 110

6.1 Feynman diagrams for the production of the A boson (a) via gluon-gluon fusion and (b) in association with b-quarks (b-associated production) [109]. 113
6.2 A conceptual design of the $A \to ZH \to \ell\ell bb$ analysis strategy. . . . 113
6.3 The $p_{\mathrm{T}}^{\ell\ell}$ distribution without any m_{bb} window requirement for the (a) $n_b = 2$ category and (b) the $n_b \geq 3$ category, and the $\sqrt{\sum p_{\mathrm{T}}^2}/m_{\ell\ell bb}$ distribution after relevant m_{bb} window selections for the (c) $n_b = 2$ category and the $n_b \geq 3$ category [109]. The solid dots in the lower panels represent the ratio of the data to the background prediction obtained from the MLE, while the open circles correspond to the ratio of data to the background prediction without any fit performed. The signal distributions are normalized to $\sigma \times \mathcal{B}(A \to ZH) \times \mathcal{B}(H \to bb) = 1\,\mathrm{pb}$ in (a) and (b). In (c) and (d) the signal normalization is scaled up to one third of the total background normalization in order to show the shape difference from background in the linear scale. . . 118
6.4 The m_{bb} distributions before any m_{bb} window selection are shown in (a) and (b) for the $n_b = 2$ and the $n_b \geq 3$ categories, respectively [109]. The gluon-gluon fusion signal with $(m_{\mathrm{A}}, m_{\mathrm{H}}) = (700, 200)\,\mathrm{GeV}$ is shown in (a), whereas b-associated production at the same $(m_{\mathrm{A}}, m_{\mathrm{H}})$ point is shown in (b). In both cases, the signal is normalized to $\sigma \times \mathcal{B}(A \to ZH) \times \mathcal{B}(H \to bb) = 1\,\mathrm{pb}$. The solid dots in the lower panels represent the ratio of the data to the background prediction obtained from the MLE, while the open circles correspond to the ratio of data to the background prediction without any fit performed. The m_{bb} window criterion is also shown as vertical solid lines for the corresponding m_{H} hypothesis. 119
6.5 The simulated $m_{\ell\ell bb}$ distributions obtained from directly using the mass of the $\ell\ell bb$ system (filled histogram) and after scaling the $\ell\ell$ and bb systems by $m_{\mathrm{Z}}/m_{\ell\ell}$ and m_{H}/m_{bb} (empty histogram) respectively for (a) gluon-gluon fusion in the $n_b = 2$ category and (b) b-associated production in the $n_b \geq 3$ category of a A boson assuming $m_{\mathrm{A}} = 500\,\mathrm{GeV}$ and $m_{\mathrm{H}} = 250\,\mathrm{GeV}$ [109]. 121
6.6 The efficiency of the m_{bb} window requirement for (a) $m_{\mathrm{H}} = 130\,\mathrm{GeV}$ as a function of m_{A} and (b) $m_{\mathrm{A}} = 700\,\mathrm{GeV}$ as a function of m_{H} [109]. 122
6.7 The signal selection efficiency for (a) $m_{\mathrm{H}} = 130\,\mathrm{GeV}$ as a function of m_{A} and (b) $m_{\mathrm{A}} = 700\,\mathrm{GeV}$ as a function of m_{H} [109]. 122
6.8 The grid of Monte Carlo simulation generated for scanning the $m_{\mathrm{A}} - m_{\mathrm{H}}$ parameter space for each production mechanism. 123

6.9 Simulated $m_{\ell\ell bb}$ distributions (closed circles) of signals produced via gluon-gluon fusion assuming (a) $m_{\mathrm{A}} = 500\,\mathrm{GeV}$ and $m_{\mathrm{H}} = 250\,\mathrm{GeV}$, and (b) $m_{\mathrm{A}} = 500\,\mathrm{GeV}$ and $m_{\mathrm{H}} = 400\,\mathrm{GeV}$ in the $n_b = 2$ category. Signal parameterizations are overlaid for comparison. The solid curves are from parameter values obtained directly from the fits to the simulated distributions, whereas the dashed curves use the interpolated parameter values. The differences between the simulation and the interpolated shape divided by the statistical uncertainties of the simulation are shown in the bottom panels. 124

6.10 Simulated signal $m_{\ell\ell bb}$ distributions (closed circles) from b-associated production assuming $m_{\mathrm{A}} = 500\,\mathrm{GeV}$ and $m_{\mathrm{H}} = 250\,\mathrm{GeV}$ in the (a) $n_b = 2$ category and (b) $n_b \geq 3$ category, and $m_{\mathrm{A}} = 500\,\mathrm{GeV}$ and $m_{\mathrm{H}} = 400\,\mathrm{GeV}$ in the (c) $n_b = 2$ category and (d) $n_b \geq 3$ category. Signal parameterizations are overlaid for comparison. The solid curves are from parameter values obtained directly from the fits to the simulated distributions, whereas the dashed curves use the interpolated parameter values. The differences between the simulation and the interpolated shape divided by the statistical uncertainties of the simulation are shown in the bottom panels. 126

6.11 Evolution of the floating parameters (a and σ) in the EGE fit to the gluon-gluon fusion signals as a function of the mass splitting between the A and H bosons. The red curve shows the result of a 3$^{\mathrm{rd}}$ degree polynomial fit to the σ evolution used for the signal shape interpolation. 128

6.12 Evolution of the floating parameters (a and σ) in the DSCB fit to the b-associated production signals in the $n_b = 2$ category as a function of the mass splitting between the A and H bosons. The red curve shows the result of a 3$^{\mathrm{rd}}$ degree polynomial fit to the σ evolution used for the signal shape interpolation. 128

6.13 Evolution of the floating parameters (a and σ) in the DSCB fit to the b-associated production signals in the $n_b \geq 3$ category as a function of the mass splitting between the A and H bosons. The red curve shows the result of a 3$^{\mathrm{rd}}$ degree polynomial fit to the σ evolution used for the signal shape interpolation. 129

6.14 Results of the two-dimensional thin-plate spline signal yield interpolation for (a) gluon-gluon fusion in the $n_b = 2$ category, (b) b-associated production in the $n_b = 2$ category, and (c) b-associated production in the $n_b \geq 3$ category. The z-axis gives the absolute percent difference between the interpolated yield and the generated yield when not using that point as input to the interpolation. 130

6.15 Comparisons between the parameterized and generated lineshapes of $m_{\mathrm{A}} = 300$ GeV, $m_{\mathrm{H}} = 130$ GeV for $\Gamma_A/m_{\mathrm{A}} = 5\%$ (left), $\Gamma_A/m_{\mathrm{A}} = 10\%$ (middle), and $\Gamma_A/m_{\mathrm{A}} = 20\%$ (right). 133

6.16 Comparisons between the parameterized and generated lineshapes of $m_{\mathrm{A}} = 500$ GeV, $m_{\mathrm{H}} = 250$ GeV for $\Gamma_A/m_{\mathrm{A}} = 5\%$ (left), $\Gamma_A/m_{\mathrm{A}} = 10\%$ (middle), and $\Gamma_A/m_{\mathrm{A}} = 20\%$ (right). 133

6.17 Comparisons between the parameterized and generated lineshapes of $m_{\mathrm{A}} = 800$ GeV, $m_{\mathrm{H}} = 130$ GeV for $\Gamma_A/m_{\mathrm{A}} = 5\%$ (left), $\Gamma_A/m_{\mathrm{A}} = 10\%$ (middle), and $\Gamma_A/m_{\mathrm{A}} = 20\%$ (right). 134
6.18 Comparisons between the parameterized and generated lineshapes of $m_{\mathrm{A}} = 800$ GeV, $m_{\mathrm{H}} = 400$ GeV for $\Gamma_A/m_{\mathrm{A}} = 5\%$ (left), $\Gamma_A/m_{\mathrm{A}} = 10\%$ (middle), and $\Gamma_A/m_{\mathrm{A}} = 20\%$ (right). 134
6.19 Comparisons of the invariant mass spectra of the $\ell\ell bb$ four-body system for $m_{\mathrm{A}} = 500$ GeV, $m_{\mathrm{H}} = 150$ GeV for different A boson widths. The dots correspond to the shape from simulation and the red histogram represents the model template based on the method described by Equation (6.6). 135
6.20 Comparisons of the invariant mass spectra of the $\ell\ell bb$ four-body system for $m_{\mathrm{A}} = 600$ GeV, $m_{\mathrm{H}} = 300$ GeV for different A boson widths. The dots correspond to the shape from simulation and the red histogram represents the model template based on the method described by Equation (6.6). 136
6.21 Comparisons of the invariant mass spectra of the $\ell\ell bb$ four-body system for $m_{\mathrm{A}} = 700$ GeV, $m_{\mathrm{H}} = 400$ GeV for different A boson widths. The dots correspond to the shape from simulation and the red histogram represents the model template based on the method described by Equation (6.6). 137
6.22 The interpolated $m_{\ell\ell bb}$ distribution assuming $m_{\mathrm{A}} = 500\,\mathrm{GeV}$ and $m_{\mathrm{H}} = 250\,\mathrm{GeV}$ with various A boson widths for: (a) gluon-gluon fusion in the $n_b = 2$ category and (b) b-associated production in the $n_b \geq 3$ category [109]. 138
6.23 The ratio of $(N(\mathrm{data}) - N(\mathrm{MC\ backgrounds}))/N(Z+\mathrm{jets})$ as a function of $p_{\mathrm{T}}(Z)$. This ratio is taken as the modeling uncertainty associated with the $p_{\mathrm{T}}(Z)$ of the Z+jets background in the respective categories. The red curve represents the parameterization used for the data-driven estimate. 140
6.24 The ratio of $(N(\mathrm{data}) - N(\mathrm{MC\ backgrounds}))/N(Z+\mathrm{jets})$ as a function of m_{bb}. This ratio is taken as the modeling uncertainty associated with the m_{bb} of the Z+jets background in the respective categories. The red curve represents the parameterization used for the data-driven estimate. 140
6.25 The ratio of $(N(\mathrm{data}) - N(\mathrm{MC\ backgrounds}))/N(t\bar{t})$ as a function of $p_{\mathrm{T}}(Z)$. This ratio is taken as the modeling uncertainty associated with the $p_{\mathrm{T}}(Z)$ of the $t\bar{t}$ background in the respective categories. The red curve represents the parameterization used for the data-driven estimate. 141
6.26 The ratio of $(N(\mathrm{data}) - N(\mathrm{MC\ backgrounds}))/N(t\bar{t})$ as a function of m_{bb}. This ratio is taken as the modeling uncertainty associated with the m_{bb} of the $t\bar{t}$ background in the respective categories. The red curve represents the parameterization used for the data-driven estimate. 141

6.27 Scan of the p-values from the q_0 test statistic for (a) the gluon-gluon fusion and (b) the b-associated production signal assumption. 144
6.28 Distributions of the $m_{\ell\ell bb}$ spectrum for the $m_{\mathrm{H}} = 610\,\mathrm{GeV}$ hypothesis in the (a) $n_b = 2$ category and (b) the $n_b \geq 3$ category. The solid dots in the lower panels represent the ratio of the data to the background prediction obtained from the conditional MLE with $\mu = 0$, while the open circles correspond to the ratio of the data to the pre-fit background prediction. The signal distributions shown in these plots assume that $\sigma \times \mathcal{B}(A \to ZH) \times \mathcal{B}(H \to bb) = 1\,\mathrm{pb}$. 145
6.29 Distributions of the $m_{\ell\ell bb}$ spectrum for the $m_{\mathrm{H}} = 130\,\mathrm{GeV}$ hypothesis in the (a) $n_b = 2$ category and (b) the $n_b \geq 3$ category. See Figure 6.28 for more explanations for the background and signal distributions. 145
6.30 Distributions of the $m_{\ell\ell bb}$ spectrum for the $m_{\mathrm{H}} = 200\,\mathrm{GeV}$ hypothesis in the (a) $n_b = 2$ category and (b) the $n_b \geq 3$ category. See Figure 6.28 for more explanations for the background and signal distributions. 146
6.31 Distributions of the $m_{\ell\ell bb}$ spectrum for the $m_{\mathrm{H}} = 300\,\mathrm{GeV}$ hypothesis in the (a) $n_b = 2$ category and (b) the $n_b \geq 3$ category. See Figure 6.28 for more explanations for the background and signal distributions. 146
6.32 Distributions of the $m_{\ell\ell bb}$ spectrum for the $m_{\mathrm{H}} = 500\,\mathrm{GeV}$ hypothesis in the (a) $n_b = 2$ category and (b) the $n_b \geq 3$ category. See Figure 6.28 for more explanations for the background and signal distributions. 147
6.33 The (a) expected and (b) observed upper limits at 95% CL on $\sigma \times \mathcal{B}(A \to ZH) \times \mathcal{B}(H \to bb)$ for gluon-gluon fusion production. 147
6.34 The (a) expected and (b) observed upper limits at 95% CL on $\sigma \times \mathcal{B}(A \to ZH) \times \mathcal{B}(H \to bb)$ for b-associated production. 148
6.35 Observed and expected 95% CL exclusion regions in the $(m_{\mathrm{A}}, m_{\mathrm{H}})$ plane for various $\tan\beta$ values for (a) Type I, (b) Type II, (c) lepton specific and (d) flipped 2HDMs. 149

LIST OF TABLES

Table

3.1 Main parameters of the inner detector system. The resolutions quoted are typical values. 25

4.1 Efficiency for prompt muons from W decays (signal) and misidentified prompt muons from in-flight decays of hadrons (background) using a $t\bar{t}$ MC sample. The results of the four identification selection criteria are shown separately for muons with low ($4 < p_{\mathrm{T}} < 20\,\mathrm{GeV}$) and high ($20 < p_{\mathrm{T}} < 100\,\mathrm{GeV}$) transverse momenta in the region $|\eta| < 2.5$. The statistical uncertainties are negligible. 39

5.1 A summary of the Monte Carlo samples used to model the background processes considered in this analysis. The corresponding cross sections times branching fractions ($\sigma \times \mathcal{B}$) are quoted at $\sqrt{s} = 13\,\mathrm{TeV}$. 58

5.2 A summary of the maximum instantaneous luminosity, the total integrated luminosity, and the average number of interactions per bunch crossing, for the data recorded in 2015 and 2016 by the ATLAS detector. 59

5.3 A summary of the criteria for object selections used in the $X \to ZV \to \ell\ell qq$ analysis. 61

5.4 The list of triggers used in the analysis. 64

5.5 A summary of the $X \to ZV \to \ell\ell qq$ selection criteria. 76

5.6 A summary of the modeling systematic uncertainties for the $t\bar{t}$ process as well as the samples used in each case [99]. The symbol Δ denotes the difference in the analysis observables using the simulation from the samples column. The notation $\pm|\Delta|$ indicates that the full difference is symmetrized and applied to the nominal sample. Without the absolute value bars, Δ indicates that the signed difference with respect to the nominal case is used to estimate the uncertainty. . . . 88

5.7 Summary of the inputs entering the likelihood function for the $H \to ZZ$ search. "N_{evt}" indicates that the number of events is used as the discriminant without any shape information and α refers to scale factors applied to the major background processes. 95

5.8 Summary of the inputs entering the likelihood function for the $W' \to ZW$ search. "N_{evt}" indicates that the number of events is used as the discriminant without any shape information and α refers to scale factors applied to the major background processes. 96

5.9 Summary of the inputs entering the likelihood function for the $G_{\mathrm{KK}} \to ZZ$ search. "N_{evt}" indicates that the number of events is used as the discriminant without any shape information and α refers to scale factors applied to the major background processes. 96

5.10 Best-fit values of the floating normalization scale factors for the background components from the background-only likelihood fits for H, W' and G_{KK} searches respectively. For each search, all signal regions and control regions are included in the fit. 100

5.11 Numbers of events observed in the data and predicted for background processes from background-only fits to the signal and control regions in the seven signal regions of the $H \to ZZ \to \ell\ell qq$ search. The numbers of signal events expected from the ggF and VBF production of a heavy Higgs boson with mass of 1 TeV are also shown. The signal yields are calculated using $\sigma \times \mathcal{B}(H \to ZZ) = 20$ fb for both processes. The uncertainties combine statistical and systematic contributions. The fit constrains the background estimate towards the observed data, which reduces the total background uncertainty by correlating those from the individual backgrounds. 100

5.12 Numbers of events observed in the data and predicted for background processes from background-only fits to the signal and control regions in the seven signal regions of the $W' \to ZW \to \ell\ell qq$ search. The numbers of signal events expected from the DY and VBF production of a W' with mass of 1 TeV are also shown. The signal yields are calculated using $\sigma \times \mathcal{B}(W' \to ZW) = 20$ fb for both processes. The uncertainties combine statistical and systematic contributions. . . . 101

5.13 Numbers of events observed in the data and predicted for background processes from background-only fits to the signal and control regions in the seven signal regions of the $G_{\mathrm{KK}} \to ZW \to \ell\ell qq$ search. The numbers of signal events expected from the production of a G_{KK} with mass of 1 TeV are also shown for $k/\overline{M}_{\mathrm{Pl}} = 0.5$ and $k/\overline{M}_{\mathrm{Pl}} = 1.0$ respectively. The signal yields are calculated using $\sigma \times \mathcal{B}(G_{\mathrm{KK}} \to ZZ) = 20$ fb for both processes. The uncertainties combine statistical and systematic contributions. 101

5.14 The relative uncertainties from the leading uncertainty sources in the best-fit signal-strength parameter μ of hypothesized signal production of ggF $H \to ZZ$ with $m(H) = 600$ GeV and $m(H) = 1.2$ TeV [60]. For this study, the $H \to ZZ$ production cross section is assumed to be 95 fb at 600 GeV and 13 fb at 1.2 TeV, corresponding to approximately the expected median upper limits at these two mass values. 111

6.1 A summary of the criteria for object selections used in the $A \to ZH \to \ell\ell bb$ analysis. 116

6.2 Summary of the $A \to ZH \to \ell\ell bb$ event selection for the $n_b = 2$ and $n_b \geq 3$ categories. Definition: $\sqrt{\sum p_{\mathrm{T}}^2}/m_{\ell\ell bb} \equiv \left(\sum_i p_{T,i}^2\right)^{1/2}/m_{\ell\ell bb}$, where i runs over the leptons and the two leading b-tagged jets in p_T. m_{bb} sidebands correspond to $[0, 0.85 \cdot m_{\mathrm{H}} - 20) \cup (m_{\mathrm{H}} + 20, \infty)$ for the $n_b = 2$ category, and $[0, 0.85 \cdot m_{\mathrm{H}} - 25) \cup (m_{\mathrm{H}} + 50, \infty)$ for the $n_b \geq 3$ category. 120
6.3 Parameter tuning schemes for (a) EGE fit of gluon-gluon fusion in $n_b = 2$ category, (b) DSCB fit of b-associated production in $n_b = 2$ category, and (c) DSCB fit of b-associated production in $n_b \geq 3$ category. Δm represents the mass splitting between the A and H bosons, $m_{\mathrm{A}} - m_{\mathrm{H}}$. 127
6.4 Summary of the inputs entering the likelihood function. "N_{evt}" indicates that the number of events is used as the discriminant without any shape information and α refers to scale factors applied to the major background processes. 142
6.5 The effects of the most important sources of uncertainty on the strength parameter (μ) at two example mass points of $(m_{\mathrm{A}}, m_{\mathrm{H}}) = (230, 130)$ GeV and $(m_{\mathrm{A}}, m_{\mathrm{H}}) = (700, 200)$ GeV for both the gluon–gluon fusion and b-associated production of a narrow-width A boson. The signal cross-sections are taken to be the expected median upper limits as shown in Figure 6.33 and Figure 6.34. JES and JER stand for jet energy scale and jet energy resolution, 'Sim. stat.' for simulation statistics, and "Bkg. model." for the background modelling. 150

LIST OF ABBREVIATIONS

2HDM	Two-Higgs-Doublet Model
ALICE	A Large Ion Collider Experiment
ATLAS	A Toroidal LHC Apparatus
CERN	European Organization for Nuclear Research
CMS	Compact Muon Solenoid
CP	Charge-Parity
CSC	Cathode Strip Chambers
DY	Drell-Yell
ECF	Energy Correlation Function
EMEC	Electromagnetic End-Cap Calorimeter
EWPT	Electroweak Phase Transition
FCal	Forward Calorimeter
FCNC	flavor changing neutral current
ggF	Gluon-Gluon Fusion
GSC	Global Sequential Calibration
HEC	Hadronic End-Cap Calorimeter
HLT	High Level Trigger
HP	High-Purity
HVT	Heavy Vector Triplet
ID	Inner Detector
IP	Interaction Point
JES	Jet Energy Scale
KK	Kaluza–Klein
LHC	Large Hadron Collider
LHCb	The Large Hadron Collider Beauty Experiment
LP	Low-Purity
MC	Monte Carlo
MDT	Muon Drift Tube
MLE	Maximium Likelihood Estimation
MS	Muon Spectrometer
MSSM	Minimal Supersymmetric Standard Model
NP	Nuisance Parameter
PDF	parton distribution function
pp	Proton-Proton
PS	Proton Synchrotron
PSB	Proton Synchrotron Booster
QCD	Quantum Cchromodynamics
QFT	Quantum Field Theory
RPC	Resistive Plate Chambers

RS Randall-Sundrum

SCT Semiconductor Tracker

SF Scale Factor

SM Standard Model

BSM beyond the Standard Model

SPS Super Proton Synchrotron

SR Signal Region

TDAQ Trigger and Data Acquisition

TGC Thin Gap Chambers

TPS Thin Plate Spline

TopCR Top Control Region

TRT Transition Radiation Tracker

VBF Vector-Boson Fusion

VEV vacuum expectation value

ZCR Z+jets Control Region

ABSTRACT

Searches are presented for heavy resonances decaying into a Z boson and another boson (a W boson, a Z boson, or a heavy Higgs boson H) using data from proton-proton collisions at a center-of-mass energy of $\sqrt{s} = 13\,\text{TeV}$. The data were collected with the ATLAS detector in 2015 and 2016 at the Large Hadron Collider and correspond to a total integrated luminosity of $36.1\,\text{fb}^{-1}$. The searches are performed in the $\ell\ell qq$ final state wherein the Z boson decays into a pair of electrons or muons ($\ell = e, \mu$), and the other boson decays into two quarks (q). The decay product of the hadronically decaying boson is reconstructed as either two jets with small radii or a single large-radius jet, depending on the transverse momentum of the boson. No evidence for resonant production of ZH, ZW, or ZZ pairs is observed. Upper limits are derived at 95% confidence level on the product of the production cross section of a resonance and its decay branching ratio(s) for the selected benchmark signal models. The results are interpreted in the context of extensions of the Standard Model with additional Higgs bosons (e.g. a two-Higgs-doublet model), heavy vector triplets (a model independent framework for the interpretation of spin-1 resonances), and the Randall-Sundrum framework with a warped extra dimension.

CHAPTER 1

Introduction

The period of nearly 50 years, from the late 1960s to 2012, represented a giant leap forward in the understanding of the elementary constituents of the Universe at the most fundamental level. The Standard Model (SM) of particle physics [1–3], which classifies all known particles and provides a unified picture of the forces of relevance to particle physics, is undoubtedly one of the greatest triumphs of modern physics. With most of its theoretical concepts developed by the end of 1960s, the SM gained strong support with the discovery of the W and Z bosons at European Organization for Nuclear Research (CERN) in the mid 1980s. Finally, the Higgs boson [4, 5] discovered by the ATLAS (A Toroidal LHC Apparatus) [6] and CMS (Compact Muon Solenoid) [7] experiments in 2012 at the Large Hadron Collider (LHC) [8] completes the full spectrum of the Standard Model particles.

Despite its tremendous success in describing the current experimental data, the Standard Model cannot be the ultimate theory of particle physics, and many important questions remain unanswered. The origin of the numerical values of the free parameters in the SM is not known and those values simply have to be put in to fit the experimental observations. Additionally, more parameters need to be introduced to account for neutrino masses and mixing. The SM is not able to explain what might have happened that tipped the balance between matter and antimatter in the early universe. There is also no strong reason as to why there should exist only three generations of matter particles. Furthermore, the model does not incorporate the last known force of gravity, not to mention how gravity should be quantized. The SM only explains a fraction of the energy present in the universe and the nature of the astrophysical dark matter cannot be explained within the context of the SM.

Many theories, either extensions of the SM or entirely novel theoretical frameworks, have been proposed to address the deficiencies of the SM. This dissertation focuses on several of these theories. Common to all the models considered is the postulation of new resonances that can decay into a pair of bosons. Using data collected by the ATLAS detector in proton-proton collisions at a center-of-mass energy of 13 TeV at the LHC, this dissertation presents searches for resonant production of a Z boson and another boson (a W boson, a Z boson, or a heavy Higgs boson) in the $\ell\ell qq$ final state, where ℓ is either an electron or a muon and q denotes a quark.

A brief description of the underlying theoretical motivations is presented in Chapter 2. An overview of the LHC and the ATLAS detector is found in Chapter 3. Chapter 4 describes the techniques for reconstructing the physics objects used in this dissertation by combining information from different parts of the detector. Chapter 5 features the analysis searching for ZW and ZZ resonances in the $\ell\ell qq$ final state, which encompasses various aspects of a physics analysis and serves as a reference work for the analysis that follows. The second analysis, presented in Chapter 6, looks for a heavy Higgs boson decaying into a Z boson and another heavy Higgs boson in the same final state. Finally, a summary of the results of the two analyses is given in Chapter 7.

CHAPTER 2

Looking Beyond the Standard Model

2.1 The Standard Model of Particle Physics

The SM of particle physics was developed in stages during the course of the 20th century. The theory attempts to describe and classify the elementary particles as well as to formulate the interactions between them. Three of the four known fundamental forces that govern the universe—electromagnetic, weak, and strong interactions—are described by the SM.

2.1.1 Brief Overview

To put the formulation of the SM in a nutshell, all matter in nature is composed of fermions, and the forces or interactions between particles are mediated by force carrying gauge bosons. The Brout-Englert-Higgs mechanism [9–14] gives rise to the masses of the gauge bosons, and the fermions acquire mass from Yukawa-type interactions with the Higgs field. The detailed content of the particles of the SM is shown in Figure 2.1. Leptons and quarks constitute the fundamental building blocks of matter. They are divided into three generations with increasing masses, although the mass hierarchy of the neutrinos has not been established experimentally. Fermions are spin-1/2 particles. Each fermion has a corresponding anti-particle which shares the same mass and spin but has the rest of the quantum numbers reversed. In each generation, there are two types of quarks, an up-type with an electric charge of 2/3 and a down-type with a charge of -1/3. Similarly, two types of leptons exist in each generation: charged leptons and neutral ones (neutrinos). Each quark comes with three colors (red, green or blue) and also possesses a quantum number called baryon number. A lepton number is assigned to each generation of the leptons and is found to be a conserved property by experiments. The particles interact with each other

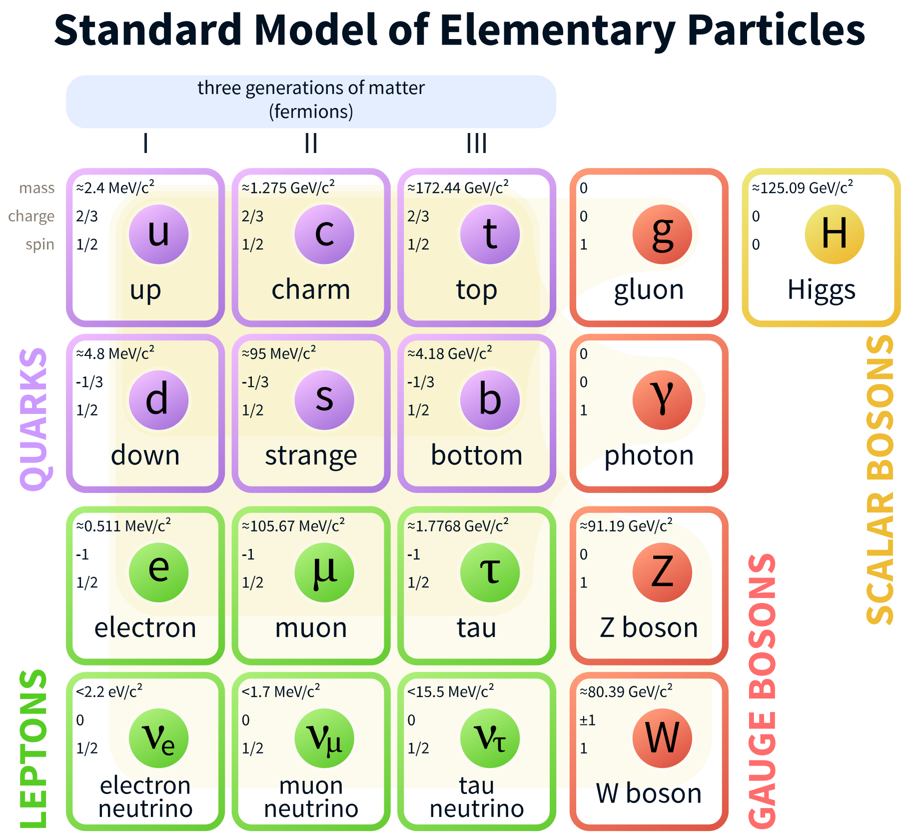

Figure 2.1: A schematic drawing of the particle content of the Standard Model Physics. The particles are classified into three broad categories: the three generations of matter particles (fermions), gauge bosons, and the Higgs boson.

through the exchange of force carrier particles. These force carriers, which are listed below, are vector gauge bosons which possess a spin quantum number of 1:

- W^+, W^-, and Z^0 bosons: massive, are force carriers of the weak nuclear force;
- Photon (γ): massless, are force carriers of the electromagnetic force;
- Eight gluons (g): massless, are force carriers of the strong force.

The dynamics of the SM is described by a Lagrangian based on the formalism of quantum field theory (QFT), with the action integrated over all space-time of the Lagrangian density $\mathcal{L}_{\text{SM}}(x)$. Symmetries play important roles in the SM because of the implications of Noether's theorem [15]. As the theorem states, if an action is invariant under some group of transformations (symmetry), then there exists one or more conserved quantities associated with these transformations. Developed as a relativistic QFT from the onset, the SM works fully in accordance with special relativity.

Therefore, Poincaré symmetry, which includes translations, rotations and boosts, is a global continuous symmetry of the theory. Associated with this global symmetry are three conserved quantities: energy, momentum, and angular momentum.

The complete local gauge symmetry of the SM Lagrangian is defined by the group $SU(3)_C \times SU(2)_L \times U(1)_Y$, which governs the strong and electroweak interactions. The transformations under this group are gauge transformations, and additional gauge fields are introduced in order to preserve the symmetry under given transformations. Only then is the Lagrangian gauge invariant under these symmetry transformations. Specifically, $SU(2)_L \times U(1)_Y$ group symmetry dictates the unified electroweak interactions of the SM. The electroweak gauge group is associated with one field from $U(1)_Y$ and three fields from $SU(2)_L$. These fields together give rise to $W^{\pm}$, Z and γ through electroweak symmetry breaking. On the other hand, the strong interactions are detailed in quantum cchromodynamics (QCD) which is a non-Abelian gauge theory transforming under the symmetry group $SU(3)_C$. $SU(3)_C$ is associated with eight gluon fields carrying three color charges and mediating interactions between colored objects (i.e. quarks and gluons).

The final component of the SM is the Higgs Mechanism without which the underlying gauge symmetry of the electroweak interaction is broken by the masses of the associated gauge bosons. A scalar field (the Higgs field) is introduced and it acquires a non-zero vacuum expectation value through spontaneous symmetry breaking in vacuum. The spontaneous breaking of the symmetry results in massless Goldstone bosons, which are absorbed by the W and Z bosons as their longitudinal polarizations as they become massive, and the remaining degree of freedom results in a massive scalar boson, the Higgs boson. Fermions acquire mass via interactions with the Higgs field which are scaled by Yukawa couplings. The SM is then complete after the addition of all the terms introduced by the Higgs field and its Lagrangian can be summarized as:

$$\mathcal{L}_{\text{SM}} = \mathcal{L}_{\text{gauge}} + \mathcal{L}_{\text{fermions}} + \mathcal{L}_{\Phi} + \mathcal{L}_{\text{Yukawa}}. \tag{2.1}$$

The $U(1)_Y$, $SU(2)_L$ and $SU(3)_C$ gauge terms are:

$$\mathcal{L}_{\text{gauge}} = -\frac{1}{4}B_{\mu\nu}B^{\mu\nu} - \frac{1}{4}W^a_{\mu\nu}W^{a\mu\nu} - \frac{1}{4}G^a_{\mu\nu}G^{a\mu\nu}, \tag{2.2}$$

where:

$$\begin{aligned}
G^a_{\mu\nu} &= \partial_\mu G^a_\nu - \partial_\nu G^a_\mu - g_3 f^{abc} G^b_\mu G^c_\nu \quad (a = 1, 2, ..., 8) && (2.3)\\
W^a_{\mu\nu} &= \partial_\mu W^a_\nu - \partial_\nu W^a_\mu - g\epsilon^{abc} W^b_\mu W^c_\nu \quad (a = 1, 2, 3) && (2.4)\\
B_{\mu\nu} &= \partial_\mu B_\nu - \partial_\nu B_\mu && (2.5)
\end{aligned}$$

are the $SU(3)_C$, $SU(2)_L$ and $U(1)_Y$ field strengths. The structure constants for $SU(3)_C$ are f^{abc} and the totally antisymmetric ϵ^{abc} (with $\epsilon^{123} = +1$) are the structure constants for $SU(2)_L$. Left-handed fermions are known to be doublets under $SU(2)_L$:

$$\begin{pmatrix} \nu_e \\ e_L \end{pmatrix}, \quad \begin{pmatrix} \nu_\mu \\ \mu_L \end{pmatrix}, \quad \begin{pmatrix} \nu_\tau \\ \tau_L \end{pmatrix}, \quad \begin{pmatrix} u_L \\ d_L \end{pmatrix}, \quad \begin{pmatrix} c_L \\ s_L \end{pmatrix}, \quad \begin{pmatrix} t_L \\ b_L \end{pmatrix}. \tag{2.6}$$

And the right-handed fermions

$$e_R, \quad \mu_R, \quad \tau_R, \quad u_R, \quad c_R, \quad t_R, \quad d_R, \quad s_R, \quad b_R, \tag{2.7}$$

are all singlets under $SU(2)_L$. The fermion terms in the Lagrangian are then written as a sum over the three families:

$$\mathcal{L}_{\text{fermions}} = \sum_f^{1,2,3} \Big[\bar{L} i\gamma^\mu D^L_\mu L^f + \bar{e}^f_R i\gamma^\mu D^R_\mu e^f_R + \bar{Q}^f_L i\gamma^\mu D^L_\mu Q^f_L + \bar{q}^f_R i\gamma^\mu D^R_\mu q^f_R \Big]. \tag{2.8}$$

In the above equation, L^f and Q^f_L denote the left-handed doublets for each family of the leptons and quarks, respectively; e^f_R represents the singlets for the charged leptons; q^f_R represents the singlets for the up-type and down-type quarks. The covariant derivatives acting on the fermion fields are:

$$\begin{aligned}
D_\mu \begin{pmatrix} \nu_L \\ e_L \end{pmatrix} &= \Big[\partial_\mu + ig' B_\mu Y_{f_L}/2 + igW^a_\mu T^a \Big] \begin{pmatrix} \nu_L \\ e_L \end{pmatrix}, && (2.9)\\
D_\mu e_R &= \Big[\partial_\mu + ig' B_\mu Y_{f_R}/2 \Big] e_R, && (2.10)\\
D_\mu \begin{pmatrix} u_L \\ d_L \end{pmatrix} &= \Big[\partial_\mu + ig' B_\mu Y_{f_L}/2 + igW^a_\mu T^a + ig_3 G^a_\mu T'^a \Big] \begin{pmatrix} u_L \\ d_L \end{pmatrix}, && (2.11)\\
D_\mu q_R &= \Big[\partial_\mu + ig' B_\mu Y_{f_R}/2 + ig_3 G^a_\mu T'^a \Big] q_R. && (2.12)
\end{aligned}$$

The $U(1)_Y$ weak hypercharge of any field f is given in terms of the electric charge and the eigenvalue of the third component of the weak isospin matrix: $Y_f = 2(Q_f - I^3_f)$.

I_f^3 is $+1/2$ for the upper component of a doublet, $-1/2$ for the lower component of a doublet, and 0 for an $SU(2)_L$ singlet. The $SU(2)_L$ representation matrix generators acting on these fields are proportional to the Pauli matrices: $T^a = \sigma^a/2$ ($a = 1, 2, 3$). The eight generators of the $SU(3)_C$ symmetry group are given by: $T'^a = \lambda^a/2$ ($a = 1, ..., 8$) where the λ^a are known as the Gell-Mann matrices. g', g and g_3 are the coupling constants of the $U(1)_Y$, $SU(2)_L$ and $SU(3)_C$ groups, respectively.

The physical W bosons can be identified as the linear combinations:

$$W_\mu^\pm \equiv \frac{1}{\sqrt{2}}(W_\mu^1 \mp iW_\mu^2). \tag{2.13}$$

The gauge eigenstate fields B_μ and W_μ^3 are both electrically neutral, and they mix as a result of spontaneous symmetry breaking. The mass eigenstate fields, which are observed as the photon field (A_μ) and the massive Z boson vector field (Z_μ), are related to the gauge eigenstate fields through a rotation in field space by an angle θ_W:

$$\begin{pmatrix} A_\mu \\ Z_\mu \end{pmatrix} = \begin{pmatrix} \cos\theta_W & \sin\theta_W \\ -\sin\theta_W & \cos\theta_W \end{pmatrix} \begin{pmatrix} B_\mu \\ W_\mu^3 \end{pmatrix}. \tag{2.14}$$

θ_W is known as the weak mixing angle or Weinberg angle and satisfies:

$$\sin\theta_W = \frac{g'}{\sqrt{g^2 + g'^2}}; \quad \cos\theta_W = \frac{g}{\sqrt{g^2 + g'^2}}. \tag{2.15}$$

The Lagrangian density for the scalar field is:

$$\begin{aligned} \mathcal{L}_\Phi &= (D^\mu\Phi)^\dagger D_\mu\Phi - V(\Phi, \Phi^\dagger) \\ &= (D^\mu\Phi)^\dagger D_\mu\Phi - \mu^2\Phi^\dagger\Phi - \lambda\left(\Phi^\dagger\Phi\right)^2, \end{aligned} \tag{2.16}$$

where the scalar Higgs field with weak hypercharge $Y_\Phi = +1$ is introduced as a complex $SU(2)_L$ doublet:

$$\Phi = \begin{pmatrix} \phi^+ \\ \phi^0 \end{pmatrix}. \tag{2.17}$$

In the case of spontaneous symmetry breaking with $\mu^2 < 0$, the vacuum expectation value (VEV) of Φ is chosen to be real, and entirely in the second component (electrically neutral) of the Higgs field:

$$\langle\Phi\rangle_0 = \begin{pmatrix} 0 \\ v/\sqrt{2} \end{pmatrix}. \tag{2.18}$$

In the unitary gauge, the neutral scalar field can be expressed in terms of its deviation from its VEV: $\phi^0 = (v + h(x))/\sqrt{2}$. The field $h(x)$ here creates and destroys the physical Higgs boson. The kinetic term of $\mathcal{L}_\Phi$ in the unitary gauge becomes:

$$\begin{aligned}\mathcal{L}_{\Phi\,\text{kinetic}} &= (D^\mu\Phi)^\dagger\, D_\mu\Phi \\ &= \frac{1}{2}\partial_\mu h\partial^\mu h + \frac{(v+h)^2}{4}\left[g^2 W^+_\mu W^{-\mu} + \frac{1}{2}(g^2 + g'^2) Z_\mu Z^\mu\right] \end{aligned} \tag{2.19}$$

There is no mass term in Equation (2.19) for the photon field A_μ; therefore, the photon remains massless and $U(1)_{\text{EM}}$ gauge invariance remains unbroken. The masses for the $W^\pm$ and Z vector bosons are predicted to be:

$$m_W^2 = \frac{g^2 v^2}{4}, \quad m_Z^2 = \frac{(g^2 + g'^2)v^2}{4} \quad \text{with } m_W/m_Z = \cos\theta_W, \tag{2.20}$$

which agrees with the experimental values provided that the VEV is approximately

$$v = \sqrt{2}\langle\phi^0\rangle = 246\,\text{GeV}. \tag{2.21}$$

The Higgs potential $V(\Phi, \Phi^\dagger)$ gives rise to a mass and self-interactions for h. In the unitary gauge:

$$V(h) = \lambda v^2 h^2 + \lambda v h^3 + \frac{\lambda}{4}h^4 \quad \text{with } m_h = \sqrt{2\lambda}v. \tag{2.22}$$

Finally, the gauge-invariant fermion mass terms are accounted for by adding interactions between the fermions and the scalar field:

$$\mathcal{L}_{\text{Yukawa}} = \sum_f^{1,2,3}\Big[- y_\ell \bar{L}\Phi e_R - y_d \bar{Q}_L \Phi d_R - y_u \bar{Q}_L (i\sigma_2)\Phi^* u_R + \text{h.c.}\Big], \tag{2.23}$$

where y_ℓ, y_d and y_u are the corresponding Yukawa coupling constants for the fermions. In the unitary gauge, the gauge-invariant Yukawa interactions can be summarized as:

$$\mathcal{L}_{\text{Yukawa}} = -\sum_f \frac{y_f}{\sqrt{2}}(v+h)\bar{f}f, \tag{2.24}$$

where the fermion mass and the h-fermion coupling are both proportional to y_f.

2.2 Looking Beyond

Despite having been tested to great precision through a great range of physics processes in various experiments, the Standard Model is not entirely satisfactory theoretically. The SM is associated with the hierarchy problem in which the bare Higgs mass must be unnaturally fine-tuned to cancel the large loop corrections. The model does not explain the quantum numbers of the particles, and it contains at least 19 arbitrary parameters. The neutrinos, which are known to have mass from various neutrino oscillation experiments, are described as massless particles in the SM. Furthermore, it is not certain whether the mass of the neutrinos would arise in the same way as the masses of the other fundamental particles in the SM. The SM, which predicts that the amount of matter and antimatter should have been the same if the initial conditions of the universe did not involve an imbalance, is not able to explain the baryon asymmetry in the observable universe. Furthermore, astronomical evidence strongly suggests that there exist dark matter and dark energy, which together account for about 95% of the total energy present in the universe, whereas the SM only explains roughly 5% of it. There is also a chase for a grand unified theory which provides a group framework for unifying all the particle interactions. A few theories beyond the Standard Model (BSM) are introduced in the remainder of this section, along with the benchmark models that are explored in the searches in this dissertation.

2.2.1 Two-Higgs-Doublet Model

A two-Higgs-doublet model (2HDM) [16–18], which introduces a second $SU(2)_L$ doublet Φ_2 with weak hypercharge $Y = +1$, is among the simplest possible extensions of the SM. 2HDMs are attractive because they are very well motivated theoretically and can lead to very rich phenomenology. Supersymmetric theories, e.g. the Minimal Supersymmetric Standard Model (MSSM), contain two Higgs doublets. The effective low-energy theory for some axion models still requires two Higgs doublets and some 2HDMs provide dark matter candidates. 2HDMs can also generate the observed baryon asymmetry, due to the flexibility of their scalar mass spectra and additional sources of Charge-Parity (CP) violation. The general scalar potential for a 2HDM contains 14 parameters and can have CP-conserving, CP-violating, and charge-violating minima. However, most phenomenological studies of the 2HDMs make simplifying assumptions. For instance, the requirement of CP conservation is often imposed in the scalar sector, in which case scalars are distinguishable from pseudo-scalars. The most general scalar Higgs potential is then given by:

$$\begin{aligned}\mathcal{V} =& m_{11}^2\Phi_1^\dagger\Phi_1 + m_{22}^2\Phi_2^\dagger\Phi_2 - m_{12}^2\left(\Phi_1^\dagger\Phi_2 + \Phi_2^\dagger\Phi_1\right) + \frac{\lambda_1}{2}\left(\Phi_1^\dagger\Phi_1\right)^2 + \frac{\lambda_2}{2}\left(\Phi_2^\dagger\Phi_2\right)^2 \\ &+ \lambda_3\Phi_1^\dagger\Phi_1\Phi_2^\dagger\Phi_2 + \lambda_4\Phi_1^\dagger\Phi_2\Phi_2^\dagger\Phi_1 + \frac{\lambda_5}{2}\left[\left(\Phi_1^\dagger\Phi_2\right)^2 + \left(\Phi_2^\dagger\Phi_1\right)^2\right],\end{aligned} \tag{2.25}$$

where all the parameters are taken to be real. The minimum of the potential corresponding to a CP-conserving vacuum yields:

$$\langle\Phi_1\rangle = \begin{pmatrix} 0 \\ v_1/\sqrt{2} \end{pmatrix}, \qquad \langle\Phi_2\rangle = \begin{pmatrix} 0 \\ v_2/\sqrt{2} \end{pmatrix}. \tag{2.26}$$

The corresponding vacuum expectation values of the neutral scalar fields are $\langle\Phi_i^0\rangle = v_i/\sqrt{2}$ $(i = 1, 2)$, with $v \equiv (v_1^2 + v_2^2)^{1/2} = 246\,\mathrm{GeV}$. There are eight degrees of freedom associated with the complex scalar $SU(2)$ doublets; three of them become the longitudinal components of $W_\mu^\pm$ and Z_μ^0 to give masses to the $W^\pm$ and Z gauge bosons. The remaining contents manifests themselves as five scalar particles: two neutral scalars (h and H), a pseudo-scalar (A) and two charged scalars ($H^\pm$). One of the most important parameters in studies of 2HDMs is defined as:

$$\tan\beta \equiv \frac{v_2}{v_1}. \tag{2.27}$$

By meeting the potential minimum conditions, six free parameters are left: m_{12}^2 and the five real Higgs self-couplings (λ_1, λ_2, ..., λ_5). From these six parameters, one can compute the four physical Higgs masses (m_h, m_H, m_A, and $m_{H^\pm}$) and the neutral CP-even Higgs mixing angle α. At the SM alignment limit, $\cos(\beta - \alpha) \simeq 0$, the couplings of the h coincide with the tree-level couplings of the SM Higgs boson.

In addition to aforementioned parameters, there are several ways of choosing the Yukawa couplings. If tree-level FCNCs are to be avoided, four arrangements are defined: Type-I, Type-II, lepton-specific, and flipped 2HDMs. In the Type-I model, the fermions only couple to the second doublet Φ_2, whereas the vector bosons only couple to Φ_1. Leptons couple to Φ_1 in the Type-II model, and up- and down-type quarks couple to separate doublets: the up-type couples to Φ_2 and the down-type to Φ_1. In the lepton-specific model, one has the quarks coupling to Φ_2 and the leptons to Φ_1. In the flipped model, the up- and down-type quarks have the same couplings as those in Type-II, and the leptons couple to Φ_2.

2.2.2 Heavy Vector Triplets

The heavy vector triplet (HVT) [19, 20] model adopts a simplified phenomenological Lagrangian to provide a framework for a large variety of explicit BSM models. The motivation of this simplified approach is to circumvent the complexity brought by the many free parameters in most of the explicit models and to make the experimental results based on the simplified Lagrangian translatable into explicit models where the parameter relations between the simplified model and an explicit model can be obtained. A real vector V^a_μ ($a = 1, 2, 3$) is considered in the adjoint representation of $SU(2)_L$ as a weak-isospin triplet with vanishing hypercharge. It describes two charged and one neutral heavy spin-1 particles with the charge eigenstate fields defined by the following relations [20]:

$$V^\pm_\mu = \frac{V^1_\mu \mp i V^2_\mu}{\sqrt{2}}, \quad V^0_\mu = V^3_\mu. \tag{2.28}$$

The dynamics of the new vector is described by a simplified phenomenological Lagrangian [20]:

$$\begin{aligned}\mathcal{L}_V = &-\frac{1}{4} D_{[\mu} V^a_{\nu]} D^{[\mu} V^{\nu]\,a} + \frac{m_V^2}{2} V^a_\mu V^{\mu\,a} \\ &+ i g_V c_H V^a_\mu H^\dagger \tau^2 \overleftrightarrow{D}^\mu H + \frac{g^2}{g_V} c_F V^a_\mu J^{\mu\,a}_F \\ &+ \frac{g_V}{2} c_{VVV} \epsilon_{abc} V^a_\mu V^b_\nu D^{[\mu} V^{\nu]\,c} + g_V^2 c_{VVHH} V^a_\mu V^{\mu\,a} H^\dagger H - \frac{g}{2} C_{VVW} \epsilon_{abc} W^{\mu\nu\,a} V^b_\mu V^c_\nu.\end{aligned} \tag{2.29}$$

In the above equation, g_V represents the typical strength of the new boson interactions, c_H and c_F are dimensionless factors parameterizing the deviation of the V coupling to SM gauge bosons and fermions from the typical value, respectively. The covariant derivatives are defined as:

$$D_{[\mu} V^a_{\nu]} = D_\mu V^a_\nu - D_\nu V^a_\mu, \quad D_\mu V^a_\nu = \partial_\mu V^a_\nu + g \epsilon^{abc} W^b_\mu V^c_\nu, \tag{2.30}$$

where g denotes the $SU(2)_L$ gauge coupling. The fermionic currents are defined as:

$$J^{\mu\,a}_F = \sum_f \bar{f}_L \gamma^\mu (\sigma^a/2) f_L \tag{2.31}$$

The first term on the second line of Equation (2.29), which is proportional to $g_V c_H$, describes its coupling to SM vector bosons and the Higgs boson. Similarly the second

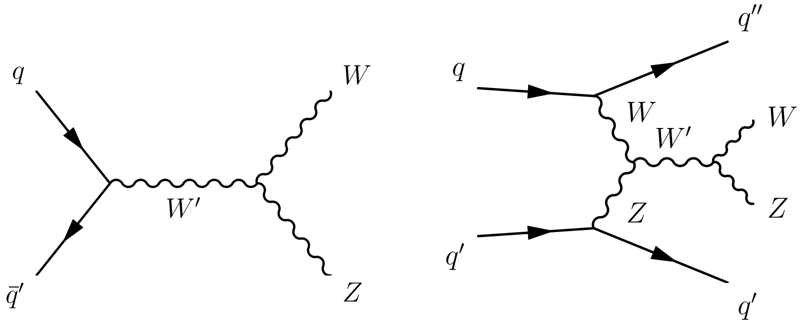

Figure 2.2: Feynman diagrams for W' produced via Drell-Yan (left) and vector-boson fusion (right) processes.

term on the same line, proportional to $\frac{g^2}{g_V}c_F$, contains the coupling between the new boson V and SM fermions. The relevant decay modes of this resonance are di-lepton, di-quark and di-boson. The decay widths of di-lepton and di-quark channels are given by:

$$\Gamma_{V_\pm \to f\bar{f}'} \simeq 2\Gamma_{V_0 \to f\bar{f}} \simeq N_c[f]\left(\frac{g^2 c_F}{g_V}\right)^2 \frac{M_V}{48\pi}, \tag{2.32}$$

where $N_c[f]$ is the number of colors and is equal to 3 for the di-quark and to 1 for the di-lepton decays. The partial decay widths of the other two channels mentioned can be computed as follows:

$$\Gamma_{V_\pm \to W_L^\pm Z_L} \simeq \Gamma_{V_0 \to W_L^+ W_L^-} \simeq \frac{g_V^2 c_H^2 M_V}{192\pi}[1 + \mathcal{O}(\varsigma^2)], \tag{2.33}$$

$$\Gamma_{V_0 \to Z_L h} \simeq \Gamma_{V_\pm \to W_L^\pm h} \simeq \frac{g_V^2 c_H^2 M_V}{192\pi}[1 + \mathcal{O}(\varsigma^2)], \tag{2.34}$$

where $\varsigma = g_V v/(2m_V)$. $\varsigma \ll 1$ is the most common situation, $\varsigma \sim 1$ only occurs in strongly coupled scenarios at very large g_V.

The predicted resonances are produced via two relevant channels as illustrated in Figure 2.2, Drell-Yell (DY) and vector-boson fusion (VBF). VBF production is sub-leading in most of the motivated part of parameter space. Searches at the LHC generally interpret two explicit benchmark models: model A and model B. Model A of the HVT is a weakly coupled model which corresponds to heavy vectors emerging from an underlying extended gauge symmetry. In model A, $g_V \sim g \sim 1$, $c_H \sim -g^2/g_V^2$ and $c_F \sim 1$. On the other hand, the strongly interacting model B describes the triplet in the context of the Minimal Composite Higgs Model where $c_H \sim c_F \sim 1$ and $g_V = 3$. Consequently, it can be seen from Equation (2.32) - (2.34) and from

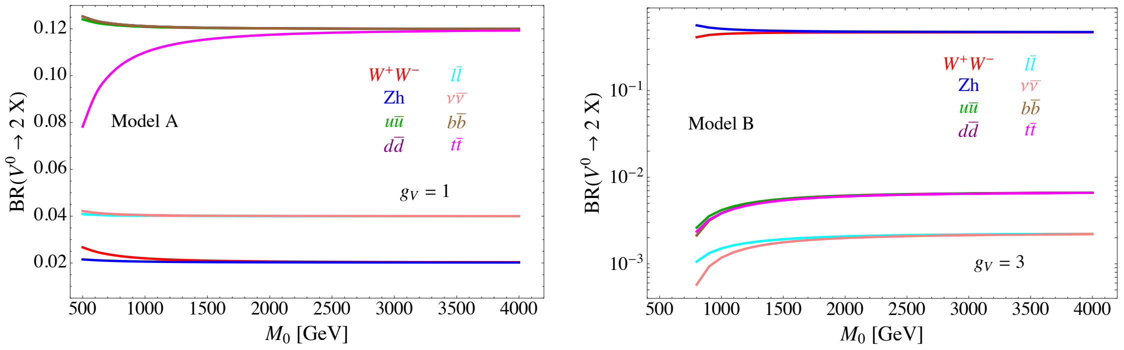

(a) (b)

Figure 2.3: Branching Ratios for the two body decays of the neutral vector V^0 for the benchmarks $A_{g_V} = 1$ (left) and $B_{g_V} = 3$ (right) [20]. Note that the left plot is in linear scale, whereas the plot on the right-hand side uses a semi-logarithmic scale on the y-axis.

Figure 2.3 that in model A—which predicts $g_V c_H \simeq g^2 c_F / g_V \simeq g^2 / g_V$—the branching ratios of the vector triplets decaying into into fermions and bosons are comparable. On the contrary, decays into fermions are extremely suppressed in model B and diboson decays become the dominant decay channels.

2.2.3 Bulk Randall-Sundrum Graviton

The Randall-Sundrum (RS) framework [21–23] attempts to explain the Planck-weak hierarchy problem by introducing a warped extra dimension as illustrated in Figure 2.4. In the RS scenarios, the universe consists of two parallel $(3+1)$-branes, called the “Planck brane” and the “weak brane” (or “TeV brane”). The observable universe is constrained to live on the weak brane, and the forces are unified on the Planck brane. The large difference between the mass scales of the two branes is generated through the deformation of the spacetime between the branes. This deformation is called “warping” and it affects the strength of gravity as it is measured at different points in space. The following non-factorizable spacetime metric comes as a solution to Einstein’s equations in a simple set-up with the two branes and appropriate cosmological terms [21]:

$$ds^2 = e^{-2kr_c\phi}\eta_{\mu\nu}dx^\mu dx^\nu + r_c^2 d\phi^2. \tag{2.35}$$

Equation (2.35) has two free parameters, k and r_c. k represents a common energy scale of the theory which is of order the Planck scale; r_c corresponds to the radius of

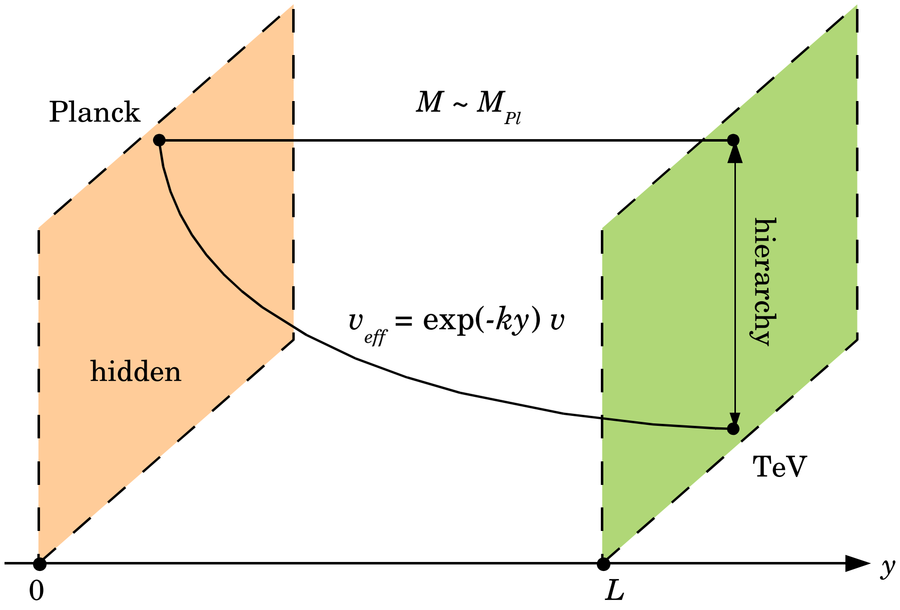

Figure 2.4: In the bulk RS model, the Planck brane is separated from the weak brane by a warped extra dimension. The generation of an exponential hierarchy is shown.

the curvature of the warped extra dimension. This warped extra dimension leads to a bulk separation between two $3 + 1$ dimensional branes, on which dynamics occur at the ultraviolet scale and the infrared scale, respectively. In the setup, the Higgs field is constrained on the weak brane. The large hierarchy of scales can then be generated with a modest-sized radius of the fifth dimension owing to the exponential warp factor: $e^{-2kr_c\phi}$. In the RS model considered in this dissertation, the SM matter fields are allowed to propagate in the extra dimension and this scenario is referred to as bulk scenario hereinafter. In the bulk scenario, contributions to the flavor changing neutral current (FCNC) processes are highly suppressed and the fermion flavor hierarchy puzzle can be solved [22].

The warped nature of the extra dimension leads to the massless graviton acquiring a tower of excited states—Kaluza–Klein (KK) modes. The KK excitations of the gravitational field appear as well separated TeV-scale spin-2 Gravitons (G_{KK}), which are accessible at the LHC. The bulk RS graviton is the first of such excitation states localized near the TeV brane. The gluon-gluon fusion (ggF) (Figure 2.5) serves as the dominant production mechanism due to the fact that the light fermions reside far from the TeV brane; the KK graviton has a small overlap with them. The decays of the KK graviton into longitudinal gauge bosons W/Z (W_L/Z_L) can be significant as a result of the enhancement through the strong coupling of the KK graviton to the Higgs field.

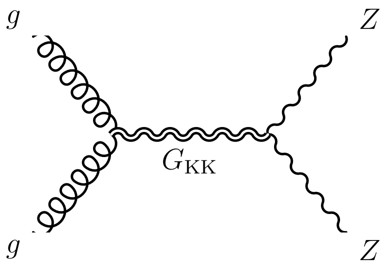

Figure 2.5: A Feynman diagram showing the gluon-gluon fusion production mode for G_{KK}.

The factor $k/\overline{M}_{\mathrm{pl}}$ dictates the width of the bulk RS graviton, where k represents the curvature scale and $\overline{M}_{\mathrm{pl}}$ is the reduced Planck mass. In this dissertation, $k/\overline{M}_{\mathrm{pl}} = 1$ and $k/\overline{M}_{\mathrm{pl}} = 0.5$ are studied since the theory will become non-perturbative ($k/\overline{M}_{\mathrm{pl}} \sim 3$) if large values of $k/\overline{M}_{\mathrm{pl}}$ are assumed.

2.3 Benchmark Models

This section describes the benchmark models and the corresponding experimental signatures considered in the searches.

2.3.1 Models Considered in the ZW/ZZ Resonance Searches

In the context of a general 2HDM, an additional neutral CP-even scalar in the mass range from 300 GeV to 3000 GeV is considered for the $H \to ZZ$ resonance search. The width of this generic spin-0 resonance is assumed to be narrow ($\Gamma_{\mathrm{H}} = 4\,\mathrm{MeV}$) and negligible when compared to the intrinsic detector resolution. Both ggF and VBF productions are taken into account and the interference between the new resonance and the SM diboson processes is neglected. A spin-1 W' boson in the context of the HVT framework with the decay $W' \to ZW$, and a spin-2 RS graviton from the bulk RS model decaying to a pair of Z bosons ($G_{\mathrm{KK}} \to ZZ$) are also considered. Both model A and model B are considered for the DY production of the W' with $g_V = 1$ and $g_V = 3$, respectively. A VBF production of the spin-1 resonance is also included in the interpretation. For the spin-2 resonance, only the dominant ggF production is taken into account for the RS graviton.

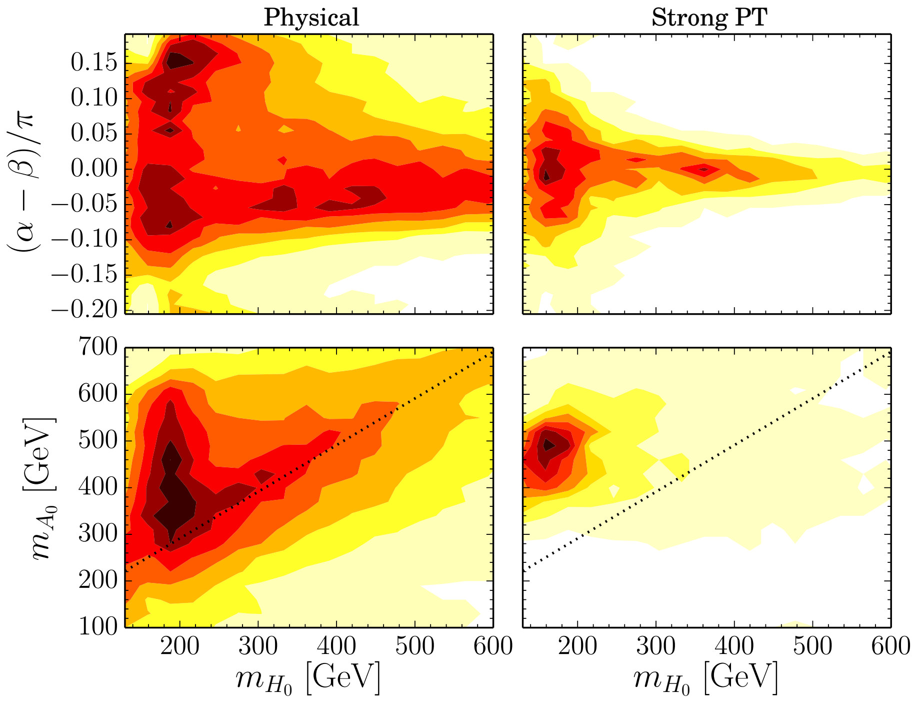

Figure 2.6: Heat-maps for the physical region (*left*) and region with a strongly first-order EWPT (*right*). *Top*: $(m_H, \alpha - \beta)$-plane. *Bottom*: (m_H, m_A)-plane. The dotted-black line corresponds to $m_A = m_H + m_Z$. Note that the $\alpha - \beta$ differs from the one defined in Section 2.2.1 by $\pi/2$ [18].

2.3.2 Models Considered in the ZH Resonance Search

The mechanism (baryogenesis) that could produce baryon asymmetry is long sought-after. In order for baryogenesis to happen at the electroweak phase transition, several requirements have to be met [24]. Firstly, the temperature evolution of the Higgs potential must be such that the electroweak phase transition is a first-order transition. This means that there exist two degenerate vacua at some critical temperature (T_c) and the phase transition proceeds through the formation of bubbles of the new vacuum that gradually increase and fill the whole space. Secondly, new sources of CP violation are needed in order to create the matter–antimatter asymmetry close to the bubble walls. Finally, in order for the asymmetry to survive the electroweak sphaleron interactions that violate baryon numbers, T_c must be low enough compared to the Higgs vacuum expectation value which implies a “strong” 1st order phase transition.

The $A \to ZH$ search is motivated by a cosmological first-order electroweak phase transition (EWPT) induced by the existence of a second Higgs doublet. CP symmetry is assumed to be conserved in the 2HDMs for simplification. Although extra sources of

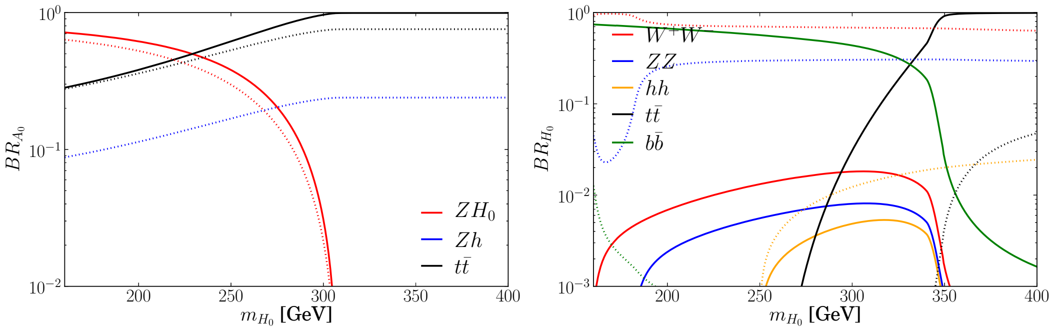

Figure 2.7: *Left*: main Branching Ratios of the CP-odd scalar A as a function of m_H for $m_A = m_{H^\pm} = 400$ GeV, $\tan\beta = 2$, $\mu = 100$ GeV, $\alpha - \beta = 0.001\pi$ (solid lines) and $\alpha - \beta = 0.1\pi$ (dotted lines). *Right*: main Branching Ratios of H as a function of m_H (same benchmark parameters as in *left*). These branching ratios are for the Type-I 2HDM. Note that the $\alpha - \beta$ differs from the one defined in Section 2.2.1 by $\pi/2$ [18].

CP violation are crucial to the electroweak baryogenesis, it is argued in Ref. [25] that the CP-violating phase does not substantially influence the phase transition, which is of interest here. Although the type of 2HDM is irrelevant to the EWPT (since all the types couple in the same way to the top quark), it does have an impact on the Higgs properties and constraints from the LHC. The Type-I 2HDM is chosen for the study; a Monte Carlo scan (Figure 2.6) over the possible values of m_H, m_A, $m_{H^\pm}$, $\tan\beta$, and $(\alpha - \beta)$ is performed to select points in the parameter space that satisfy unitarity, perturbativity, electroweak precision and bounds [18]. In Figure 2.6, the heat-maps for the physical region is displayed in the left column and the right column corresponds to the region with a strongly first-order EWPT in planes $(m_H, \alpha-\beta)$ and (m_H, m_A). The results suggest that a strong EWPT prefers a SM-like h; therefore, the lightest CP-even Higgs boson h is assumed to be SM-like in the benchmark models, i.e. $\cos(\beta - \alpha) \simeq 0$.

Current 2HDM searches at the LHC are primarily motivated by the MSSM, in which the scalar mass splittings are dictated by the gauge couplings and do not exceed m_Z. In these searches, $A \to b\bar{b}$, $A \to \tau\tau$ and $A \to t\bar{t}$ are of relevance. However, a strongly first-order EWPT in 2HDM as shown in Figure 2.6 tends to prefer a relatively large mass splitting between A and H ($m_A - m_H \gtrsim v$) at the alignment limit. Consequently, the decay $A \to ZH$ is favored because the amount of parameter space available is large and that $g_{AZH} \sim \sin(\alpha - \beta)$ is unsuppressed. On the contrary, g_{AZh} is proportional to $\cos(\alpha - \beta)$ and vanishes at the alignment limit. In Figure 2.7 (left) branching ratios of the main decay modes of A are shown as a function of m_H for two benchmark scenarios A and B. In both cases, the decay

$A \to ZH$ dominates largely in the regime $m_A - m_H \gtrsim v$ and is more pronounced for scenario A which is closer to the alignment limit. It can also be observed in Figure 2.7 (right) that as one approaches the alignment limit, the subsequent decay of $H \to bb$ becomes the most important decay mode in the same regime where $m_H \lesssim 300$ GeV. Therefore, for searches for 2HDMs with a strongly first-order EWPT at the LHC, $A \to ZH \to \ell\ell bb$ is one of the most practical search channels.

2.4 Proton-Proton Collisions

Protons are composite particles comprised of quarks and gluons (partons). The inelastic scattering of protons are modeled in terms of interacting partons. Cross sections of various processes depend on the parton distribution functions (PDFs), which are defined as the probability to find a parton of a particular flavor with x fraction of the proton's momentum at some energy scale Q. Figure 2.8 shows example PDFs at two energy scales. The valence quarks, up and down, carry most of the momentum; the fraction carried by the up-quark is roughly twice that carried by the down-quark because there are two up-quarks and one down-quark in a proton. At higher energy scales, the sea quarks and gluons carry more of the proton's momentum; thus, for higher energy collisions, processes initiated with gluons or sea quarks become more prominent.

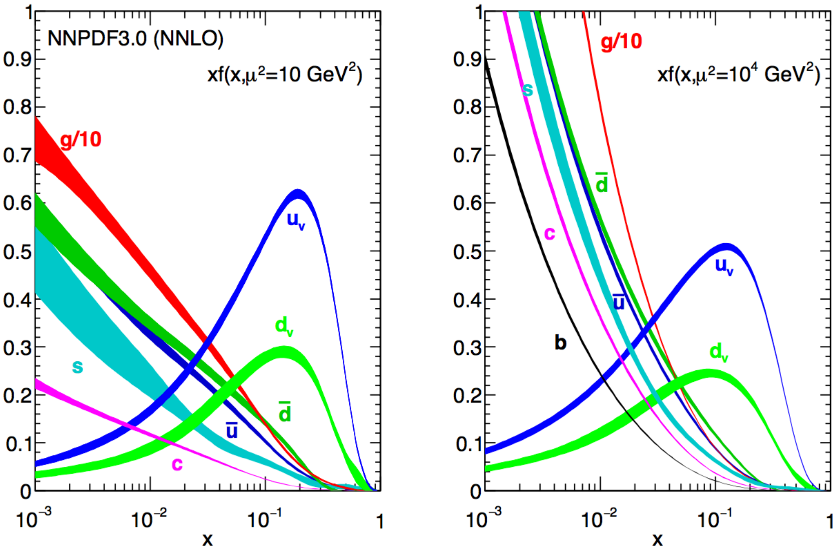

Figure 2.8: Fraction of energy x carried by the parton times the parton distribution function $f(x, \mu^2)$ for protons at scales $\mu^2(Q^2) = 10\,\mathrm{GeV}^2$ and $10^4\,\mathrm{GeV}^2$ [26].

CHAPTER 3

The LHC and the ATLAS Detector

3.1 The Large Hadron Collider

The LHC [8, 27–29], situated beneath the France-Switzerland border, is a superconducting circular particle accelerator designed to probe the energy frontier at TeV scale. The LHC allows scientists to reproduce the conditions that existed within a billionth of a second after the Big Bang and potentially access extremely rare phenomena by colliding beams of high-energy protons or heavy-ions close to the speed of light. Currently the world's largest and highest-energy particle accelerator, the collider is contained in a circular tunnel, with a circumference of 26.7 km, at a depth ranging from 50 to 175 m underground. The Run-I (2010-2012) operation of the LHC operated at a center-of-mass energy of $\sqrt{s} = 7$–8 TeV. Following two years of scheduled upgrades and repairs, the LHC began the current phase, Run-II (2015-2018), and now operates at a center-of-mass energy of $\sqrt{s} = 13$ TeV.

The LHC can operate in proton-proton (*pp*), lead-lead (*Pb*-*Pb*) and proton-lead (*p*-*Pb*) collision modes. Before beams of particles are injected into the collider, the particles are prepared by a series of systems comprised of previous accelerators which successively increase their energy. The full accelerator complex is shown in Figure 3.1. As the first stage of the injection chain, protons are produced from diatomic hydrogen gas using a metal cylinder, called a Duoplasmatron, in an electric field. The plasma beam of bare protons of 100 keV is accelerated up to 750 keV in the Radio-Frequency Quadrupole after exiting the Duoplasmatron. In the next phase photons are accelerated by a linear accelerator, LINAC2. The 200 MHz radio-frequency cavities accelerate the protons to an energy of 50 MeV over 30 m. The protons are transported through 80 m of connecting pipe, with 20 focusing quadrupole magnets, to the Proton Synchrotron Booster (PSB). In the 25 m radius PSB, four superimposed rings accelerate the protons further to 1.4 GeV. The protons are then transported into the Proton Synchrotron (PS) and are further accelerated to reach 25 GeV. In the PS, the proton bunches form trains where each bunch of approximately 1.15×10^{11} protons is separated by 25 ns. Three or four bunch trains of protons are then injected into the Super Proton Synchrotron (SPS) which accelerates them up to 450 GeV and then injects them into the LHC ring. After being injected into the main LHC ring, they are accelerated by 16 radio-frequency cavities up to the maximum velocity. In Run-II, beams are ramped up to 6.5 TeV and two beams travel in opposite directions before collisions. These collisions occur at four interaction points (IPs) around the LHC ring as shown in Figure 3.1. Each IP is instrumented with a detector. There are two general-purpose experiments designed to probe a broad spectrum of physics with the high luminosity proton-proton collisions: ATLAS [6] and CMS [7]. A third experiment, The Large Hadron Collider Beauty Experiment (LHCb) [30], accumulates luminosities at a reduced rate to allow for precision studies of B physics. A fourth experiment, A Large Ion Collider Experiment (ALICE) [31], is a heavy-ion detector designed specifically to study the phenomenology of strongly interacting matter in heavy ion collisions.

Luminosity

The likelihood of an interaction event between two particles can be quantified by cross section. Given a cross section σ of a specific physics process, the total interaction rate dN/dt and the number of collisions N are given by:

$$\frac{dN}{dt} = \sigma \times \mathcal{L} \qquad N = \sigma \times \int \mathcal{L} dt = \sigma \times L \tag{3.1}$$

where $\mathcal{L}$ is the instantaneous luminosity, which is a measure of the pp flux at each bunch crossing and an important characterization of the performance of the LHC, and L is the integrated luminosity over time. Given a Gaussian beam distribution, the instantaneous luminosity can be expressed as [32]:

$$\mathcal{L} = \frac{N_b^2 n_b f_{\text{rev}} \gamma_r}{4\pi \epsilon_n \beta^*} F \tag{3.2}$$

where N_b is the number of particles per bunch, n_b represents the number of bunches per beam, f_{rev} is the revolution frequency, γ_r denotes the relativistic gamma factor, ϵ_n is the normalized transverse beam emittance, β^* represents the beta function at the interaction point which characterizes the horizontal and vertical beam size, and F is the geometric luminosity reduction factor due to the crossing angle at the IP.

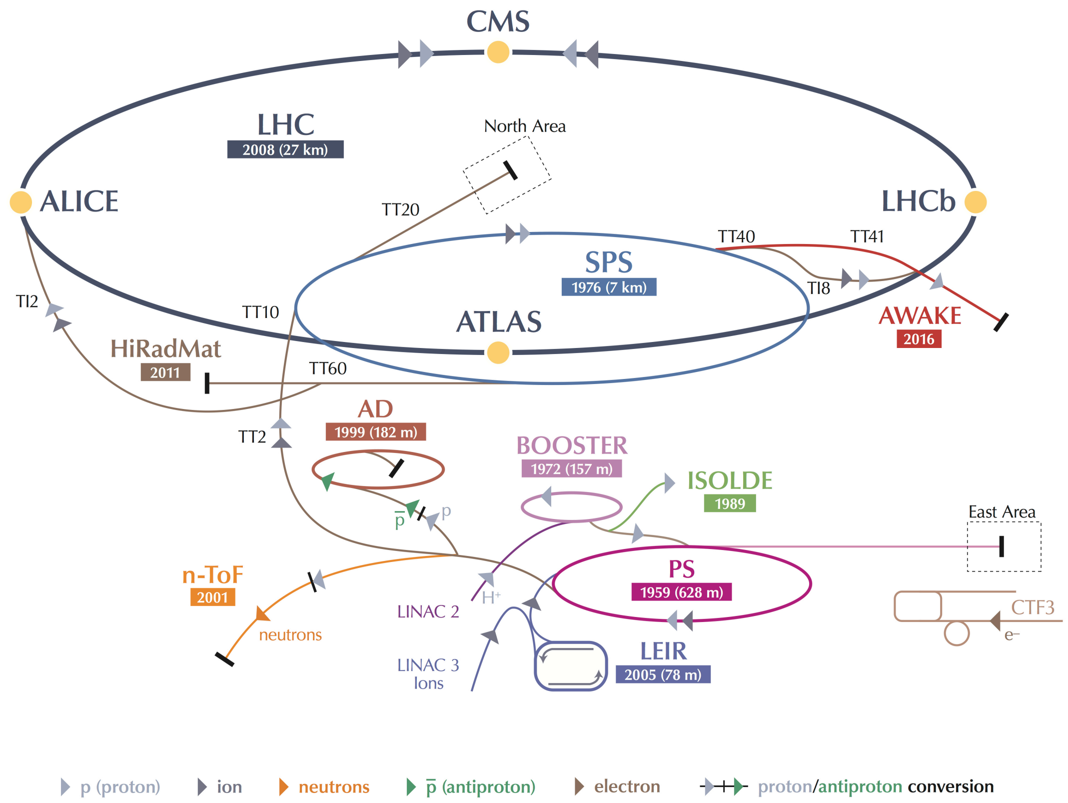

Figure 3.1: The schematic layout of the accelerator complex at CERN. The protons are accelerated through Linac 2, PSB, PS and SPS before being injected into the LHC. Several other experiments not associated with the LHC are also depicted.

The integrated luminosity is a measure of the total amount data collected expressed in terms of an inverse cross section (typically in fb^{-1}). Another important quantity related to the instantaneous luminosity during collisions is the average number of pp inelastic interactions per bunch crossing, and is often referred to as the pile-up parameter (μ). A high instantaneous luminosity leads to additional proton-proton interactions at each bunch crossing, known as in-time pile-up. Additionally, the high frequency of collisions (up to 40 MHz), and the inherent latency of the hardware used in the detectors causes further out-of-time pile-up situations. These collision events are uncorrelated with the hard-scattering process, and can be approximated as contributing a background of soft energy depositions that have particularly adverse and complex effects on the jet reconstruction.

The data used in this dissertation was collected during the first two years of the Run-II operation of the LHC (Figure 3.2).

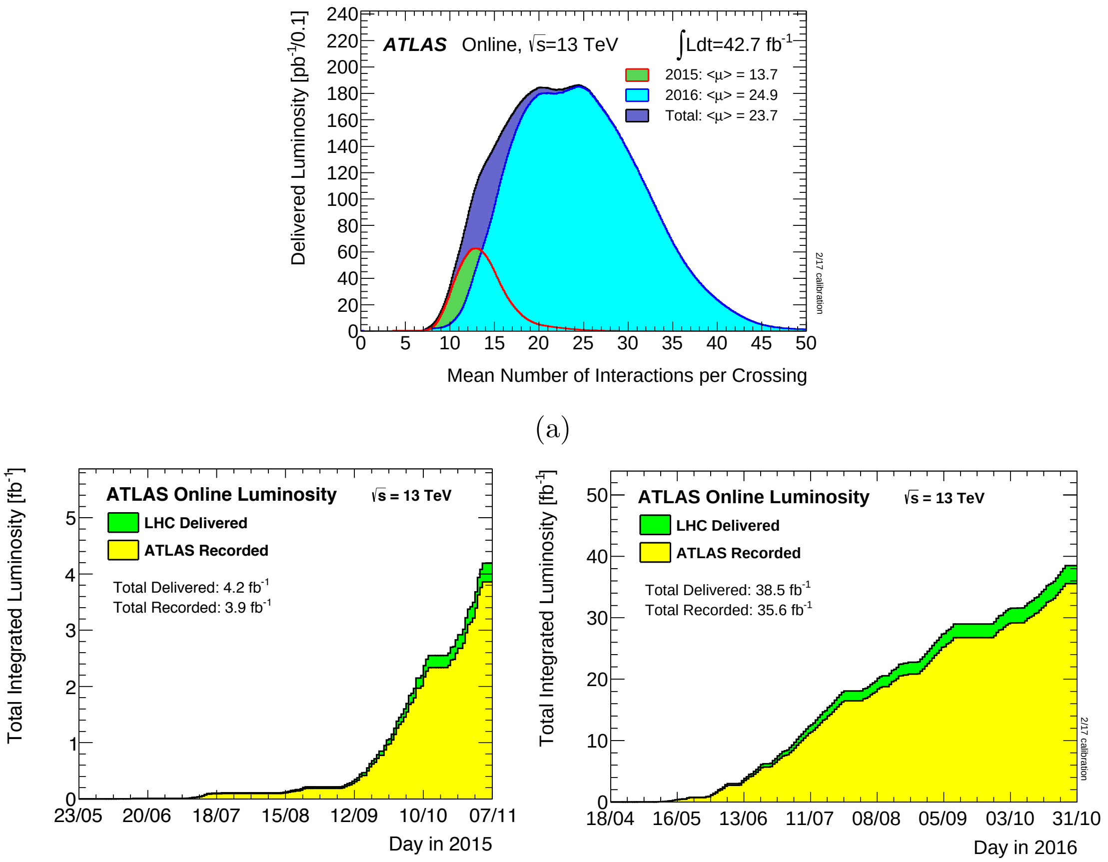

(a)

(b)

(c)

Figure 3.2: (a) The luminosity-weighted distribution of the average number of interactions per crossing for the combined 2015 and 2016 *pp* collision data at 13 TeV center-of-mass energy; (b) cumulative luminosity versus time delivered to (green) and recorded by ATLAS (yellow) during stable beams for *pp* collisions at 13 TeV center-of-mass energy in 2015. (c) same as (b) but for 2016.

3.2 The ATLAS Detector

The ATLAS detector is a multi-purpose symmetric cylindrical detector that probes both proton-proton and heavy ion collisions. It is designed to operate in a high luminosity environment and accurately reconstruct *pp* collisions. The detector is also designed and configured to be sensitive to a wide range of physics processes, from precision tests of the SM to numerous searches for new phenomena.

Measuring 44 m in length and 25 m in diameter, the multi-layered instrument sits in a cavern 100 m below the surface, weighs 7000 tonnes, and covers nearly 4π steradians around the IP. The detector has a layout typical for a particle detector at a collider, and it consists of six different detecting subsystems wrapped concentrically in layers around the collision point. These six subsystems can be broadly grouped into two general types of detector components – tracking detectors (trackers) and calorimeters. A schematic view of the ATLAS detector can be seen in Figure 3.3. From the interaction point outwards, the entire ATLAS detector comprises the inner detector (tracking detectors) housed inside a solenoid of magnet, calorimeters (divided into electromagnetic and hadronic calorimeters) surrounded by the toroidal magnets arranged in an eight-fold azimuthal symmetry, and the outermost muon spectrometer (tracking detectors again). The Trigger and Data Acquisition (TDAQ) system, responsible for selecting events of interesting from the collisions at a high rate, are also discussed.

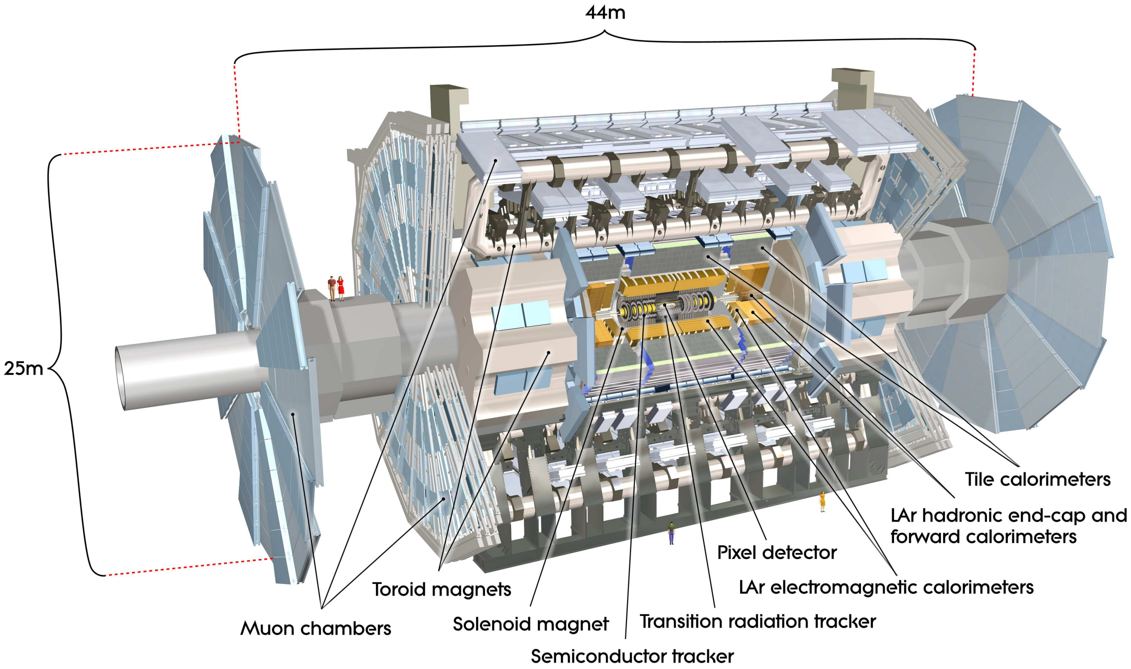

Figure 3.3: Cut-away view of the ATLAS detector. The dimensions of the detector are 25 m in height and 44 m in length. The overall weight of the detector is approximately 7000 tonnes [6].

The ATLAS experiment utilizes a right-handed Cartesian coordinate system with the interaction point designated as the origin. The z-axis lies along the beam direction. The x-y plane is transverse to the beam direction. The positive x-axis points from the IP to the center of the LHC ring, while the positive y-axis perpendicular to the x-axis points upwards in the transverse plane. The azimuthal angle, ϕ, is measured around the beam pipe and the polar angle, θ, is measured from the positive z-axis. In hadron collider physics, it is more convenient to use rapidity (y) or pseudo-rapidity (η) if the particles involved are massless, to describe the angle relative to the beam axis because differences in rapidity/pseudo-rapidity are Lorentz invariant under boosts along the longitudinal axis. The ATLAS detector is split into a barrel part (small $|\eta|$), where detector layers are positioned on the cylindrical surfaces around the beam axis, and two end-caps bookending the barrel region, where detector layers are placed in planes of large $|z|$ perpendicular to the beam axis. Finally, ΔR is introduced to describe the angular distances in the η-ϕ space. The mathematical formulae of y, η and ΔR are described as follows:

$$y = \frac{1}{2} \ln \left(\frac{E + p_z}{E - p_z} \right), \tag{3.3}$$

$$\eta = \frac{1}{2} \ln \left(\frac{|\mathbf{p}| + p_z}{|\mathbf{p}| - p_z} \right), \tag{3.4}$$

$$\Delta R = \sqrt{(\Delta\eta)^2 + (\Delta\phi)^2}. \tag{3.5}$$

3.2.1 Inner Detector

Immersed in a strong magnetic field of 2 tesla parallel to the beam pipe, the inner detector (ID) [33–36], as shown in Figure 3.4, provides accurate particle tracking while bombarded with intense radiation created at high rates during collision. Within a coverage of $|\eta| < 2.5$, the inner detector is capable of delivering outstanding momentum measurement, the potential for robust pattern recognition, and precise vertex measurements for charged particles traveling at transverse momenta above a p_T threshold of 0.5 GeV. In addition, the inner detector also provides electron identification for

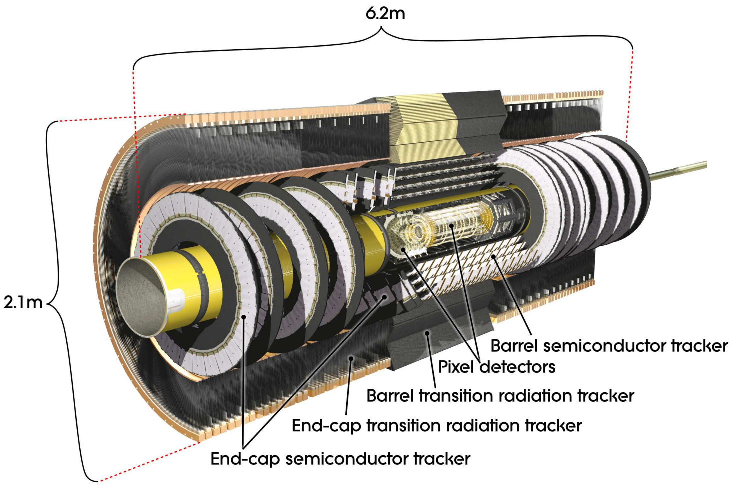

Figure 3.4: Diagram of the ATLAS Inner Detector [6].

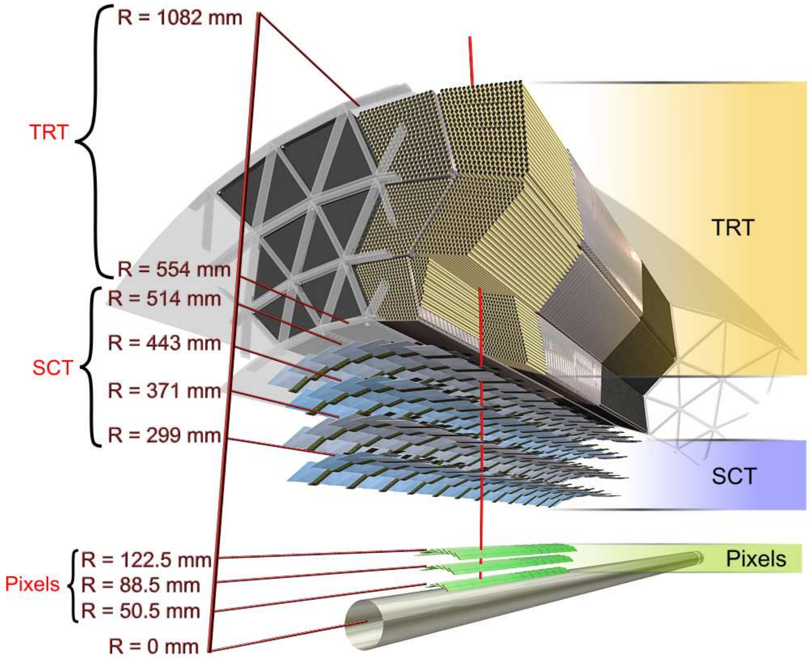

Figure 3.5: A schematic drawing of the inner detector showing the sensors and structural elements traversed by a charged track of 10 GeV p_T in the barrel inner detector ($\eta = 0.3$) [6].

electrons within the pseudo-rapidity range of $|\eta| < 2.0$ and energies between 0.5 GeV and 150 GeV, which is described in Chapter 4. As illustrated in Figure 3.5, the inner detector consists of three independent but complementary components. The main parameters of the ID are summarized in Table 3.1.

Type	Position	Area (m^2)	Resolution $\sigma(\mu m)$	Channels (10^6)	$\|\eta\|$ coverage
Pixels	IBL	0.2	$R\phi = 12,\ z = 66$	16	± 2.5
	2 barrel layers	1.4	$R\phi = 12,\ z = 66$	81	± 1.7
	5 end-cap disks	0.7	$R\phi = 12,\ z = 77$	43	$1.7 - 2.5$
Silicon	4 barrel layers	34.4	$R\phi = 16,\ z = 580$	3.2	± 1.4
strips	9 end-cap wheels	26.7	$R\phi = 16,\ z = 580$	3.0	$1.4 - 2.5$
TRT	Axial barrel straws		170 (per straw)	0.1	± 0.7
	Radial end-cap straws		170 (per straw)	0.32	$0.7 - 2.0$

Table 3.1: Main parameters of the inner detector system. The resolutions quoted are typical values.

Pixel Detector and The Insertable B-Layer

Being the innermost component of the ATLAS detector, the primary objective of the pixel detector is to provide high-precision measurements per track as close to the IP as possible. It plays a vital role in determining the impact parameter resolution, vertex identification, and the identification of short-lived particles such as B hadrons and τ leptons. The original pixel detector consists of three cylindrical layers (B-layer, layer 1, layer 2) in the barrel, and three disk layers in the forward regions perpendicular to the beam pipe. These two configurations provide a coverage up to $|\eta| < 2.5$. In Run-II, a fourth layer—the insertable B-layer (IBL)—was mounted to gear up the inner detector for the high luminosity run.

The active part of the pixel detector is composed of silicon detector modules partitioned into small pixels with dimensions of 50 by 400 μm. There are 1744 modules with 80 million readout channels in total. This allows the pixel detector to obtain extremely precise spatial measurements in the $(r,\ \phi)$ plane, as well as cope with the high flux of particles from different bunch crossings. The latest addition of the IBL to the inner detector is aimed at improving the efficiencies of both vertex resolution and b-tagging, compensating for the inefficiencies in the pixel B-layer which can arise over time due to the irreversible damage from radiation, and meeting the increasing bandwidth requirements for the LHC Run-II operation.

The Semiconductor Tracker

Outside of the pixel detector, the semiconductor tracker (SCT) system consists of stereo pairs of silicon microstrip layers and is designed to provide eight precision measurements in the intermediate radial range. It functions in a similar way as the pixel detector and guarantees excellent track reconstruction and charged particle p_T resolution. Since the SCT is further from the IP, the requirements for radiation hardness and spatial resolution are less stringent. The SCT also differs from the pixel detector in that readings from two silicon strips are needed to provide a full (η, ϕ) measurement, whereas a simultaneous measurement of (η, ϕ) can be obtained from individual pixels. The four layers of trackers equipped in the barrel region combined with nine disks instrumented in each end-cap region ensure a pseudo-rapidity coverage out to $|\eta| < 2.5$.

Transition Radiation Tracker

The outermost component of the inner detector is the transition radiation tracker (TRT), which is composed of straw tubes filled with a mixture of xenon gas and carbon dioxide with a gold plated tungsten wire held under tension in the center of each tube which is kept at a high voltage with respect to the tube. The TRT is intrinsically radiation hard and provides continuous tracking for particles within $|\eta| < 2$. When a charged particle traverses a tube, the gas is ionized and electrons drift to the wire, get collected and register as hits. This extends the measurement of tracks after they pass through the pixel and SCT detectors. In addition to providing supplementary precision to the measurement of tracks from charged particles, the TRT also facilitates discriminating high-energy electrons from charged pions through the measurement of the amount of transition-radiation photons which is much smaller for a pion than an electron.

3.2.2 The Calorimetry System

The ATLAS calorimetry system [37, 38] consists of a number of sampling detectors with full ϕ-symmetry and coverage around the beam axis. The calorimetry system comprises both electromagnetic and hadronic calorimeters, instrumented to measure the energy that particles (with the exception of muons and neutrinos) deposit in the calorimeters. There is one barrel and two end-cap cryostats housing the calorimeters closest to the beam line. The barrel cryostat encompasses the electromagnetic barrel calorimeter, whereas the two end-cap cryostats each contain an electromagnetic end-cap calorimeter (EMEC), a hadronic end-cap calorimeter (HEC) located immediately behind the EMEC, and an innermost forward calorimeter (FCal) to cover the region closest to the beam. All these calorimeters adopt liquid argon as the active detector medium. Liquid argon has a linear behavior, is stable in response over time, and exhibits intrinsic radiation-hardness. The outermost calorimetry system is a hadronic sampling calorimeter consisting of alternate scintillator tiles (as the sampling medium) and steel (as the absorber). The tile calorimeter is divided into three parts, one central barrel and two extended barrels. The whole structure and geometry of the calorimeters can be seen in Figure 3.6.

The precision electromagnetic calorimeters are lead-liquid argon detectors with accordion-shaped absorbers and electrodes. These calorimeters are responsible for measuring energies of electrons and photons, and are situated directly outside of the inner detector. The barrel electromagnetic calorimeter spans $|\eta| < 1.475$, and the

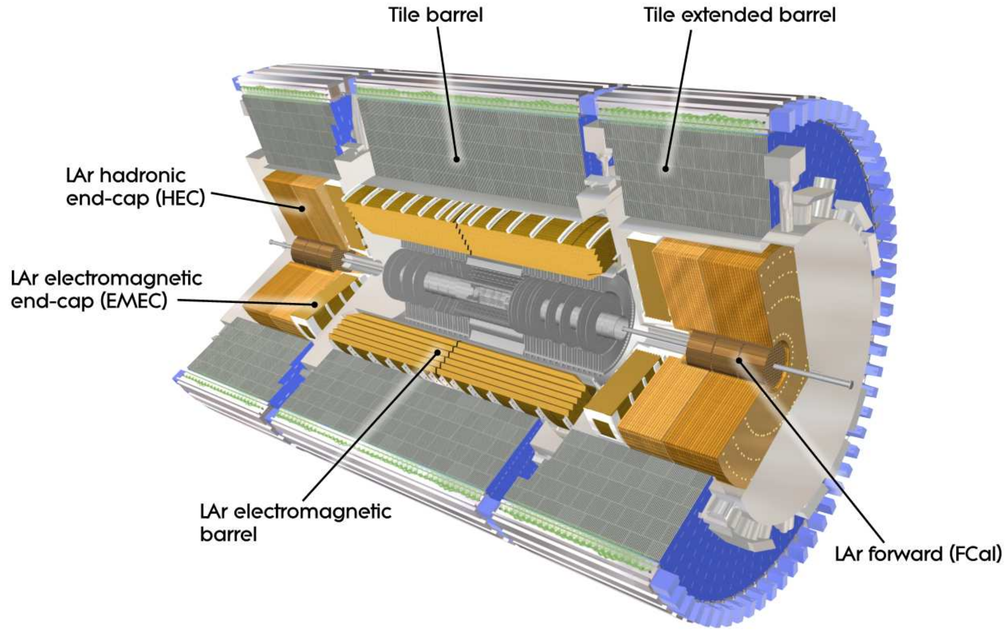

Figure 3.6: Cut-away view of the ATLAS calorimeter system [6].

two EMECs extend this coverage to $1.375 < |\eta| < 3.2$. The accordion shape allows the calorimeters to have several active layers in depth. There are three layers in the precision-measurement region where $|\eta| < 2.5$, and two layers in the higher-η region ($2.5 < |\eta| < 3.2$) as well as in the overlap region between the barrel and the EMEC. The first layer of the precision-measurement region is finely segmented in η in order to achieve an accurate measurement of position. The calorimeter system also has electromagnetic coverage at higher η ($3.1 < |\eta| < 4.9$) provided by the FCal. Furthermore in the region ($|\eta| < 1.8$) the electromagnetic calorimeters are complemented by presamplers, an instrumented argon layer, which provides a measurement of the energy lost in front of the electromagnetic calorimeters.

The outer hadronic tile calorimeter samples the energy of hadrons as they interact with atomic nuclei. Situated directly outside of the LAr calorimeters, the main barrel covers the region $|\eta| < 1.0$, and the two extended barrels cover $0.8 < |\eta| < 1.7$. Ultraviolet light, which is produced when hadrons strike the tile scintillators, is transmitted through the wavelength shifting fibers and eventually collected by photomultiplier tubes. The barrel and extended barrels of the tile calorimeter are divided into 64 modules azimuthally. Furthermore, the tile calorimeter is split into three layers in depth. The thicknesses of the layers are approximately 1.5, 4.1 and 1.8 interaction lengths (λ) for the barrel and 1.5, 2.6, and 3.3 λ for the two extended barrels. Together with the EM calorimeters, of which the total thickness is about 22 radiation lengths (X_0) in the barrel and 24 X_0 in the end-cap region, the hadronic calorimeters can effectively contain the majority of the particle showers and prevent punch-through which occurs when the shower of a particle penetrates into the surrounding muon spectrometer.

3.2.3 The Muon Spectrometer

The muon spectrometer (MS) [39] is the outermost system of the ATLAS detector and is designed to reliably identify muons and measure their momenta. Muon tracks measured in the inner detector usually suffer from poor momentum resolution at high transverse momentum. And the energy a muon deposits in the calorimeters is very small, because muons lose energy much more slowly than electrons through Bremsstrahlung radiation and therefore they are not stopped in the calorimeters. Therefore, a dedicated muon tracking system is essential for high precision reconstruction of muons. The conceptual layout of the muon spectrometer is shown in Figure 3.7. The MS is instrumented with three layers of tracking chambers and the toroid magnets. The principle of detecting muons by the MS is based on the deflection of muon tracks in the (r, z) plane in the magnetic filed created by the superconducting air-core toroid magnets. In addition, fast triggering chambers of the MS also play a vital role in accurate identifications of bunch crossing and quick triggering decisions in the region $|\eta| < 2.4$.

The four different technologies involved in the MS are monitored drift-tube chambers (MDT), thin gap chambers (TGC), cathode strip chambers (CSC), and resistive plate chambers (RPC). They are all designed to detect the presence of muons by collecting the charges produced from the ionization of gaseous mixtures when a muon traverses them, but each has their own specific applications. The MDTs operates in a similar way as TRT straw tubes; MDTs operate at a 3-bar pressure to provide better spatial resolution. A MDT measures the coordinates of the muons by recording the drift time of electrons from the gas ionization process. The TGCs are multi-wire proportional chambers consisting of a gap between two conducting cathodes which contains parallel wires to collect electric charges. The TGCs are capable of triggering due to fast readout and also complement the measurements of MDTs in the bending direction. The CSCs are constructed in a similar way as the TGCs but with a reduced spacing between the strips. The RPC, which also has triggering capabilities, collects the ionized charges on two parallel resistive plates separated by a small gap and is configured to operate in an avalanche mode which allows for fast readout. The

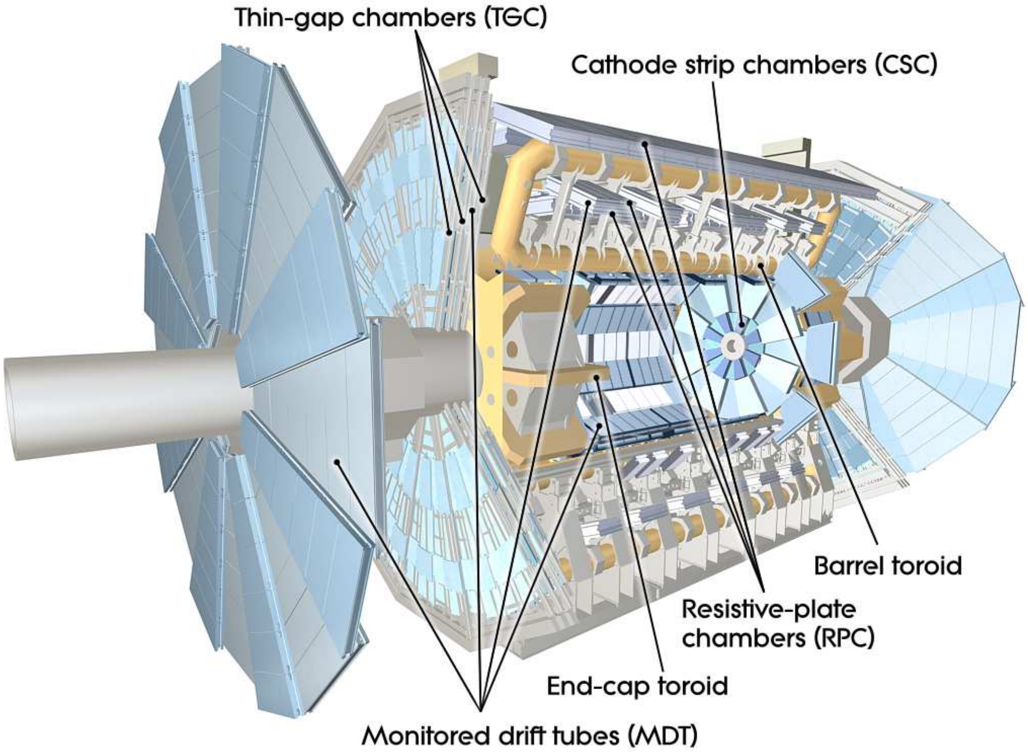

Figure 3.7: Schematic illustration of the muon spectrometer system composed of the detector panels and the toroid magnets [6].

cross-section views of the MS in a plane perpendicular to and a plane containing the beam axis are illustrated in Figure 3.8. The muon system is broadly divided into two types: precision-tracking chambers and fast-triggering chambers. High-precision measurements of the track coordinates are achieved with the former. The fast-triggering chambers of the MS serve the threefold purpose of providing bunch-crossing identification, offering well-defined p_{T} thresholds, and measuring the muon coordinate in the direction orthogonal to that determined by the precision-tracking chambers.

Precision-Tracking Chambers

In the barrel region, three concentric cylindrical layers of precision-tracking muon chambers are located around the beam axis at radii of approximately 5 m, 7.5 m and 10 m. Muon chambers with three layers form large wheels in the end-cap region, sitting in front of and behind the end-cap toroidal magnets. These wheels are perpendicular to the beam axis and are located at distances of approximately $|z| = 7.4\,\mathrm{m}$, 10.8 m, 14 m, and 21.5 m. The muon chambers consist of six to eight layers of MDTs and can reach an average resolution of $80\,\mu\mathrm{m}$ per tube, or equivalently about $35\,\mu\mathrm{m}$

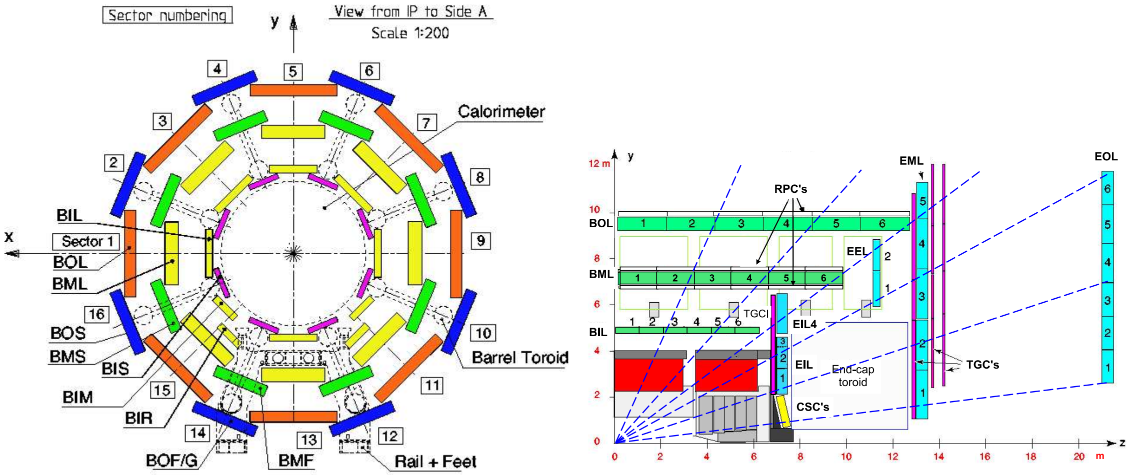

Figure 3.8: *Left*: Cross-section of the barrel muon system perpendicular to the beam axis (non-bending plane), showing three concentric cylindrical layers of eight large and eight small chambers. The outer diameter is about 20m. *Right*: Cross-section of the muon system in a plane containing the beam axis (bending plane). Infinite-momentum muons would propagate along straight trajectories which are illustrated by the dashed lines and typically traverse three muon stations [6].

per chamber. The MDTs cover a pseudo-rapidity range of $|\eta| < 2.7$. The MDTs have a relatively long drift time up to 700 ns due to the properties of the Ar/CO_2 gas mixture. In the forward region $2 < |\eta| < 2.7$, CSCs are used in the innermost tracking layer due to their higher rate capability and time resolution. As mentioned above, CSCs are multi-wire proportional chambers where the cathodes are segmented into strips and are configured in a way that allows for a small drift time of 40 ns.

Fast-Triggering Chambers

The capability of triggering on muon tracks is an essential design criterion for the muon system. The drift time of the MDT is generally long, hence additional chambers are needed to assign events to a specific bunch crossing. The precision-tracking muon chambers are complemented by a system of fast trigger chambers which are capable of sending information of tracks within a few tens of nanoseconds after the passage of a muon. RPCs are instrumented in the barrel region $|\eta| < 1.05$ for triggering purposes, whereas in the end-cap region $1.05 < |\eta| < 2.4$ TGCs are responsible. An RPC consists of two resistive parallel plates separated by insulating spacers of 2 mm filled with a gaseous mixture of 94.7% $C_2H_2F_4$, 5% Iso-C_4H_{10}, and 0.3% SF_6. An electric field of 4.9 kV/mm is applied between the plates to facilitate avalanches from the ionizations of gasses. The RPCs have the advantage of a short drift time due to the selected gas and can ensure a temporal resolution of 1.5 ns.

In the forward region, however, the trigger system (TGCs) is faced with intense radiation and the lack of bending of muon tracks due to the fact that the chambers lie outside the end-cap toroidal magnets. To fulfill the triggering requirements, high granularity in η and quick response times are achieved with the TGCs. In the TGCs, a wire-to-cathode distance of 1.4 mm and a wire-to-wire distance of 1.8 mm lead to quick responses. A high spatial resolution is then achieved by densely packed wires per read-out channel.

3.2.4 Trigger and Data Acquisition

The Trigger and Data Acquisition (TDAQ) system [40] plays an essential role when the ATLAS detector is operating. With the size of a raw event being approximately $\mathcal{O}(1)$ MB, the rate of collision data at the designed LHC bunch crossings of 40 MHz is nearly $\mathcal{O}(10)$ TB/s. This enormous recording rate is unmanageable due to the limitations in both processing power and data storage capacity. A competent trigger system is essential to reducing the rate to only a small fraction by rapidly deciding which events of interest to keep. The trigger system is usually complemented by a data acquisition system which efficiently gather and process the data from the readout architecture.

A schematic layout of the ATLAS TDAQ system is shown in Figure 3.9. The ATLAS trigger system in Run-II comprises a hardware-based first level trigger (Level-1 or L1) and software-based high level trigger (HLT). The Level-2 and event filter, which were separate components in the TDAQ system in Run-I, are consolidated into a single homogeneous farm (i.e., HLT) in Run-II to improve resource sharing and for simplification. This change along with other upgrades to the TDAQ system is necessary to deal with the increased center-of-mass energy, the increased pile-up conditions, and the shortened bunch spacing interval from 50 ns to 25 ns. The L1 trigger reduces the LHC bunch crossing rate to 100 kHz with a decision time of 2.5 μs for an L1 accept. The HLT further reduces the event rate to about 1 kHz on average within a processing time of about 200 ms.

The hardware-based L1 trigger attempts to rapidly identify relatively high-p_{T} objects. The L1 calorimeter (L1Calo) trigger makes use of information from both electromagnetic and hadronic calorimeters, with a reduced granularity of approximately $\Delta\eta \times \Delta\phi = 0.1 \times 0.1$. It tries to identify electrons, photons, taus, jets, as well as the missing transverse energy. The L1 Muon (L1Muon) trigger system consists of a barrel and two end-cap sections and provides fast trigger decisions after collect-

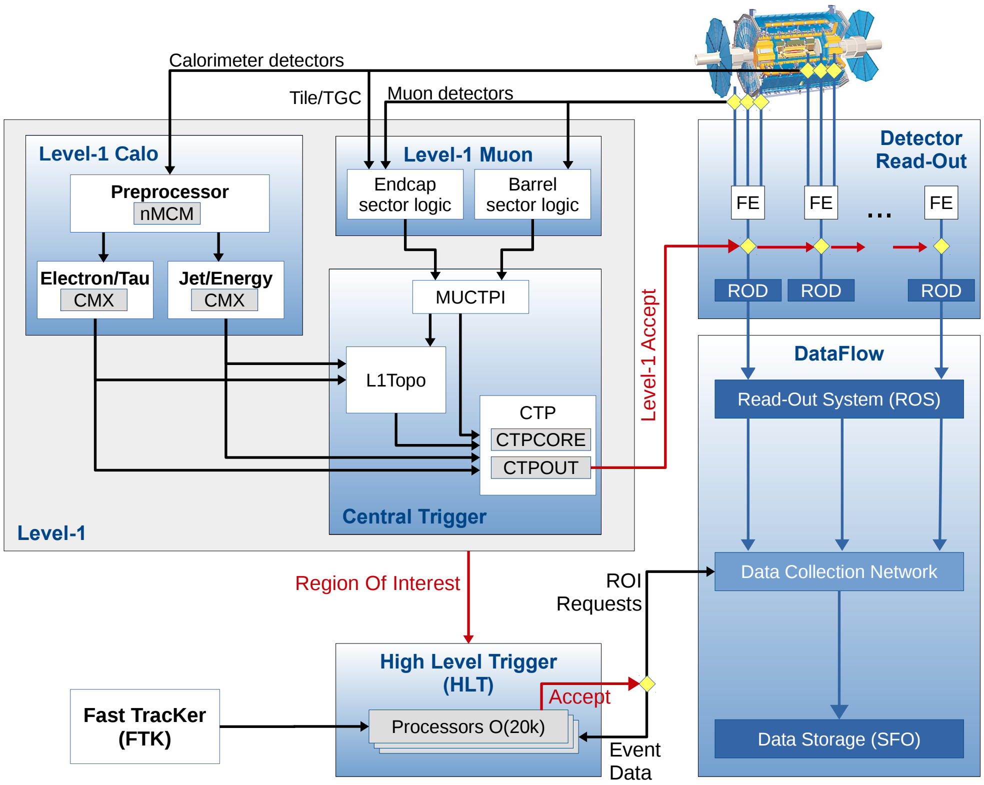

Figure 3.9: Schematic layout of the ATLAS trigger and data acquisition system in Run-II [6].

ing track information from RPC and TGC to identify muons. A topological trigger processor (L1Topo) is also instrumented to allow for applying topological selections on L1 trigger objects from both L1Calo and L1Muon triggers. The Central Trigger Processor (CTP) finally forms a trigger decision within 2.5 μs by processing logical combinations of trigger inputs from L1Calo, L1Muon and L1Topo. These logical combinations of trigger inputs constitute the trigger items in the L1 trigger menu. Some of the trigger items are prescaled to only randomly retain part of the accepted events in order to maintain a desirable rate.

Event data are buffered on detector-specific front-end electronics and upon an L1 accept, the buffered data are transfered to a readout system (ROS). The ROS is interfaced with a data collection (DC) system which provides requested event information to the next level of trigger system, the HLT. The HLT is a software-based trigger system and it reduces the L1 trigger rate of 100 kHz to 1 kHz event output rate. The HLT utilizes regions of interest (ROI) to access full or partial information of the events from the ROS via the DC interface. The HLT adopts a two-pass approach in which a quick reconstruction to reject the majority of the events is performed at first and secondly a slower reconstruction with greater precision is done to filter the remaining ones. The HLT is capable of making these high-level decisions due to its access to the full granularity of the calorimeter information, precision muon measurements, as well as the ID tracking information. Pending an HLT accept, event data will be transfered to the Tier-0 storage and the buffer in the ROS will be cleared.

The primary event processing occurs at CERN in a Tier-0 facility [41]. The RAW data are archived at CERN and transfered, along with the primary processed data, to the Tier-1 facilities around the world. Derived datasets produced by the physics groups are transfered to the Tier-2 facilities for further analysis. Tier-3 centers provide complementary computing resources are for data processing and analysis.

CHAPTER 4

Particle Reconstruction and Identification

All physics analyses start out by gathering raw information from the detector to reconstruct physics objects and build events. These reconstructed and identified physics objects represent the characteristics of the particles observed as they traverse the detector volume. By combining and analyzing the measurements from various components of the ATLAS detector, physics objects like electrons, photons, muons and hadrons are reconstructed and identified. In this dissertation, the reconstructed physics objects of interest are electrons, muons and jets (reconstructed hadrons). In addition, the missing transverse energy, $E_{\mathrm{T}}^{\mathrm{miss}}$, is used to identify neutrinos which escape the detection of the detector. This chapter describes the reconstruction algorithms that are used to reconstruct and identify these physics objects, as well as an overlap removal procedure to remove ambiguities when an object is reconstructed simultaneously as several different physics objects.

4.1 Electrons

An electron candidate is composed of an ID track matched to an EM calorimeter cluster (energy deposit). The process of building an EM cluster is done using a sliding window algorithm [42]. The algorithm uses a window of fixed size $N_\eta \times N_\phi = 3 \times 5$ in units of 0.025×0.025, corresponding to the granularity of the middle layer of the EM calorimeter. The energies in those grid of cells are summed up across all the longitudinal layers which form a tower. EM clusters are then seeded from towers of energy deposits with total transverse energy above 2.5 GeV. Pattern recognition and track fitting are then performed to identify tracks consistent with those coming from electrons and tracks with $p_{\mathrm{T}} > 0.5\,\mathrm{GeV}$ are extrapolated from their last measured point in the ID to the middle layer of the EM calorimeter [43]. The extrapolated η and ϕ coordinates of the impact point are compared to a corresponding seed cluster position in that layer. If a track is loosely matched to a seed cluster, an optimized electron-specific track fit is performed using the Gaussian Sum Fitter (GSF) [44] in order to take into account the non-linear bremsstrahlung effects. Therefore, the electron candidates are required to have at least one ID track matched to the seed cluster, and the EM cluster associated with the candidate is then rebuilt by summing energy in a grid of 3×7 longitudinal towers of cells. Energies of the electron candidates are then calibrated and corrected based on Monte-Carlo samples [43] using the energy measurements from the EM cluster and the η and ϕ measurements from the track.

Reconstructed electrons are often required to satisfy certain criteria, including electron identification and isolation. This is primarily to distinguish genuine electron objects from background. Hadronic jets, non-prompt electrons from photon conversions, non-isolated electrons from semi-leptonic decays of quarks can all be reconstructed as electron candidates. However, only isolated prompt electrons are of interest in most situations. The identification criteria for electron candidates are optimized using a likelihood-based method which is essentially a multivariate analysis (MVA) that simultaneously evaluates several properties of the electron candidates when making a selection decision. The likelihood method calculates the probability of an electron candidate being a real signal electron, and different working points (thresholds) are devised to make the trade-off between signal efficiency and background rejection (as shown in Figure 4.1) [43][45]. The analyses in this dissertation consider the “LooseLH” and “MediumLH” working points, where “MediumLH” is a subset of “LooseLH”. High signal efficiency and light-flavor jet discrimination are achieved using the LooseLH working point. The MediumLH working point in addition rejects heavy-flavor jets as well as photon conversions, but at the cost of signal efficiencies.

In addition to the identification criteria described above, isolation requirements provide further suppression of background events [43]. The isolation variables attempt to quantify how well the electron in question is isolated from its surroundings by inspecting the energy deposits produced around the electron candidate. The isolation criteria allow one to disentangle the prompt electrons (from resonance decays, such as $W \to e\nu$, $Z \to ee$) from non-isolated electron candidates such as those originating from converted photons or from heavy flavor hadron decays, and light hadrons misidentified as electrons. Two discriminating variables, a calorimetric isolation and a track isolation, have been chosen to select isolated electrons in the calorimeters and ID respectively. The calorimetric isolation variable, $E_{\mathrm{T}}^{\mathrm{cone0.2}}$, is defined as the sum of transverse energies of the of topological clusters within a cone of $\Delta R = 0.2$

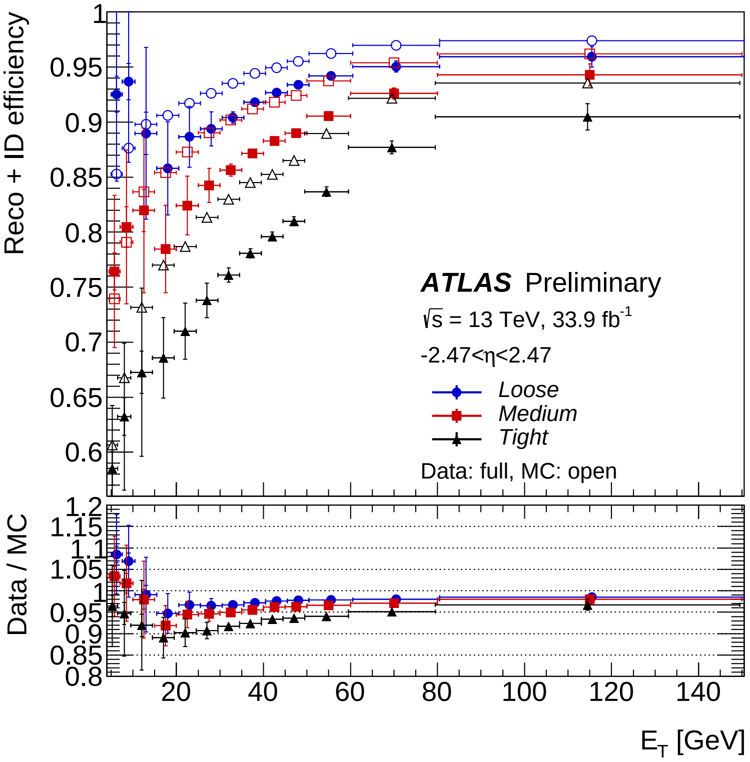

Figure 4.1: Electron reconstruction and identification efficiencies in $Z \to ee$ events as a function of transverse energy E_{T}, integrated over the full pseudo-rapidity range. The efficiencies are shown in data and MC for three operating points that are based on a likelihood approach, Loose, Medium and Tight [45].

around the candidate electron cluster. The transverse energy contained in the 5×7 rectangular cell window around the electron cluster is subtracted. The track isolation variable $p_{\mathrm{T}}^{\mathrm{varcone0.2}}$, on the other hand, calculates the sum of transverse momenta of all the tracks satisfying the quality requirements within a cone of variable size defined as $\Delta R = \min(0.2,\, 10\,\mathrm{GeV}/E_{\mathrm{T}}(e))$. The track associated with the electron candidate is excluded from the cone and only tracks originating from the reconstructed primary vertex of the hard collision are considered. A "LooseTrackOnly" working point based on track isolation is used in dissertation, which yields a flat 99% efficiency for the signal electrons. This "LooseTrackOnly" selection is desirable because the parameter space of interest here typically exhibits high transverse momenta and maintaining a signal efficiency without introducing significant amount of background contamination is of great importance.

4.2 Muons

A muon object is reconstructed independently in the ID and MS first, followed by matching the track candidates to form the final muon tracks. Different algorithms are used for the combined muon reconstruction and four types of muons are defined depending on the algorithm and sub-detector information used in reconstruction. These types are as follows [46]:

- Combined (CB) muon: A CB muon is reconstructed as a combined track formed by performing a fit uses the hits from both the ID and the MS sub-detectors.
- Segment-tagged (ST) muon: the ID track of an ST muon is extrapolated to the MS and is associated with at least one local track segment in the MDT or CSC chambers. ST muons are used when muons cross only one layer of the MS chambers, either due to their low transverse momenta or that they fall in regions with reduced MS acceptance. This type of muons recovers muons in the range $2.5 < |\eta| < 2.7$ where the ID coverage is relatively poor.
- Calorimeter-tagged (CT) muon: a CT muon does not have corresponding measurements in the MS. Instead, its ID track is extrapolated to the calorimeter to match to an energy deposit compatible with a minimum-ionizing particle. CT muons have the lowest purity, but they serve to recover acceptance in the region where the MS is only partially instrumented.
- Standalone (SA) muon: the trajectory of the SA muons is reconstructed solely using the MS tracks and a loose requirement that the corresponding track is compatible with originating from the IP.

When two types of muons share the same ID track, the preference is given to CB muons, ST muons, and CT muons in decreasing order of priority. The ambiguity associated with SA muons in the muon system is resolved by analyzing the track hit content and selecting the track with better fit quality and larger number of hits.

Similar to the case of the electron objects, prompt muon candidates are selected by requiring some identification criteria. Muon identification requirements suppress the background objects primarily coming from pion and kaon decays, while maintaining high efficiencies and robust momentum measurements for prompt muons. Additional selection cuts based on ID and MS track information, track fit quality are applied on muon candidates and four working points targeting different analysis needs are designed. The identification efficiencies for signal and background obtained from a

Selection	$4 < p_{\mathrm{T}} < 20\,\mathrm{GeV}$		$20 < p_{\mathrm{T}} < 100\,\mathrm{GeV}$	
	$\epsilon^{\mathrm{MC}}_{\mathrm{Sig}}$ [%]	$\epsilon^{\mathrm{MC}}_{\mathrm{Bkg}}$ [%]	$\epsilon^{\mathrm{MC}}_{\mathrm{Sig}}$ [%]	$\epsilon^{\mathrm{MC}}_{\mathrm{Bkg}}$ [%]
Loose	96.7	0.53	98.1	0.76
Medium	95.5	0.38	96.1	0.17
Tight	89.9	0.19	91.8	0.11
High-p_{T}	78.1	0.26	80.4	0.13

Table 4.1: Efficiency for prompt muons from W decays (signal) and misidentified prompt muons from in-flight decays of hadrons (background) using a $t\bar{t}$ MC sample. The results of the four identification selection criteria are shown separately for muons with low ($4 < p_{\mathrm{T}} < 20\,\mathrm{GeV}$) and high ($20 < p_{\mathrm{T}} < 100\,\mathrm{GeV}$) transverse momenta in the region $|\eta| < 2.5$. The statistical uncertainties are negligible.

$t\bar{t}$ simulation are summarized in Table 4.1. In this dissertation, the "Loose" and "Medium" working points are used. The Loose working point consider all four types of muons, whereas the Medium working point only uses CB and SA candidates. Muons isolations are carried out analogously to electron isolations, using either track isolation, calorimetric isolation or both. The track-based isolation variable, $p_{\mathrm{T}}^{\mathrm{varcone0.3}}$, calculates the scalar sum of the transverse momenta of the tracks ($p_{\mathrm{T}} > 1\,\mathrm{GeV}$) within the cone of size $\Delta R = \min(0.3,\, 10\,\mathrm{GeV}/p_{\mathrm{T}}^{\mu})$ after excluding the muon track itself. The size of the variable cone is p_{T}-dependent which is intended to improve the performance for muons of high transverse momenta. The calorimetric isolation variable, $E_{\mathrm{T}}^{\mathrm{cone0.2}}$, is defined in a similar way as that for the electrons. In this dissertation, the "LooseTrackOnly" working point for muons is used to achieve a constant 99% efficiency.

4.3 Jets

Jets are reconstructed calorimetric objects representing hadrons from the hadronizations of quarks or gluons. Jets are reconstructed by clustering nearby calorimeter cells using the anti-k_t algorithm [47] and matching the clustered object with ID tracks. Specifically, topo-clusters, with their energies reconstructed on either electromagnetic scale or hadronic scale, form the basic constituents of a jet [48]. Topo-clusters are topologically connected three dimensional cell clusters and can take on variable cluster size during reconstruction.

The anti-k_t algorithm is one of the many sequential clustering algorithms which are infrared and collinear safe by construction. Two distance measures are defined for the anti-k_t algorithm:

$$d_{ij} = \min\left(\frac{1}{p_{\mathrm{T},i}^2}, \frac{1}{p_{\mathrm{T},j}^2}\right) \times \frac{\Delta R_{ij}^2}{R^2}, \tag{4.1}$$

$$d_{iB} = \frac{1}{p_{\mathrm{T},i}^2}, \tag{4.2}$$

where d_{ij} measures the distance between two topo-clusters, d_{iB} describes the distance between a certain topo-cluster and the beam line, and R is another distance parameter quantifying the desired size of the jet. The algorithm first finds the smallest distances in the entire set $\{d_{ij},\, d_{iB}\}$. Particle i and j are combined into one particle by summing their four-vectors if d_{ij} is the minimum. However, if the minimum distance is between a topo-cluster and the beam line, the cluster is defined as a jet and subsequently removed from the set considered by the anti-k_t algorithm. The procedure continues iteratively until either all the particles are exhausted and belong to the clustered jet or the size of the jet (the distance between the jet axes) exceeds the value of the parameter R. From Equation (4.1), one can see that the anti-k_t algorithm prefers constituents with high transverse momenta and will cluster those components first. As a result, the jet area is relatively stable and tends to be conical. ID tracks are associated with jets through a procedure known as “ghost association” [49] and the matched tracks are treated as particles with infinitesimal momenta. In this dissertation, two sets of jet collections are introduced, with $R = 0.4$ and $R = 1.0$ respectively. Jets in the former collection are referred to as small-R jets, and as large-R jets in the latter.

4.3.1 Small-R Jets

Small-R jets are reconstructed at the electromagnetic energy scale with the anti-k_t algorithm and radius parameter $R = 0.4$ using the FastJet 2.4.3 software package [50]. The energies of the small-R jets are first corrected for pile-up contributions. A jet area-based pile-up correction is applied first as a function of event pile-up p_{T} density and jet area, followed by a residual pile-up correction [51]. Subsequently the jet energy scale (JES) and η calibration aims to correct the four-momentum of the reconstructed jet to the particle-level energy scale and to account for any potential biases in the jet η reconstruction. The JES specifically corrects for the non-compensating nature (for a compensating calorimeter, the electron/hadron signal ratio should be close to one) of the calorimeters and energy loss in the region where the detector has no measurements. Residual dependency of the JES on the longitudinal and transverse features of the jet still exists following the previous absolute MC-based calibrations. In order to further improve the jet energy resolution, a global sequential calibration (GSC) is designed to reduce the flavor dependence and energy leakage effects using calorimeter, track, and muon-segment variables. At last, an in situ calibration is applied to data only in order to account for the residual differences in the jet response between data and MC simulation.

Flavor Tagging

Z and Higgs bosons can decay into a pair of bottom quarks with large branching ratios—about 15% and 58%, respectively. Therefore, identifying jets originating from b-quarks, often referred to as b-tagging, is an important task for the physics program of the ATLAS experiment. b-tagging is very useful for suppressing background that is predominantly composed of jets initiated by light-flavor jets (from gluons or u, d, or s quarks) and thus warrants either high precision for precision measurements or excellent sensitivity for searches for new phenomena. Generally speaking, b-tagging algorithms work by exploiting the long lifetime, large mass and decay multiplicity of the b hadrons, and the hard b-quark fragmentation function. A specialized multivariate algorithm called “MV2”, which utilizes the Boosted Decision Tree (BDT) classifier, is employed in Run-II to discriminate between b-jets and jets of other flavors. The MV2 algorithm takes as input the outputs of several other b-tagging algorithms based on impact parameters, secondary vertex reconstruction, and reconstruction of the full decay chains [52]. Three variants of the MV2 algorithm exist, MV2c00, MV2c10 and MV2c20, where the name of the taggers indicates the c-jet fraction used in the training samples, e.g. in MV2c10, the background sample is composed of 10% (90%) c- (light-flavor) jets. The BDT output for the MV2c10 tagger can be seen in Figure 4.2 and the fixed-cut working point is used in this dissertation which yields a 65%–70% efficiency for b-jets. This particular working point of the MV2c10 algorithm also reduces the proportion of the light-flavor (c-quark) initiated jets by a factor of about 250–550 (10–20) depending on the jet kinematics [53].

4.3.2 Large-R Jets

The high center-of-mass energy of the LHC has made it possible for the production of the SM particles with significant Lorentz boosts or the production of new massive

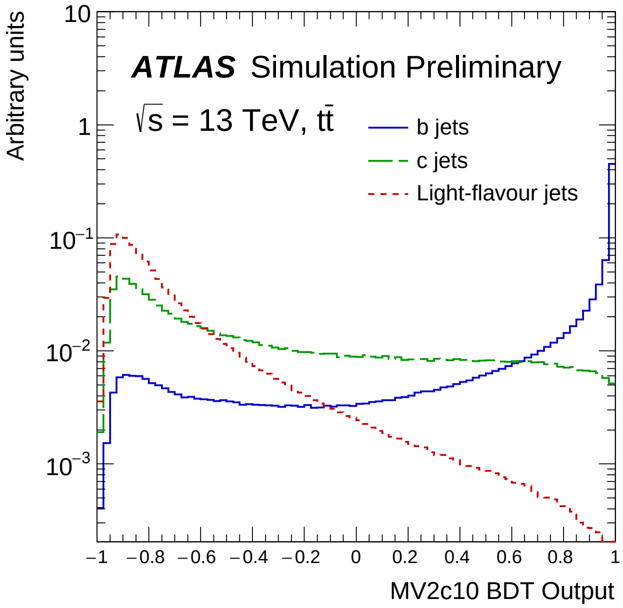

Figure 4.2: MV2c10 BDT output for b- (solid blue), c- (dashed green) and light-flavor (dotted red) jets evaluated with $t\bar{t}$ events [53].

particles that decay to highly Lorentz-boosted SM particles. For example, when sufficiently boosted, the hadronic decay products of the $W/Z/$Higgs bosons and the top quarks can become collimated to the point where the traditional reconstruction of a small-R jet is not able to capture the entirety of the boosted decay products. Moreover, the description of the substructure of these jets goes beyond the four-momentum description of a single parton. For example, the Z' particle, which is a heavy gauge boson proposed by some BSM theories, can decay into top-quark pairs with significant Lorentz boosts. The angular separation between the W and the b in the top decays decreases as the transverse momentum of the top quark increases. So does the angular separation between the subsequent hadronic decay products of the W boson as the p_{T} of the W boson increases as shown in Figure 4.3. The angular separation between the decay products in this case can be approximated by

$$\Delta R \approx \frac{2m}{p_{\mathrm{T}}}, \tag{4.3}$$

where m and p_{T} are the mass and the transverse momentum of the mother particle, respectively. For $p_{\mathrm{T}}^{W} > 200\,\mathrm{GeV}$, the ability to resolve the individual hadronic decay products using standard narrow-radius jet algorithms begins to degrade as $\Delta R < 1.0$. Large-R jets with $R = 1.0$ are then used to describe boosted particle decays

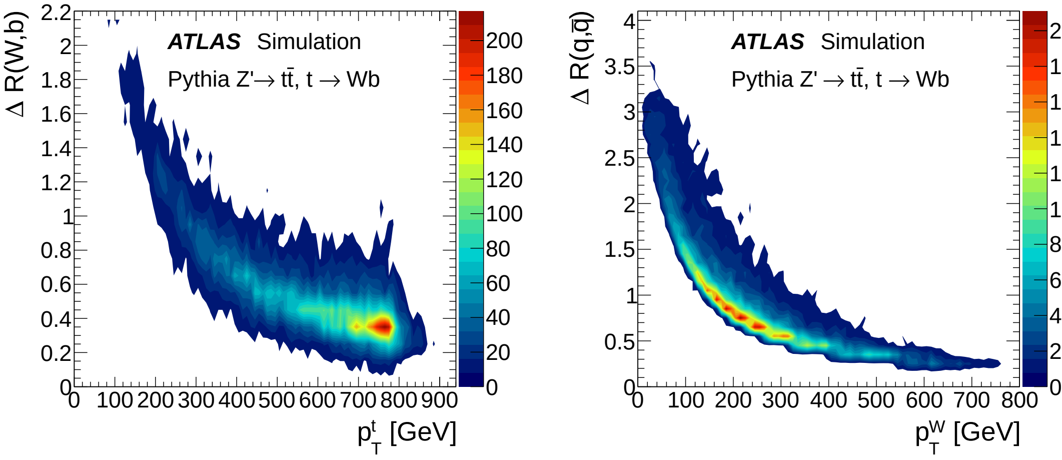

(a)

(b)

Figure 4.3: (a) The angular separation between the W boson and b-quark in top decays, $t \rightarrow Wb$, as a function of the top-quark transverse momentum (p_{T}^{t}) in simulated Pythia $Z' \rightarrow t\bar{t}$ ($m_{Z'} = 1.6\,\mathrm{TeV}$) events. (b) The angular distance between the light quark and anti-quark from $W \rightarrow q\bar{q}'$ decays as a function of the p_{T} of the W boson (p_{T}^{W}). Both distributions are at the generator level and do not include effects due to initial and final-state radiation, or the underlying event [54].

that are fully contained within individual large-area jets. A single large-R jet that contains all of the decay products of a massive particle has distinctive characteristics (substructures) of two-body or three-body decays which are absent in a single jet of the same p_{T} originating from a quark or gluon.

Large-R jets are reconstructed using the anti-k_t algorithm with $R = 1.0$. Jet grooming [54], which selectively removes the soft radiation from the jets, is subsequently performed to both improve the mass resolution and better elucidate the substructure properties of the large-R jets. In particular, a grooming technique called trimming is used in this dissertation as depicted in Figure 4.4. The trimming algorithm aims to remove contamination from initial-state radiation, multiple parton interactions, as well as the pile-up interactions. The procedure starts by re-clustering the constituents of the large-R jets into subjets using the anti-k_t algorithm with the distance parameter $R = 0.2$. Following the re-clustering, any subjets with $p_{\mathrm{T}}^{i}/p_{\mathrm{T}}^{\mathrm{jet}} < f_{\mathrm{cut}}$ are removed, where p_{T}^{i} is the transverse momentum of the i^{th} subjet, $p_{\mathrm{T}}^{\mathrm{jet}}$ represents the transverse momentum of the large-R jet being trimmed and the parameter $f_{\mathrm{cut}} = 0.05$ in this dissertation. Finally, The remaining constituents are recombined to form the trimmed jet.

A calorimeter-based jet mass [55] (m^{calo}) for a large-R jet J with calorimeter-cell

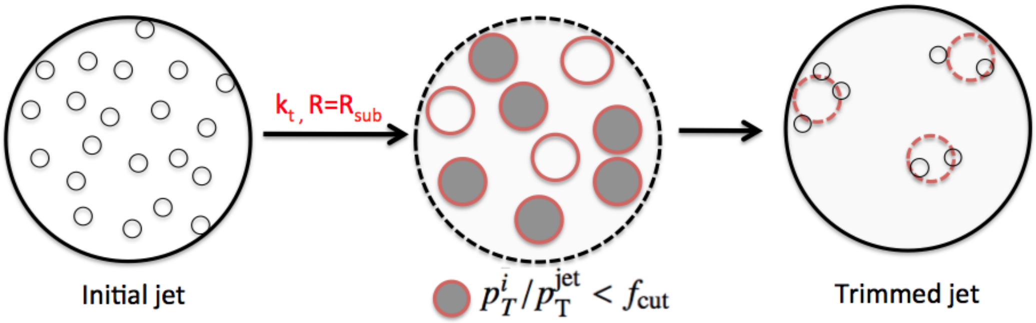

Figure 4.4: A schematic diagram depicting the trimming procedure for the large-R jets [54].

cluster constituents i with energy E_i, momentum $\vec{p}_i$ ($|\vec{p}_i| = E_i$) is defined as:

$$m^{\text{calo}} = \sqrt{\left(\sum_{i\in J} E_i\right)^2 - \left(\sum_{i\in J} \vec{p}_i\right)^2}. \tag{4.4}$$

Since the angular spread in the decay products of a boosted massive particle is approximately inversely proportional to the transverse momentum of the large-R jet, the spread becomes comparable to the calorimeter granularity for a sufficiently high Lorentz boost. Tracking information can be used in this case to maintain performance beyond this granularity limit. A track mass (m^{track}) is defined based on the ID tracks with $p_{\text{T}} > 0.4$ GeV that can be ghost-associated to the large-R jet. A track-assisted jet mass, m^{TA}, is then defined to compensate for the contributions from the missing neutral particle tracks to m^{track} by applying the ratio of the calorimeter-based to track-based transverse momentum to the track mass:

$$m^{\text{TA}} = \frac{p_{\text{T}}^{\text{calo}}}{p_{\text{T}}^{\text{track}}} \times m^{\text{track}}. \tag{4.5}$$

A weighted combination of the calorimeter-based mass and the track-assisted mass, m^{comb}, is defined to take advantage of both jet mass definitions and to keep a consistent mass definition across the p_{T} range [55]:

$$m^{\text{comb}} \equiv w^{\text{calo}} \times m^{\text{calo}} + w^{\text{TA}} \times m^{\text{TA}}, \tag{4.6}$$

and

$$w^{\text{calo}} = \frac{\sigma_{\text{calo}}^{-2}}{\sigma_{\text{calo}}^{-2} + \sigma_{\text{TA}}^{-2}}, \quad w^{\text{TA}} = \frac{\sigma_{\text{TA}}^{-2}}{\sigma_{\text{calo}}^{-2} + \sigma_{\text{TA}}^{-2}}, \tag{4.7}$$

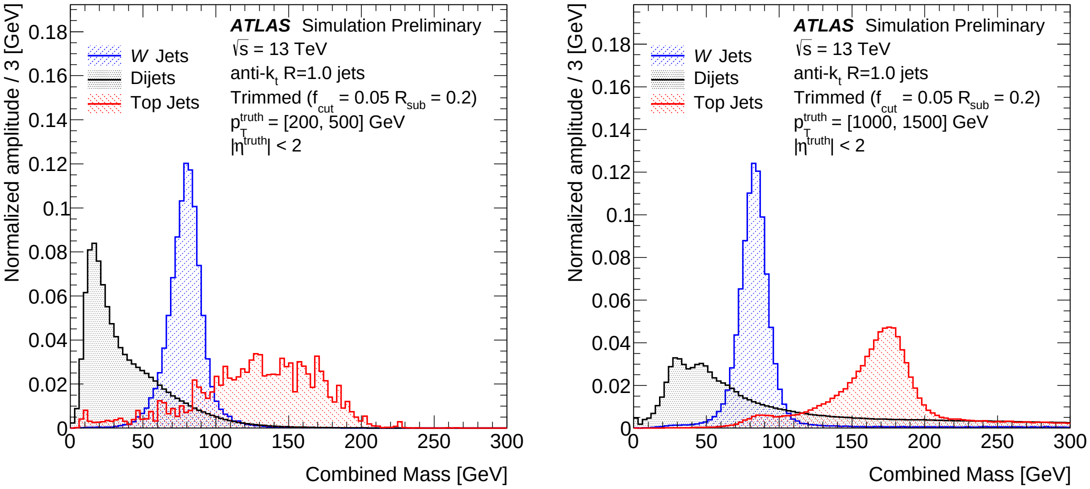

(a) (b)

Figure 4.5: Distributions of the combined track-assisted and calorimeter large-R jet mass for low p_{T} [200, 500] GeV (left) and high p_{T} [1000, 1500] GeV (right) W, top and QCD jets [55].

where σ_{calo} and σ_{TA} are the calorimeter- and the track-assisted mass resolution functions respectively. Distributions of the combined track-assisted and calorimeter jet mass are shown in Figure 4.5 and the improvement in the jet mass resolution using the combined mass is shown in Figure 4.6. Similarly, the transverse momentum of the large-R jet is also scaled to be compatible with the combined mass according to:

$$p_{\mathrm{T}}^{\text{comb}} = p_{\mathrm{T}}^{\text{calo}} \times \frac{m^{\text{comb}}}{m^{\text{calo}}}. \tag{4.8}$$

Different techniques have been developed to to probe the substructures of the large-R jets originated either from a two-body or three-body decay. These turn out to be extremely useful for rejecting QCD background jets. Since only the boosted W and Z bosons are of interest in this dissertation, only techniques relevant to these boosted objects will be discussed in the following text. A substructure variable $D_2^{\beta=1}$ is used to identify the two-pronged substructure of a large-R jet. The $D_2^{\beta=1}$ variable is defined in terms of generalized energy correlation functions (ECFs). The ECFs identify the N-pronged substructure of a jet by studying the angular separation and transverse momentum of combinations of its constituents. The two-point and three-

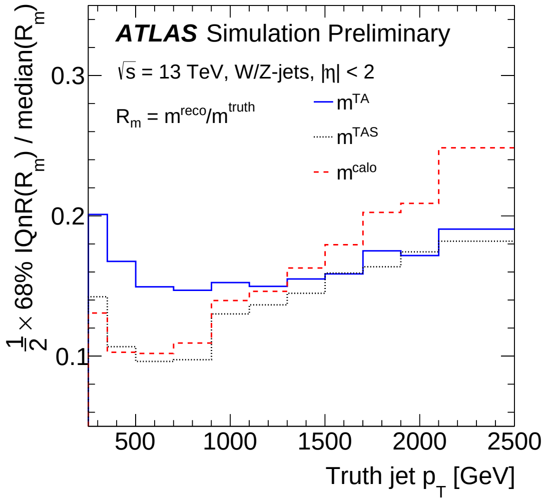

(a) (b)

Figure 4.6: The large-R jet mass resolution as a function of jet p_{T} for jets produced from boosted W bosons (left) and from boosted top quarks (right) [55]. m^{TAS} is the track-assisted subjet mass, which is the invariant mass of the sum of all track-assisted subjet four-vectors. The 68% interquartile range (IQnR) is defined as $q_{84\%} - q_{16\%}$, where $q_{16\%}$ and $q_{84\%}$ denote the 16th and the 84th percentiles of a given distribution. The resolution is shown as the ratio of $0.5 \cdot (q_{84\%} - q_{16\%})$ to the median location of the peak.

point normalized ECFs are summed over the jet constituents and defined as [56][57]:

$$e_2^\beta = \frac{1}{\left(p_{\mathrm{T}}^{\mathrm{jet}}\right)^2} \sum_{i<j\in J} p_{\mathrm{T}}^i p_{\mathrm{T}}^j R_{ij}^\beta \tag{4.9}$$

$$e_3^\beta = \frac{1}{\left(p_{\mathrm{T}}^{\mathrm{jet}}\right)^3} \sum_{i<j<k\in J} p_{\mathrm{T}}^i p_{\mathrm{T}}^j p_{\mathrm{T}}^k R_{ij}^\beta R_{jk}^\beta R_{ik}^\beta \tag{4.10}$$

where R_{ij} is the euclidean distance in η and ϕ between constituent i and j, p_{T}^i is the transverse momentum of constituent i, and $p_{\mathrm{T}}^{\mathrm{jet}}$ is the transverse momentum of the large-R jet. The e_{N+1}^β function approaches zero and will be much smaller than e_N^β for a jet with only N constituents. Therefore, the $D_2^{\beta=1}$ variable is defined as Equation (4.11) and is used as a discriminant for W and Z tagging.

$$D_2^{\beta=1} = \frac{e_3^{\beta=1}}{\left(e_2^{\beta=1}\right)^3} \tag{4.11}$$

A few representative distributions of the $D_2^{\beta=1}$ (also referred to as D_2 hereinafter)

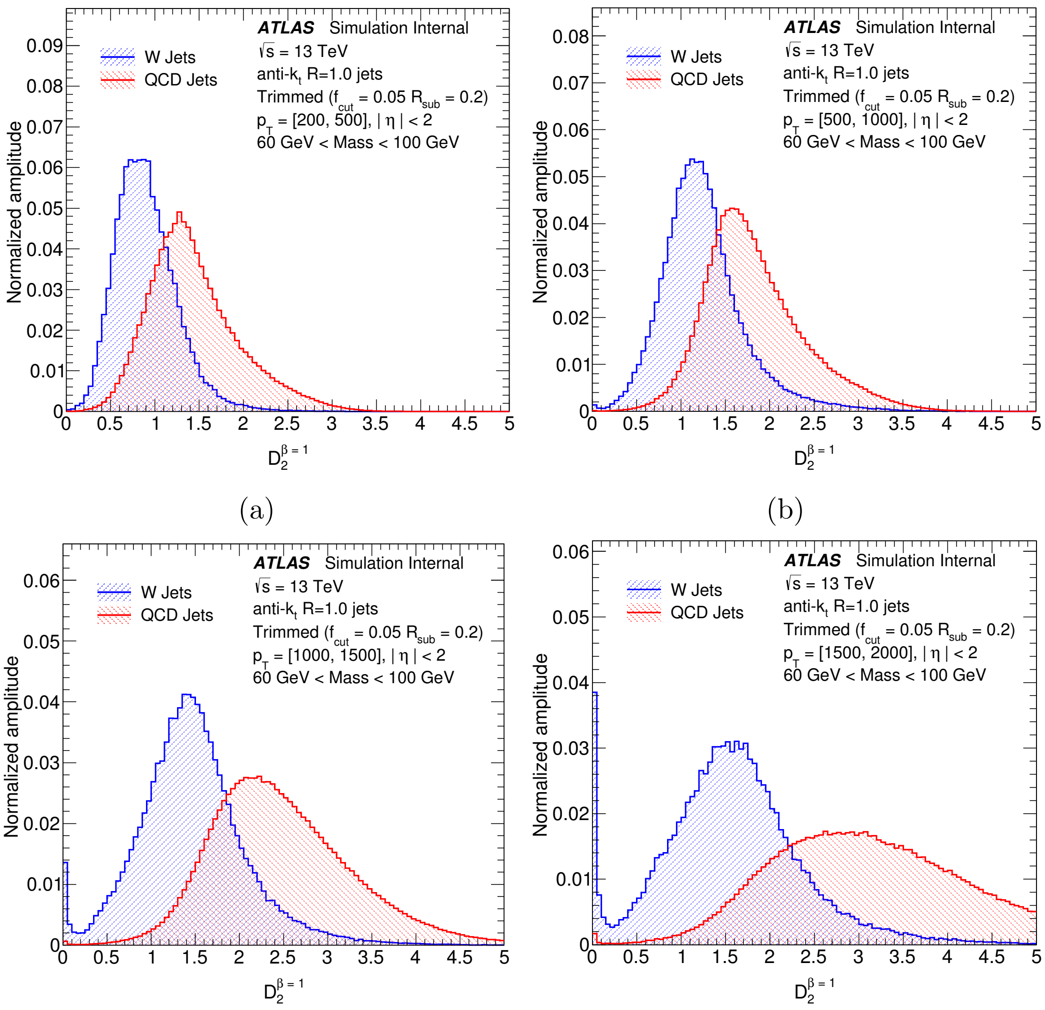

(a) (b) (c) (d)

Figure 4.7: Distributions of the $D_2^{\beta=1}$ variable for the background di-jet samples and the signal W boson jets for different p_{T} bins of the truth-matched jets [55].

variable are shown in Figure 4.7 for both background and signal processes. The W and Z tagging algorithms are then optimized separately based on the combined mass and the $D_2^{\beta=1}$ variable. A 50% and a 80% efficiency working points are defined for both tagging algorithms. The former one is used to define "high-purity" signal regions in this dissertation because it ensures better background rejection, whereas the latter one with higher signal efficiency but lower background rejection power is used to define "low-purity" regions. The optimized cut definitions and performances of each tagger as a function of the jet p_{T} are shown in Figures 4.8-4.10 [58].

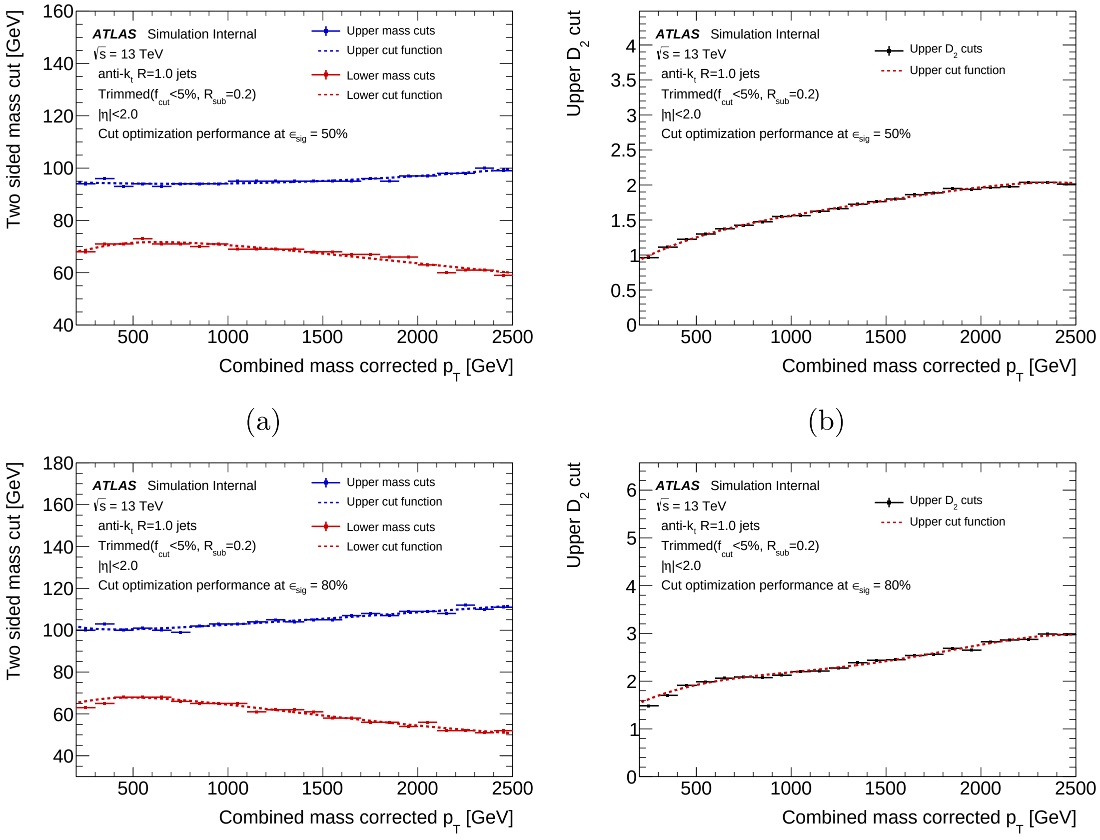

(a) (b)

(c) (d)

Figure 4.8: Smoothed cut functions fitted to optimized fixed cuts for W-boson tagging using the substructure variable combination: combined mass + $D_2^{\beta=1}$. These cut functions are shown at $\epsilon_{\text{sig}} = 50\%$ (a, b) and $\epsilon_{\text{sig}} = 80\%$ (c, d) [58].

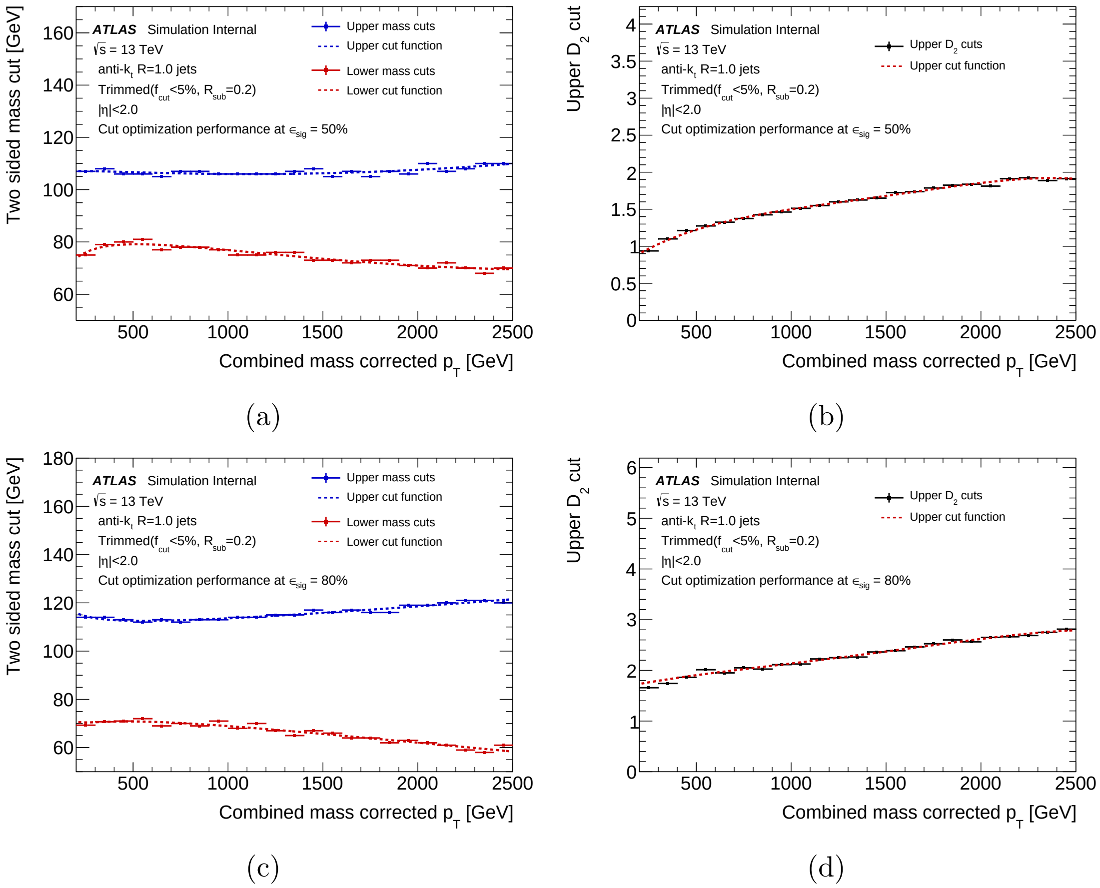

(a) (b)

(c) (d)

Figure 4.9: Smoothed cut functions fitted to optimized fixed cuts for Z-boson tagging using the substructure variable combination: combined mass + $D_2^{\beta=1}$. These cut functions are shown at $\epsilon_{\text{sig}} = 50\%$ (a, b) and $\epsilon_{\text{sig}} = 80\%$ (c, d) [58].

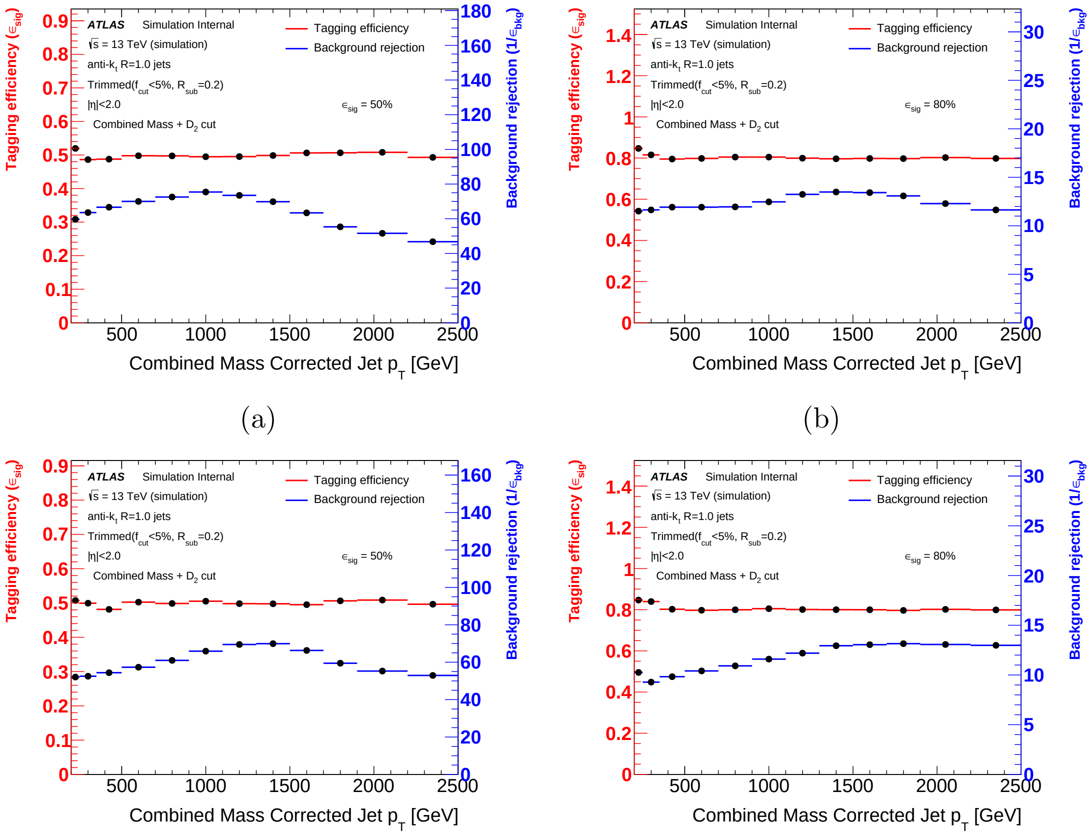

(a)

(b)

(c)

(d)

Figure 4.10: Recommended W-boson and Z-boson tagger performance (both signal efficiency and background rejection) as a function of combined mass corrected jet p_{T}. The performance is presented for W-boson tagging at $\epsilon_{\mathrm{sig}} = 50\%$ (a) and $\epsilon_{\mathrm{sig}} = 80\%$ (b), and for Z-boson tagging at $\epsilon_{\mathrm{sig}} = 50\%$ (c) and $\epsilon_{\mathrm{sig}} = 80\%$ (d) [58].

4.4 Missing Transverse Momentum

The missing transverse momentum ($\boldsymbol{E}_{\mathrm{T}}^{\mathrm{miss}}$) is defined as the momentum imbalance in the plane transverse to the beam axis. Large momentum imbalance may signal the presence of particles which escape the detector, such as neutrinos or stable, weakly-interacting particles. Observables related to the missing transverse momentum can be reconstructed from the transverse momenta of the reconstructed physics objects and additional "soft terms" which correspond to tracks from the primary vertex that are not matched to any reconstructed objects. The two components of $\boldsymbol{E}_{\mathrm{T}}^{\mathrm{miss}}$ are given by:

$$E_{x(y)}^{\mathrm{miss}} = -\left\{ \sum_{i\in\{\text{hard objects}\}} p_{x(y),i} + \sum_{j\in\{\text{soft signals}\}} p_{x(y),j} \right\} \tag{4.12}$$

The following observables can then be constructed:

$$\boldsymbol{E}_{\mathrm{T}}^{\mathrm{miss}} = (E_x^{\mathrm{miss}}, E_y^{\mathrm{miss}}), \tag{4.13}$$

$$E_{\mathrm{T}}^{\mathrm{miss}} = |\boldsymbol{E}_{\mathrm{T}}^{\mathrm{miss}}| = \sqrt{(E_x^{\mathrm{miss}})^2 + (E_y^{\mathrm{miss}})^2}, \tag{4.14}$$

$$\phi^{\mathrm{miss}} = \tan^{-1}\left(E_y^{\mathrm{miss}}/E_x^{\mathrm{miss}}\right) \tag{4.15}$$

Hard objects in Equation (4.12) include identified electrons, muons, as well as jets. Soft terms included in Equation (4.12) are exclusively reconstructed from ID tracks from the hard-scatter vertex, therefore only using the p_{T}-flow from soft charged particles. The soft terms ignore signals from soft neutral particles which are normally reconstructed by using the calorimeter-based $E_{\mathrm{T}}^{\mathrm{miss,\,soft\,calo}}$ from topo-clusters. However, the track-only-based method leads to better reconstruction performance and overall $E_{\mathrm{T}}^{\mathrm{miss}}$ resolution due to a minimal residual dependence on pile-up conditions [59].

4.5 Overlap Removal

Clusters of energy deposits or tracks measured in the ID can be shared by several physics objects simultaneously during the reconstruction procedure since electrons, muons, and jets all use a combination of tracking and calorimetric measurements. Therefore, ambiguities have to be resolved before any physics analysis is carried out. An overlap removal procedure is defined to prioritize the reconstructed objects and remove any ambiguity. The procedure proceeds as follows:

- If an electron candidate shares the same ID track with a muon candidate, the electron is removed. This occurs when a muon radiates a hard photon via the bremsstrahlung process; consequently, the muon is also reconstructed as an electron in the calorimeter which then shares the same ID track with the muon.

- Secondly, a small-R jet is removed if it coincides with an electron candidate with $\Delta R(\text{jet}, e) < 0.2$. This is due to the electron being clustered as a jet at the same time. However, an electron candidate is removed if $0.2 < \Delta R(\text{jet}, e) < \min(0.4,\, 0.04 + 10\,\text{GeV}/p_{\text{T}}(e))$. Electrons reconstructed near the edge of a jet arise from non-prompt decays during the hadronization in most cases.

- Similarly, if a muon and small-R jet satisfy $\Delta R(\text{jet}, \mu) < 0.2$, and either 1) the jet has fewer than two tracks or 2) $p_{\text{T}}(\mu)/p_{\text{T}}(\text{jet}) > 0.5$ and $p_{\text{T}}(\mu)/\sum p_{\text{T}}(\text{tracks}) > 0.7$, the jet candidate is discarded. This indicates that the jet is most likely due to energy loss of the muon in the calorimeter. On the other hand, the muon candidate is removed if $\Delta R(\text{jet}, \mu) < \min(0.4,\, 0.04 + 10\,\text{GeV}/p_{\text{T}}(\mu))$.

- Finally, if there is a large-R jet and an lepton ($\ell = e,\, \mu$) with $\Delta R(\text{jet},\, \ell) < 1.0$, the large-$R$ jet is removed. This criterion is to address the case when a leptonically decaying Z boson with relatively high momentum is reconstructed as a large-R jet in the calorimeter.

CHAPTER 5

Searches for ZW and ZZ Resonances

5.1 Analysis Overview and Strategy

This chapter presents searches for heavy diboson resonances, which are generically referred to as Xs, in the $X \to ZW \to \ell\ell qq$ or $X \to ZZ \to \ell\ell qq$ ($\ell = e$, μ) semi-leptonic channel in a mass range from 300 to 5000 GeV [60]. As motivated in Chapter 2, diboson events are a valuable probe of new physics, particularly in the high mass region. The $\ell\ell qq$ semi-leptonic final state has the advantage of combining the clean signature of a dilepton event with the hadronic decays of W or Z bosons, which have large branching ratios. Techniques for identifying jets originating from bottom quarks and for tagging large-radius W/Z-boson jets (Chapter 4) further enhance the sensitivities of searches with this particular type of event topology. Benchmark signal models considered include a heavy neutral Higgs boson with narrow-width approximation (negligible width compared to the detector resolution) [61], a spin-1 W' boson in the context of the HVT framework [19, 20], and a spin-2 RS graviton (G_{KK}) in the bulk Randall-Sundrum model [21–23]. A detailed description of these models can be found in Chapter 2. Each spin hypothesis corresponds to an individual search: $H \to ZZ \to \ell\ell qq$ search for the spin-0 hypothesis, $W' \to ZW \to \ell\ell qq$ search for the spin-1 hypothesis, and $G_{\mathrm{KK}} \to ZZ \to \ell\ell qq$ search for the spin-2 hypothesis. Different production modes (e.g. gluon-gluon fusion, vector boson fusion etc.) are also considered in the searches. The invariant mass spectrum of the dilepton and large-R jet system, $m_{\ell\ell J}$, or that of the dilepton and dijet system, $m_{\ell\ell jj}$, is used to extract signals from the SM background in the merged and resolved regimes, respectively.

The $V \to qq$ ($V = W$, Z) decay can be reconstructed either as a di-jet system (jj) or a single large-R jet (J) depending on the transverse momentum of the V boson. For a hadronically decaying W or Z boson ($V \to qq$), the angular distance between the decay products can be approximately expressed as [62]:

$$\Delta R_{qq} \sim \frac{2m_V}{p_{\mathrm{T}}^V} \tag{5.1}$$

In the case of searching for heavy diboson resonances, the two SM bosons emerging from the new resonance will have similar momenta in the transverse plane due to the resonance being produced approximately at rest. The transverse momenta of these two bosons are about half the mass of the new resonance. Therefore, for a resonance with mass below 500 GeV, the majority of the hadronic decays of the daughter W/Z bosons will be reconstructed as two separate jets of small radius. These kind of events are said to be in the "resolved" regime. Bosons coming from heavier resonances have larger boosts in the transverse plane. Their decay products become collimated and can be reconstructed as large-R jets when $p_{\mathrm{T}}(V) \gtrsim 200$ GeV (Equation (5.1)). Events with boosted large-R jets are classified into the "merged" regime.

The transition from the resolved to the merged regime is not clear-cut. Merged and resolved topologies could exist simultaneously for resonances with mass between 0.4 TeV and 1.2 TeV. Therefore, a decision as to which object(s) to select has to be made when the decay products are reconstructed at the same time in the two ways mentioned. In this analysis, the merged topology is prioritized because the boson tagging algorithm proves to be a better discriminating tool because of the technique for probing the substructure of a large-radius jet.

The $H \to ZZ \to \ell\ell qq$ search probes both gluon-gluon fusion (ggF) and vector boson fusion (VBF) production mechanisms. Similarly for the $W' \to ZW \to \ell\ell qq$ search, both Drell-Yan (DY) and VBF topologies are studied. However, only the ggF production mechanism is considered for the RS graviton model due to ggF being the absolute dominant production mode. Feynman diagrams representing these production mechanisms are shown in Figure 5.1 [60]. The unique VBF topology has two additional jets typically with large separation in η and high di-jet invariant mass. This distinguishable feature provides a powerful means to discriminate between signal and background processes. In this analysis, the VBF topology is always considered first to improve the search sensitivity due to its unique features and smaller background contamination.

In the remainder of this section, major backgrounds relevant to this analysis, Monte Carlo (MC) generators employed to generate various background and signal processes, and the dataset upon which this analysis is built are discussed.

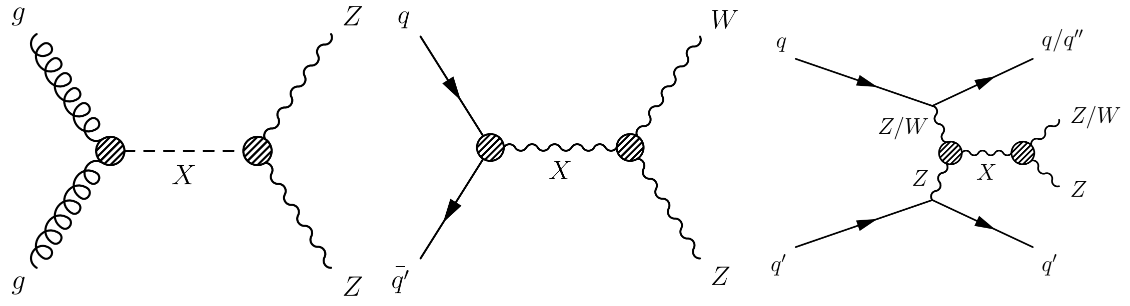

(a) gluon-gluon fusion (b) Drell-Yan (c) vector-boson fusion

Figure 5.1: Representative Feynman diagrams for the production of heavy resonances X with their decays into a pair of vector bosons [60].

5.1.1 Main Background Processes

Relevant background contributions from the SM must be understood and estimated properly in order to achieve an accurate presentation of the data and a reliable interpretation of the results. The dominant background processes for this analysis are all irreducible backgrounds as they have the exact $\ell\ell qq$ final state.

The most significant background source is the production of jets in association with a Z boson that decays leptonically. The Z+jets background is the dominant source in both merged and resolved regimes (Figure 5.12). The jets of the Z+jets background after selections have a non-resonant mass spectrum and can be either reconstructed as two separate jets or one large-R jet depending on the kinematics. Since the jets in association with the Z boson are not from boson decays and have a smaller heavy-flavor content, boson tagging and b-tagging algorithms can help to suppress the Z+jets in the merged and resolved regimes, respectively.

The second largest background source in the merged regime is the non-resonant production of vector-boson pairs (ZZ, WZ and WW), denoted as SM diboson production hereinafter. Top quark production and the SM diboson production have comparable contributions in the resolved regime, with the former being much larger in the region where there are two b-tagged jets identified (Figure 5.12). The top quark production considered includes the production of a top-antitop quark pair ($t\bar{t}$), and the electroweak production of a single top quark. s-channel, t-channel and the tW mode are all considered for the single top production. Single-top contributions become negligible after the requirement of two leptons.

Other sources of background from the SM are found to be negligible and therefore not considered.

5.1.2 Background and Signal Modeling

Monte Carlo (MC) techniques are extensively used in the field of high energy physics to model both known SM processes and signal processes predicted by theories beyond the Standard Model. Matrix elements for the initial hard scattering processes are calculated with a fixed number of incoming and outgoing partons using a perturbative method. The cross section of a hard scattering process is calculated at the leading order (LO) in α_s (the strong coupling constant) with or without incorporating next-to-leading order (NLO) or even next-to-next-to-leading order (NNLO) corrections. Subsequent activities at the parton level, involving initial- and final-state radiations, multiple parton-parton interactions and the structure of beam remnants, are modeled next. At this stage, a more or less realistic interaction picture has been formed, which generally includes broadened jets, underlying events etc. Hadronization of the color connected constituents are generated next, along with decays of the unstable particles. Pile-up interactions, which are collisions in addition to the collision of interest, are also simulated. The pile-up profile, a distribution of the average number of interactions per bunch crossing $\langle\mu\rangle$, can be adjusted later to match the pile-up condition of the recorded data. This procedure is referred to as "pile-up reweighting" of the MC samples [63]. The particles in the simulated events are then propagated through a detailed detector simulation based on GEANT4 [64] and subsequently the same reconstruction algorithms [65] used for data are employed to process the MC events.

Background Modeling

The Z+jets background is modeled by the SHERPA 2.2.1 [66] event generator with the NNPDF3.0 NNLO [26] PDF set, in which the matrix elements are calculated up to four partons at LO and two partons at NLO using the Comix [67] and OpenLoops [68] packages. The samples are first grouped based on the number of b and c quarks produced, and then split into different slices according to max(h_{T}, $p_{\mathrm{T}}(Z)$), where h_{T} represents the scalar sum of the transverse momenta of the jets in an event. The jets produced are labeled based on the truth flavors of the hadrons that can be matched to the respective reconstructed small-R jets. The matched hadrons are required to have

$p_{\mathrm{T}} > 5\,\mathrm{GeV}$ and an angular separation of $\Delta R < 0.3$ with respect to the reconstructed jet axes. In Z+jets MC samples, a jet is labeled as a b-jet (in contrast to a b-tagged jet identified by the b-tagging algorithm at reconstruction level) if a b-hadron is found. c-jet is assigned analogously and a jet is labeled as a light jet (i.e., u-, d-, or s-quark, or gluon), if neither a b-hadron or a c-hadron is found in the vicinity of the jet. An event is classified as a "Z+heavy-flavor" event if a b- or c-jet is found in the event. Similarly, an event will be labeled as "Z+light-flavor" if only light jets are associated. This classification allows for flavor-dependent corrections to discrepancies between data and MC.

SM diboson processes are simulated using Sherpa 2.1.0 with the CT10 [69] PDF set, where one of the bosons is required to decay hadronically and the other one leptonically. A maximum of three additional partons are generated at LO for these samples, and up to one (zero) additional parton(s) at NLO are calculated for ZZ (WZ and WW). An alternative set of SM diboson samples is also generated using the Powheg-Box v1 [70–72] generator in conjunction with the CT10 PDF set. This set of samples is compared with the nominal set in order to estimate the modeling systematic uncertainties.

Top quark pair production, single top production in the s-channel, and single top production in the associated tW channel are realized using the Powheg-Box v2 [73] event generator with the CT10 PDF set. The t-channel of the single top process is generated by Powheg-Box v1 using the CT104f [69] PDF set in a fixed four-flavor scheme. For all top quark processes, the top quark mass is set to 172.5 GeV. Spin correlations of the top quark are also preserved. In addition, one of the top quarks is required to decay leptonically in the $t\bar{t}$ event generation. Pythia 6.428 [74] with the CTEQ6L1 [75] PDF set and the corresponding Perugia 2012 tune (P2012) [76] are used for parton shower, fragmentation, and underlying event simulation. The EvtGen v1.2.0 program [77] is used to model the decays of the bottom and charm quarks.

Cross sections of all the SM background processes considered in this analysis are determined at NNLO order, with the exception of the SM diboson and the single top productions. Cross sections of the V+jets productions are calculated with up to NNLO QCD corrections [78]. Cross sections are calculated at NLO including LO contributions with two additional partons [66, 79] for the SM diboson processes. The cross section of the top pair production is calculated at NNLO in QCD, including resummation of next-to-next-to-leading logarithmic (NNLL) soft-gluon terms [80, 81]. The single-top production cross sections are calculated to NLO in QCD [82] with the soft-gluon resummation at NNLL [83] for the tW process. A summary of the Monte

Table 5.1: A summary of the Monte Carlo samples used to model the background processes considered in this analysis. The corresponding cross sections times branching fractions ($\sigma \times \mathcal{B}$) are quoted at $\sqrt{s} = 13\,\text{TeV}$.

Process	MC Generator	PDF Set	$\sigma \times \mathcal{B}$ (pb)
$Z \to ee$+jets	Sherpa 2.2.1	NNPDF3.0 NNLO	2084.46
$Z \to \mu\mu$+jets	Sherpa 2.2.1	NNPDF3.0 NNLO	2085.48
$Z \to \tau\tau$+jets	Sherpa 2.2.1	NNPDF3.0 NNLO	2086.66
SM WW	Sherpa 2.1.0	CT10	45.27
SM WZ	Sherpa 2.1.0	CT10	19.74
SM ZZ	Sherpa 2.1.0	CT10	2.14
$t\bar{t}$	Powheg+Pythia6	CT10	831.76
s-channel single top	Powheg+Pythia6	CT10	3.35
t-channel single top	Powheg+Pythia6	CT104f	70.43
tW-channel single top	Powheg+Pythia6	CT10	71.67

Carlo samples used is presented in Table 5.1.

Signal Modeling

The heavy neutral Higgs boson with the decay $H \to ZZ$ is generated using Powheg-Box v1 with the CT10 PDF set. The width of Higgs boson is set to be negligible (Section 2.3.1) compared to the experimental resolution (Figure 5.17) of the ATLAS detector and any interference effects with the SM Higgs boson and SM diboson productions are neglected. Both ggF and VBF topologies are considered and these two production modes are simulated independently.

MadGraph5_aMC@NLO 2.2.2 [84] with the NNPDF23LO [26] PDF set is used for the production and decay of the spin-1 $W' \to ZW$. Both DY and VBF production modes of the charged vector triplet W' are considered. In the VBF production mode, its coupling to fermions is explicitly set to zero ($c_F = 0$). For the DY production, Model A ($g_V = 1$) and Model B ($g_V = 3$) are considered for the interpretation of the final results. The width of the new resonance from the DY production of Model A is approximately 2.6% of its mass, and is much narrower in VBF production due to that its couplings to fermions are set to zero [20]. Model A and B share similar resonance widths and experimental signatures, and the differences are further diluted by detector related effects. Therefore, samples generated for the Model A interpretation are directly used for the interpretation of Model B as well, after a rescaling of the relevant branching ratios.

The RS graviton ($G_{\mathrm{KK}} \to ZZ$) with $k/\overline{M}_{\mathrm{Pl}} = 1.0$ is produced using the same generator as for W'. Gravitons with $k/\overline{M}_{\mathrm{Pl}} = 0.5$ are also generated by reweighting the corresponding $k/\overline{M}_{\mathrm{Pl}} = 1.0$ samples to account for the differences in decay widths (with $k/\overline{M}_{\mathrm{Pl}} = 0.5$ being about four times smaller) and cross sections. The width of G_{KK} depends on the resonance mass, varying from $3.7\% \cdot m(G_{\mathrm{KK}})$ at 0.5 TeV to $6.4\% \cdot m(G_{\mathrm{KK}})$ at 5 TeV in the $k/\overline{M}_{\mathrm{Pl}} = 1.0$ scenario.

Parton showering, hadronization and the underlying events are modeled by interfacing the generated events with Pythia 8.186 [85]. The A14 set of the tuned parameters (tune) [86] for the underlying event is used for the spin-1 and spin-2 signals, and the AZNLO tune [87] is used for the Higgs samples.

5.1.3 Dataset

The full dataset recorded by the ATLAS experiment at 13 TeV during the 2015-2016 run period is used in this analysis. The total integrated luminosity amounts to $36.1\,\mathrm{fb}^{-1}$, after rejecting the lumi-blocks of insufficient quality (with details described in Section 5.3.2). A summary of the luminosity and pile-up conditions is presented in Table 5.2.

Table 5.2: A summary of the maximum instantaneous luminosity, the total integrated luminosity, and the average number of interactions per bunch crossing, for the data recorded in 2015 and 2016 by the ATLAS detector.

Year	Maximal $\mathcal{L}_{\text{inst.}}$ [$\mathrm{cm}^{-2}\mathrm{s}^{-1}$]	$\int \mathcal{L}dt$ [fb^{-1}]	$\langle\mu\rangle$
2015	0.50×10^{34}	3.2	3.7
2016	1.37×10^{34}	32.9	24.9

5.2 Object Selection

This section describes the selections applied on the reconstructed physics objects described in Chapter 4. Physics objects are required to satisfy certain kinematic criteria to ensure the quality of these objects, pass the trigger requirement, and possibly improve the sensitivity of the analysis. A summary of the object selections used in this analysis is presented in Table 5.3 with more verbose descriptions provided in the subsections that follow.

5.2.1 Electron Selection

After the reconstruction and overlap removal stage, corrections on the electron energy scale and resolution are applied as documented in [88]. Electron candidates are then selected by requiring the following criteria:

- Kinematic cuts:
  - $p_{\mathrm{T}} > 7\,\mathrm{GeV}$
  - $|\eta| < 2.47$
- Identification:
  - LooseLH identification
  - Requirement of a hit in the IBL
- Isolation:
  - "LooseTrackOnly" isolation ($\epsilon_{\mathrm{sig}} \sim 99\%$)
- Impact parameter requirements:
  - $|d_0/\sigma(d_0)| < 5$
  - $|z_0 \sin\theta| < 0.5$ mm

Furthermore, electrons are labeled as "signal" electrons if they satisfy $p_{\mathrm{T}} > 28\,\mathrm{GeV}$. Scale factors, which are exclusively applied to Monte Carlo, are used to correct the identification, reconstruction, trigger, and isolation efficiencies [43] in Monte Carlo to match that obtained in data.

Table 5.3: A summary of the criteria for object selections used in the $X \rightarrow ZV \rightarrow \ell\ell qq$ analysis.

Object	Kinematics	Quality	Additional
Electrons	p_T >7 GeV $\lvert\eta\rvert < 2.47$	LooseLH $\lvert d_0/\sigma(d_0)\rvert$ <5 $\lvert z_0 \sin\theta\rvert < 0.5\,\mathrm{mm}$ LooseTrackOnly	B-layer (IBL) hit requirement
Muons	p_T >7 GeV $\lvert\eta\rvert < 2.5$	Loose quality $\lvert d_0/\sigma(d_0)\rvert$ <3 $\lvert z_0 \sin\theta\rvert < 0.5\,\mathrm{mm}$ LooseTrackOnly	
Large-R jets	p_T >200 GeV $\lvert\eta\rvert < 2.0$	anti-k_t R =1.0 trimmed ($R_{\mathrm{subjet}} = 0.2$, $f_{\mathrm{cut}} = 5\%$)	
Small-R jets	p_T >30 GeV $\lvert\eta\rvert < 4.5$	anti-k_t R =0.4	jet-vertex-tagger if p_{T} <60 GeV, $\lvert\eta\rvert < 2.4$

5.2.2 Muon Selection

Corrections on the momentum scale and resolution [46] of the muon candidates are applied to the Monte Carlo following the reconstruction and overlap removal procedure. Muon candidates used in this analysis are then selected by applying the following selections:

- Kinematic cuts:
  - $p_{\mathrm{T}} > 7\,\mathrm{GeV}$
  - $|\eta| < 2.5$
- Identification:
  - Loose quality: all the CB and SA muons are included; CT and ST muons are restricted to the region $|\eta| < 0.1$ (see Section 4.2).
- Isolation:
  - "LooseTrackOnly" isolation ($\epsilon_{\mathrm{sig}} \sim 99\%$)
- Impact parameter requirements:

  - $|d_0/\sigma(d_0)| < 3$
  - $|z_0 \sin\theta| < 0.5$ mm

Similar to the electron case, "signal" muon candidates must satisfy $p_{\mathrm{T}} > 28\,\mathrm{GeV}$. Additionally, scale factors are applied to correct the identification and isolation efficiencies [46] in Monte Carlo to match that obtained in data.

5.2.3 Small-R Jet Selection

Small-R jets are built from topological clusters, formed from calorimeter cell deposits, and calibrated to the electromagnetic (EM) scale. They are reconstructed using the anti-k_t algorithm with a distance parameter of $R = 0.4$ (Section 4.3). The four momentum of a jet is then corrected for the beam-spot and a jet energy scale calibration is performed. Certain low-p_{T} jets are required to pass a selection called jet vertex tagging (JVT) [89]. The JVT algorithm attempts to remove pile-up jets originating from QCD effects from a single pile-up vertex and stochastic effects which could be due to contributions from several vertices. The jet-vertex-tagger uses the fraction of tracks in the jet coming from the primary vertex to identify jets that are likely to arise from pile-up effects. In this dissertation, the 92% efficiency working point of the jet-vertex-tagger is used for jets with $p_{\mathrm{T}} < 60\,\mathrm{GeV}$ and $|\eta| < 2.4$ which reduces the residual pile-up jet roughly to a 2% level. The detailed selection criteria for jets are as follows:

- Kinematic requirements:
  - $p_{\mathrm{T}} > 30\,\mathrm{GeV}$ and $|\eta| < 2.5$, the jet is labeled as a "signal jet" or,
  - $p_{\mathrm{T}} > 30\,\mathrm{GeV}$ and $2.5 < |\eta| < 4.5$, the jet is labeled as a "forward jet".
- Pile-up removal criterion:
  - A jet must satisfy the 92% JVT working point if $p_{\mathrm{T}} < 60\,\mathrm{GeV}$ and $|\eta| < 2.4$
- b-tagging (discretionary):
  - When identifying a b-jet, the `MV2c10` algorithm and the corresponding 70% fixed-cut working point are used (Section 4.3).

5.2.4 Large-R Jet Selection

A large-R jet is formed by clustering the topological clusters using the anti-k_t algorithm with a distance parameter of $R = 1.0$ and subsequently applying the trimming procedure with $R_{\text{subjet}} = 0.2$ and $f_{\text{cut}} = 0.05$ as described in Section 4.3. The *in-situ* calibrations of the jet energy scale and the jet mass scale [90] are applied and a large-R jet is then selected if:

- $p_{\text{T}} > 200\,\text{GeV}$,
- $|\eta| < 2.0$ (centrality ensures a good overlap between the ID tracking and the calorimeter information).

Boson tagging algorithm (Section 4.3) is then applied to identify hadronically decaying a W or Z boson with a large Lorentz boost in the transverse plane. The application of boson tagging is only used for classifying events into the signal and control regions in the merged regime (Section 5.3).

5.3 Event Selection and Categorization

Event selection represents the architectural design of an analysis, and careful thoughts have to be given to characteristics unique to each signal in order to distinguish it from its background. This section describes the sequence of selection criteria applied, including trigger requirements, preselection of $Z \to \ell\ell$ events, and the selection of $X \to ZV \to \ell\ell qq$ optimized individually for each signal hypothesis. VBF and ggF/DY categories, which are designed for searches that probe VBF production, are defined and discussed. Finally, the expected signal performance is presented.

5.3.1 Trigger

The union (logical OR) of multiple high-level un-prescaled single-lepton triggers [91, 92] is used to efficiently select the type of events suitable for this analysis. Each trigger attempts to identify electrons or muons with varying transverse energies or momenta, and imposes some preliminary quality and isolation requirements prior to the full event reconstruction. The triggers employed in this analysis during different data taking periods are listed in Table 5.4.

Table 5.4: The list of triggers used in the analysis.

Period	Electron triggers	Muon triggers
2015	HLT_e24_lhmedium_L1EM20VH HLT_e60_lhmedium HLT_e120_lhloose	HLT_mu20_iloose_L1MU15 HLT_mu50
2016, A	HLT_e24_lhtight_nod0_ivarloose HLT_e60_lhmedium_nod0 HLT_e140_lhloose_nod0 HLT_e300_etcut	HLT_mu24_ivarloose HLT_mu50
2016, B-D3	HLT_e24_lhtight_nod0_ivarloose HLT_e60_lhmedium_nod0 HLT_e140_lhloose_nod0 HLT_e300_etcut	HLT_mu24_ivarmedium HLT_mu50
2016, D4 and beyond	HLT_e26_lhtight_nod0_ivarloose HLT_e60_lhmedium_nod0 HLT_e140_lhloose_nod0 HLT_e300_etcut	HLT_mu26_ivarmedium HLT_mu50

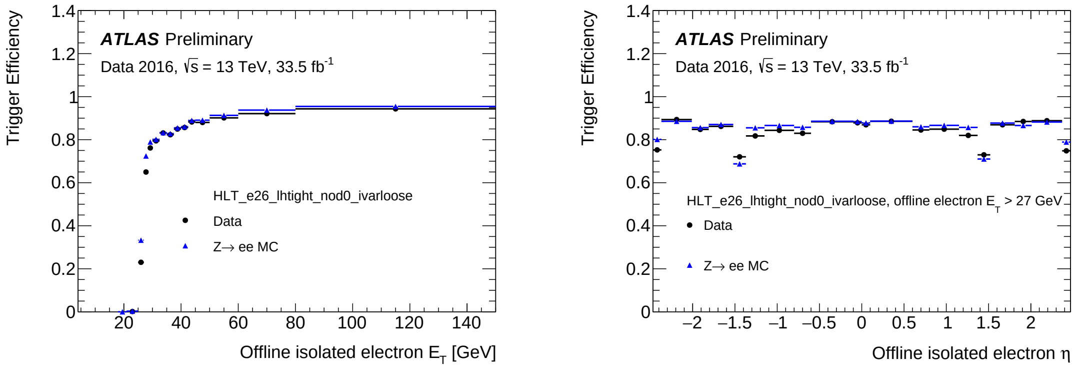

(a) (b)

Figure 5.2: Efficiencies of the HLT_e26_lhtight_nod0_ivarloose trigger as a function of the offline electron candidate's (a) transverse energy, and (b) pseudo-rapidity, which are obtained from $Z \to ee$ events [91].

Take HLT_e26_lhtight_nod0_ivarloose for example, the name of a trigger can be decoded in the following manner. The HLT_e26_lhtight_nod0_ivarloose trigger requires that an electron must have $E_{\mathrm{T}} > 26\,\mathrm{GeV}$ and that the electron candidate satisfy the tight likelihood-based identification criteria at HLT level. The trigger also applies a loose variable-size cone isolation (ivarloose), whereas the transverse impact parameter requirements are omitted (nod0).

The efficiencies of the HLT_e26_lhtight_nod0_ivarloose trigger as a function of the offline electron candidate's transverse energy and pseudo-rapidity are shown in Figure 5.2. The efficiency of this trigger versus E_{T} of the electron candidate quickly reaches its plateau when the offline transverse energy of the electron goes above the threshold value. The trigger efficiency as a function of the electron's pseudo-rapidity is relatively uniform except in the trasition region ($|\eta| = 1.37 - 1.52$) where the efficiency decreases by about 15%. The lowest un-prescaled single-lepton trigger in each data taking period is complemented by the corresponding un-prescaled triggers with higher E_{T} threshold values. These higher E_{T} triggers typically have no isolation requirements and progressively looser identification criteria. Figure 5.3 shows the efficiencies of the union of all the un-prescaled single-electron triggers in 2016, as a function of the transverse energy and the pseudo-rapidity of the electron candidates respectively. It is evident from Figure 5.2 and Figure 5.3 that the overall efficiency of the electron triggers increases by taking into account those triggers with higher E_{T} threshold values. The efficiency of these electron triggers is at least 90% in the plateau region. The p_{T} threshold for the signal electrons (defined in Section 5.2.1) is chosen to be 28 GeV, which is above the trigger threshold, to steer away from the

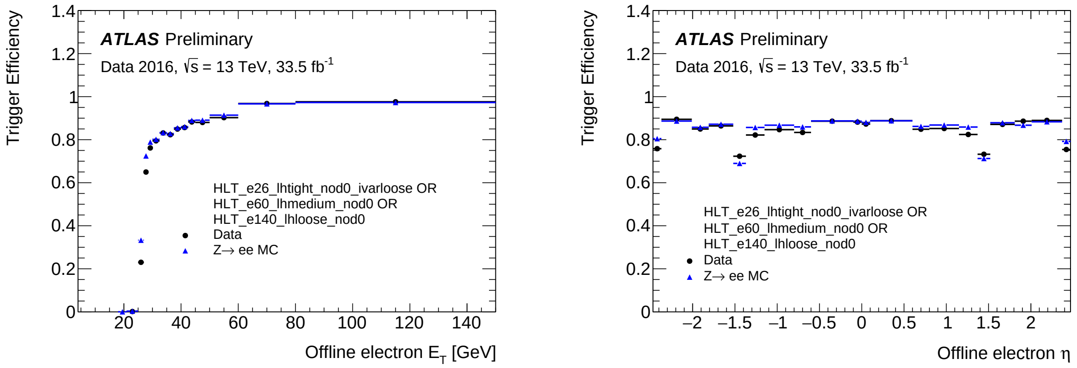

(a) (b)

Figure 5.3: Efficiencies of the logical OR between HLT_e26_lhtight_nod0_ivarloose, HLT_e60_lhmedium_nod0 and HLT_e140_lhloose_nod0 triggers as a function of the offline electron candidate's (a) transverse energy, and (b) pseudo-rapidity , which are obtained from $Z \to ee$ events [91].

turn-on region of the trigger efficiency and to account for the offline calibration effects that may lead to different measurements of the electron E_{T} at trigger level and offline reconstruction level.

The muon trigger names are encoded in a similar way as those for electrons. The efficiency of the union of the muon triggers is shown in Figure 5.4. The leading muon is also required to have $p_{\mathrm{T}} > 28\,\mathrm{GeV}$. Notice that in the barrel region, the un-prescaled lowest p_{T}-threshold single-muon trigger have a 70% efficiency in the plateau region, due to a limited coverage of the muon trigger detector. The detailed usage of these triggers will be described in Section 5.3.2.

5.3.2 Preselection of Dilepton Events

Preselection of dilepton events is applied before any topological requirements specific to each signal hypothesis. Firstly, a standard event cleaning procedure is carried out as follows:

- Application of good run list (GRL). A GRL serves to keep record of the quality of data taken for each lumi-block (a continuous period of data taking) and is therefore only applied to data. A good lumi-block corresponds to a period in which the detector was fully functional, and the data collected were of desired quality. For example, the beams delivered by the LHC have to be stable, the magnetic field must be present, and all the sub-detectors are required to be active without too much noise.

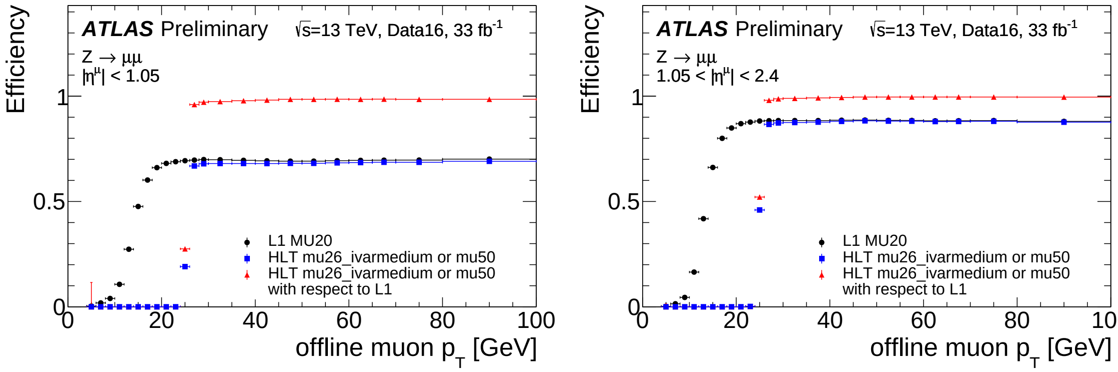

(a) Barrel region: $|\eta| < 1.05$ (b) End-cap region: $1.05 < |\eta| < 2.4$

Figure 5.4: Absolute efficiency of Level 1 (L1) MU20 trigger, and absolute and relative (with respect to the L1 trigger) efficiencies of the union of mu26_ivarmedium and mu50 high-level triggers as a function of p_{T} of offline muon candidates in the (a) barrel, and (b) end-cap regions [92].

- Selection of primary vertex. The primary vertex of an event is chosen to be the vertex with the highest sum of squares of the transverse momenta of the selected tracks ($\sum p^2_{\mathrm{T,trk}}$) and this primary vertex must also have at least two tracks, each with $p_{\mathrm{T}} > 400\,\mathrm{MeV}$.

- Rejection of erroneous or incomplete events. An event is vetoed if there is any corruption in the LAr calorimeter, tile calorimeter or the SCT, or if it occurs close to noise bursts in the LAr calorimeter. An event will also be rejected if for any reason it is missing detector information.

- Jet Cleaning. Fake jets (backgrounds for jets) mostly arise from 1) calorimeter noise from large scale coherent noise or isolated pathological cells, 2) cosmic-ray showers overlapping with collision events, or 3) beam induced background (BIB) due to proton losses upstream of the interaction point. Since these fake jets can interfere with the reconstruction of leptons and degrade the resolution of $E_{\mathrm{T}}^{\mathrm{miss}}$, a high efficiency working point ("BadLoose") [93] is defined to reject events containing "bad" jets after the overlap removal procedure.

Subsequently, the following selection criteria are applied:

- Lepton selection. Exactly two leptons satisfying the electron/muon criteria described in Section 5.2 are required. The leading lepton in p_{T} must have $p_{\mathrm{T}} > 28\,\mathrm{GeV}$, therefore fulfilling the "signal" lepton requirement as listed in Section 5.2.1 and Section 5.2.2.

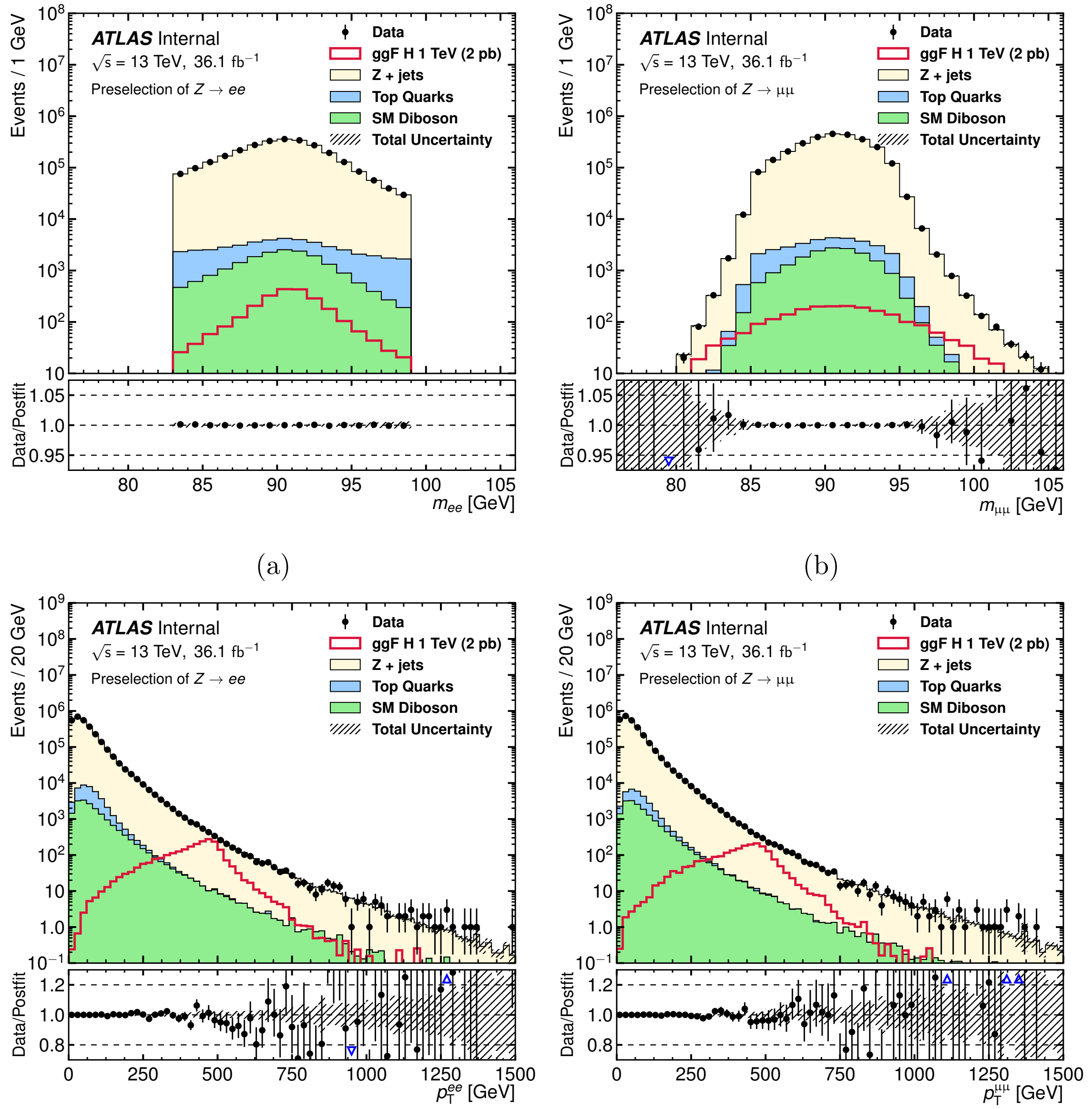

(a) (b)

(c) (d)

Figure 5.5: Observed and expected distributions of dilepton invariant mass and transverse momentum in the (a, c) di-electron channel and the (b, d) di-muon channel after preselection of the $Z \to \ell\ell$ candidates. For illustration, expected distributions from the ggF production of a 1 TeV Higgs boson with $\sigma \times \mathcal{B}(H \to ZZ) = 2\,\text{pb}$ are also shown. Background contributions are obtained from a combined likelihood fit to the data. The ratio of the observed data to the background prediction is shown at the bottom, along with the uncertainty on the total background prediction after combining the statistical and systematic contributions.

- Trigger decision and matching. An event is required to be triggered by one of the un-prescaled single-lepton triggers listed in Section 5.3.1. In addition, at least one of the leptons selected is required to match the corresponding physics object that triggered the event. The trigger efficiency for signal is approximately 100% for di-electron events, and over 90% for di-muon events (Section 5.3.1).

- Dilepton requirements:
  - $Z \to ee$ candidates must satisfy $83 < m(ee) < 99$ GeV, where the size of the mass window corresponds to roughly twice the mass resolution for the $Z \to ee$ decay. Note that the electrons are not required to be of opposite sign because electrons are more susceptible to charge misidentification at high E_{T} due to radiation of photons from bremsstrahlung.
  - $Z \to \mu^{\pm}\mu^{\mp}$ candidates must satisfy a) the two muons carry opposite charges; b) $85.6\,\mathrm{GeV} - 0.0117 \cdot p_{\mathrm{T}}(\ell\ell) < m(\mu\mu) < 94.0\,\mathrm{GeV} + 0.0185 \cdot p_{\mathrm{T}}(\ell\ell)$. The p_{T}-dependent mass window is chosen to account for the degradation of the mass resolution of $Z \to \mu\mu$ when the transverse momentum of Z boson is high.
  - Dilepton selection for $e\mu$ events requires exactly one electron and one muon with $76 < m(e\mu) < 106\,\mathrm{GeV}$.

Distributions of the dilepton candidates after the event preselection are shown in Figure 5.5.

5.3.3 VBF and ggF/DY Categories

Signal events from VBF production possess unique features, in which the pair of vector bosons from the resonance decay are accompanied by two additional jets with a large separation in pseudo-rapidity and a high dijet invariant mass. This unique topology provides a powerful means to discriminate between signal and background events. A tag-jet selection is defined to identify the two additional jets from VBF production, and the jets selected are referred to as tag-jets hereinafter.

Tag-jets are selected from small-R jets that are not tagged by the b-tagging algorithm (Chapter 4). They must reside in opposite pseudo-rapidity hemispheres (namely, $\eta_{j1}^{\mathrm{tag}} \cdot \eta_{j2}^{\mathrm{tag}} < 0$) with a pseudo-rapidity separation $|\Delta\eta_{jj}^{\mathrm{tag}}| > 4.7$, have the highest dijet invariant mass (m_{jj}^{tag}), and $m_{jj}^{\mathrm{tag}} > 770\,\mathrm{GeV}$. These criteria are optimized to enhance the search sensitivity to VBF signals for all masses considered [60]. Once identified as tag-jets, the two jets are not considered in the $ZV \to \ell\ell qq$ selection; moreover, large-R jets in close proximity to the tag-jets ($\Delta R < 1.5$) are also excluded

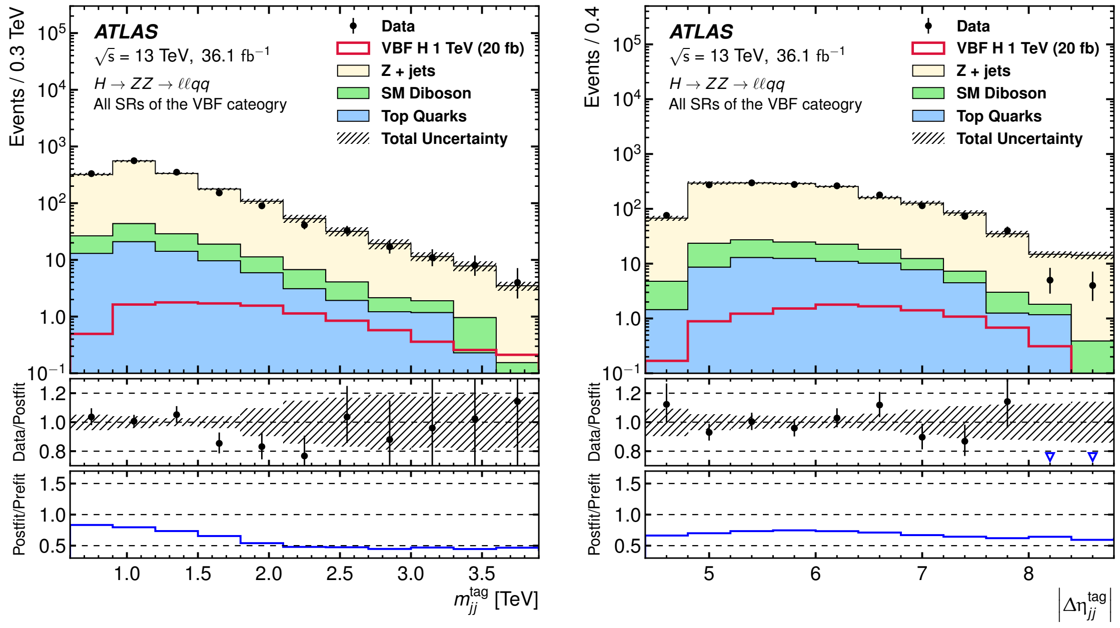

(a) (b)

Figure 5.6: Observed data and expected background distributions of dijet (a) invariant mass and (b) pseudo-rapidity separation of the two tag-jets of the VBF $H \to ZZ \to \ell\ell qq$ search, combining all signal regions [60]. For illustration, expected distributions from the VBF production of a 1 TeV Higgs boson with $\sigma \times \mathcal{B}(H \to ZZ) = 20$ fb are also shown. The middle panes show the ratio of the observed data to the background predictions. The uncertainty in the total background prediction, shown as bands, combines statistical and systematic contributions. The blue triangles in the middle panes indicate bins where the ratio is nonzero and outside the vertical range of the plot. The bottom panes are the ratios of the post-fit and pre-fit background predictions.

to avoid overlaps. Once a pair of tag-jets is found, an event is assigned to the VBF category if it passes the $ZV \to \ell\ell qq$ selection.

Events that fail the above selection criteria, which include the ones that contain two tag-jets but fail the $ZV \to \ell\ell qq$ selection, are treated in the ggF/DY category. No tag-jet requirement is applied in this case and an event is classified into the ggF/DY category if it satisfies the $ZV \to \ell\ell qq$ selection identical to that for the VBF category.

In summary, events are divided into VBF and ggF/DY categories in the $H \to ZZ$ and $W' \to ZW$ searches, for which the VBF production is considered. The selection for VBF production is performed first, followed by the selection for ggF or DY production. An event is assigned to the VBF category if it passes the former selection, and the ggF/DY category if it only passes the latter. For the $G_{\text{KK}} \to ZZ$ search, which exclusively probes the ggF production, only the ggF/DY category is

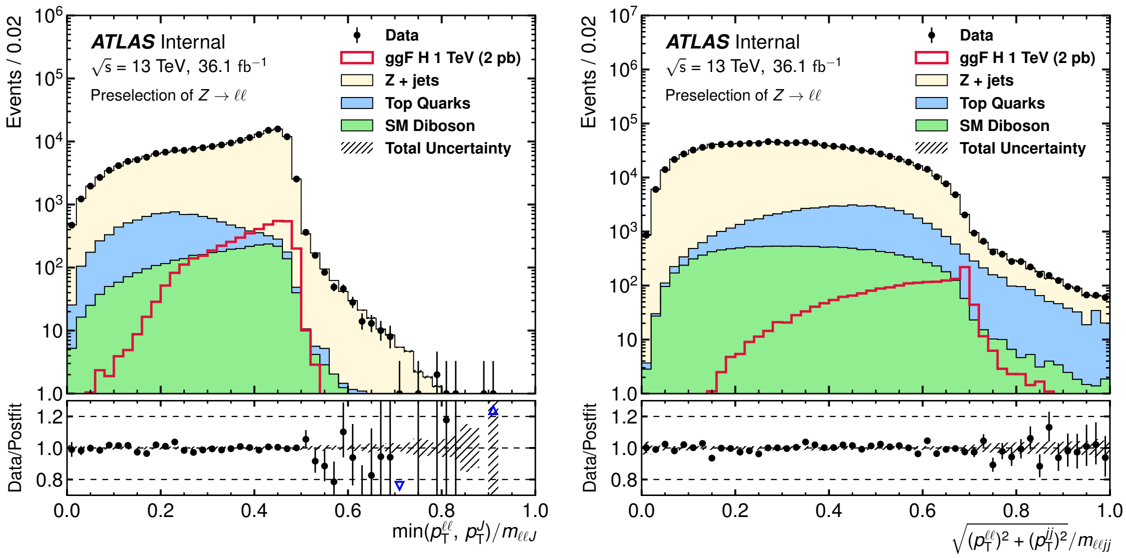

(a)

(b)

Figure 5.7: Observed and expected distributions of (a) $\min(p_{\mathrm{T}}^{\ell\ell},\, p_{\mathrm{T}}^{J})/m_{\ell\ell J}$ before boson tagging and (b) $\sqrt{\left(p_{\mathrm{T}}^{\ell\ell}\right)^2 + \left(p_{\mathrm{T}}^{jj}\right)^2}/m_{\ell\ell jj}$ after preselection of the $Z \to \ell\ell$ candidates. For illustration, expected distributions from the ggF production of a 1 TeV Higgs boson with $\sigma \times \mathcal{B}(H \to ZZ) = 2\,\mathrm{pb}$ are also shown. Background contributions are obtained from a combined likelihood fit to the data. The ratio of the observed data to the background prediction is shown at the bottom, along with the uncertainty on the total background prediction after combining the statistical and systematic contributions.

considered. Distributions of the tag-jets selected for the VBF category are shown in Figure 5.6.

5.3.4 Selection of $ZV \to \ell\ell qq$

Identification of $ZV \to \ell\ell qq$ decays proceeds by applying the merged $ZV \to \ell\ell J$ selection followed by the resolved $ZV \to \ell\ell jj$ selection. This prioritization is motivated by a smaller background expected in the merged regime after applying the W/Z boson tagging.

Merged $ZV \to \ell\ell J$ selection

Following the preselection of $Z \to \ell\ell$ events, at least one large-R jet is required for $ZV \to \ell\ell J$ candidates and the large-R jet with the highest p_{T} ($p_{\mathrm{T}} > 200\,\mathrm{GeV}$) is assumed to be from the $V \to qq$ decay. Events must further satisfy $\min(p_{\mathrm{T}}^{\ell\ell},\, p_{\mathrm{T}}^{J})/m_{\ell\ell J} > 0.3$ for the $H \to ZZ$ search, and > 0.35 for the $W' \to ZW$ and $G_{\mathrm{KK}} \to ZZ$ searches.

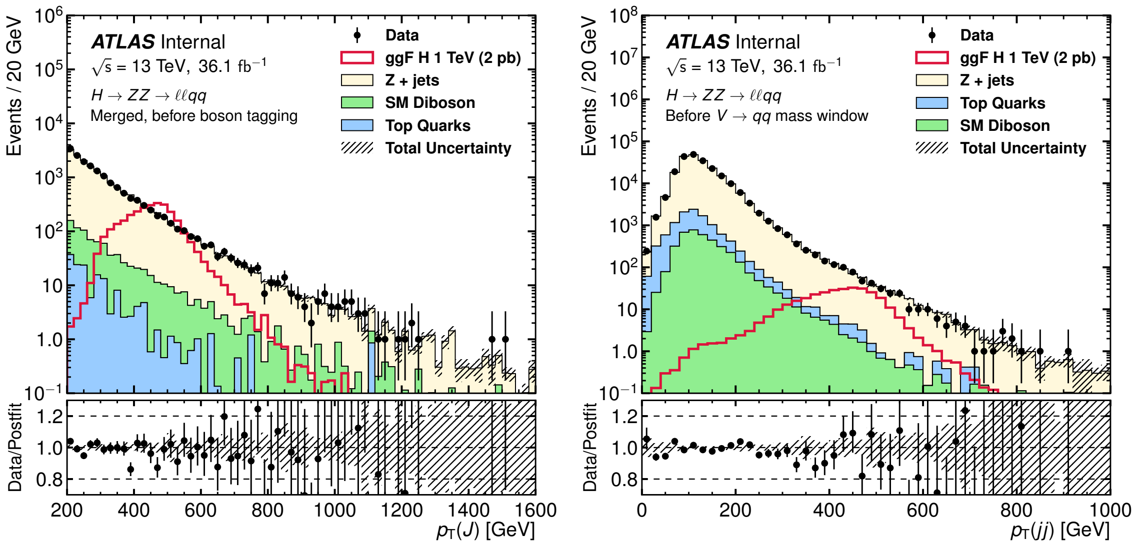

(a) (b)

Figure 5.8: Observed and expected distributions of (a) $p_{\mathrm{T}}(J)$ before boson tagging and (b) $p_{\mathrm{T}}(jj)$ before the $V \to qq$ mass window cut. For illustration, expected distributions from the ggF production of a 1 TeV Higgs boson with $\sigma \times \mathcal{B}(H \to ZZ) = 2\,\text{pb}$ are also shown. Background contributions are obtained from a combined likelihood fit to the data. The ratio of the observed data to the background prediction is shown at the bottom, along with the uncertainty on the total background prediction after combining the statistical and systematic contributions.

These kinematic requirements, which are optimized for all the signal masses considered in each search, effectively reduce the background events while maintaining a high efficiency for the signal. This is because the transverse momenta of the dilepton and large-R jet are found to be larger and more balanced for heavy resonances. A looser requirement of $\min(p_{\mathrm{T}}^{\ell\ell},\, p_{\mathrm{T}}^{J})/m_{\ell\ell J}$ is adopted for the $H \to ZZ$ search because the expected $p_{\mathrm{T}}^{\ell\ell}$ and p_{T}^{J} spectra from a spin-0 resonance are softer. The distribution of $\min(p_{\mathrm{T}}^{\ell\ell},\, p_{\mathrm{T}}^{J})/m_{\ell\ell J}$ after the event preselection is shown in Figure 5.7(a).

Z-boson tagging is subsequently applied for the $H \to ZZ$ and $G_{\mathrm{KK}} \to ZZ$ searches to select the $V \to qq$ decay, and W-boson tagging for the $W' \to ZW$ search. Signal efficiency working points of 50% and 80% are defined for the boson tagging algorithm (Section 4.3.2), in which the latter working point is inclusive of the former; consequently, two signal regions are defined for each search, one for events passing the jet mass (m_J) and substructure (D_2) requirements of the 50% working point and the other for events only passing the requirements of the 80% working point. The former signal region is designated as a high-purity (HP) signal region (SR) because of a higher fraction of signal events expected, and the latter as a low-purity (LP) SR.

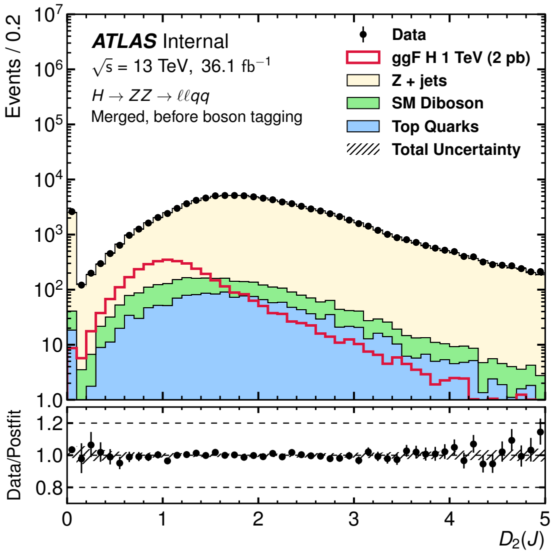

Figure 5.9: Observed and expected distributions of $D_2(J)$ before boson tagging. For illustration, expected distributions from the ggF production of a 1 TeV Higgs boson with $\sigma \times \mathcal{B}(H \to ZZ) = 2$ pb are also shown. Background contributions are obtained from a combined likelihood fit to the data. The ratio of the observed data to the background prediction is shown at the bottom, along with the uncertainty on the total background prediction after combining the statistical and systematic contributions.

Similarly, high-purity and low-purity Z+jets control regions (ZCRs) are defined by requiring m_J to be outside the large-R jet mass window defined by the 80% working point of the boson tagging. Events in the high-purity (low-purity) ZCR are further required to satisfy the D_2 requirement of the 50% (80%) working point of the boson tagging.

Resolved $ZV \to \ell\ell jj$ selection

$ZV \to \ell\ell jj$ candidates are selected from the $Z \to \ell\ell$ events that fail the $ZV \to \ell\ell J$ selection. The events are required to have at least two small-R "signal" jets (Section 5.2.3) with the leading jet p_{T} greater than 60 GeV. The two leading signal jets are selected to reconstruct the resolved $V \to qq$ decay.

The kinematic quantity, $\sqrt{\left(p_{\mathrm{T}}^{\ell\ell}\right)^2 + \left(p_{\mathrm{T}}^{jj}\right)^2}/m_{\ell\ell jj}$, is then required to be greater than 0.4 for $H \to ZZ$, and 0.5 for $W' \to ZW$ and $G_{\mathrm{KK}} \to ZZ$. Here p_{T}^{jj} refers to the transverse momentum of the dijet candidate. Similar to the merged $Z \to \ell\ell J$ selection, this requirement suppresses background but has a small impact on the expected signals. The distribution of $\sqrt{\left(p_{\mathrm{T}}^{\ell\ell}\right)^2 + \left(p_{\mathrm{T}}^{jj}\right)^2}/m_{\ell\ell jj}$ after the event preselection is shown in Figure 5.7(b). Signal events are expected to have a dijet invariant mass (m_{jj})

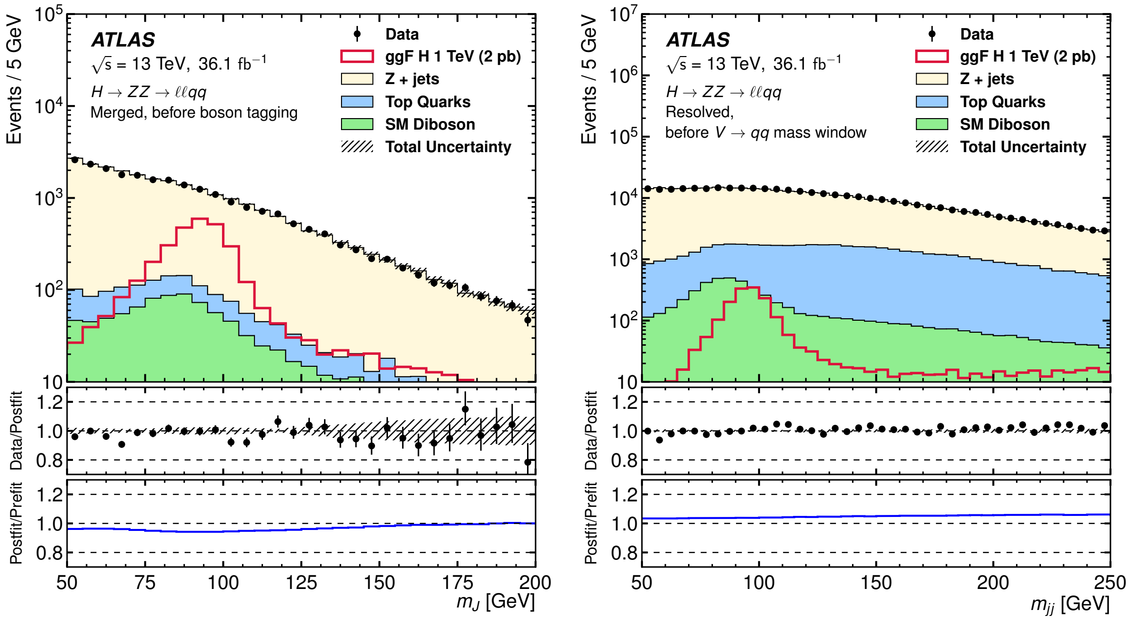

(a) (b)

Figure 5.10: Observed and expected distributions of (a) the large-R jet mass m_J of the $ZV \to \ell\ell J$ candidate and (b) the dijet mass m_{jj} of the $ZV \to \ell\ell jj$ candidate [60]. These distributions are for the $H \to ZZ$ search before the identification of the $V \to qq$ decay, combining VBF and ggF/DY categories. Background contributions are obtained from a combined likelihood fit to the data. For illustration, expected distributions from the ggF production of a 1 TeV Higgs boson with $\sigma \times \mathcal{B}(H \to ZZ) = 2\,\text{pb}$ are also shown. The middle panes show the ratios of the observed data to the background predictions. The uncertainty on the total background prediction, shown as bands, combines statistical and systematic contributions. The bottom panes are the ratios of the post-fit and pre-fit background predictions.

consistent with the $V \to qq$ decay. Therefore, m_{jj} must be in the window [70, 105] GeV for $Z \to qq$ and [62, 97] GeV for $W \to qq$. An asymmetric window around m_Z is chosen to minimize the overlap with the hadronic decays of the Higgs boson.

About 21% of $Z \to qq$ decays have two b-quark jets, whereas the dominant background, Z+jets, has a smaller heavy-quark content. To further enhance the search sensitivity, $ZV \to \ell\ell jj$ candidates are classified into two signal regions: a b-tagged SR and an untagged SR. An event is rejected if there are more than two b-tagged jets in the event, and is assigned to the b-tagged (untagged) SR if there are exactly (fewer than) two b-tagged jets. Since no enhancement of b-tagged jets is expected from $W \to qq$ decays, a single resolved SR is defined for the $W' \to ZW$ search by combining the b-tagged and untagged signal regions. The two regions are also combined for the VBF category due to a small number of events expected.

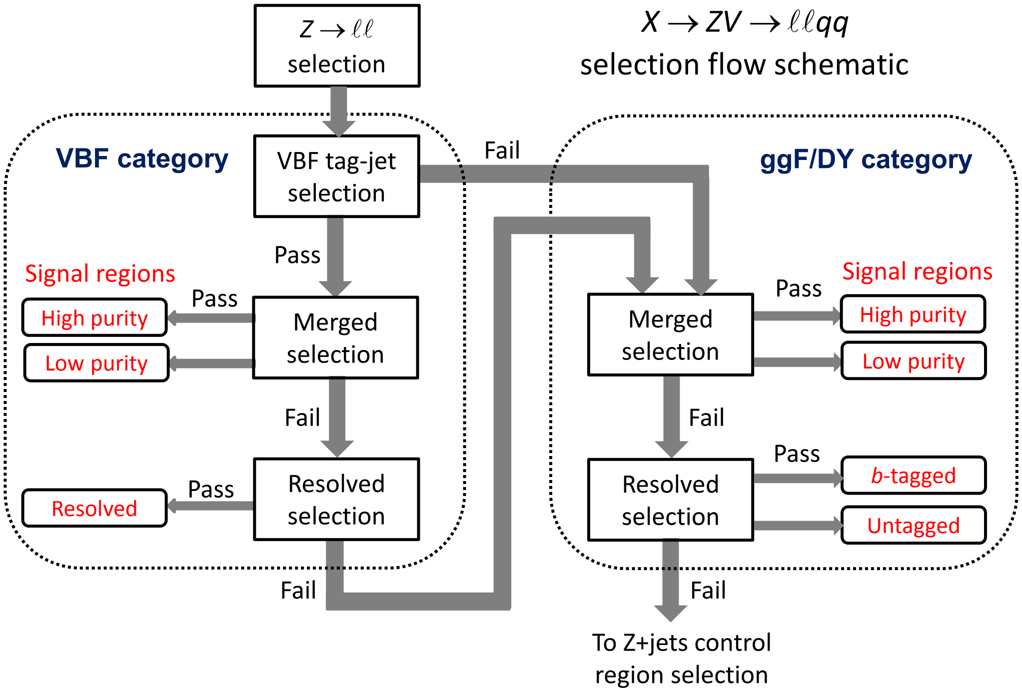

Figure 5.11: Illustration of the selection flow and seven signal regions of the $X \to ZV \to \ell\ell qq$ search [60]. The VBF category is targeted for VBF production. The selected VBF tag-jets are removed from the subsequent selection for the VBF category. However, if an event fails to be selected for the VBF category, these jets are kept for the ggF/DY category selection. The $H \to ZZ$ search utilizes all seven signal regions and the $W' \to ZW$ search uses six signal regions by combining the b-tagged and untagged regions of the ggF/DY category. The $G_{\mathrm{KK}} \to ZZ$ search bypasses the VBF selection, so it has only four signal regions.

A Z+jets control region is defined for each signal region. The ZCR and its corresponding signal region share the same traits except that m_{jj} must be in the sidebands defined as $[50,\ 62] \cup [105,\ 150]$ GeV for the ZCR. Top quark production is a significant background source in the b-tagged signal region; consequently, a top-quark-enhanced region is defined to constrain the top-quark background. Events in the top control region (TopCR) must have two b-tagged jets and two leptons of different flavors, i.e., $e\mu$. The leading b-tagged jet is required to have $p_{\mathrm{T}} > 60\,\mathrm{GeV}$. Furthermore, the invariant mass of the dilepton and dijet candidates must be within [76, 106] GeV and [50, 150] GeV, respectively. This selection yields a sample of top-quark events with a purity higher than 99%. The TopCR is subsequently used to constrain the top quark contributions in all the signal regions (Section 5.5.3).

Distributions of the transverse momentum of the leading large-R jet and the re-

Table 5.5: A summary of the $X \to ZV \to \ell\ell qq$ selection criteria.

Regime	$ZV \to \ell\ell J$	$ZV \to \ell\ell jj$
Triggers	Un-prescaled single-lepton triggers	
Leptons	1 signal ($p_{\mathrm{T}} > 28\,\mathrm{GeV}$) + 1 loose leptons	
$Z \to \ell\ell$	$83 < m(ee) < 99$ GeV, $85.63 - 0.01170 \times p_T^{\mu\mu} < m(\mu^{\pm}\mu^{\mp}) < 94 + 0.01850 \times p_T^{\mu\mu}$ GeV	
Tag-jet selection for the VBF category	Two non-b-tagged small-R jets with $\eta_1 \cdot \eta_2 < 0$, $\left\|\Delta\eta_{jj}^{\mathrm{tag}}\right\| > 4.7$, and $m_{jj}^{\mathrm{tag}} > 770\,\mathrm{GeV}$	
Jet requirements	≥ 1 large-R jet $p_T^J > 200$ GeV	$p_{\mathrm{T}}^{\mathrm{leadjet}} > 60$ GeV, $n_{\mathrm{jet}}^{\mathrm{sig}} \geq 2$
b-tagged region	—	2 b-tagged jets
untagged region		0 or 1 b-tagged jet
Kinematic criteria	$\min(p_{\mathrm{T}}^{\ell\ell}, p_{\mathrm{T}}^{J})/m_{\ell\ell J}$	$\sqrt{\left(p_{\mathrm{T}}^{\ell\ell}\right)^2 + \left(p_{\mathrm{T}}^{jj}\right)^2}/m_{\ell\ell jj}$
H	> 0.3	> 0.4
W' or G_{KK}	> 0.35	> 0.5
$W/Z \to qq$ (SR)	$62/70 < m_{W/Z\to jj} < 97/105$ GeV	p_{T}-dependent
W/Z sidebands (ZCR)	[50, 62] GeV and [105, 150] GeV	W/Z tagging algorithm

solved dijet candidates are shown in Figure 5.8, before applying the boson tagging algorithm and the $V \to qq$ mass requirement, respectively. Figure 5.9 shows the substructure variable (D_2) of the leading large-R jet. Similarly, invariant mass distributions of the leading large-R jet and the resolved dijet candidates are shown in Figure 5.10 at the same selection stage. The background distributions in Figures 5.5-5.10 are obtained from a combined likelihood fit to the data and the statistical procedure for performing the likelihood fit is outlined in Section 5.5. Table 5.5 shows a summary of the event selection criteria. A schematic view of the event selection and categorization is shown in Figure 5.11, which visualizes the complex selection sequence in a less clumsy way. Approximate background compositions after the event categorization are summarized in Figure 5.12 for the $H \to ZZ$ search. For simplicity, the VBF and ggF categories are combined in Figure 5.12 as similar compositions are expected. Similar background compositions are observed in the other two searches with insubstantial differences.

5.3.5 Signal Acceptance

The acceptance times efficiency ($A \times \epsilon$) for various signals after the event selection and categorization is shown in Figures 5.13-5.15. The $A \times \epsilon$ curves for the merged and

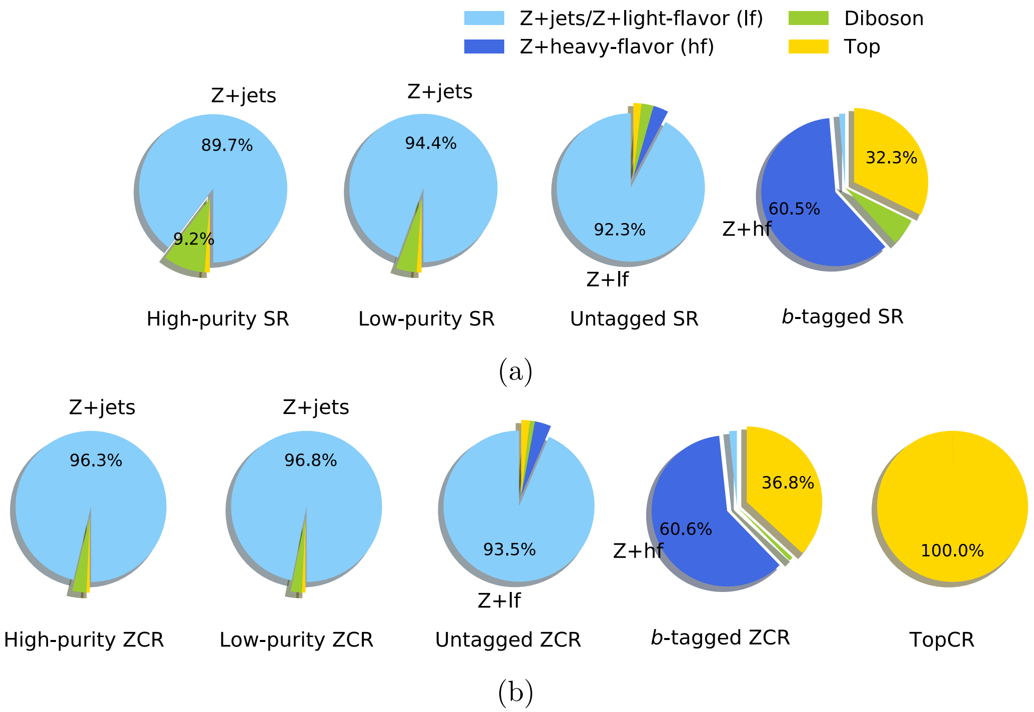

Figure 5.12: Background compositions in the (a) signal regions and (b) control regions of the $H \to ZZ \to \ell\ell qq$ search. For simplicity, VBF and ggF categories are combined as similar compositions are expected.

the resolved selections cross at around 500 GeV, and the $A \times \epsilon$ of the merged selection becomes dominant as the resonance mass further increases. In the intermediate mass range of approximately 400 to 1200 GeV, the $V \to qq$ decay can be reconstructed as a large-R jet and two small-R jets simultaneously. The inefficiency beginning at a resonance mass of approximately 2.5 TeV (for all types of signals) is primarily due to merging of electrons, which become collimated at high p_{T} of the Z boson. The electron reconstruction algorithm would fail when the angular distance between the two electrons becomes too small ($\Delta R \lesssim 0.2$).

5.3.6 Signal Resolution

To improve the resolution of the $m_{\ell\ell J}$ or $m_{\ell\ell jj}$ spectrum, the four momentum of the di-muon system from the $Z \to \mu\mu$ decay is scaled by $m_{\mathrm{Z}}/m_{\mu\mu}$ ($m_{\mathrm{Z}} = 91.187$ GeV [94]). This mass constraint mitigates the impact of muon momentum-resolution degradation at high p_{T}. The resolution of the $m_{\ell\ell J}$ spectrum is improved by approximately 13% for a 1 TeV heavy Higgs boson and 40% for a 3 TeV heavy Higgs boson. Similarly, a scale factor of m_V/m_{jj} is also applied to the dijet system of the $ZV \to \ell\ell jj$ candidates. The value of m_{V} is set to be 91.187 GeV (80.385 GeV [94]) if a large-R jet passes the

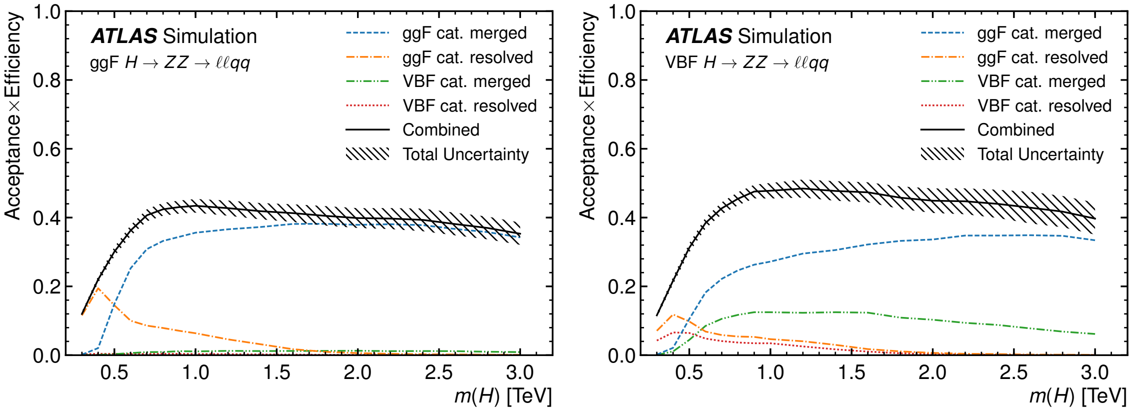

(a) (b)

Figure 5.13: Selection acceptance times efficiency for the $H \to ZZ \to \ell\ell qq$ events from MC simulations as a function of the Higgs boson mass for (a) ggF and (b) VBF production, combining the high- and low-purity signal regions of the $ZV \to \ell\ell J$ selection and the b-tagged and untagged regions of the $ZV \to \ell\ell jj$ selection [60]. The hatched band represents the total statistical and systematic uncertainties.

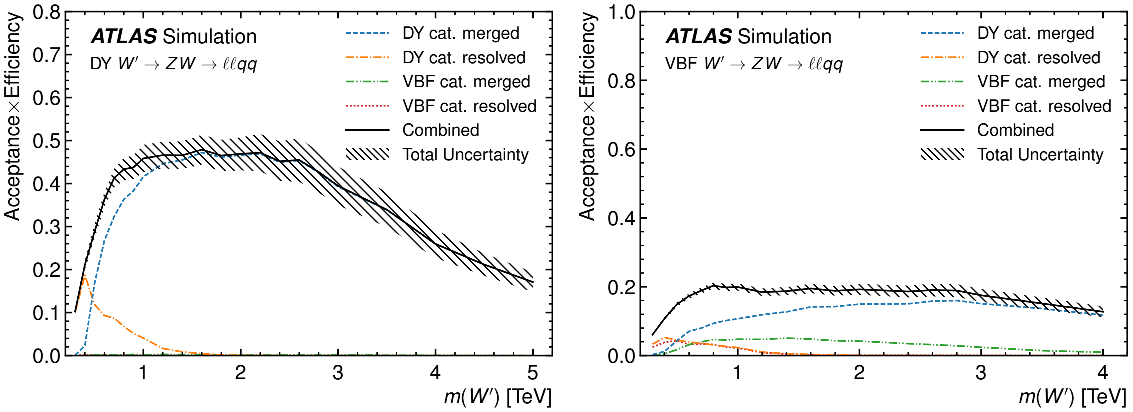

(a) (b)

Figure 5.14: Selection efficiencies of $W' \to ZW \to \ell\ell qq$ events from MC simulations as functions of the W' mass for (a) DY and (b) VBF production, combining the high- and low-purity signal regions of the merged $ZV \to \ell\ell J$ selection and the b-tagged and untagged regions of the resolved $ZV \to \ell\ell jj$ selection [60]. The decrease in the $\ell\ell qq$ selection efficiency above approximately 2.5 TeV of the HVT W' boson mass is mainly due to the merging of electrons from the $Z \to ee$ decay.

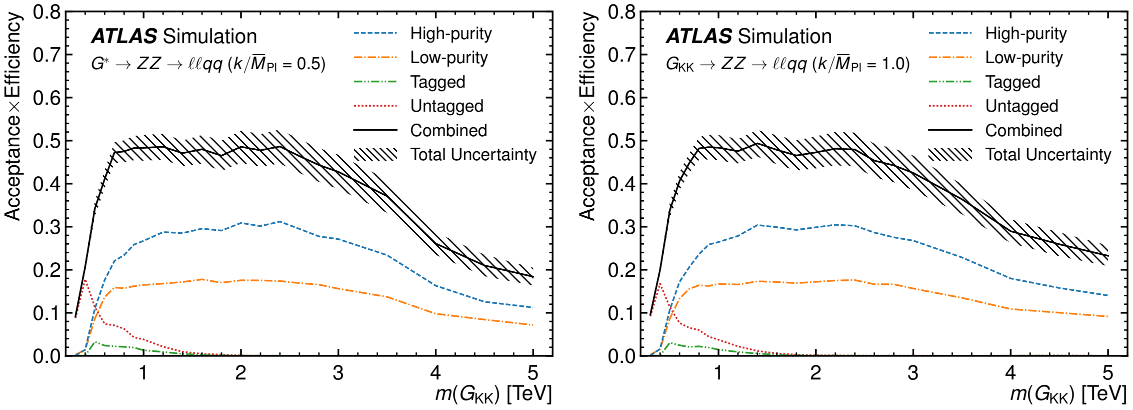

(a) (b)

Figure 5.15: Selection efficiencies of $G_{\rm KK} \to ZZ \to \ell\ell qq$ events from MC simulations as functions of the $G_{\rm KK}$ mass for (a) $k/\overline{M}_{\rm Pl} = 0.5$ and (b) $k/\overline{M}_{\rm Pl} = 1.0$ productions, combining the high- and low-signal regions of the $ZV \to \ell\ell J$ selection and the b-tagged and untagged regions of the $ZV \to \ell\ell jj$ selection [60]. The decrease in the $\ell\ell qq$ selection efficiency above approximately 2.5 TeV of the $G_{\rm KK}$ boson mass is mainly due to the merging of electrons from the $Z \to ee$ decay.

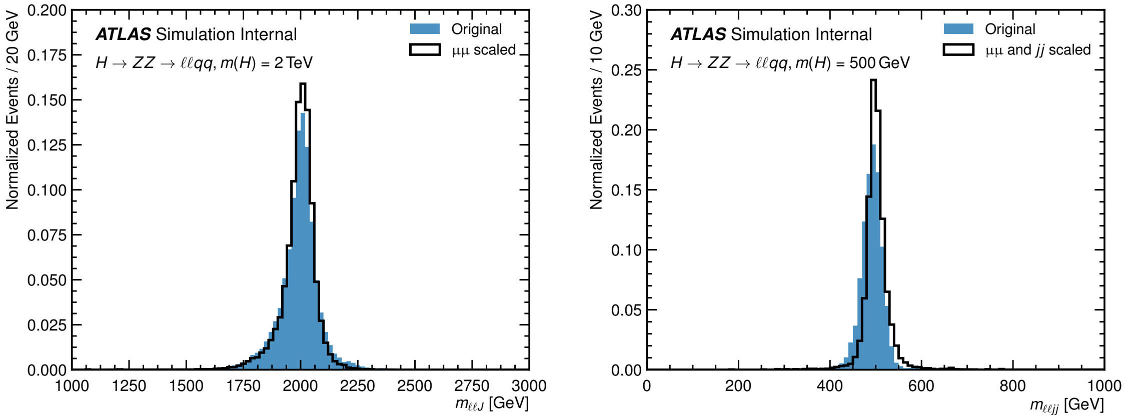

(a) (b)

Figure 5.16: The simulated (a) $m_{\ell\ell J}$ and (b) $m_{\ell\ell jj}$ distributions obtained from directly using the mass of the $\ell\ell J/\ell\ell jj$ system (filled histogram) and after scaling the $\mu\mu$ and jj systems (empty histogram).

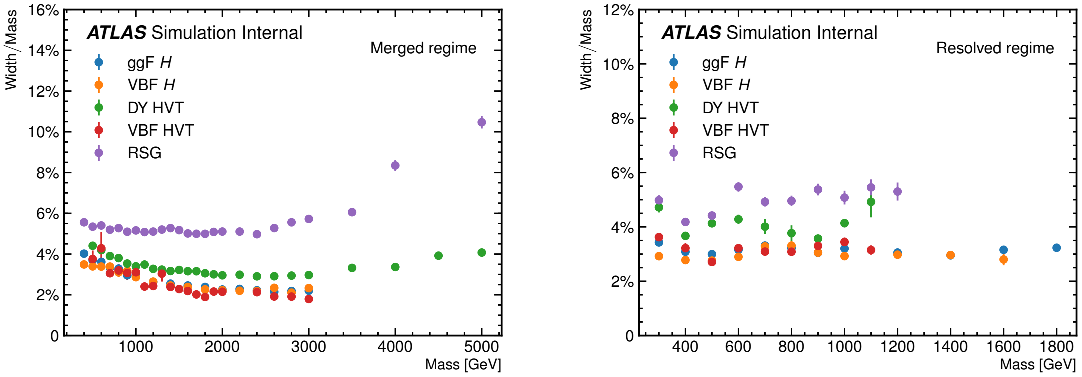

(a) (b)

Figure 5.17: Signal mass resolutions for the (a) merged and (b) resolved regimes.

Z-boson (W-boson) tagging requirements [95]. The resolution of the $m_{\ell\ell jj}$ spectrum is improved by approximately 14% for a 600 GeV Higgs boson as a result. No scaling of large-R jets is applied as this simple mass constraint method is not effective for the trimmed jets (Section 4.3.2). Figure 5.16 illustrates the effects of the mass constraints in the resolved and merged regimes. Figure 5.17 shows the reconstructed signal resolution as a function of the signal mass in the merged and the resolved regimes.

5.4 Systematic Uncertainties

The extent to which the physics processes can be understood is limited by both statistical and systematic uncertainties. Systematic uncertainties may arise from a lack of complete understanding of many sources of mis-measruement of the physics objects as well as pertinent theoretical uncertainties. This section describes the sources of systematic uncertainty considered in this analysis. These uncertainties are divided into three groups: experimental uncertainties, modeling uncertainties related to the background processes, and theoretical uncertainties on the signal processes.

5.4.1 Experimental Uncertainties

Leptons

Uncertainties associated with leptons (electrons or muons) include those corresponding to energy/momentum scale, energy/momentum resolution, trigger efficiency, reconstruction and identification efficiencies, and isolation efficiency.

After the Monte Carlo based calibration and in-situ corrections using $Z \to ee$ events [88], the main sources of uncertainty associated with the energy scale and resolution of the electrons are from presampler (Section 3.2.2), layer inter-calibration, in-situ corrections, and pileup [88]. Muon momentum scale and resolution are studied using $J/\psi \to \mu\mu$ and $Z \to \mu\mu$ events [46]. The major contributions to the final systematic uncertainty include the mass window width for the $Z \to \mu\mu$ candidate selection and background parameterization for the J/ψ fit. The scale and resolution uncertainties on both electrons and muons are less than 1%. The efficiency measurements of the trigger, reconstruction, identification and isolation are performed using the tag-and-probe method in which well known resonances decaying into leptons (namely $Z \to \ell^{\pm}\ell^{\mp}$ and $J/\psi \to \ell^{\pm}\ell^{\mp}$) are employed. The relevant uncertainties that arise from this procedure, which are both p_{T} and η dependent, are propagated to the scale factors used to correct the Monte Carlo. The reconstruction and identification uncertainties are less than 0.5% and 1.0% for electrons and muons respectively. The uncertainty corresponding to the track-to-vertex association efficiency is also included for muon objects. Uncertainties associated with the isolation efficiency measurement are generally below 1.0% for both types of leptons.

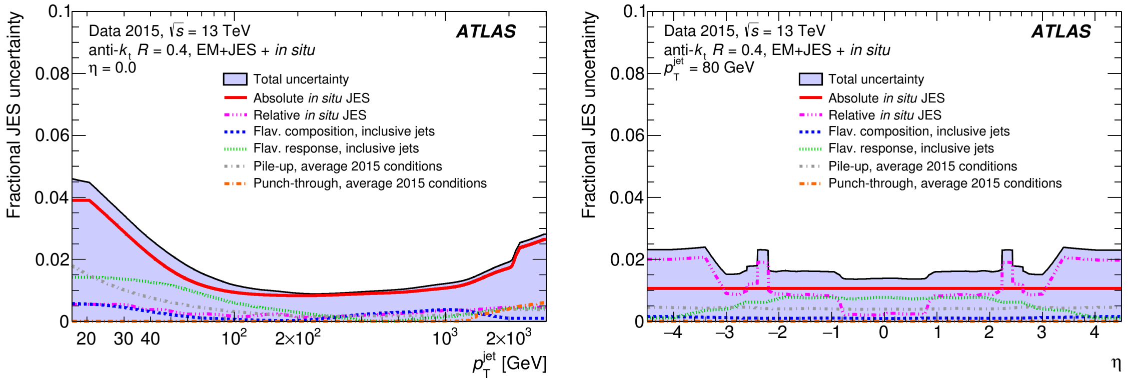

(a) (b)

Figure 5.18: Combined fractional JES uncertainty associated with fully calibrated small-R jets as a function of (a) jet p_T at $\eta = 0$ and (b) η at $p_\mathrm{T} = 80\,\mathrm{GeV}$ [51].

Small-R Jets

Uncertainties associated with the small-R jets are included to account for jet energy scale (JES) and jet energy resolution (JER) calibrations, b-tagging efficiencies, as well as the efficiency of jet vertex tagging.

Systematic uncertainties on JES are the dominant sources of uncertainty for small-R jets. In the final calibration, a set of 80 JES systematic uncertainty terms from the individual calibrations are propagated. These uncertainties, represented by 80 independent components, are statistically combined into a globally reduced set of 21 components that depend on both p_T and η of a jet [51]. The majority of uncertainties are associated with the Z/γ+jet and in-situ calibrations [51]. These uncertainties arise from assumptions made in the event topology, MC simulation, sample statistics, and propagated uncertainties of the electron, muon, and photon energy scales. The remaining nuisance parameters account for effects including pile-up, η inter-calibration, and jet flavor. The total JES uncertainties are shown in Figure 5.18 as a function of p_T at $\eta = 0$ and as a function of η at $p_\mathrm{T} = 80\,\mathrm{GeV}$. These uncertainties assume a flavor composition consistent with an inclusive di-jet selection using Pythia 8. The total JES uncertainty ranges from 4.5% at $p_\mathrm{T} = 20\,\mathrm{GeV}$ to 2% for jets with $p_\mathrm{T} = 2\,\mathrm{TeV}$, as derived from an inclusive di-jet sample. The uncertainties on the energy resolution of the small-R jets range from 10%-20% at $p_\mathrm{T} = 20\,\mathrm{GeV}$ to approximately 5% for jets with $p_\mathrm{T} > 200\,\mathrm{GeV}$. The JVT efficiency of the small-R jets has an associated uncertainty of approximately 1%.

Uncertainties related to b-tagging efficiencies are also considered [53]. These uncertainties include those for the modeling of heavy flavor production, modeling of decay and fragmentation of the b-quark, imperfect knowledge of the jet energy scale and resolution, as well as the modeling of additional pile-up interactions [52]. A "medium" configuration scheme of the uncertainties is used for describing uncertainties on b-tagging efficiency in this analysis. Three, four and five uncertainty terms are included for tagging efficiency of jets originating from b, c and light-flavor quarks respectively. An additional uncertainty is assigned to jets with transverse momenta beyond the prescription of calibration samples. The uncertainty related to extrapolating c-jet efficiency to τ-induced jets is also considered. These uncertainties generally have an effect at a level of approximately 5% to 10% on the overall efficiency of the b-tagging algorithm.

Large-R Jets

An in-situ R_{trk} procedure is adopted to derive the systematic uncertainties associated with the large-R jet scales [58, 90]. The R_{trk} method uses two independent measurements on the same jet object — calorimeter and track jets. Comparisons between the calorimetric and track scales in data and Monte Carlo are performed to extract any possible mis-modeling in MC simulations. R_{trk} is defined as the ratio of track to calorimeter jet p_{T} between data and MC simulation:

$$R_{\mathrm{trk}} = \frac{\left(p_{\mathrm{T}}^{\mathrm{calo}}/p_{\mathrm{T}}^{\mathrm{track}}\right)^{\mathrm{data}}}{\left(p_{\mathrm{T}}^{\mathrm{calo}}/p_{\mathrm{T}}^{\mathrm{track}}\right)^{\mathrm{MC}}}, \tag{5.2}$$

where the four terms of the ratio represent the jet transverse momentum from the calorimeter or the tracker, in data and Monte Carlo. Uncertainties associated with the scales of the p_{T}, mass, and D_2 of the large-R jets are all taken into account. In the final prescription for the configuration of these uncertainties, uncertainties related to the mass and p_{T} scales are correlated with each other, whereas the D_2 scale uncertainty is left independent. These uncertainties are composed of four components. A "baseline" component measures the difference between data and Pythia 8. A second "modeling" component aims to capture any modeling issues by looking at the difference between Pythia 8 and Herwig generators. Uncertainties on the reference tracks contribute as the third "tracking" component to the scale uncertainties. Finally, the statistical uncertainty on the measurement is designated as the "TotalStat" component. The measured scale uncertainties on the large-R jets range from 2% – 6% approximately, as shown in Figure 5.19.

A uniform 2% absolute uncertainty on the large-R jet p_{T} resolution is assigned.

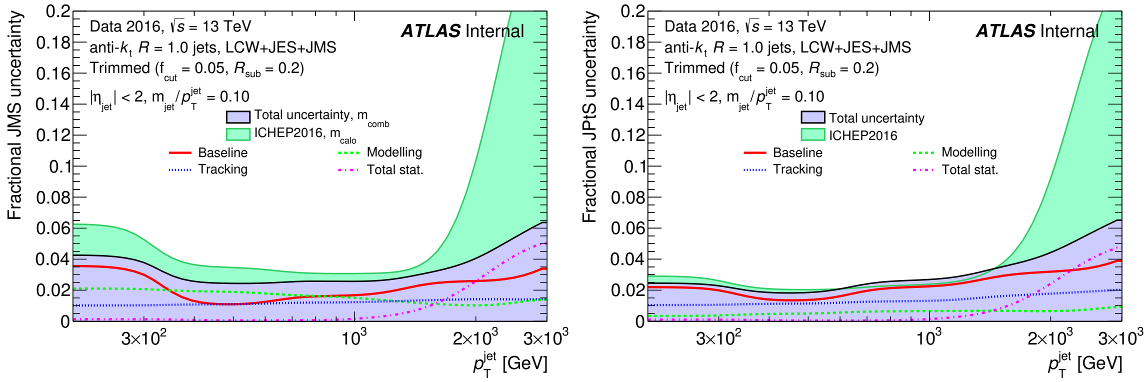

(a) Large-R jet mass scale

(b) Large-R jet p_{T} scale

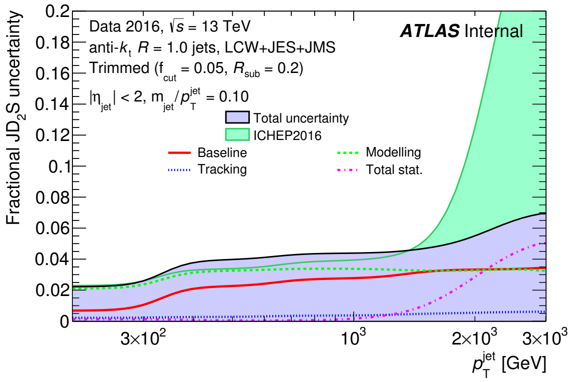

(c) Large-R jet D_2 scale

Figure 5.19: The fractional scale uncertainties associated with large-R jets [96]. "ICHEP2018" refers to superseded results.

The absolute uncertainty is applied by smearing the p_{T} of the large-R jet using a Gaussian function with the width parameter set to $\sigma = p_{\mathrm{T}} \times 2\%$. A relative uncertainty of 20% on the mass resolution and a relative uncertainty of 15% on the D_2 resolution of the large-R jets are also taken into account. The relative uncertainty is stated with respect to the corresponding quantity and is applied in the following manner. First, the width of the Monte Carlo response, which is defined as the ratio of the reconstructed to the truth value of the corresponding quantity, is extracted by calculating the 68% inter-quartile of the response distribution. The nominal resolution of the response is taken as half of the 68% inter-quartile. The inter-quartile proves to be a better estimate of the resolution than a Gaussian function when the response distribution is asymmetric and therefore cannot be well approximated by a single Gaussian function. Given the nominal resolution, the corresponding quantity can be smeared accordingly based on the size of the relative uncertainty. In addition, p_{T}-dependent nominal resolutions are generated based on truth MC information for

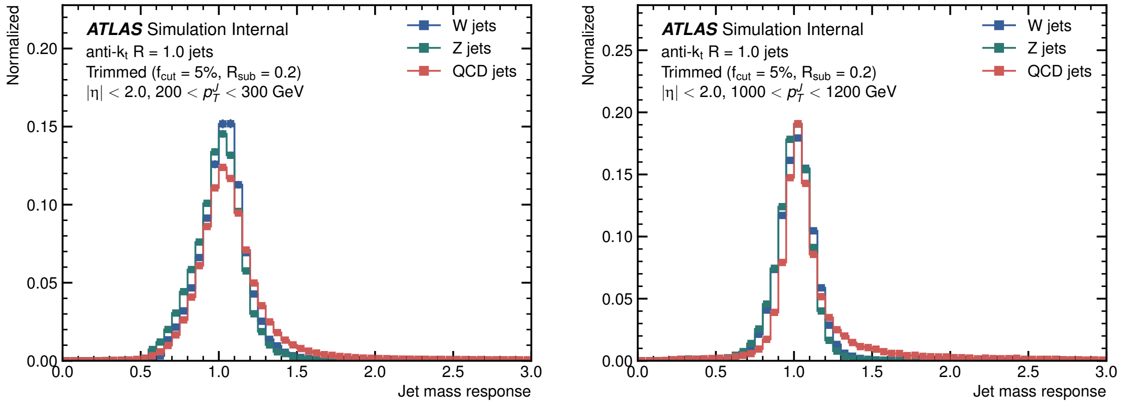

(a) Mass response in $p_{\mathrm{T}}^J \in [200, 300]$ GeV (b) Mass response in $p_{\mathrm{T}}^J \in [1000, 1200]$ GeV

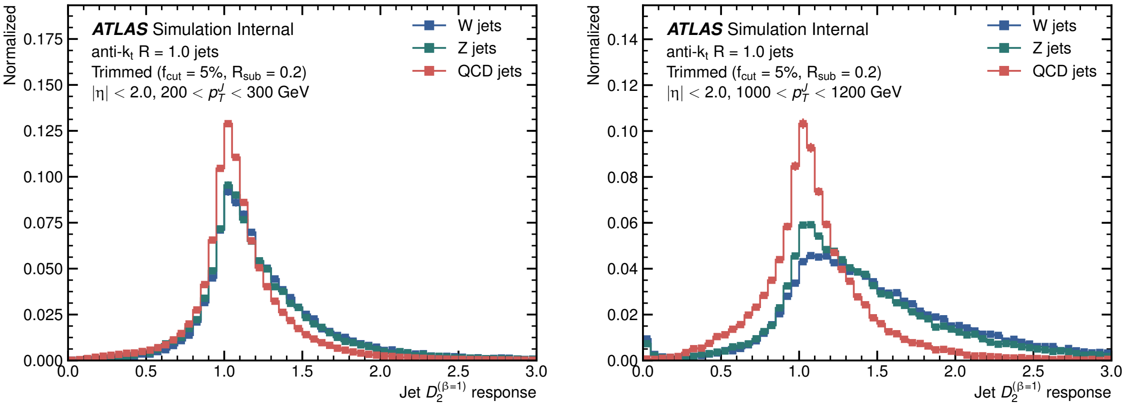

(c) D_2 response in $p_{\mathrm{T}}^J \in [200, 300]$ GeV (d) D_2 response in $p_{\mathrm{T}}^J \in [1000, 1200]$ GeV

Figure 5.20: Distributions of mass and D_2 responses of the large-R jets in different p_{T} bins.

background jets, W-boson jets and jets originating from Z bosons individually, since the respective response distributions are different. A few representative MC response distributions are shown in Figure 5.20 and the resulting resolutions are presented in Figure 5.21 as a function of the jet p_{T}.

Missing Transverse Energy

The main sources of uncertainty on the missing transverse energy correspond to the propagated systematic uncertainties associated with all the reconstructed objects that are used to build the $E_{\mathrm{T}}^{\mathrm{miss}}$. An additional uncertainty is also included to account for the soft terms during the reconstruction of the missing transverse energy. This includes tracks that are not associated with any reconstructed objects. Variations in the resolution and scale of the soft terms are covered by an uncertainty of approximately 2% [97].

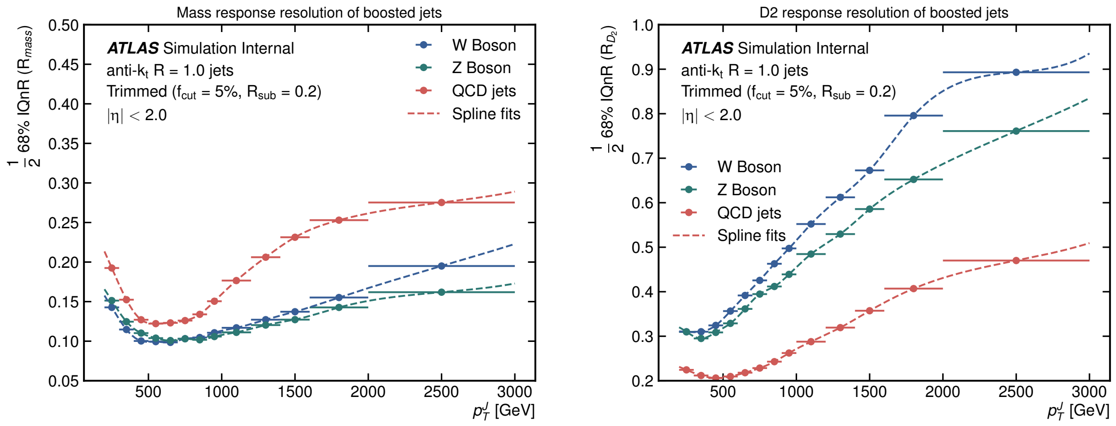

(a) Mass resolution (b) D_2 resolution

Figure 5.21: Resolutions of the large-R jet (a) mass and (b) D_2 responses as a function of reconstructed jet p_T for W/Z boson jets and QCD jets. IQnR (inter-quartile range) is defined as $q_{84\%} - q_{16\%}$, whereby $q_{16\%}$ and $q_{84\%}$ are the 16th and 84th percentiles of a given distribution.

Other Uncertainties

An uncertainty of 3.2% is associated with the total integrated luminosity of the dataset. This is derived by calibrating the luminosity scale with $x-y$ beam separation scans. The corresponding uncertainty is applied to all the MC processes of which the normalization is not determined in a data-driven way. Variations in the pile-up reweighting procedure of the Monte Carlo samples are also included to account for the uncertainties on the ratio between the measured and predicted inelastic cross sections in the fiducial volume defined by $M > 13\,\text{GeV}$, where M represents the mass of the hadronic system [98].

5.4.2 Background Uncertainties

Modeling uncertainties associated with the major background processes are important sources of systematic uncertainties. These uncertainties are assumed to be shape-only (without any impact on the normalization of the background) and implicitly reflect the level of degree to which the background template based the nominal Monte Carlo samples can be trusted. Techniques involving data-driven methods and comparisons between different Monte Carlo generators are often employed to address this issue. In this section, modeling systematic variations relevant to this analysis will be discussed. These systematics are taken as shape variations on the nominal $m_{\ell\ell jj}$ and $m_{\ell\ell J}$ shape templates.

Z+jets Modeling Uncertainty

The Z+jets modeling uncertainty will be taken into consideration using the data driven background estimation called α-ratio method. The data in the Z+jets control region is compared to the MC in the same control region. Subsequently the data in the control region is multiplied by the α ratio, which is defined as the ratio of the MC yield in the signal region to that of the control region:

$$\alpha(m_{\ell\ell J}) = \frac{MC(SR)}{MC(CR)} \tag{5.3}$$

α ratio is derived in a bin-wise manner for each signal region after the subtraction of the other background processes. The shape of data in the control region corrected by the α ratio is then used as the data-driven background estimate of the signal region. Comparison between the Monte Carlo based estimate and the data-driven estimate is performed and the shape difference will be taken as the modeling uncertainty associated with the Monte Carlo shape template. There are several potential advantages in using the differential ratio for modeling Z+jets in the signal regions:

- Adequate amount of data is available in the Z+jets control region;
- The α-ratio estimation is less sensitive to the absence of higher-order matrix-element corrections for the background and to theory systematic uncertainties (e.g. normalization and factorization scales, PDFs, etc.) due to the fact that the background composition is similar in the two regions;
- Taking the ratio between signal and control regions might lead to cancellation of certain experimental systematic effects (e.g. the luminosity of the collected sample, pile-up corrections, etc.).

A few representative results of the α-ratio method are displayed in Figure 5.22.

$t\bar{t}$ Modeling Uncertainty

The nominal $t\bar{t}$ prediction uses the NLO matrix element (ME) generator POWHEG-BOX v2 along with the CT10 PDF set, which is interfaced with PYTHIA 6 using the Perugia 2012 tune. Alternative MC samples are used to assess the uncertainties associated with the modeling of the $t\bar{t}$ production [99]. Table 5.6 summarizes the modeling systematic uncertainties for the $t\bar{t}$ process and the alternative samples used.

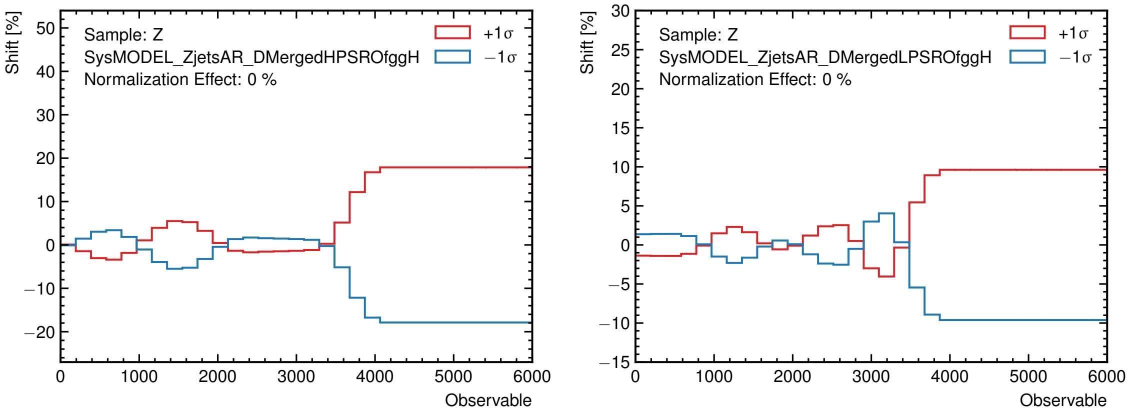

(a) Merged high-purity signal region

(b) Merged low-purity signal region

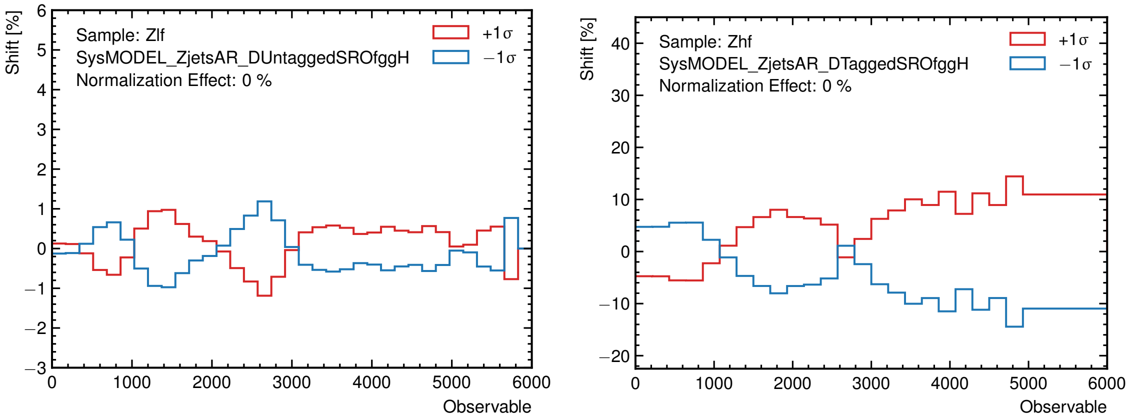

(c) Resolved untagged signal region

(d) Resolved tagged signal region

Figure 5.22: Modeling uncertainties of the Z+jets background estimated using the α-ratio method. The uncertainties shown are for the spin-0 signal regions.

Table 5.6: A summary of the modeling systematic uncertainties for the $t\bar{t}$ process as well as the samples used in each case [99]. The symbol Δ denotes the difference in the analysis observables using the simulation from the samples column. The notation $\pm|\Delta|$ indicates that the full difference is symmetrized and applied to the nominal sample. Without the absolute value bars, Δ indicates that the signed difference with respect to the nominal case is used to estimate the uncertainty.

Source of Uncertainty	Samples	Procedure
Nominal	Powheg+Pythia6	N/A
Hard Scatter Generation	Powheg+Herwig++ vs. aMC@NLO+Herwig++	$\pm\|\Delta\|$
Parton Shower and Hadronization Model	Powheg+Pythia6 vs. Powheg+Herwig++	$\pm\|\Delta\|$
Scales and Additional Radiation	Powheg+Pythia6 Variations	Δ

Modeling Uncertainty of Diboson Processes

Alternative diboson samples generated by Powheg-Box v2 are compared to the corresponding nominal samples. The difference is taken as the systematic variation due to different generators.

5.4.3 Signal Uncertainties

Theoretical uncertainties associated with the signal samples mostly affect the event yield for the signal production. In this subsection, uncertainties due to the choice of parton distribution function (PDF) are considered, as well as those coming from initial-state and final-state radiation (ISR/FSR) tunes.

Parton Distribution Function

Uncertainties on the signal yield due to the choice of PDF are estimated by taking the acceptance difference due to internal PDF error sets and the difference between choice of PDF sets. Uncertainty on the signal yield due to PDF set is evaluated by comparing the nominal choice, NNPDF3.0, to samples generated with alternative MMHT2014 [100] and CT14 [101] PDF sets. Following the prescriptions described in [102], a 68% uncertainty band for each PDF set is evaluated and the envelop of the errors form the signal uncertainty due to different PDF choices. The uncertainty is measured on the ratio of the acceptance times efficiency of the variation samples to that of the nominal samples. The impact of PDF uncertainties on the signal yield is generally small, ranging from 1% to 2% for the HVT W' model and less than 1% for the other two signal hypotheses.

Initial-State and Final-State Radiation

The uncertainties due to ISR/FSR are estimated by varying relevant parameters in the MC generator following the prescription described in [86]. These include systematic variations responsible for uncertainties related with the underlying event, variations to account for substructures of jets, and variations for different aspects of extra jet production. The resulting undertainties are summed quadratically and the differences with respect to the nominal distribution are taken as estimates for uncertainties coming from ISR/FSR. ISR/FSR uncertainties range from approximately 1% to 4% among the signal models. In addition, the effect of the QCD scale uncertainty on the yield of the heavy Higgs signal is estimated to be around 1%–4% by varying the factorisation and renormalisation scales.

5.5 Statistical Analysis

Statistical analysis is a crucial element in a physics analysis, as it provides a means to quantify the correspondence between theoretical predictions and experimental observations. While the statistical analysis of the data is often treated as a final subsidiary step to an experimental physics result, thinking through the requirements for a robust statistical statement is an efficient way to organize an analysis strategy. This section introduces the template for constructing a likelihood model for an analysis, the treatment of systematic uncertainties as a set of nuisance parameters (NPs), and test statistics used in different hypothesis testing scenarios. These scenarios include the evaluation the significance of a discovery and the derivation of the upper limit on the production rate of some model. More specifically, inputs to the likelihood model used for this analysis are discussed as well.

5.5.1 Likelihood Function

A likelihood function is defined based on the product of the Poisson models for each selection region in the following way [103]:

$$\mathcal{L}_{\text{tot}}(\mu, \theta|\mathcal{D}, \mathcal{G}) = \prod_{r\in\text{regions}} \left[\text{Pois}(n_r|\nu_r(\theta)) \prod_{e=1}^{n_r} f_r(x_{re}|\theta) \right] \cdot \prod_{p\in\mathbb{S}} f_p(a_p|\theta_p), \tag{5.4}$$

where μ represents the set of parameters of interest (e.g. mass, $\sigma \times \mathcal{B}$), θ denotes the set of nuisance parameters that the model depends upon, $\mathcal{D} = \{\mathcal{D}_1, \mathcal{D}_2, ..., \mathcal{D}_{r_{\max}}\}$ represents the collection of the observed events in each region labeled from 1 to $r_{\max}$, $\text{Pois}(n_r|\nu_r(\theta))$ is the Poisson probability density function for the overall event count of each analysis region, $f_r(x_{re}|\theta)$ is the the probability density for the observable x for a single event in the region r, the set $\mathbb{S}$ includes all the nuisance parameters constrained by some prior auxiliary measurements, $f_p(a_p|\theta_p)$ represents the probability density function obtained from the auxiliary measurement of the nuisance parameter θ_p, and $\mathcal{G} = \{a_1, ..., a_p\}$ represents the set of the observed values of the nuisance parameters.

For the searches considered in this dissertation, a binned likelihood formulation is adopted and the probability model for each region can be written as:

$$\text{Pois}\big(n|\nu(\theta)\big) \prod_{e=1}^{n} f(x_e|\theta) = \text{Pois}\left(n|\mu S(\theta) + B(\theta)\right) \left[\prod_{b\in\text{bins}}^{n} \frac{\mu\nu_b^{\text{sig}}(\theta) + \nu_b^{\text{bkg}}(\theta)}{\mu S(\theta) + B(\theta)} \right], \tag{5.5}$$

where μ, the parameter of interest, is the signal strength parameter which multiplies the expected signal yield $\nu_b^{\mathrm{sig}}(\theta)$ in each bin of the histogram, $\nu_b^{\mathrm{bkg}}(\theta)$ represents the background count in the bin b, and $S(\theta)$ and $B(\theta)$ are the total signal and background event rates, respectively. The dependence of the signal and background predictions on the systematic uncertainties is described by the set of nuisance parameters ($\mathbb{S}$). Nuisance parameters are usually constrained by auxiliary measurements or measured in control regions, which can be used to better estimate or reduce the effect of systematic uncertainties. The constraints from auxiliary measurements correspond to the last product in Equation (5.4). The constraints are normally parameterized by either Gaussian or log-normal function terms, where the log-normal constraints are used for normalization uncertainties in order to maintain a positive likelihood. Normalizations of major background processes can often be measured in their respective control regions, where the corresponding background is the dominant process. Systematic uncertainties can also be further reduced if additional information is present with respect to the dedicated auxiliary measurement. For example, this could happen when an analysis region focuses on a reduced jet p_{T} range whereas the global auxiliary experiment measure the entire p_{T} spectrum.

After the construction of the binned likelihood function, the method of maximium likelihood estimation (MLE) is applied to estimate the values of the parameters that the model depends on. Let $\hat{\mu}$ and $\hat{\boldsymbol{\theta}}$ denote the set of the parameters that maximizes the likelihood function, the corresponding likelihood is expressed as $\mathcal{L}(\hat{\mu}, \hat{\boldsymbol{\theta}})$. To test a hypothesized value of the strength parameter μ, the profile likelihood ratio is defined as follows [103, 104]:

$$\lambda(\mu) = \frac{\mathcal{L}(\mu, \hat{\hat{\boldsymbol{\theta}}})}{\mathcal{L}(\hat{\mu}, \hat{\boldsymbol{\theta}})}, \tag{5.6}$$

where $\mathcal{L}(\mu, \hat{\hat{\boldsymbol{\theta}}})$ is the definition of a profile likelihood function and it conditionally maximizes the likelihood at a fixed value of μ. The presence of the nuisance parameters broadens the profile likelihood curve as a function of μ compared to what one would have if the values of these NPs were known exactly. This is related to the loss of information about μ due to the systematic uncertainties associated with the analysis. It can be easily seen from Equation (5.6) that $0 \leq \lambda(\mu) \leq 1$.

A modified profile likelihood ratio is also defined for scenarios where the signal process necessarily has $\mu \geq 0$. That is, the presence of the signal process can only increase the average event rate. The profile likelihood ratio in this case is defined as

[104]:

$$\tilde{\lambda}(\mu) = \begin{cases} \mathcal{L}(\mu, \hat{\hat{\boldsymbol{\theta}}})/\mathcal{L}(\hat{\mu}, \hat{\boldsymbol{\theta}}) & \hat{\mu} \geq 0 \\ \mathcal{L}(\mu, \hat{\hat{\boldsymbol{\theta}}})/\mathcal{L}(0, \hat{\boldsymbol{\theta}}) & \hat{\mu} < 0, \end{cases} \tag{5.7}$$

where the choice of 0 when $\hat{\mu} < 0$ is justified by the fact that the best level of agreement between the data and any physical value of μ occurs at $\mu = 0$.

5.5.2 Test Statistics

A test statistic is a quantity that maps the observed data to a single real number during a statistical hypothesis testing. A good test statistic treats the null and the alternative hypotheses in an asymmetric way and therefore the corresponding hypothesis test has the power to distinguish the null from the alternative hypothesis. One example of the test statistic could be [104]:

$$t_\mu = -2 \ln \lambda(\mu). \tag{5.8}$$

The test statistic generally serves as a measure of the incompatibility between observed data and the hypothesis at a specific value of μ. Higher values of t_μ therefore indicate the increasing discrepancy between data and the strength parameter. A p-value can be computed for a test statistic in order to quantify the level of disagreement:

$$p_\mu = \int\limits_{t_{\mu,\mathrm{obs}}}^{\infty} f(t_\mu|\mu)\; dt_\mu, \tag{5.9}$$

where $t_{\mu,\mathrm{obs}}$ corresponds the the observed value of the test statistic given data and μ, and $f(t_\mu|\mu)$ is the probability density function of the test statistic assuming a signal strength of μ.

Test statistic $\tilde{q}_0$ for discovery

The test statistic q_0 [103, 104] quantifies the incompatibility between the background-only hypothesis with $\mu = 0$ and the hypothesis in which a class of model has $\mu > 0$. It quantifies the significance of an excess and rejecting the background-only hypothesis could lead to the discovery a signal. The test statistic defined for discovery of a positive signal reads:

$$q_0 = \begin{cases} -2 \ln \lambda(0) & \hat{\mu} \geq 0 \\ 0 & \hat{\mu} < 0. \end{cases} \tag{5.10}$$

In case of signal process which might have $\mu < 0$ (i.e. destructive interference), Equation (5.10) is slightly modified in order to probe p-values larger than 50% (which indicates a downward fluctuation) [103]:

$$q_0 = \begin{cases} -2\ln\lambda(0) & \hat{\mu} \geq 0 \\ +2\ln\lambda(0) & \hat{\mu} < 0. \end{cases} \tag{5.11}$$

To quantify the level of disagreement between the data and the background-only hypothesis, the p-value can be calculated as follows based on the observed value of q_0:

$$p_0 = \int\limits_{q_{0,\mathrm{obs}}}^{\infty} f(q_0|0)\ dq_0, \tag{5.12}$$

where the distribution of test statistic, $f(q_0|0)$, is discussed in [104]. It is customary to transform the obtained p-value to an equivalent significance Z, which is expressed in terms of the quantile function, Φ^{-1} ,of a standard Gaussian distribution:

$$Z = \Phi^{-1}(1 - p_0). \tag{5.13}$$

Test statistic q_μ for upper limits

For purposes of establishing an upper limit on the strength parameter μ, the following test statistic is defined [103, 104]:

$$\tilde{q}_\mu = \begin{cases} -2\ln\tilde{\lambda}(\mu) & \hat{\mu} \leq \mu \\ 0 & \hat{\mu} > \mu. \end{cases} \tag{5.14}$$

The test statistic $\tilde{q}_\mu$ has the power to distinguish the hypothesis of the signal events being produced at a certain rate from alternative hypotheses in which signal events are produced at lesser rates. The corresponding p-value in this case is calculated as follows:

$$p_\mu = \int\limits_{\tilde{q}_{\mu,\mathrm{obs}}}^{\infty} f(\tilde{q}_\mu|\mu, \hat{\hat{\boldsymbol{\theta}}})\ d\tilde{q}_\mu, \tag{5.15}$$

where $\hat{\hat{\boldsymbol{\theta}}}$ represents the set of nuisance parameters that conditionally maximizes the likelihood function $\mathcal{L}(\mu, \hat{\hat{\boldsymbol{\theta}}})$. As a result, the distribution of the test statistic $\tilde{q}_\mu$ itself depends on the value of the strength parameter, unlike the case of q_0.

Upper limits on the signal strength are usually derived using the CL_s procedure.

The CL_s is a function of the strength parameter and is defined as:

$$\mathrm{CL}_s(\mu) = \frac{p_\mu}{1 - p_b}, \tag{5.16}$$

where p_b is the p-value derived from the test statistic $\tilde{q}_\mu$ under the background-only hypothesis ($\mu = 0$, not the null hypothesis in this case):

$$p_b \equiv 1 - \int\limits_{\tilde{q}_{\mu,\mathrm{obs}}}^{\infty} f\left(\tilde{q}_\mu | 0, \hat{\hat{\boldsymbol{\theta}}}(\mu = 0)\right) \, d\tilde{q}_\mu. \tag{5.17}$$

The CL_s method has the advantage of reducing the rate of type-I error, in which the null hypothesis assuming a signal strength of μ is incorrectly rejected. This is because by taking the ratio, the CL_s method avoids yielding small p-values when the distributions of the test statistics for the signal and background-only hypotheses largely overlap (i.e. when the sensitivity of the search is extremely limited). The CL_s upper limit on μ (denoted by μ_{up}) at 95% confidence level is then obtained by solving for $\mathrm{CL}_s(\mu_{\mathrm{up}}) = 5\%$. Consequently, the range of the strength parameter $\mu > \mu_{\mathrm{up}}$ will be excluded at 95% confidence level. Assuming the validity of the Wald approximation, the upper limit can be calculated asymptotically [104]:

$$\mathrm{med}\left[\mu_{\mathrm{up}} | \hat{\mu}\right] = \hat{\mu} + \sigma \cdot \Phi^{-1}(1 - \alpha), \tag{5.18}$$

where $1 - \alpha$ represents the desired confidence level and σ can be obtained from the covariance matrix of the estimators for all the parameters in the MLE. The corresponding $\pm N\sigma$ error band is given by:

$$\mathrm{band}_{N\sigma} = \hat{\mu} + \sigma \cdot \left[\Phi^{-1}(1 - \alpha) \pm N\right]. \tag{5.19}$$

5.5.3 Fit inputs

The overarching principle of the analysis design is to use the shape of the $m_{\ell\ell J}$ or $m_{\ell\ell jj}$ spectrum to extract signals in various signal regions. The fit inputs entering the likelihood function for the $H \to ZZ$ search are summarized in Table 5.7. Similarly, Table 5.8 and Table 5.9 show those for the $W' \to ZW$ and $G_{\mathrm{KK}} \to ZZ$ searches, respectively. The detailed event selection and the definitions of the signal and control regions used in this analysis are outlined in Section 5.3. For each signal region, the input to the likelihood is the invariant mass distribution of the ZV system: $m_{\ell\ell jj}$ in the resolved regime and $m_{\ell\ell J}$ in the merged regime. For the control regions of

Table 5.7: Summary of the inputs entering the likelihood function for the $H \to ZZ$ search. "N_{evt}" indicates that the number of events is used as the discriminant without any shape information and α refers to scale factors applied to the major background processes.

Fit inputs for the $H \to ZZ$ search		
Input region	Discriminant	Scale factor(s)
VBF category		
HP SR (ZCR)	$m_{\ell\ell J}$ spectrum (N_{evt})	$\alpha^{J,\,\text{VBF}}_{Z+\text{jets}}$, $\alpha_{t\bar{t}}$
LP SR (ZCR)	$m_{\ell\ell J}$ spectrum (N_{evt})	$\alpha^{J,\,\text{VBF}}_{Z+\text{jets}}$, $\alpha_{t\bar{t}}$
Resolved SR (ZCR)	$m_{\ell\ell jj}$ spectrum (N_{evt})	$\alpha^{n_b \leq 2}_{Z+\text{jets}}$, $\alpha_{t\bar{t}}$
ggF category		
HP SR (ZCR)	$m_{\ell\ell J}$ spectrum (N_{evt})	$\alpha^{J,\,\text{ggF}}_{Z+\text{jets}}$, $\alpha_{t\bar{t}}$
LP SR (ZCR)	$m_{\ell\ell J}$ spectrum (N_{evt})	$\alpha^{J,\,\text{ggF}}_{Z+\text{jets}}$, $\alpha_{t\bar{t}}$
b-tagged SR (ZCR)	$m_{\ell\ell jj}$ spectrum (N_{evt})	$\alpha^{n_b=2}_{Z+\text{hf}}$, $\alpha_{t\bar{t}}$
Untagged SR (ZCR)	$m_{\ell\ell jj}$ spectrum (N_{evt})	$\alpha^{n_b<2}_{Z+\text{lf}}$, $\alpha_{t\bar{t}}$
Top control region	N_{evt}	$\alpha_{t\bar{t}}$

the major backgrounds, the overall event counts (N_{evt}) are used without any shape information.

Minor backgrounds modeled by MC simulations are normalized to their respective theoretical cross sections, whereas the normalizations of the primary background processes (i.e., Z+jets and $t\bar{t}$) are determined by the observed data. To achieve this, a set of scale factors (SFs), which are defined as the ratio of the number of simulated events after the fit to that before the fit, is applied to the major backgrounds in the relevant regions. These scale factors are implemented as free parameters in the fit, and are constrained by the data in both signal and control regions. Separate Z+jets SFs are applied in the ggF and the VBF categories. A common Z+jets SF is applied to both HP and LP regions in each category. For the ggF category, two independent SFs are used for the b-tagged and untagged regions in the $H \to ZZ$ and $G_{\text{KK}} \to ZZ$ searches: one for the Z+heavy-flavor component and the other for the Z+light-flavor component (Section 5.1.2). This is motivated by the fact that the relative fractions of the heavy-flavor and the light-flavor contents are not accurately predicted by the Z+jets MC, which is shown in Table 5.10. The top quark production is a significant background source in the b-tagged regions but a minor background in the other regions (Figure 5.12); consequently, a b-tagged top quark control region is

Table 5.8: Summary of the inputs entering the likelihood function for the $W' \to ZW$ search. "N_{evt}" indicates that the number of events is used as the discriminant without any shape information and α refers to scale factors applied to the major background processes.

Fit inputs for the $W' \to ZW$ search		
Input region	Discriminant	Scale factor(s)
VBF category		
HP SR (ZCR)	$m_{\ell\ell J}$ spectrum (N_{evt})	$\alpha^{J,\,\mathrm{VBF}}_{Z+\mathrm{jets}}$
LP SR (ZCR)	$m_{\ell\ell J}$ spectrum (N_{evt})	$\alpha^{J,\,\mathrm{VBF}}_{Z+\mathrm{jets}}$
Resolved SR (ZCR)	$m_{\ell\ell jj}$ spectrum (N_{evt})	$\alpha^{n_b\leq 2}_{Z+\mathrm{jets}}$
ggF category		
HP SR (ZCR)	$m_{\ell\ell J}$ spectrum (N_{evt})	$\alpha^{J,\,\mathrm{ggF}}_{Z+\mathrm{jets}}$
LP SR (ZCR)	$m_{\ell\ell J}$ spectrum (N_{evt})	$\alpha^{J,\,\mathrm{ggF}}_{Z+\mathrm{jets}}$
Resolved SR (ZCR)	$m_{\ell\ell jj}$ spectrum (N_{evt})	$\alpha^{n_b\leq 2}_{Z+\mathrm{jets}}$

Table 5.9: Summary of the inputs entering the likelihood function for the $G_{\mathrm{KK}} \to ZZ$ search. "N_{evt}" indicates that the number of events is used as the discriminant without any shape information and α refers to scale factors applied to the major background processes.

Fit inputs for the $G_{\mathrm{KK}} \to ZZ$ search		
Input region	Discriminant	Scale factor(s)
ggF category		
HP SR (ZCR)	$m_{\ell\ell J}$ spectrum (N_{evt})	$\alpha^{J,\,\mathrm{ggF}}_{Z+\mathrm{jets}}$, $\alpha_{t\bar{t}}$
LP SR (ZCR)	$m_{\ell\ell J}$ spectrum (N_{evt})	$\alpha^{J,\,\mathrm{ggF}}_{Z+\mathrm{jets}}$, $\alpha_{t\bar{t}}$
b-tagged SR (ZCR)	$m_{\ell\ell jj}$ spectrum (N_{evt})	$\alpha^{n_b=2}_{Z+\mathrm{hf}}$, $\alpha_{t\bar{t}}$
Untagged SR (ZCR)	$m_{\ell\ell jj}$ spectrum (N_{evt})	$\alpha^{n_b<2}_{Z+\mathrm{lf}}$, $\alpha_{t\bar{t}}$
Top control region	N_{evt}	$\alpha_{t\bar{t}}$

defined and a single top quark SF is applied to all the regions.

All the systematic uncertainties enter the profile likelihood fit as nuisance parameters with prior constraints. Nuisance parameters with constraints contain information from dedicated auxiliary measurements and the constraints are included in the likelihood function as global functions, which are parameterized as either Gaussian or log-normal function terms (Section 5.5.1). The size of a systematic uncertainty, e.g.

a 5% effect on the jet energy scale, usually refers to the standard deviation of the corresponding Gaussian constraint.

The statistical uncertainties associated with the background MC samples are taken into account in the profile likelihood using a light-weight version of the Barlow-Beeston method [105]. This adds an extra nuisance parameter representing the statistical uncertainty on the total MC background in each bin, which is completely uncorrelated across bins. These nuisance parameters are added to bins where the relative statistical uncertainty of the total background in each bin is above a threshold value of 0.1%.

5.6 Results

This section presents the results of this analysis after carrying out the statistical procedure outlined in Section 5.5. In this analysis, two charged leptons (ee or $\mu\mu$) are selected to reconstruct the Z boson in the $X \rightarrow ZV$ decay and the final state will be referred to as $\ell\ell qq$. A similar analysis has also been performed, in which the $Z \rightarrow \nu\nu$ decay is exploited and the other boson is also required to decay hadronically. The final state (referred to as $\nu\nu qq$ hereinafter) of this counterpart analysis has two neutrinos, which will be reconstructed as missing transverse energy, and two quarks, where only the merged topology is investigated and therefore large-R jets are used to reconstruct the $V \rightarrow qq$ decay.

The sensitivity of the $\ell\ell qq$ analysis dominates in the intermediate mass region of approximately 400 to 1200 GeV, in which the merged and resolved topologies coexist for the $V \rightarrow qq$ decay (Section 5.3.5). The $\nu\nu qq$ analysis, however, excels at the high mass end because of a higher branching ratio of the $Z \rightarrow \nu\nu$ decay. Since these two analyses probe exactly the same diboson resonances, the analysis regions of both analyses are combined statistically in the same likelihood model. This amounts to a simultaneous fit to all the regions used. Although the likelihood fit encompasses both analyses, only the mass spectra of the $\ell\ell qq$ analysis will be shown in this section. Due to the absence of significant excesses, upper limits are set on the product of the cross section of the new resonances and their respective decay branching ratios, $\sigma \times \mathcal{B}(X \rightarrow ZV)$, which will be discussed in Section 5.6.2. Maximum likelihood fits are performed independently for each type of the signal models considered, as the results are interpreted separately.

5.6.1 Background-Only Fit

A background-only fit corresponds to a conditional maximum likelihood fit with the strength parameter fixed at zero. It is the sensible thing to do in the absence of an evident excess with respect to the SM background prediction. The observed mass spectra of the $H \rightarrow ZV \rightarrow \ell\ell J$ and $H \rightarrow ZV \rightarrow \ell\ell jj$ candidates selected by the VBF category are shown in Figure 5.23, along with the SM background estimates after performing the background-only fit. Figure 5.24 corresponds to the distributions of the $H \rightarrow ZV \rightarrow \ell\ell qq$ search in the ggF category. Various control regions are used to constrain and determine the normalizations of the major background processes as mentioned in Section 5.5. The numbers of events observed and estimated in control regions are summarized in Figure 5.25.

The distributions of the $W' \to ZW \to \ell\ell qq$ search are shown in Figure 5.26 and Figure 5.27, for the VBF category and ggF category respectively. Similarly, the observed and expected $m_{\ell\ell J}/m_{\ell\ell jj}$ distributions for the $G_{\mathrm{KK}} \to ZZ \to \ell\ell qq$ search are presented in Figure 5.28.

Reasonable agreement between the observed data and the SM estimates is observed within the total uncertainty assigned. The largest deviation from the SM prediction occurs in the high-purity signal region of the ggF category in the $H \to ZZ \to \ell\ell qq$ analysis. A downward fluctuation relative to the background estimation is observed in data around 800 GeV in the $m_{\ell\ell J}$ spectrum. The deficit is evaluated to have a local significance of $3.0\,\sigma$, and a global significance of $1.9\,\sigma$ after taking into account the look-elsewhere effect [106]. Similar downward fluctuations of the data are also seen in the high purity regions of the other two spin hypotheses and the significance levels are similar.

Normalization scale factors assigned to major background processes are allowed to be adjusted freely in the MLE, as mentioned in Section 5.5. These factors will be measured and constrained simultaneously by the relevant signal and control regions. In Table 5.10, a summary of the best-fit values of the various background normalization scale factors is shown. These scale factors are expressed ratios of the pre-fit to post-fit background normalizations. Scale factors with values close to one indicate an accurate prediction of the cross sections of the respective background processes by the MC simulation. The most notable scale factor deviating from unity is the one for Z+heavy-flavor, which is also seen in other analyses [107, 108].

In Tables 5.11-5.13, the number of observed events, estimated yields of various SM background processes, and the expected number of signal events assuming certain $\sigma \times \mathcal{B}(X \to ZV)$ are summarized for each spin hypothesis.

Table 5.10: Best-fit values of the floating normalization scale factors for the background components from the background-only likelihood fits for H, W' and G_{KK} searches respectively. For each search, all signal regions and control regions are included in the fit.

Normalization scale factor		$X \to ZV$ search				
Background component	region	H		W'		G_{KK}
		ggF/DY cat.	VBF cat.	ggF/DY cat.	VBF cat.	
Z+jets	merged	1.07 ± 0.04	0.80 ± 0.08	1.04 ± 0.04	0.79 ± 0.10	1.10 ± 0.04
Z+light-flavour	resolved	1.11 ± 0.05	0.68 ± 0.06	1.05 ± 0.06	0.67 ± 0.06	1.12 ± 0.07
Z+heavy-flavor	resolved	1.34 ± 0.12				1.28 ± 0.12
W+jets	merged	1.13 ± 0.06	0.76 ± 0.13	1.09 ± 0.06	0.68 ± 0.14	1.12 ± 0.07
$t\bar{t}$ ($\ell\ell qq$)	–	1.00 ± 0.07		–	–	1.00 ± 0.07
$t\bar{t}$ ($\nu\nu qq$)	–	0.99 ± 0.08		0.97 ± 0.08		1.02 ± 0.07

Table 5.11: Numbers of events observed in the data and predicted for background processes from background-only fits to the signal and control regions in the seven signal regions of the $H \to ZZ \to \ell\ell qq$ search. The numbers of signal events expected from the ggF and VBF production of a heavy Higgs boson with mass of 1 TeV are also shown. The signal yields are calculated using $\sigma \times \mathcal{B}(H \to ZZ) = 20$ fb for both processes. The uncertainties combine statistical and systematic contributions. The fit constrains the background estimate towards the observed data, which reduces the total background uncertainty by correlating those from the individual backgrounds.

$V \to qq$	Signal	H (1 TeV)		Background estimates				Data
recon.	regions	ggF	VBF	Z+jets	Diboson	Top quarks	Total	
				VBF category				
Merged	HP	0.42 ± 0.08	5.1 ± 1.0	29.0 ± 2.6	3.8 ± 0.6	1.1 ± 0.4	33.9 ± 2.7	32
	LP	0.33 ± 0.08	3.4 ± 0.4	113 ± 7	8.4 ± 1.2	1.8 ± 0.6	123 ± 7	109
Resolved		0.23 ± 0.05	2.3 ± 0.4	1307 ± 34	60 ± 9	66 ± 7	1433 ± 34	1434
				ggF category				
Merged	HP	14.2 ± 1.6	11.0 ± 2.1	1728 ± 34	177 ± 21	20.6 ± 2.2	1926 ± 32	1906
	LP	10.0 ± 0.9	7.5 ± 0.8	6060 ± 60	285 ± 31	69 ± 6	6420 ± 60	6375
Resolved	b-tagged	1.02 ± 0.12	0.62 ± 0.08	1740 ± 40	167 ± 22	908 ± 24	2810 ± 40	2843
	Untagged	3.31 ± 0.34	2.5 ± 0.5	82200 ± 400	2280 ± 250	1500 ± 130	86030 ± 280	85928

Table 5.12: Numbers of events observed in the data and predicted for background processes from background-only fits to the signal and control regions in the seven signal regions of the $W' \to ZW \to \ell\ell qq$ search. The numbers of signal events expected from the DY and VBF production of a W' with mass of 1 TeV are also shown. The signal yields are calculated using $\sigma \times \mathcal{B}(W' \to ZW) = 20$ fb for both processes. The uncertainties combine statistical and systematic contributions.

$V \to qq$	Signal	W' (1 TeV)		Background estimates				Data
recon.	regions	DY	VBF	Z+jets	Diboson	Top quarks	Total	
				VBF category				
Merged	HP	0.039 ± 0.022	0.98 ± 0.13	17.1 ± 2.0	3.3 ± 0.6	0.42 ± 0.11	20.8 ± 2.1	23
	LP	0.023 ± 0.009	0.58 ± 0.06	59 ± 5	4.9 ± 0.8	0.51 ± 0.21	64 ± 5	64
Resolved		0.0054 ± 0.0032	0.72 ± 0.06	1015 ± 31	36 ± 5	8.1 ± 2.1	1059 ± 30	1068
				DY category				
Merged	HP	8.4 ± 1.2	2.17 ± 0.30	1193 ± 26	137 ± 16	12.2 ± 1.2	1343 ± 26	1333
	LP	5.3 ± 0.5	1.34 ± 0.15	3960 ± 50	195 ± 23	27 ± 5	4180 ± 50	4117
Resolved		1.34 ± 0.15	0.76 ± 0.07	46320 ± 250	1270 ± 140	265 ± 26	47850 ± 210	47802

Table 5.13: Numbers of events observed in the data and predicted for background processes from background-only fits to the signal and control regions in the seven signal regions of the $G_{\mathrm{KK}} \to ZW \to \ell\ell qq$ search. The numbers of signal events expected from the production of a G_{KK} with mass of 1 TeV are also shown for $k/\overline{M}_{\mathrm{Pl}} = 0.5$ and $k/\overline{M}_{\mathrm{Pl}} = 1.0$ respectively. The signal yields are calculated using $\sigma \times \mathcal{B}(G_{\mathrm{KK}} \to ZZ) = 20$ fb for both processes. The uncertainties combine statistical and systematic contributions.

$V \to qq$	Signal	G_{KK} (1 TeV)		Background estimates				Data
recon.	regions	$k/\overline{M}_{\mathrm{Pl}} = 0.5$	$k/\overline{M}_{\mathrm{Pl}} = 1.0$	Z+jets	Diboson	Top quarks	Total	
Merged	HP	18.2 ± 2.0	18.0 ± 2.0	1398 ± 29	144 ± 17	11.0 ± 1.1	1553 ± 30	1541
	LP	11.2 ± 1.1	11.4 ± 1.1	4800 ± 80	240 ± 80	34 ± 4	5070 ± 60	5031
Resolved	b-tagged	0.89 ± 0.1	0.98 ± 0.11	1770 ± 60	180 ± 60	950 ± 24	2890 ± 40	2917
	Untagged	2.6 ± 0.4	2.55 ± 0.33	47240 ± 270	1410 ± 160	960 ± 80	49620 ± 210	49605

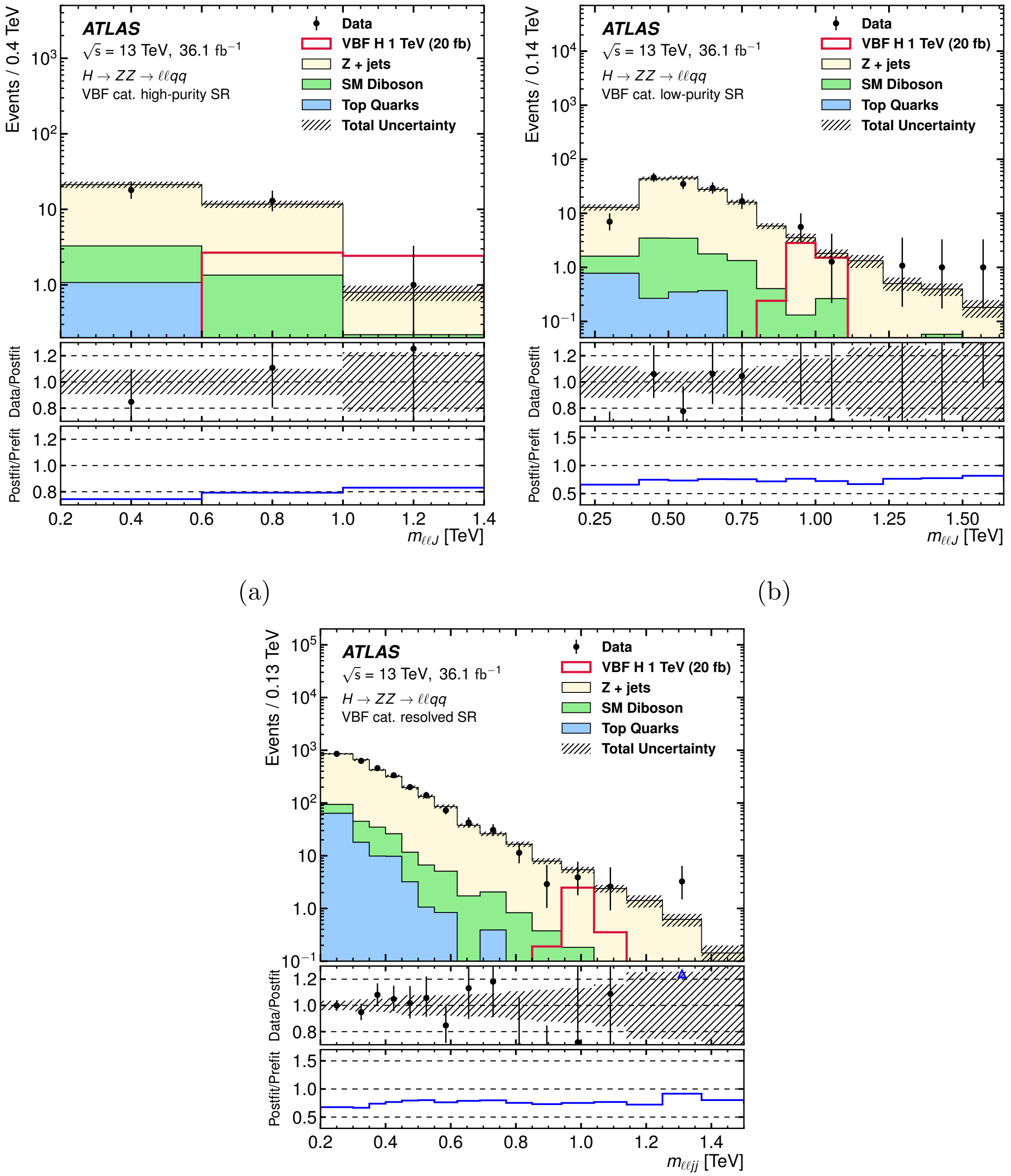

(a)

(b)

(c)

Figure 5.23: Comparisons of the observed data and expected background distributions of the final discriminants of the VBF category for the $H \rightarrow ZZ \rightarrow \ell\ell qq$ search: $m_{\ell\ell J}$ of (a) high-purity and (b) low-purity signal regions; (c) $m_{\ell\ell jj}$ of the resolved signal region [60]. For illustration, expected distributions from the VBF production of a 1 TeV Higgs boson with $\sigma \times \mathcal{B}(H \rightarrow ZZ) = 20$ fb are also shown. The middle panes show the ratios of the observed data to the background predictions. The uncertainty in the total background prediction, shown as bands, combines statistical and systematic contributions. The blue triangles in the middle panes indicate bins where the ratio is nonzero and outside the vertical range of the plot. The bottom panes show the ratios of the post-fit and pre-fit background predictions.

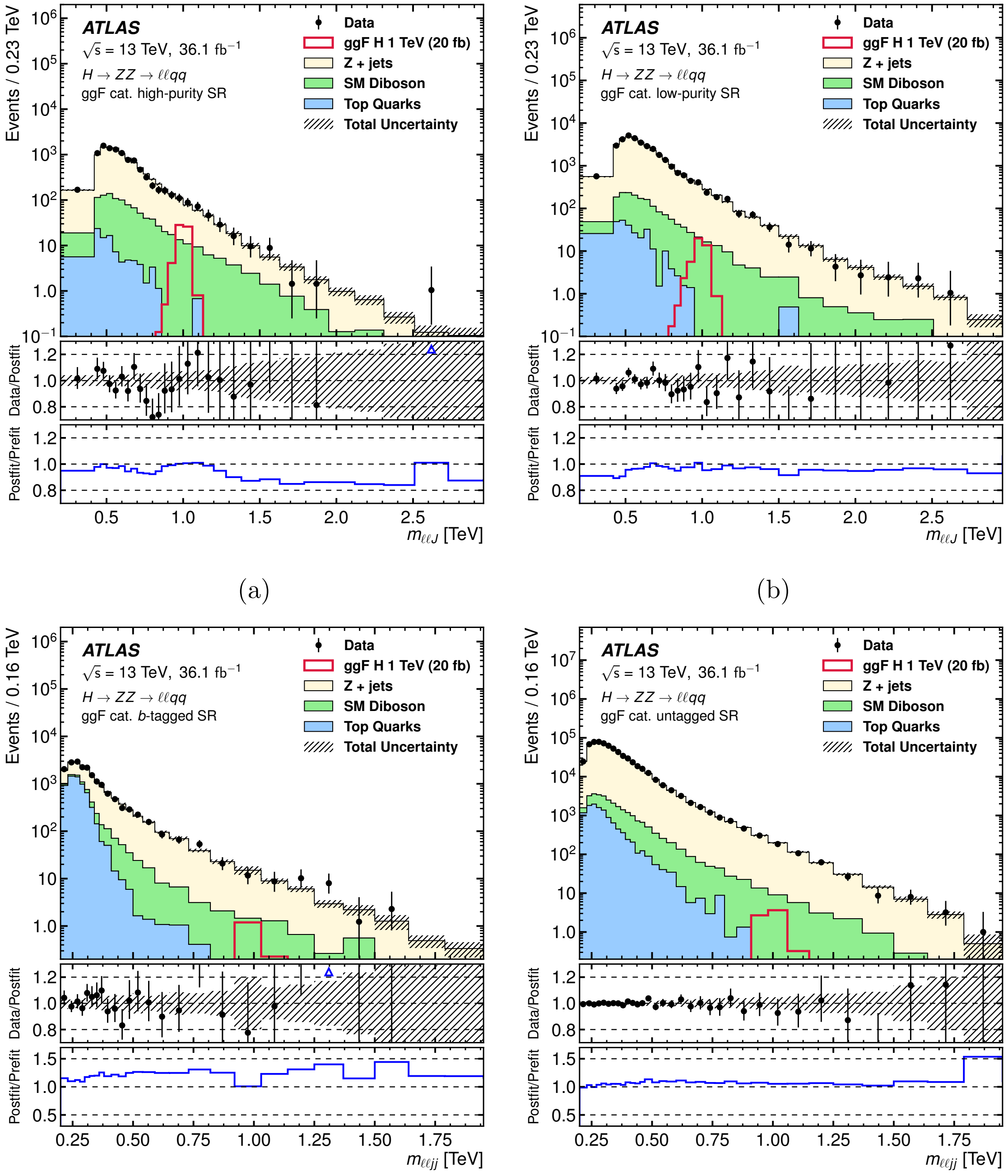

(a) (b)

(c) (d)

Figure 5.24: Comparisons of the observed data and expected background distributions of the final discriminants of the ggF category for the $H \rightarrow ZZ \rightarrow \ell\ell qq$ search: $m_{\ell\ell J}$ of (a) high-purity and (b) low-purity signal regions; $m_{\ell\ell jj}$ of (c) b-tagged and (d) untagged signal regions [60]. For illustration, expected distributions from the ggF production of a 1 TeV Higgs boson with $\sigma \times \mathcal{B}(H \rightarrow ZZ) = 20$ fb are also shown. The middle panes show the ratios of the observed data to the background predictions. The uncertainty in the total background prediction, shown as bands, combines statistical and systematic contributions. The blue triangles in the middle panes indicate bins where the ratio is nonzero and outside the vertical range of the plot. The bottom panes show the ratios of the post-fit and pre-fit background predictions.

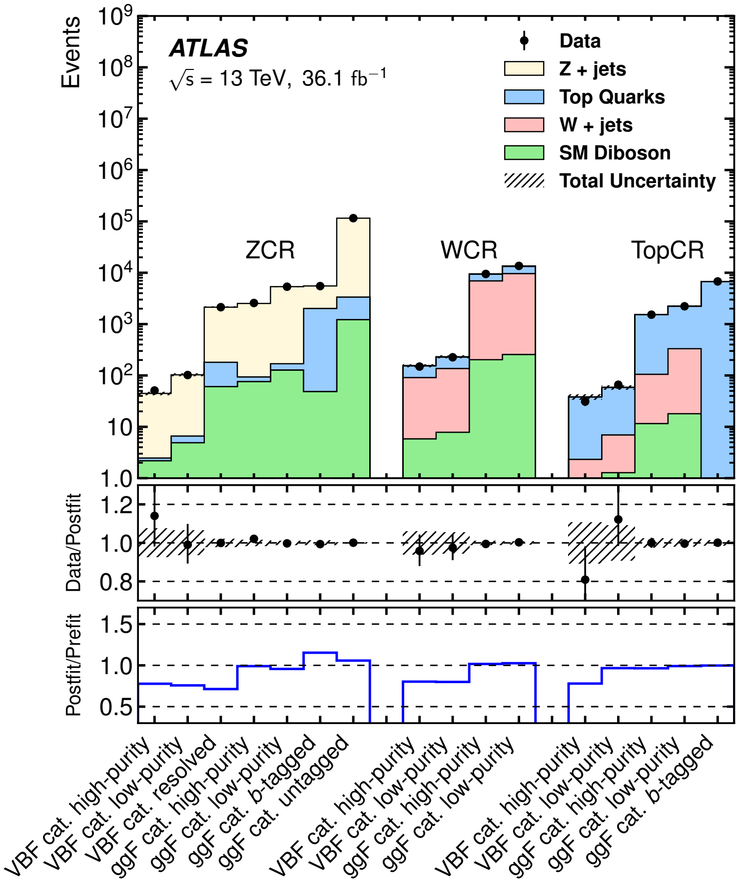

Figure 5.25: Comparisons of the observed data and expected background event yields in each control region [60]. The middle pane shows the ratios of the observed data to the post-fit background predictions. The uncertainty in the total background prediction, shown as bands, combines statistical and systematic contributions. The bottom pane shows the ratios of the post-fit and pre-fit background predictions.

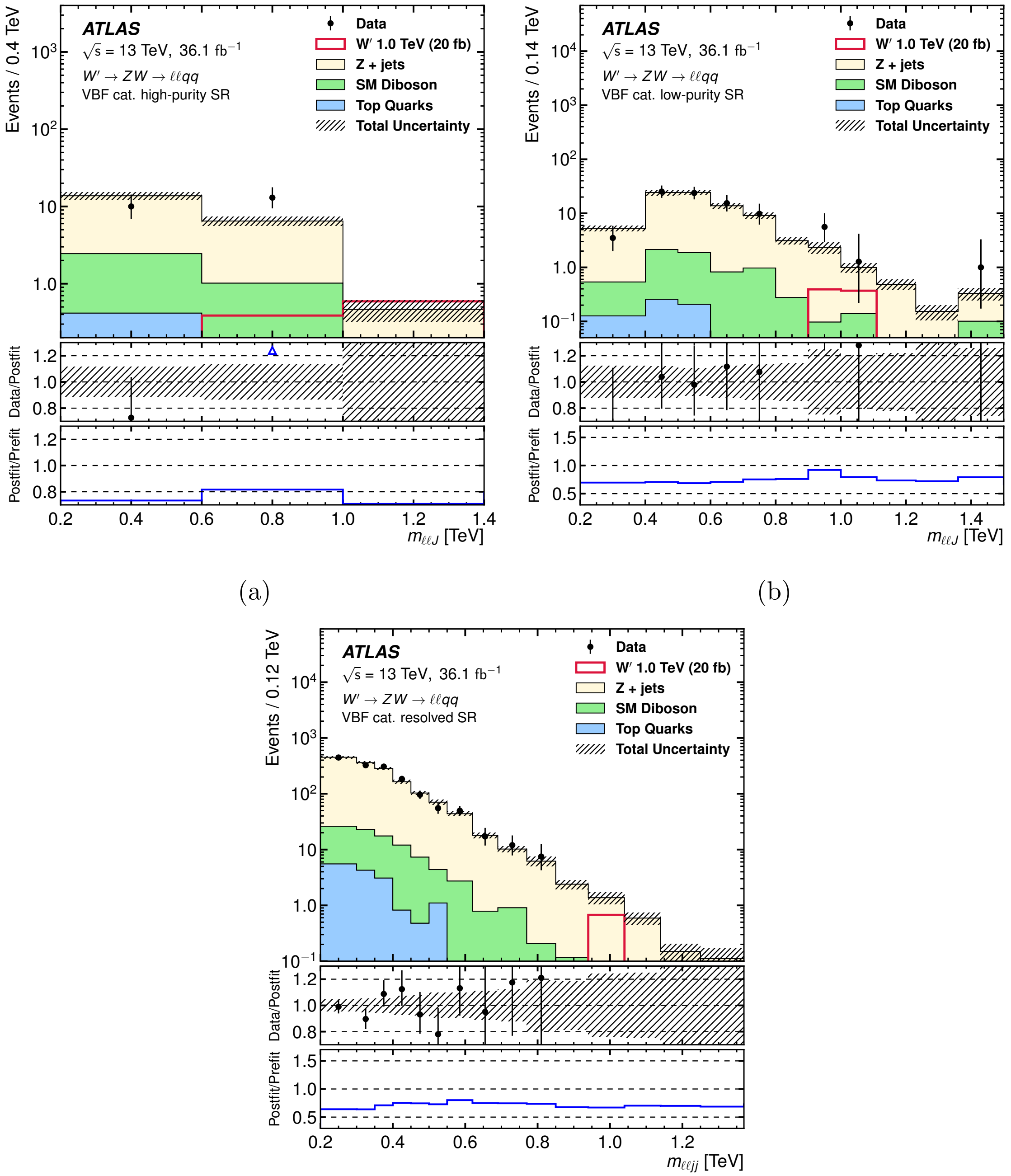

(a)

(b)

(c)

Figure 5.26: Comparisons of the observed data and expected background distributions of the final discriminants of the VBF category for the HVT $W' \to ZW \to \ell\ell qq$ search: $m_{\ell\ell J}$ of (a) high-purity and (b) low-purity signal regions; (c) $m_{\ell\ell jj}$ of the resolved signal region [60]. For illustration, expected distributions from the VBF production of a 1 TeV W' with $\sigma \times \mathcal{B}(W' \to ZW) = 20$ fb are also shown. The middle panes show the ratios of the observed data to the background predictions. The uncertainty in the total background prediction, shown as bands, combines statistical and systematic contributions. The blue triangles in the middle panes indicate bins where the ratio is nonzero and outside the vertical range of the plot. The bottom panes are the ratios of the post-fit and pre-fit background predictions.

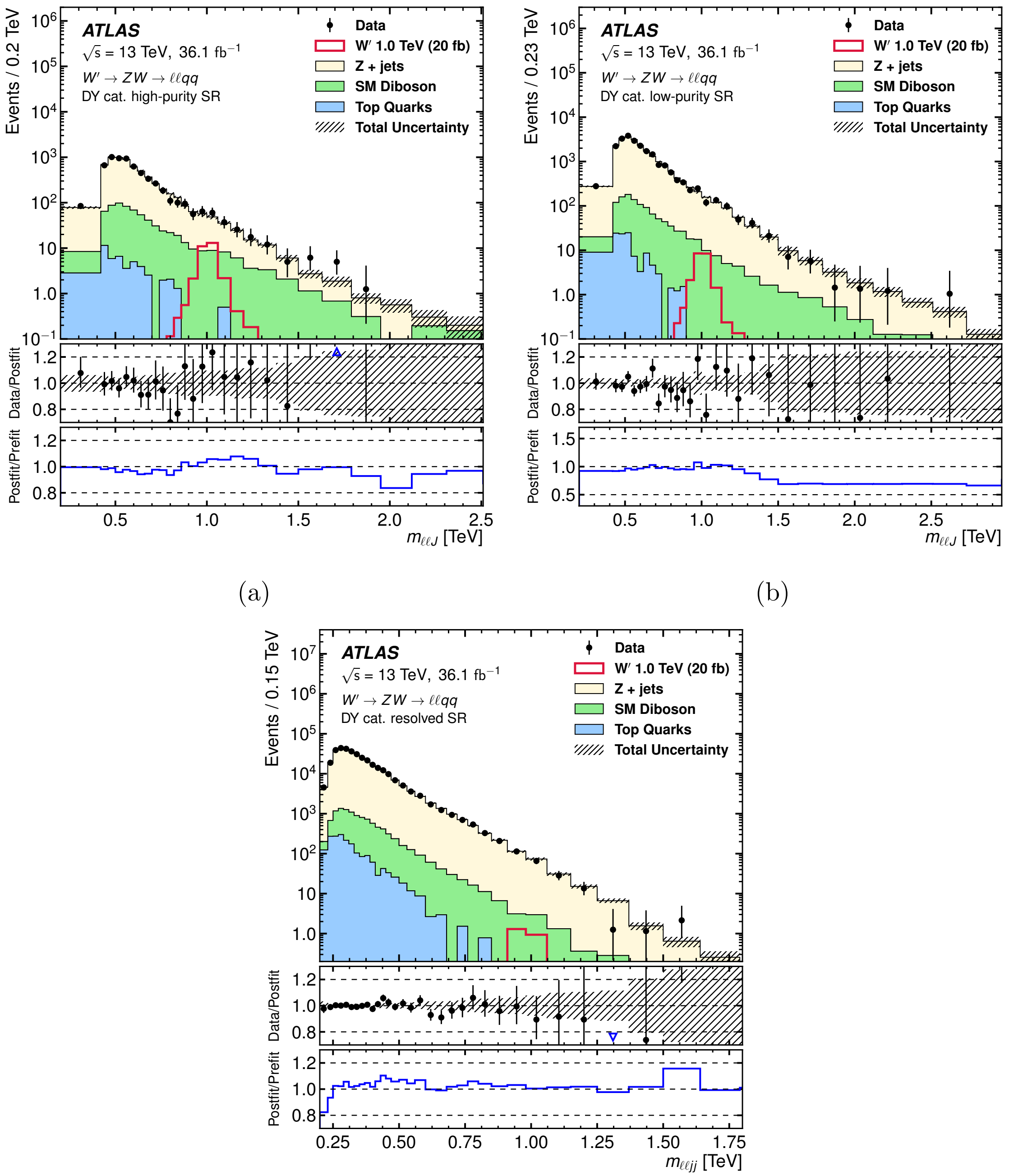

(a)

(b)

(c)

Figure 5.27: Comparisons of the observed data and expected background distributions of the final discriminants of the DY category for the HVT $W' \to ZW \to \ell\ell qq$ search: $m_{\ell\ell J}$ of (a) high-purity and (b) low-purity signal regions; $m_{\ell\ell jj}$ of (c) resolved signal region [60]. For illustration, expected distributions from the DY production of a 1 TeV W' with $\sigma \times \mathcal{B}(W' \to ZW) = 20$ fb are also shown. The middle panes show the ratios of the observed data to the background predictions. The uncertainty in the total background prediction, shown as bands, combines statistical and systematic contributions. The blue triangles in the middle panes indicate bins where the ratio is nonzero and outside the vertical range of the plot. The bottom panes are the ratios of the post-fit and pre-fit background predictions.

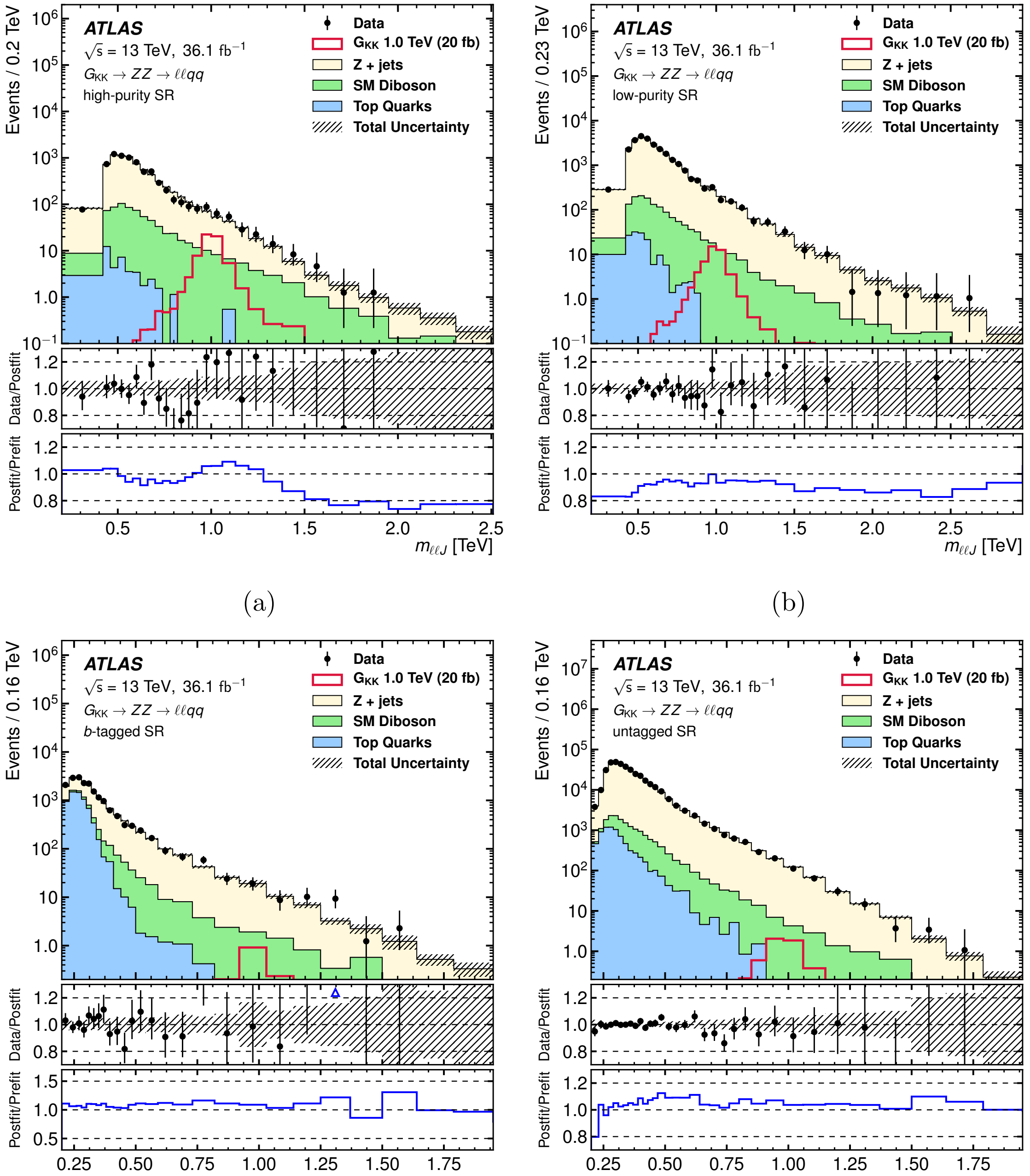

(a) (b)

(c) (d)

Figure 5.28: Comparisons of the observed data and expected background distributions of the final discriminants for the $G_{\mathrm{KK}} \to ZZ \to \ell\ell qq$ search: $m_{\ell\ell J}$ of (a) high-purity and (b) low-purity signal regions; $m_{\ell\ell jj}$ of (c) b-tagged and (d) untagged signal regions [60]. For illustration, expected distributions from a 1 TeV G_{KK} with $k/\overline{M}_{\mathrm{Pl}} = 1$ and $\sigma \times \mathcal{B}(G_{\mathrm{KK}} \to ZZ) = 20$ fb are also shown. The middle panes show the ratios of the observed data to the background predictions. The uncertainty in the total background prediction, shown as bands, combines statistical and systematic contributions. The blue triangles in the middle panes indicate bins where the ratio is nonzero and outside the vertical range of the plot. The bottom panes are the ratios of the post-fit and pre-fit background predictions.

5.6.2 Upper Limits on $\sigma \times \mathcal{B}(X \to ZV)$

With no significant excesses above the SM background prediciton observed, upper limits on the product of the cross section of the new resonances and their respective decay branching ratios, $\sigma \times \mathcal{B}(X \to ZV)$, are derived at 95% CL using the CL_s method described in Section 5.5. The limits for resonances with mass below 2 TeV are calcuated using the aysmptotic approximation. Above 2 TeV, the asymptotic assumption does not hold anymore due to small numbers of events (< 10) observed in the high mass tails. Therefore, pseudo-experiments are generated for the high mass region to sample the distributions of the test statistics in order to derive the upper limits.

The expected and observed limits are shown in Figure 5.29, for the gluon-gluon fusion and vector boson fusion productions of a heavy Higgs boson decaying to ZZ. The observed limit on $\sigma \times \mathcal{B}(H \to ZZ)$ varies from 1.7 (0.42) pb at 300 GeV to 1.4 (1.1) fb at 3 TeV for the ggF (VBF) production mode.

The limits on $\sigma \times \mathcal{B}(W' \to ZW)$ are shown in Figure 5.30, for both DY and VBF production modes. The observed limit ranges from 5.7 pb at 300 GeV to 1.3 fb at 5 TeV for DY production and from 0.98 pb at 300 GeV to 2.8 fb at 4 TeV for VBF production. For DY production, theoretical predictions of $\sigma \times \mathcal{B}(W' \to ZW)$ for Model A and Model B are shown. The DY production of the HVT W' is excluded up to a mass of 2.9 (3.2) TeV for model A (B). Theory curve of the HVT VBF model is overlaid as well. However, the observed limit is well above the theoretical prediction and therefore has no exclusion power with the current dataset.

For the $G_{\mathrm{KK}} \to ZZ$ search, limits are presented for $k/\overline{M}_{\mathrm{Pl}} = 1$ and $k/\overline{M}_{\mathrm{Pl}} = 0.5$ in Figure 5.31. The observed limit varies from 3.3 pb at 300 GeV to 0.74 fb at 5 TeV for $k/\overline{M}_{\mathrm{Pl}} = 1$. The G_{KK} resonance is excluded up to 1.0 TeV in the $k/\overline{M}_{\mathrm{Pl}} = 0.5$ scenario and 1.3 for $k/\overline{M}_{\mathrm{Pl}} = 1.0$.

5.6.3 Effects of Systematic Uncertainties

The effects of systematic uncertainties are estimated on the strength parameter (μ), as a proxy for studying the impact of systematic uncertainties on the search sensitivity. These effects are studied by decomposing the relative uncertainties on the best-fit value of the strength parameter. Signals from ggF production of $H \to ZZ$ with $m(H) = 600\,\mathrm{GeV}$ and $1.2\,\mathrm{TeV}$ are used and the value of the strength parameter is set to be that from the corresponding expected upper limit. Pseudo-data, including both background processes and the expected signal process, are generated with MC

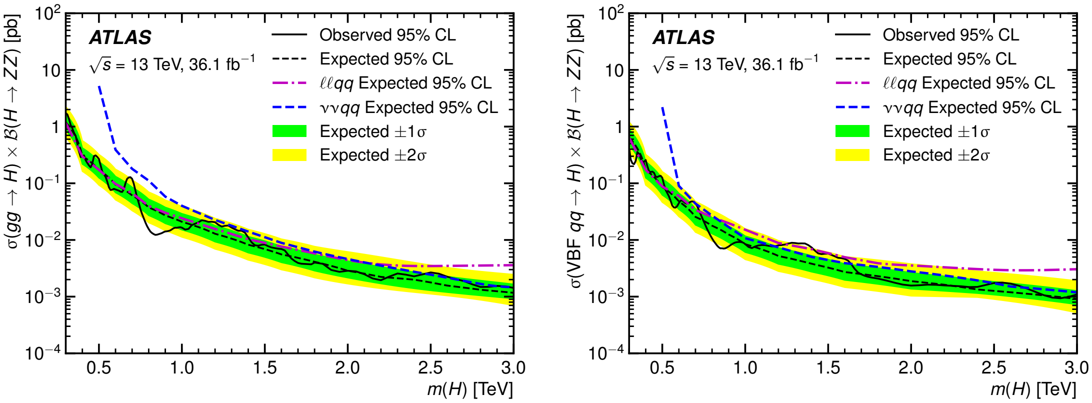

(a) (b)

Figure 5.29: Observed (black solid curve) and expected (black dashed curve) 95% CL upper limits on $\sigma \times \mathcal{B}(H \to ZZ)$ at $\sqrt{s} = 13$ TeV for the (a) ggF and (b) VBF production of a heavy Higgs boson as a function of its mass, combining $\ell\ell qq$ and $\nu\nu qq$ searches [60]. Limits expected from individual searches (dashed curves in blue and magenta) are also shown for comparison. Limits are calculated in the asymptotic approximation below 2 TeV and are obtained from pseudo-experiments above that. The green (inner) and yellow (outer) bands represent the $\pm 1\sigma$ and $\pm 2\sigma$ uncertainty in the expected limits.

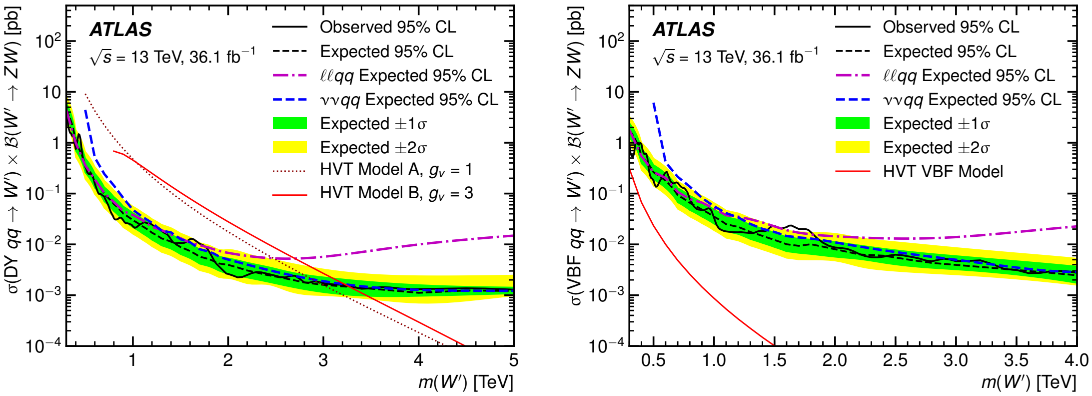

(a) (b)

Figure 5.30: Observed (black solid curve) and expected (black dashed curve) 95% CL upper limits on $\sigma \times \mathcal{B}(W' \to ZW)$ at $\sqrt{s} = 13$ TeV for the (a) DY and (b) VBF production of a W' boson in the HVT model as a function of its mass, combining $\ell\ell qq$ and $\nu\nu qq$ searches [60]. Limits expected from individual searches (dashed curves in blue and magenta) are also shown for comparison. Limits are calculated in the asymptotic approximation below 2 TeV and are obtained from pseudo-experiments above that. Theoretical predictions are overlaid in (a) for HVT *Model A* and *Model B* and in (b) for HVT *VBF Model*. The green (inner) and yellow (outer) bands represent the $\pm 1\sigma$ and $\pm 2\sigma$ uncertainty in the expected limits.

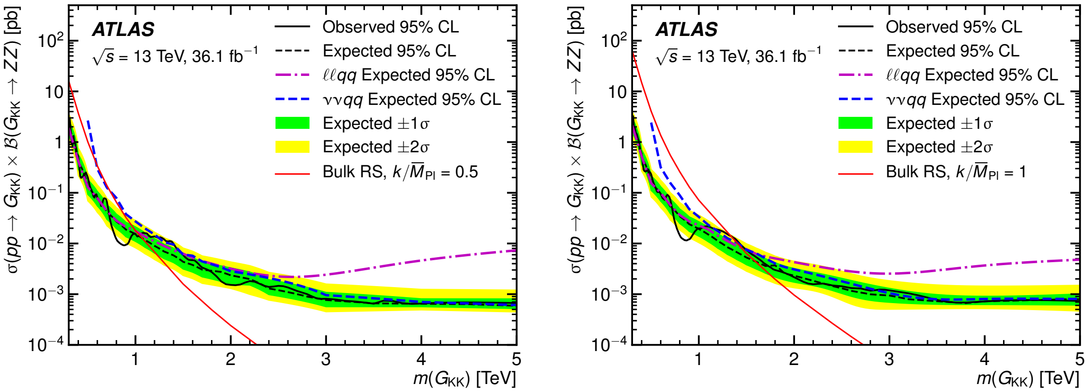

(a) (b)

Figure 5.31: Observed (black solid curve) and expected (black dashed curve) 95% CL upper limits on $\sigma \times \mathcal{B}(G_{\rm KK} \to ZZ)$ at $\sqrt{s} = 13$ TeV for the production of a $G_{\rm KK}$ in the bulk RS model with couplings of (a) $k/\overline{M}_{\rm Pl} = 0.5$ and (b) $k/\overline{M}_{\rm Pl} = 1.0$ as a function of the graviton mass, combining $\ell\ell qq$ and $\nu\nu qq$ searches [60]. Limits expected from individual searches (dashed curves in blue and magenta) are also shown for comparison. Limits are calculated in the asymptotic approximation below 2 TeV and are obtained from pseudo-experiments above that. The theoretical predictions for $\sigma \times \mathcal{B}(G_{\rm KK} \to ZZ)$ as a function of resonance mass for a bulk RS graviton are also shown. The green (inner) and yellow (outer) bands represent the $\pm 1\sigma$ and $\pm 2\sigma$ uncertainty in the expected limits.

samples normalized to 36.1 fb^{-1}. The leading sources of systematic uncertainty and their respective effects on the strength parameter are summarized in Table 5.14. The search is largely limited by the amount of data collected, as reflected in the impact of pseudo-data statistics. The total effect of the systematic uncertainties is comparable at low mass, but has a less significant role as mass increases. Among all the sources of uncertainties, the MC sample size and experimental systematic uncertainties associated with jets and $E_{\rm T}^{\rm miss}$ are the dominant ones at $m(H) = 600\,{\rm GeV}$. At $m(H) = 1200\,{\rm GeV}$, uncertainties on the modeling of various background processes become more influential.

Table 5.14: The relative uncertainties from the leading uncertainty sources in the best-fit signal-strength parameter μ of hypothesized signal production of ggF $H \rightarrow ZZ$ with $m(H) = 600$ GeV and $m(H) = 1.2$ TeV [60]. For this study, the $H \rightarrow ZZ$ production cross section is assumed to be 95 fb at 600 GeV and 13 fb at 1.2 TeV, corresponding to approximately the expected median upper limits at these two mass values.

$m(H) = 600$ GeV		$m(H) = 1.2$ TeV	
Uncertainty source	$\Delta\mu/\mu$ [%]	Uncertainty source	$\Delta\mu/\mu$ [%]
Pseudo-data statistics	36	Pseudo-data statistics	41
Total systematics	33	Total systematics	29
MC statistics	20	Large-R jet	20
Large-R jet	16	Background modeling	13
$E_{\mathrm{T}}^{\mathrm{miss}}$ uncertainties	13	MC statistics	13
Small-R jet	11	Luminosity	6.5
Background modeling	9.6	Small-R jet	5.9
Luminosity	9.1	Leptons	3.9

CHAPTER 6

Search for ZH Resonances

6.1 Analysis Overview and Strategy

Although the Higgs boson recently discovered at the LHC bears great resemblance to the Higgs boson predicted by the Standard Model, other theories, such as models with an extended scalar sector, could still accommodate this SM-like particle by conforming to the so-called SM alignment limit. In principle there can be many Higgs doublets instead of just one, and one of the simplest extensions of the SM is a two-Higgs-doublet model (2HDM) as mentioned in Chapter 2. The 2HDM contains one CP-odd Higgs boson, A, two CP-even ones, h and H with $m_h < m_{\mathrm{H}}$, and two charged scalars, $H^{\pm}$. By staying near the SM alignment limit $\cos(\beta - \alpha) = 0$, the lighter CP-even Higgs boson, h, has couplings like the SM Higgs boson.

The addition of the second Higgs doublet leads to a richer phenomenology and many analyses searching for the heavy neutral Higgs bosons of the 2HDM have been carried out at the LHC. However, the heavy Higgs bosons, A and H, are typically assumed to be degenerate in mass, i.e. $m_{\mathrm{A}} = m_{\mathrm{H}}$, in these searches. The mass degeneracy requirement is relaxed in this analysis, as motivated by electroweak baryogenesis in the context of 2HDM. The decay $A \to ZH$ with a mass splitting $m_{\mathrm{A}} - m_{\mathrm{H}} \gtrsim v$ is greatly correlated with a strongly first order electroweak phase transition (EWPT) in 2HDMs (as needed for Electroweak Baryogenesis), due to the large amount of parameter space available as shown in Figure 2.6. Since the coupling $g_{AZH} \sim \sin(\beta - \alpha)$ is unsuppressed at the alignment limit, the decay $A \to ZH$ is strongly favored in the majority of the 2HDM parameter space considered in this analysis. Gluon-gluon fusion and b-associated production are the two main production modes of the A boson in the relevant 2HDM parameter space. Feynman diagrams of the signal production via these two mechanisms are shown in Figure 6.1.

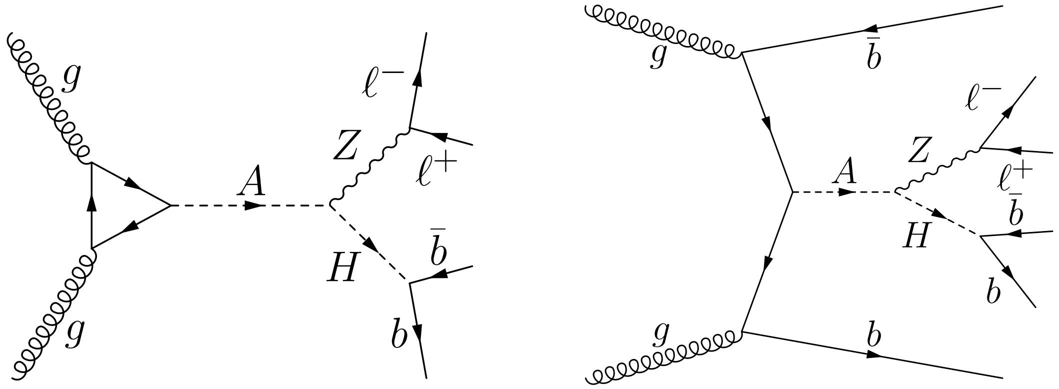

(a) (b)

Figure 6.1: Feynman diagrams for the production of the A boson (a) via gluon-gluon fusion and (b) in association with b-quarks (b-associated production) [109].

This analysis searches for the decay $A \to ZH$ in the mass range $m_\mathrm{A} \leq 800\,\mathrm{GeV}$ [109]. The subsequent decays of $Z \to \ell\ell$, where $\ell = e, \mu$, and $H \to bb$ are considered to exploit the clean leptonic decay of the Z boson and the large branching of $H \to bb$ in the relevant parameter space. The $\ell\ell bb$ final state allows a full reconstruction of the A boson's decay kinematics. Unlike the $X \to ZV \to \ell\ell qq$ analysis, the two-dimensional parameter space $(m_\mathrm{A}, m_\mathrm{H})$ probed by this analysis complicates the design of the analysis strategy as well as the interpretation of the final results. Instead of investigating the vast parameter space in both dimensions at the same time, the analysis is carried out strategically as shown in Figure 6.2.

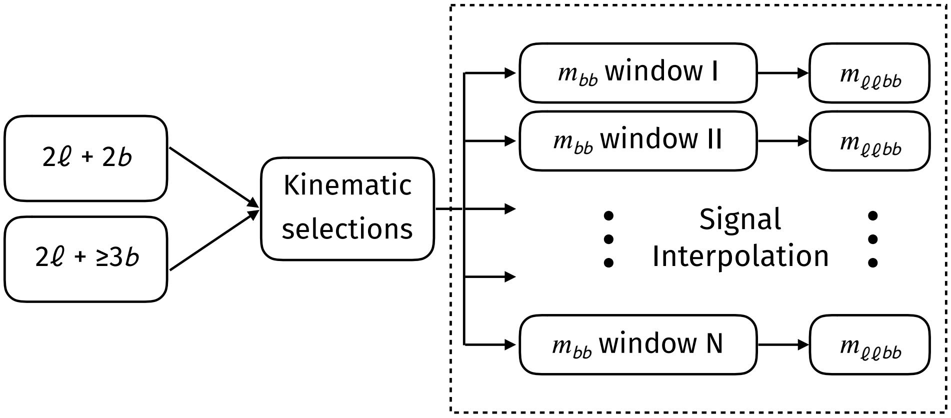

Figure 6.2: A conceptual design of the $A \to ZH \to \ell\ell bb$ analysis strategy.

Firstly, two event categories are arranged to account for both gluon-gluon fusion and b-associated production mechanisms. Both categories have dilepton in common in the events, but differ in the number of b-quarks, which are identified as b-tagged jets at the reconstruction level. Subsequent to the selection of the event kinematics specific to each category, the events are considered for one of the m_{bb} windows as denoted by, e.g. "m_{bb} window I". A m_{bb} window assumes a specific H hypothesis, for which the mass of the H boson is known and fixed. After selecting the events satisfying the m_{bb} selection criterion and therefore consistent with the m_{H} hypothesis, the analysis proceeds with scanning the invariant mass spectrum of the A boson, $m_{\ell\ell bb}$. This routine is performed independently for every m_{H} hypothesis considered. The m_{bb} windows for any two adjacent m_{H} hypotheses could overlap with each other, but this does not raise concerns for double counting due to that the result is interpreted separately for each m_{H} hypothesis. The large amount of parameter space in the m_{A}-m_{H} plane and the good mass resolution of the detector (Section 6.3.1) lead to a proliferation of signal hypotheses to be tested. Signal interpolation techniques (Section 6.4) are employed to accurately construct the intermediate signal points within the range of a discrete set of MC simulations generated. Narrow-width A bosons, as well as those with large-widths as prescribed by some explicit 2HDMs, are taken into account in the analysis.

Signal events produced via gluon-gluon fusion are generated by MadGraph5_aMC @NLO 2.3.3 [84, 110] at leading order, and subsequently interfacing with Pythia 8.210 [85] with the A14 tune [86] for parton showering. For A bosons produced in association with b-quarks, MadGraph5_aMC@NLO 2.1.2 [84, 111, 112] is used following Ref. [113], together with Pythia 8.2.12 with the A14 tune. The NNPDF2.3LO [26] (CT10nlo_nf4 [69]) set of parton distribution functions is used for gluon-gluon fusion production (b-associated production). The narrow-width samples are generated with the following settings: $\Gamma_A = 1\,\mathrm{MeV}$, m_{A} in the range of 230–800 GeV, $\Gamma_H = 1\,\mathrm{MeV}$, and m_{H} in the range of 130–700 GeV. Samples with widths up to 20% of m_{A} are also produced using the same generators. The width of the H boson is fixed at 1 MeV for these large-width samples, which is approximately valid for $\Gamma_A/\Gamma_H \gg 1$.

The major background contributions after the event selection and categorization are from Z+jets and top-quark productions. Other background processes, including diboson, single top, the SM Higgs boson production in association with a Z boson, and the top-quark-pair production in association with a vector boson, are also considered. Contributions from these minor background processes are typically 5% of the total background. For all the relevant background processes, Monte Carlo simulations are used to predict their respective contributions in the final analysis regions. The SM Zh production is simulated with Powheg-Box v2 and the NNPDF3.0NLO PDF set, and the parton shower is subsequently performed with Pythia 8.186 using the AZNLO tune. For the production of top-quark pairs in association with a vector boson, MadGraph5_aMC@NLO 2.3.3, the NNPDF3.0NLO PDF set, and Pythia 8.186 with the A14 tune are used. The generation of the other samples has been described in details in Section 5.1. Diboson samples are normalized to cross sections with NNLO corrections [114–117]. Single-top-quark samples and samples for top-quark-pair in association with a vector boson are normalized to NLO cross sections based on Refs. [118–120] and Ref. [84], respectively. The normalization of the SM Zh production follows the recommendation from Ref. [113] with NNLO QCD and NLO electroweak corrections.

Similar to the $X \to ZV \to \ell\ell qq$ analysis, jets from the Z+jets MC are labeled as b-, c-, or light-jets based on the matching hadrons (Section 5.1.2). The simulated Z+jets events are then labeled as "$Z + (bb, bc, bl, cc)$" if a b-jet or two c-jets are found in the events, and as "$Z + (cl, l)$" if otherwise. The $Z + (cl, l)$ background becomes insignificant after the requirement of two b-tagged jets (Section 4.3.1) and is therefore normalized based on the MC prediction. The normalizations of $Z + (bb, bc, bl, cc)$ and $t\bar{t}$, which are the two major background contributions, are determined by the signal region and their respective control regions in each category.

The dataset used in this analysis is identical to the one described in Section 5.1.3.

6.2 Object Selection

The object selection criteria for the $A \to ZH \to \ell\ell bb$ analysis are largely the same as those for the $X \to ZV \to \ell\ell qq$ analysis described in Section 5.2. However, large-R jets are not used in the $A \to ZH \to \ell\ell bb$ analysis and the transverse momentum thresholds for leptons and jets differ from those used in the $X \to ZV \to \ell\ell qq$ analysis. The p_{T} of the leading leptons must satisfy $p_{\mathrm{T}} > 27\,\mathrm{GeV}$ and the small-R jets are required to have $p_{\mathrm{T}} > 20\,\mathrm{GeV}$ in the central region. A summary of the object selections used in this analysis is presented in Table 6.1 with details of the common selection criteria provided in Section 5.2 of the $X \to ZV \to \ell\ell qq$ analysis.

Table 6.1: A summary of the criteria for object selections used in the $A \to ZH \to \ell\ell bb$ analysis.

Object	Kinematics	Quality	Additional
Electrons	p_T >7 GeV $\lvert\eta\rvert < 2.47$	LooseLH $\lvert d_0/\sigma(d_0)\rvert$ <5 $\lvert z_0 \sin\theta\rvert < 0.5\,\mathrm{mm}$ LooseTrackOnly	B-layer (IBL) hit requirement
Muons	p_T >7 GeV $\lvert\eta\rvert < 2.5$	Loose quality $\lvert d_0/\sigma(d_0)\rvert$ <3 $\lvert z_0 \sin\theta\rvert < 0.5\,\mathrm{mm}$ LooseTrackOnly	
Small-R jets	$p_T > 20$ (30) GeV if $\lvert\eta\rvert < 2.5$ ($2.5 < \lvert\eta\rvert < 4.5$)	anti-k_t R =0.4	jet-vertex-tagger if p_{T} <60 GeV, $\lvert\eta\rvert < 2.4$

6.3 Event Selection and Categorization

The event selection of the $A \to ZH \to \ell\ell bb$ analysis consists of trigger requirements, event pre-selection, and selection criteria for reducing the background contamination.

Single-electron and single-muon triggers are firstly used to filter the events, as described in Section 5.3.1 of the $X \to ZV \to \ell\ell qq$ analysis. Event pre-selection follows by firstly subjecting the events to the event cleaning procedure defined in Section 5.3.2. The rest of the pre-selection steps proceed as follows:

- Lepton selection. Exactly two leptons satisfying the criteria described in Section 6.2 are required. The transverse momentum of the leading lepton must exceed 27 GeV.
- Trigger decision and matching as defined in Section 5.3.2.
- Dilepton requirements:
  - $Z \to \ell\ell$ candidates must satisfy $80 < m(\ell\ell) < 100$ GeV, to be compatible with the mass of the Z boson. In di-muon events, the two muons must carry opposite electric charges. No such requirement is applied to events with two electrons due to the same argument presented in Section 5.3.2.
  - Dilepton selection in the top control region requires exactly one electron and one muon with the dilepton mass satisfying $80 < m(e\mu) < 100$ GeV. The different flavor requirement ensures that the top control region is orthogonal to the signal regions.
- Jet selection. An event is required to contain at least two b-tagged jets in the central region $|\eta| < 2.5$. All the jets must satisfy the object selection criteria detailed in Section 6.2. Additionally, the leading b-tagged jet must have $p_{\mathrm{T}} > 45$ GeV.

The $H \to bb$ decay is then reconstructed using the two highest-p_{T} b-tagged jets. The top-quark background has considerable contribution in events with b-tagged jets (Section 5.3.4). A requirement of $E_{\mathrm{T}}^{\mathrm{miss}}/\sqrt{H_{\mathrm{T}}} < 3.5\sqrt{\mathrm{GeV}}$ is imposed to suppress the top background, where H_{T} denotes the scalar sum of the p_{T} of all the leptons and jets in the event. The signal and Z+jets background, which do not contain intrinsic missing transverse energy, are less affected by this requirement. An additional kinematic requirement of $\sqrt{\sum p_{\mathrm{T}}^2}/m_{\ell\ell bb} > 0.4$ is also applied, where the summation

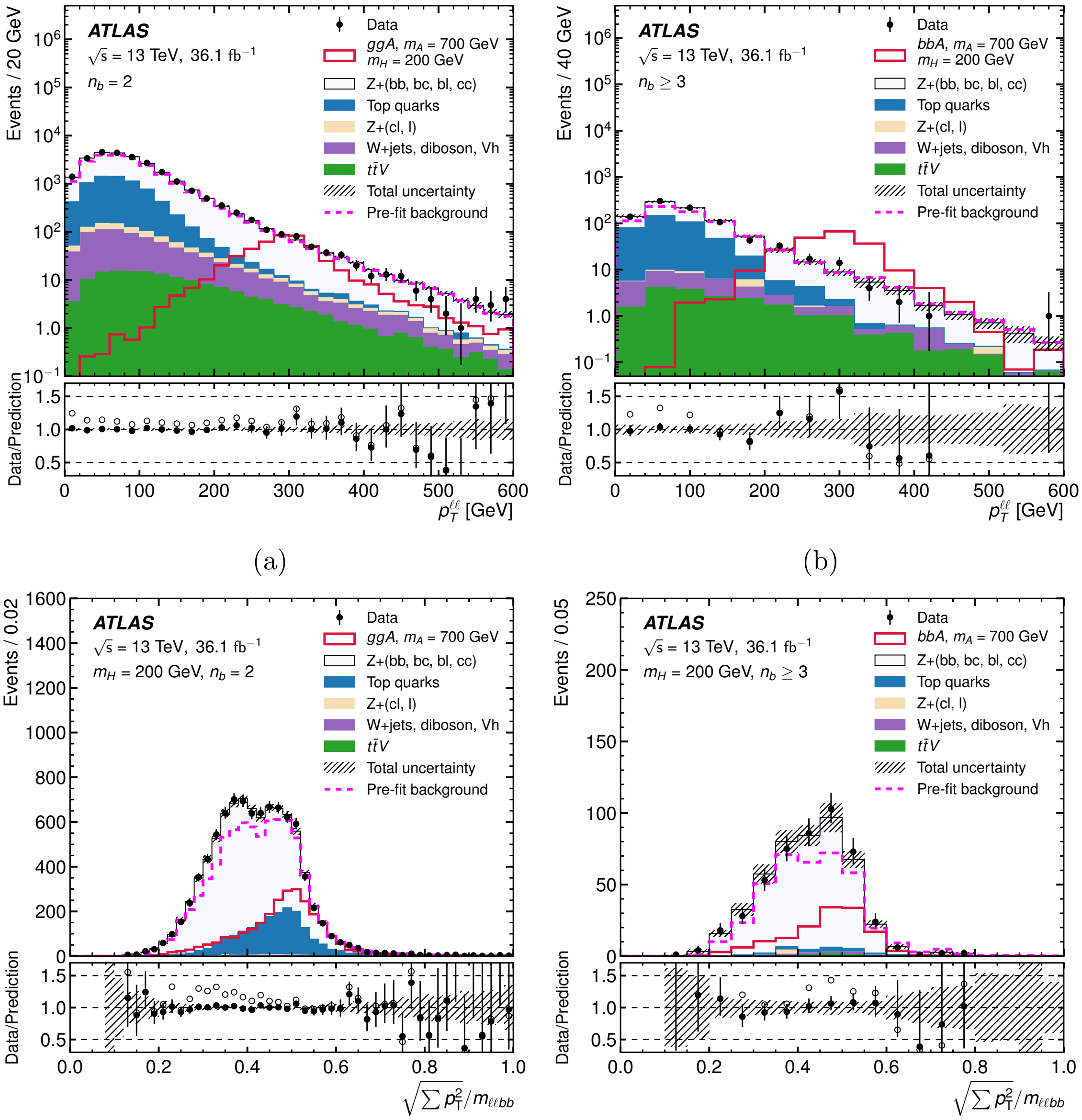

(a) (b) (c) (d)

Figure 6.3: The $p_{\mathrm{T}}^{\ell\ell}$ distribution without any m_{bb} window requirement for the (a) $n_b = 2$ category and (b) the $n_b \geq 3$ category, and the $\sqrt{\sum p_{\mathrm{T}}^2}/m_{\ell\ell bb}$ distribution after relevant m_{bb} window selections for the (c) $n_b = 2$ category and the $n_b \geq 3$ category [109]. The solid dots in the lower panels represent the ratio of the data to the background prediction obtained from the MLE, while the open circles correspond to the ratio of data to the background prediction without any fit performed. The signal distributions are normalized to $\sigma \times \mathcal{B}(A \to ZH) \times \mathcal{B}(H \to bb) = 1\,\mathrm{pb}$ in (a) and (b). In (c) and (d) the signal normalization is scaled up to one third of the total background normalization in order to show the shape difference from background in the linear scale.

runs over the transverse momenta of the individual leptons and b-tagged jets used to reconstruct the invariant mass ($m_{\ell\ell bb}$) of the A boson. This selection criterion turns out to be an effective discriminating variable to reduce the Z+jets background. Distributions of the transverse momentum of the Z boson and the $\sqrt{\sum p_{\mathrm{T}}^2}/m_{\ell\ell bb}$ variable are shown in Figure 6.3.

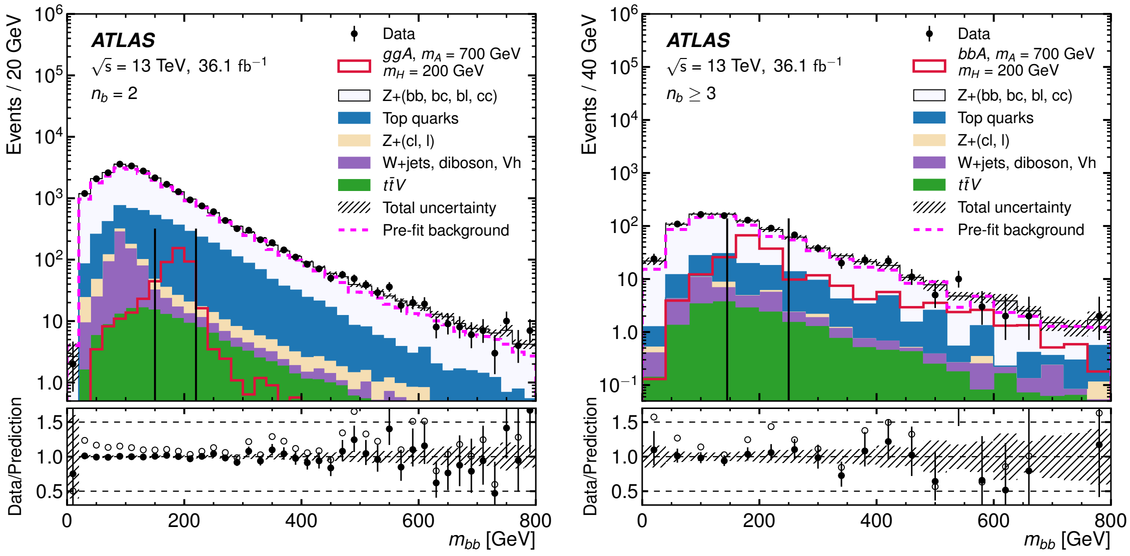

(a) (b)

Figure 6.4: The m_{bb} distributions before any m_{bb} window selection are shown in (a) and (b) for the $n_b = 2$ and the $n_b \geq 3$ categories, respectively [109]. The gluon-gluon fusion signal with $(m_{\mathrm{A}}, m_{\mathrm{H}}) = (700, 200)$ GeV is shown in (a), whereas b-associated production at the same $(m_{\mathrm{A}}, m_{\mathrm{H}})$ point is shown in (b). In both cases, the signal is normalized to $\sigma \times \mathcal{B}(A \to ZH) \times \mathcal{B}(H \to bb) = 1$ pb. The solid dots in the lower panels represent the ratio of the data to the background prediction obtained from the MLE, while the open circles correspond to the ratio of data to the background prediction without any fit performed. The m_{bb} window criterion is also shown as vertical solid lines for the corresponding m_{H} hypothesis.

The events are subsequently classified into two categories based on the number of b-tagged jets. An event is assigned to the $n_b = 2$ category if it contains exactly two b-tagged jets, and the $n_b \geq 3$ category if more than two b-tagged jets are present. Following the event categorization, selection on the the invariant mass of the two leading b-tagged jets, m_{bb}, is applied to be consistent with the assumed H boson mass. $0.85 \cdot m_{\mathrm{H}} - 20\,\mathrm{GeV} < m_{bb} < m_{\mathrm{H}} + 20\,\mathrm{GeV}$ is required for the $n_b = 2$ category, and $0.85 \cdot m_{\mathrm{H}} - 25\,\mathrm{GeV} < m_{bb} < m_{\mathrm{H}} + 50\,\mathrm{GeV}$ for the $n_b \geq 3$ category. The enlarged m_{bb} window for the $n_b \geq 3$ category is to account for a slightly degraded resolution of the di-jet invariant mass. Since there are at least three b-tagged jets in the $n_b \geq 3$

Table 6.2: Summary of the $A \to ZH \to \ell\ell bb$ event selection for the $n_b = 2$ and $n_b \geq 3$ categories. Definition: $\sqrt{\sum p_{\mathrm{T}}^2}/m_{\ell\ell bb} \equiv \left(\sum_i p_{T,i}^2\right)^{1/2}/m_{\ell\ell bb}$, where i runs over the leptons and the two leading b-tagged jets in p_T. m_{bb} sidebands correspond to $[0, 0.85 \cdot m_{\mathrm{H}} - 20) \cup (m_{\mathrm{H}} + 20, \infty)$ for the $n_b = 2$ category, and $[0, 0.85 \cdot m_{\mathrm{H}} - 25) \cup (m_{\mathrm{H}} + 50, \infty)$ for the $n_b \geq 3$ category.

Event selection	$n_b = 2$ category	$n_b \geq 3$ category
Triggers	Un-prescaled single-lepton triggers	
Leptons	exactly 2 leptons, p_{T}(leading lepton) $> 27\,\mathrm{GeV}$	
SR and ZCR	ee or $\mu\mu$ pair	
Top CR	$e\mu$ pair	
Jets	n(b-tagged jets) $= 2$	n(b-tagged jets) ≥ 3
	p_{T}(leading jet) > 45 GeV	
$Z \to \ell\ell$	$80 < m(\ell\ell) < 100$ GeV If two muons, they must carry opposite charges.	
Topological criteria	$E_{\mathrm{T}}^{\mathrm{miss}}/\sqrt{H_{\mathrm{T}}} < 3.5\sqrt{\mathrm{GeV}}$, $\sqrt{\sum p_{\mathrm{T}}^2}/m_{\ell\ell bb} > 0.4$	
m_{bb} window [GeV]		
SR and Top CR	$[0.85 \cdot m_{\mathrm{H}} - 20, m_{\mathrm{H}} + 20]$	$[0.85 \cdot m_{\mathrm{H}} - 25, m_{\mathrm{H}} + 50]$
ZCR	m_{bb} sidebands	m_{bb} sidebands

category, potential mis-assignment of b-tagged jets could occur by simply choosing the leading two jets to reconstruct the $H \to bb$ decay. This combinatorial background leads to the m_{bb} resolution degradation. The top control region adopts the same m_{bb} window definition as the signal region, whereas the Z+jets control region inverts the m_{bb} window criterion defined for each specific H boson mass hypothesis. The di-jet invariant mass distributions are shown in Figure 6.4 for the $n_b = 2$ and $n_b \geq 3$ categories. A summary of the event selection criteria is listed in Table 6.2.

For gluon-gluon fusion production, 94%–97% of the expected signal events passing the event selection fall into the $n_b = 2$ category. However, for b-associated production, which has two additional b-quarks in the final state, only 27%–36% of the expected signal events fall into the $n_b \geq 3$ category. The remaining events are classified into the $n_b = 2$ category due to the relatively soft p_{T} spectrum of the associated b-jets and the efficiency of the b-tagging being approximately 70%.

6.3.1 Signal Resolution and Acceptance

For each m_{H} hypothesis, the $m_{\ell\ell bb}$ distribution will be used to extract the signal after the corresponding m_{bb} requirement. A better signal resolution will lead to a greater discriminating power to distinguish signal from background. One of the advantages of the $\ell\ell bb$ final state is that the decay kinematics of the A boson can be fully reconstructed. By assuming a specific m_{H} hypothesis in each signal region, the $m_{\ell\ell bb}$ resolution of the signal can be improved by scaling the components of the four-momentum of the bb and $\ell\ell$ systems to the assumed H boson mass and the Z boson mass, respectively. A similar procedure is also applied in the $X \to ZV \to \ell\ell qq$ analysis (Section 5.3.6). As a result, the $m_{\ell\ell bb}$ resolution can be improved by a factor of two without distorting the background distributions. The consequent resolution of the reconstructed A boson mass ranges from 0.3% to 4% as shown in Figure 6.11-6.13. Figure 6.5 demonstrates the improvement in the $m_{\ell\ell bb}$ resolution after applying the mass constraints.

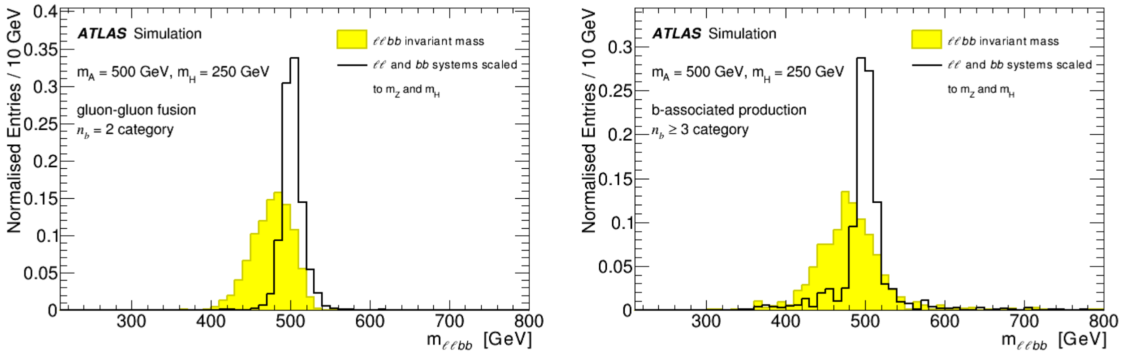

(a) (b)

Figure 6.5: The simulated $m_{\ell\ell bb}$ distributions obtained from directly using the mass of the $\ell\ell bb$ system (filled histogram) and after scaling the $\ell\ell$ and bb systems by $m_{\mathrm{Z}}/m_{\ell\ell}$ and m_{H}/m_{bb} (empty histogram) respectively for (a) gluon-gluon fusion in the $n_b = 2$ category and (b) b-associated production in the $n_b \geq 3$ category of a A boson assuming $m_{\mathrm{A}} = 500\,\mathrm{GeV}$ and $m_{\mathrm{H}} = 250\,\mathrm{GeV}$ [109].

The overall signal efficiency for $A \to ZH \to \ell\ell bb$ is about 6%–13% for gluon-gluon fusion and 4%–8% for b-associated production in the $n_b = 2$ category. The efficiency of the b-associated production signal in the $n_b \geq 3$ category is approximately 2%–4%, depending on the m_{A} and m_{H} values. Figure 6.6 shows the relative efficiency of the m_{bb} window criterion and Figure 6.7 shows a few representative distributions of the signal efficiency as a function of either m_{A} or m_{H}.

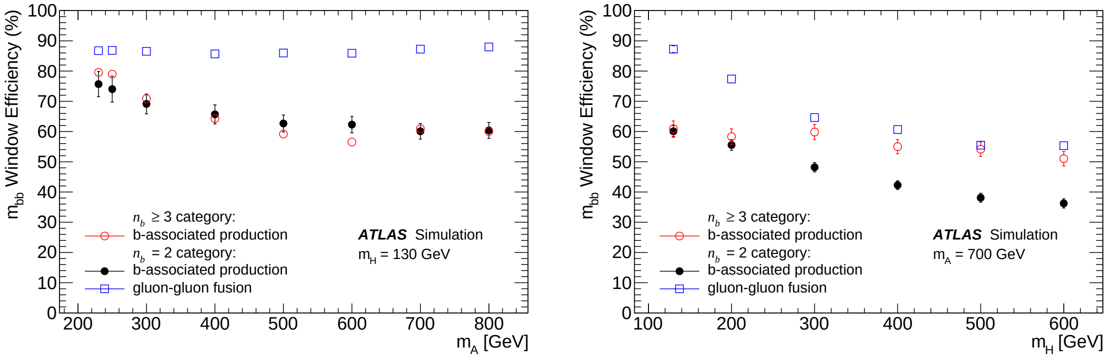

(a)

(b)

Figure 6.6: The efficiency of the m_{bb} window requirement for (a) $m_{\mathrm{H}} = 130\,\mathrm{GeV}$ as a function of m_{A} and (b) $m_{\mathrm{A}} = 700\,\mathrm{GeV}$ as a function of m_{H} [109].

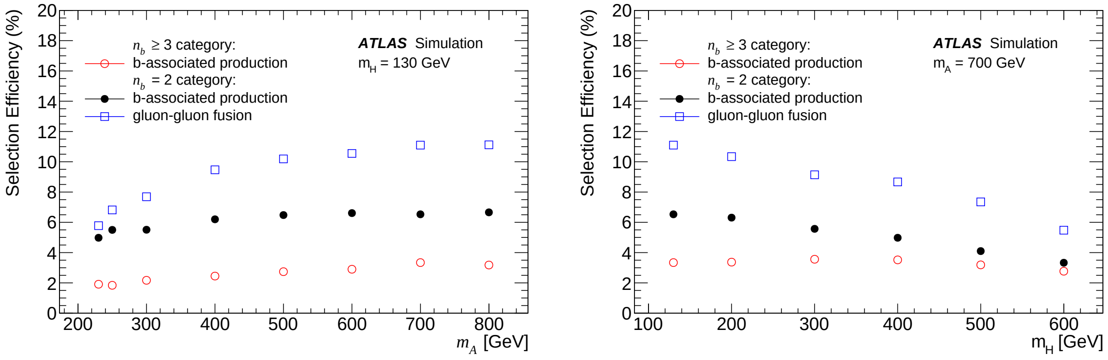

(a)

(b)

Figure 6.7: The signal selection efficiency for (a) $m_{\mathrm{H}} = 130\,\mathrm{GeV}$ as a function of m_{A} and (b) $m_{\mathrm{A}} = 700\,\mathrm{GeV}$ as a function of m_{H} [109].

6.4 Signal Modeling

This analysis utilizes the shape of the $m_{\ell\ell bb}$ invariant mass spectrum to interpret the observed data. A meaningful interpretation of the observed data requires continuous and smooth signal models in a statistical test, either for the construction of confidence intervals on model parameters or the discovery of potential signals. Monte Carlo simulation is an indispensable tool in particle physics experiments, as it incorporates both modeling of fundamental physics processes and a detailed detector simulation. However, MC simulations are time-consuming and demand a fair amount of computing resources.

The two-dimensional parameter space considered in this analysis can be enormous given the fine $m_{\ell\ell bb}$ resolution. A reasonable scan of the $m_{\mathrm{A}} - m_{\mathrm{H}}$ plane requires thousands of MC samples generated for both gluon-gluon fusion and b-associated productions. This section focuses on techniques that are used to interpolate the intermediate signal points using a discrete set of MC simulations, thereby ensuring continuity for the two-dimensional scan of the parameter of interest in a practical way.

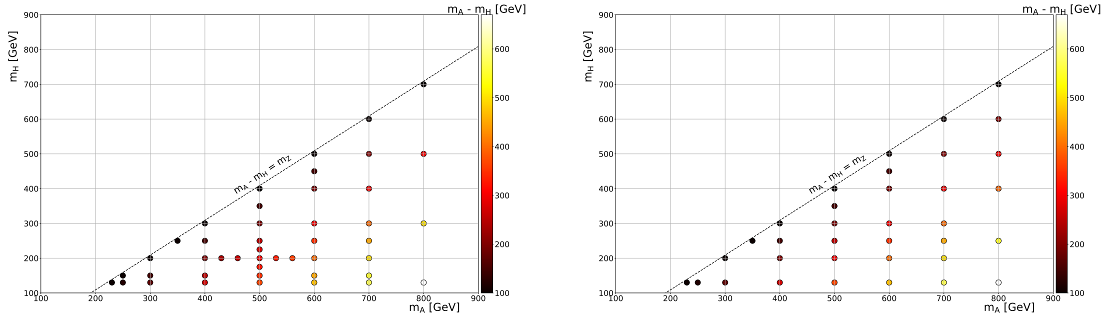

(a) gluon-gluon fusion

(b) b-associated production

Figure 6.8: The grid of Monte Carlo simulation generated for scanning the $m_{\mathrm{A}} - m_{\mathrm{H}}$ parameter space for each production mechanism.

6.4.1 Signal Shape Interpolation

The $m_{\ell\ell bb}$ distribution of a A boson produced via gluon-gluon fusion can be adequately modeled by the following function after the corresponding m_{bb} selection in the $n_b = 2$ category:

$$f_{\mathrm{EGE}}(x; a, \sigma, k_L, k_H) = \begin{cases} \exp\left[\dfrac{{k_L}^2}{2} + k_L\left(\dfrac{x-a}{\sigma}\right)\right] & \text{for} \quad \dfrac{x-a}{\sigma} \leq -k_L \\ \exp\left[-\dfrac{1}{2}\left(\dfrac{x-a}{\sigma}\right)^2\right] & \text{for} \quad -k_L < \dfrac{x-a}{\sigma} \leq k_H \\ \exp\left[\dfrac{{k_H}^2}{2} - k_H\left(\dfrac{x-a}{\sigma}\right)\right] & \text{for} \quad \dfrac{x-a}{\sigma} > k_H \end{cases} \tag{6.1}$$

The probability density function in Equation (6.1) is referred to as the EGE function, short for *ExpGaussExp* [121]. The EGE function consists of a Gaussian core with mean a and variance σ^2, and two exponential tails on both sides of the Gaussian. k_L and k_H represent the decay constants of the exponential tails, and they indicate the transition points as well. Continuity of the EGE function and its first derivative are implicitly enforced.

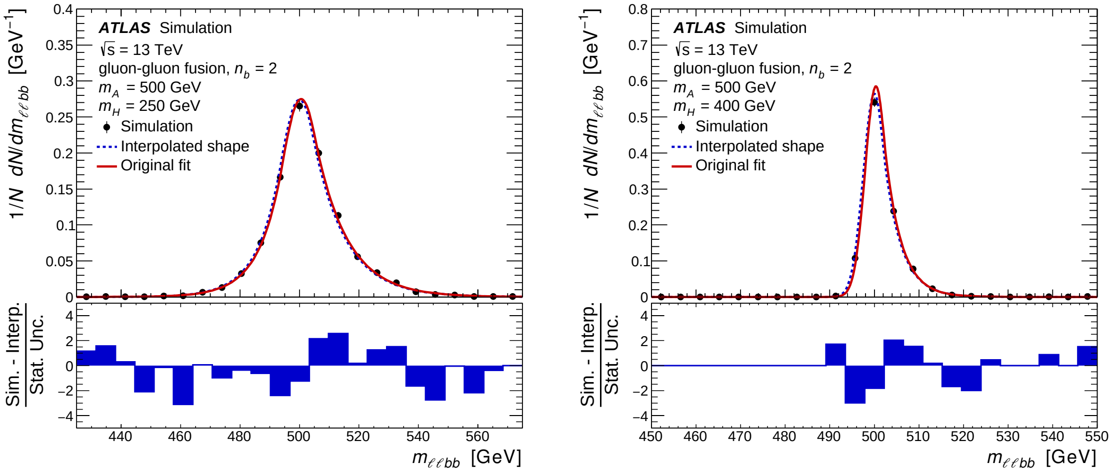

(a) $n_b = 2$ category

(b) $n_b = 2$ category

Figure 6.9: Simulated $m_{\ell\ell bb}$ distributions (closed circles) of signals produced via gluon-gluon fusion assuming (a) $m_{\mathrm{A}} = 500\,\mathrm{GeV}$ and $m_{\mathrm{H}} = 250\,\mathrm{GeV}$, and (b) $m_{\mathrm{A}} = 500\,\mathrm{GeV}$ and $m_{\mathrm{H}} = 400\,\mathrm{GeV}$ in the $n_b = 2$ category. Signal parameterizations are overlaid for comparison. The solid curves are from parameter values obtained directly from the fits to the simulated distributions, whereas the dashed curves use the interpolated parameter values. The differences between the simulation and the interpolated shape divided by the statistical uncertainties of the simulation are shown in the bottom panels.

On the other hand, a double-sided Crystal Ball (DSCB) function [122] is used to describe the $m_{\ell\ell bb}$ distribution of a A boson produced in association with b-quarks in both $n_b = 2$ and $n_b \geq 3$ categories. The DSCB function reads as follows:

$$f_{\mathrm{DSCB}}(x; a, \sigma, n_1, \alpha_1, n_2, \alpha_2) = \begin{cases} A_1 \cdot \left(B_1 - \frac{x-a}{\sigma}\right)^{-n} & \text{for} \quad \frac{x-a}{\sigma} < -\alpha_1 \\ \exp\left[-\frac{1}{2}\left(\frac{x-a}{\sigma}\right)^2\right] & \text{for} \quad -\alpha_1 < \frac{x-a}{\sigma} \leq \alpha_2 \\ A_2 \cdot \left(B_2 + \frac{x-a}{\sigma}\right)^{-n} & \text{for} \quad \frac{x-a}{\sigma} > \alpha_2 \end{cases} \tag{6.2}$$

where

$$A_i = \left(\frac{n_i}{|\alpha_i|}\right)^n \cdot \exp\left[-\frac{|\alpha_i|^2}{2}\right], \qquad B_i = \frac{n_i}{|\alpha_i|} - |\alpha_i|. \tag{6.3}$$

The DSCB probability density function in Equation (6.2) consists of a Gaussian core portion, flanked by a power-law low-end tail and a second power-law high-end tail. The function itself and its first derivative are both continuous. The DSCB function is chosen because it can better describe than the EGE function the longer tails of the $m_{\ell\ell bb}$ distributions from b-associated production (compared to those produced via gluon-gluon fusion). The prolonged tails of the $m_{\ell\ell bb}$ distribution from b-associated production are due to the mispairing effect described in Section 6.3.

For signal distributions from both production mechanisms in each relevant category, the corresponding fit procedure is carried out for all the available MC samples. The grid of the simulated MC signal points is shown in Figure 6.8. Interpolation on the EGE or DSCB function at any (m_{A}, m_{H}) point is then achieved by interpolating the parameter values obtained from the fit outcomes. These values are extracted from a series of maximum-likelihood estimations (MLEs).

It is found that the EGE (DSCB) function can describe the gluon-gluon fusion (b-associated production) signal samples decently when only a and σ are allowed to float freely in the MLE and suitable choices are made for fixing the remaining parameter values. As the kinematics of the final state objects largely depends on the mass splitting between the A and H bosons in the narrow-width regime, these fixed values are determined by first allowing all of the parameters to float in the fit and inspecting whether their best-fit values are independent of the specific signal point. The suitable sets of values for the remaining parameters in the EGE and DSCB functions are then obtained by observing the evolution of their best-fit values; consequently, the parameter tuning schemes are shown in Table 6.3(a) for gluon-gluon fusion in the $n_b = 2$ category, Table 6.3(b) for b-associated production in the $n_b = 2$ category, and Table 6.3(c) for b-associated production in the $n_b \geq 3$ category.

The values of the parameters but a and σ are found to be well-behaved and

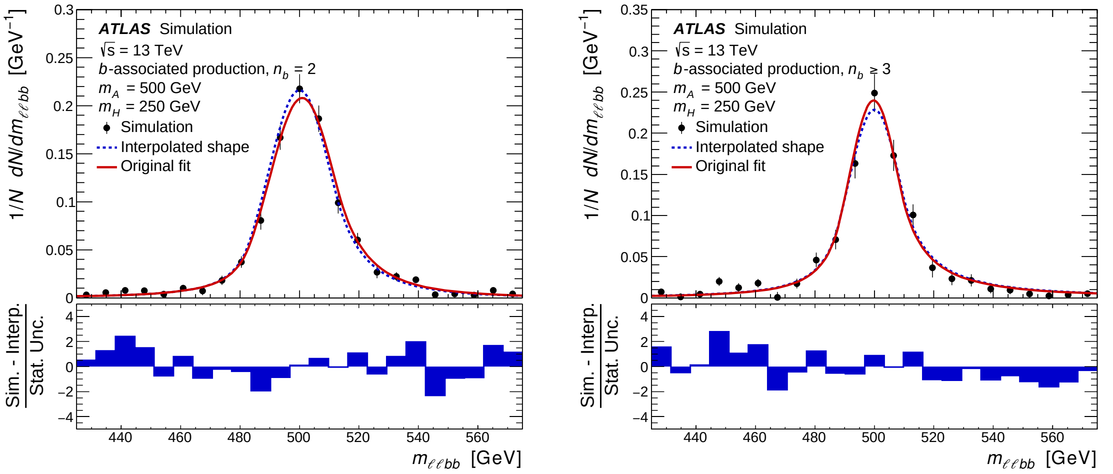

(a) $n_b = 2$ category (b) $n_b \geq 3$ category

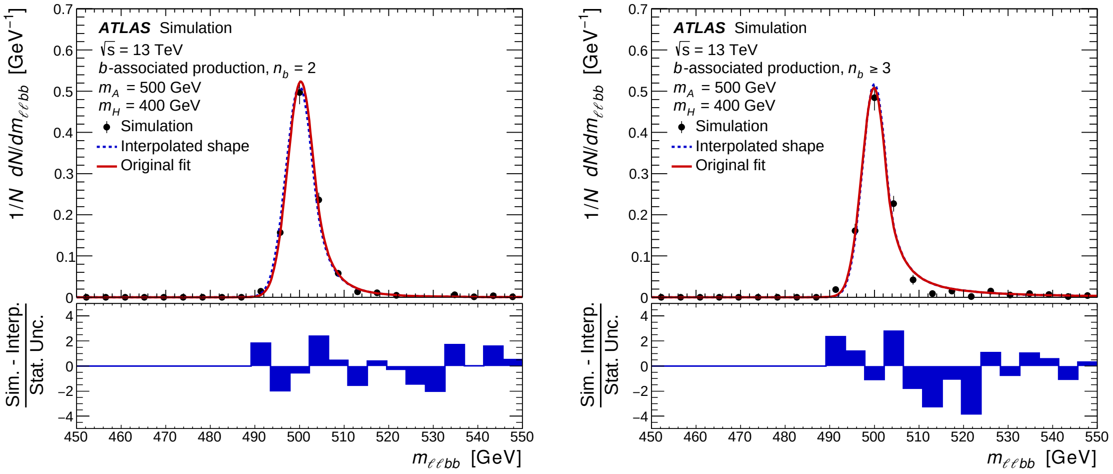

(c) $n_b = 2$ category (d) $n_b \geq 3$ category

Figure 6.10: Simulated signal $m_{\ell\ell bb}$ distributions (closed circles) from b-associated production assuming $m_{\mathrm{A}} = 500\,\mathrm{GeV}$ and $m_{\mathrm{H}} = 250\,\mathrm{GeV}$ in the (a) $n_b = 2$ category and (b) $n_b \geq 3$ category, and $m_{\mathrm{A}} = 500\,\mathrm{GeV}$ and $m_{\mathrm{H}} = 400\,\mathrm{GeV}$ in the (c) $n_b = 2$ category and (d) $n_b \geq 3$ category. Signal parameterizations are overlaid for comparison. The solid curves are from parameter values obtained directly from the fits to the simulated distributions, whereas the dashed curves use the interpolated parameter values. The differences between the simulation and the interpolated shape divided by the statistical uncertainties of the simulation are shown in the bottom panels.

relatively independent of the mass splitting. Therefore, they are fixed to their respective average values. However, two different choices of the parameter values pertaining to the low-end tail are arranged in each tuning scheme for $\Delta m = 100\,\mathrm{GeV}$ and $\Delta m > 100\,\mathrm{GeV}$, where $\Delta m = m_{\mathrm{A}} - m_{\mathrm{H}}$. The special treatment of the $\Delta m = 100\,\mathrm{GeV}$ case is attributed to being near the kinematic cutoff for the $A \to ZH$ process, which manifests itself as a steep low-end tail. Two illustrative outcomes of the EGE fit to

Parameter	Value
a	Floating
σ	Floating
k_L	5.06 for $\Delta m = 100\,\text{GeV}$
	0.91 for $\Delta m > 100\,\text{GeV}$
k_H	0.66

(a) EGE fit in $n_b = 2$ category

Parameter	Value
a	Floating
σ	Floating
α_1	4.11 for $\Delta m = 100\,\text{GeV}$
	1.64 for $\Delta m > 100\,\text{GeV}$
α_2	1.15
n_1	39.0 for $\Delta m = 100\,\text{GeV}$
	2.10 for $\Delta m > 100\,\text{GeV}$
n_2	3.89

(b) DSCB fit in $n_b = 2$ category

Parameter	Value
a	Floating
σ	Floating
α_1	4.00 for $\Delta m = 100\,\text{GeV}$
	1.38 for $\Delta m > 100\,\text{GeV}$
α_2	1.09
n_1	39.0 for $\Delta m = 100\,\text{GeV}$
	2.07 for $\Delta m > 100\,\text{GeV}$
n_2	1.87

(c) DSCB fit in $n_b \geq 3$ category

Table 6.3: Parameter tuning schemes for (a) EGE fit of gluon-gluon fusion in $n_b = 2$ category, (b) DSCB fit of b-associated production in $n_b = 2$ category, and (c) DSCB fit of b-associated production in $n_b \geq 3$ category. Δm represents the mass splitting between the A and H bosons, $m_{\text{A}} - m_{\text{H}}$.

the simulated $m_{\ell\ell bb}$ distributions are shown in Figure 6.9, as represented by the red curves with the label "Original fit". Representative fit outcomes using the DSCB function are shown in Figure 6.10. The respective parameter tuning schemes outlined in Table 6.3 are utilized in the MLE and the agreement between the fit outcome and the MC simulation is satisfactory. The kinematic cutoff effect on the low-end tail can be seen from the $m_{\ell\ell bb}$ distributions with $\Delta m = 100\,\text{GeV}$.

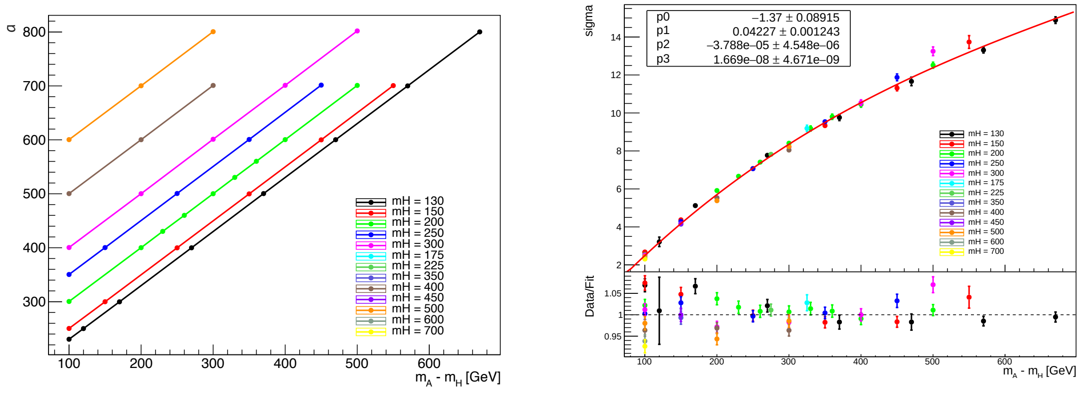

(a) a evolution of the EGE function

(b) σ evolution of the EGE function

Figure 6.11: Evolution of the floating parameters (a and σ) in the EGE fit to the gluon-gluon fusion signals as a function of the mass splitting between the A and H bosons. The red curve shows the result of a 3rd degree polynomial fit to the σ evolution used for the signal shape interpolation.

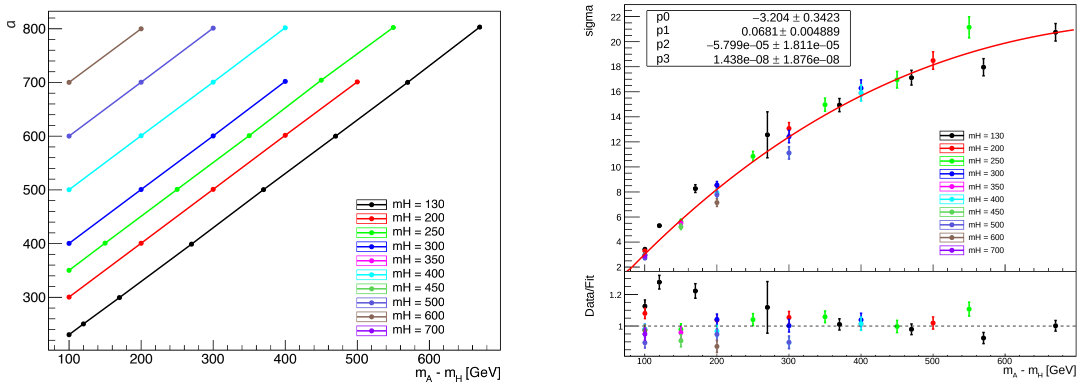

(a) a evolution of the DSCB function

(b) σ evolution of the DSCB function

Figure 6.12: Evolution of the floating parameters (a and σ) in the DSCB fit to the b-associated production signals in the $n_b = 2$ category as a function of the mass splitting between the A and H bosons. The red curve shows the result of a 3rd degree polynomial fit to the σ evolution used for the signal shape interpolation.

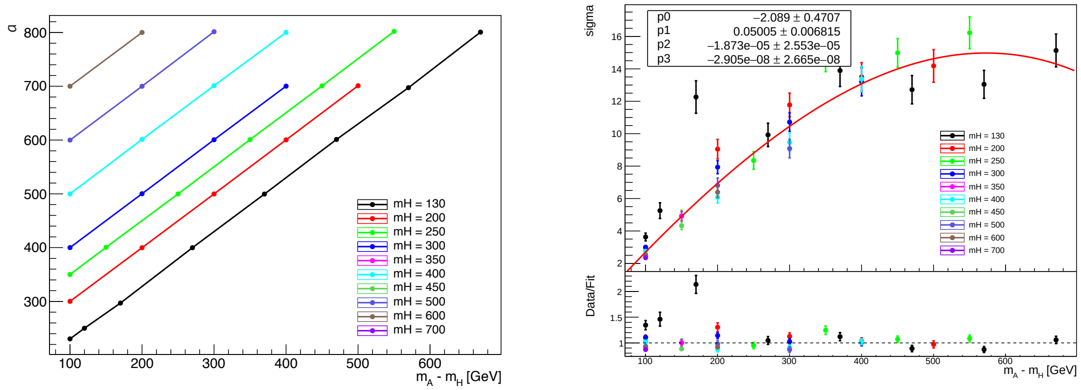

(a) a evolution of the DSCB function

(b) σ evolution of the DSCB function

Figure 6.13: Evolution of the floating parameters (a and σ) in the DSCB fit to the b-associated production signals in the $n_b \geq 3$ category as a function of the mass splitting between the A and H bosons. The red curve shows the result of a 3$^{\text{rd}}$ degree polynomial fit to the σ evolution used for the signal shape interpolation.

Apart from the mean and the variance of the Gaussian function, fixing the rest of the parameters greatly simplifies the procedure for interpolating the model parameters. Evolutions of a and σ are inspected as a function of the mass splitting (Δm) and are found to be well-behaved, as shown in Figure 6.11 for gluon-gluon fusion in the $n_b = 2$ category, Figure 6.12 for b-associated production in the $n_b = 2$ category, and Figure 6.13 for b-associated production in the $n_b \geq 3$ category. The mean of the Gaussian behaves linearly as expected and is set to m_{A}. A third-degree polynomial fit describes well the evolution of σ of the Gaussian. The parameterization of σ as a function of the mass splitting is found to be able to capture entirely the dependence of σ on both m_{A} and m_{H}. Figures 6.9-6.10 show good levels of agreement between the interpolated $m_{\ell\ell bb}$ distributions and the simulated ones, where the dashed curves are obtained using the interpolated parameter values.

6.4.2 Signal Yield Interpolation

Signal yield interpolation amounts to interpolating the product of signal acceptance and selection efficiency ($A \times \epsilon$) in the two-dimensional parameter space. Since the yield interpolation only involves estimating numerical values from the values of the surrounding MC signal points, a non-parametric two-dimensional spline-based technique, the thin plate spline (TPS) [123], is employed. Validations of the TPS estimates are shown in Figure 6.14(a) for gluon-gluon fusion in the $n_b = 2$ category, Figure 6.14(b) for b-associated production in the $n_b = 2$ category, and Figure 6.14(c)

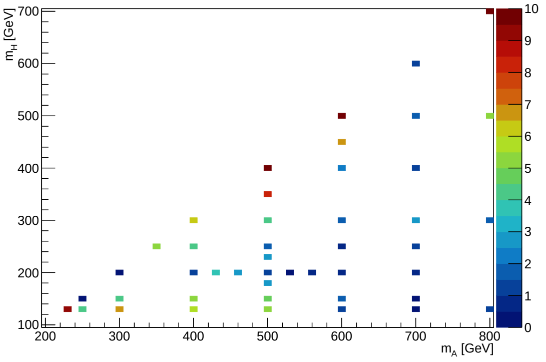

(a) $n_b = 2$: gluon-gluon fusion

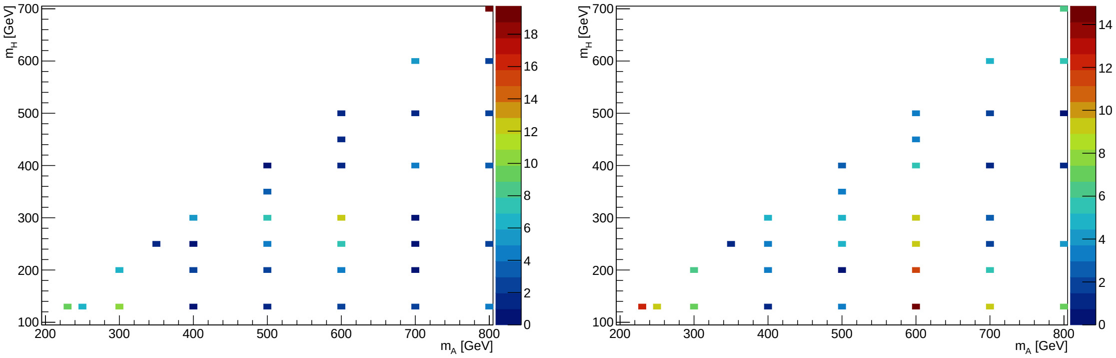

(b) $n_b = 2$: b-associated production

(c) $n_b \geq 3$: b-associated production

Figure 6.14: Results of the two-dimensional thin-plate spline signal yield interpolation for (a) gluon-gluon fusion in the $n_b = 2$ category, (b) b-associated production in the $n_b = 2$ category, and (c) b-associated production in the $n_b \geq 3$ category. The z-axis gives the absolute percent difference between the interpolated yield and the generated yield when not using that point as input to the interpolation.

for b-associated production in the $n_b \geq 3$ category. The z-axis corresponds to the difference between the signal yield from simulation and the interpolated yield after excluding the signal point in question in the TPS estimation. The largest differences occur at the boundary of the MC grid (e.g. $(m_{\mathrm{A}}, m_{\mathrm{H}}) = (800, 700)\,\mathrm{GeV}$ in Figure 6.14(a)). This is because extrapolations have to be made at points beyond the input range and the consequent yields are subject to greater uncertainty than the interpolated results. Unlike the validation of the TPS method, the analysis itself only involves signal points within the MC grid that can be obtained using interpolation. In Figure 6.14, variations of the interpolated yield are approximately within 10% with respective to the original yield. Treatment of the uncertainties arising from the yield interpolation procedure is discussed in Section 6.5.

6.4.3 Parameterization of the Large-Width Signals

The parameterization of the large-width signals is done analytically based on the modeling of the narrow-width signals. The $m_{\ell\ell bb}$ distribution of a narrow-width ($\Gamma_{\mathrm{A}} = 1\,\mathrm{MeV}$) A boson produced via gluon-gluon fusion can be described adequately by the EGE function (Section 6.4.1), which can be expressed in a slightly different way as:

$$f_{\mathrm{NW}}(x)\Big|_{m_{\mathrm{H}}} \cong \int_{0}^{\infty} \delta(m - m_{\mathrm{A}}) \cdot f_{\mathrm{EGE}}\Big(x \big| a(m), \sigma(m), k_{\mathrm{L}}, k_{\mathrm{H}}\Big)\Big|_{m_{\mathrm{H}}}\, dm \tag{6.4}$$

In the above equation, the approximation that the width of the narrow resonance is zero is made (for that $\Gamma_{\mathrm{A}}/m_{\mathrm{A}} \ll 1$), ergo the Dirac delta function $\delta(m - m_{\mathrm{A}})$. $f_{\mathrm{NW}}(x)$ is evaluated at a specific m_{H}, implying that the mass of the A boson becomes the sole variable in the $(m_{\mathrm{A}}, m_{\mathrm{H}})$ plane. The width of H ($\Gamma_{\mathrm{H}} = 1\,\mathrm{MeV}$) is also negligible in the model considered in this analysis, i.e. $\Gamma_{\mathrm{H}}/m_{\mathrm{H}} \ll 1$. Therefore, Equation (6.4) is equivalent to taking the expectation of $f_{\mathrm{EGE}}(m)$ with respect to its probability measure:

$$\begin{aligned} f_{\mathrm{NW}}(x)\Big|_{m_{\mathrm{H}}} &\cong \int_{0}^{\infty} g_{\mathrm{NW}}(m) \cdot f_{\mathrm{EGE}}(x \big| a(m), \sigma(m), k_{\mathrm{L}}(m), k_{\mathrm{H}}(m)\Big)\Big|_{m_{\mathrm{H}}}\, dm \\ &= E_m\left[f_{\mathrm{EGE}}(x, m)\Big|_{m_{\mathrm{H}}} \right] \end{aligned} \tag{6.5}$$

where $g_{\mathrm{NW}}(m) = \delta(m - m_{\mathrm{A}})$ is the probability density function of m, the mass of the resonance.

In taking the EGE function $f_{\mathrm{EGE}}(x, m)\Big|_{m_{\mathrm{H}}}$ as the approximated form of the detector response that one would have for a narrow-width signal, generalization can be made for the large-width scenarios on the same basis:

$$\begin{aligned} f_{\mathrm{LW}}(x)\Big|_{m_{\mathrm{H}}} &\cong E_m\left[f_{\mathrm{EGE}}(x, m)\Big|_{m_{\mathrm{H}}} \right] \\ &= \int_{0}^{\infty} g_{\mathrm{LW}}(m) \cdot f_{\mathrm{EGE}}(x \big| a(m), \sigma(m), k_{\mathrm{L}}, k_{\mathrm{H}}\Big)\Big|_{m_{\mathrm{H}}}\, dm \end{aligned} \tag{6.6}$$

where $g_{\mathrm{LW}}(m)$ is the normalized lineshape of the resonance production for a specific $\Gamma_{\mathrm{A}}/m_{\mathrm{A}}$ assumption and can be naturally interpreted as the density function of m in the large-width scenario. For modeling the large-width A bosons produced via

b-associated production, the same approach is used with EGE replaced by the DSCB function.

To account for the distortion of the lineshape near the kinematic cutoff $m_\mathrm{A} - m_\mathrm{H} \simeq m_\mathrm{Z}$ ($A \to ZH$ is enforced in the MC generator), a modified Breit-Wigner function is employed to parameterize the lineshape of the A boson as a function of its width:

$$g_\mathrm{LW}(m) = \frac{k_0}{(m^2 - M^2)^2 + (\Gamma M)^2} \cdot \texttt{LogNormal}(m, k_1, k_2, k_3) \tag{6.7}$$

By fitting to the generated lineshapes of the A boson, the following parameterization of the parameters in Equation (6.7) is adopted:

- $M = m_\mathrm{A}$ and is constant.
- $\Gamma = \Gamma_\mathrm{A}$ and is constant.
- k_0 is the normalization factor.
- $k_1 = 1.43 \times 10^{-9} \cdot X_s^3 - 2.66 \times 10^{-6} \cdot X_s^2 + 1.61 \times 10^{-3} \cdot X_s + 0.55$, where $X_s = m_\mathrm{A}$ for $m_\mathrm{A} < 500$ GeV and $X_s = 500$ GeV for $m_\mathrm{A} \geq 500$ GeV.
- $k_2 = m_\mathrm{H} + m_\mathrm{Z} - 20$ and is constant.
- $k_3 = 3.05 \times 10^{-6} \cdot \Delta m^3 - 4.06 \times 10^{-3} \cdot \Delta m^2 + 0.69 \cdot \Delta m + 59.18 + m_\mathrm{A}$, where $\Delta m = m_\mathrm{A} - m_\mathrm{H}$.

The above parameterization is obtained by firstly letting all the parameters float freely in the fit procedure and subsequently using polynomial functions to capture the evolution of the relevant parameters as a function of m_A, Γ_A and m_H.

Figures 6.15–6.18 compare some of the generated lineshapes with the modified Breit-Wigner function using the aforementioned parameterization. It is evident that the modified Breit-Wigner function is able to describe the lineshapes of the resonance production exceedingly well for different A boson widths and signal points considered.

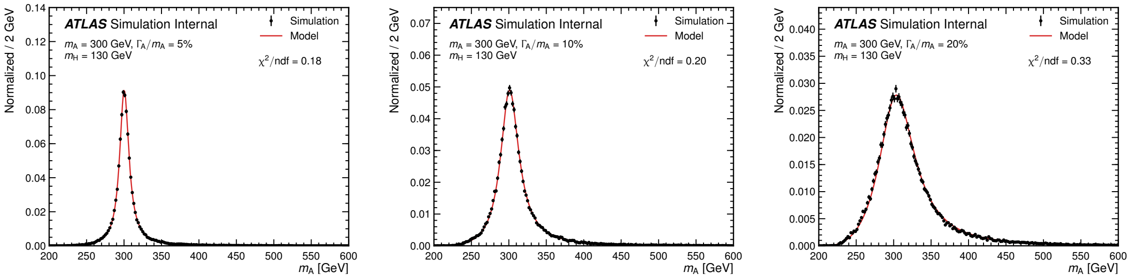

(a) Linear plots

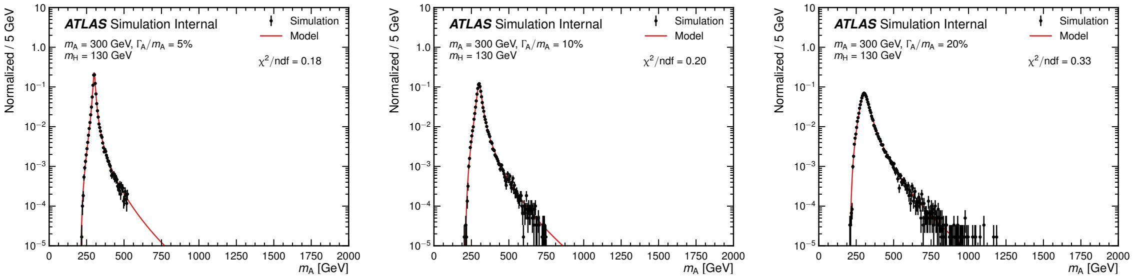

(b) Semi-logarithmic plots

Figure 6.15: Comparisons between the parameterized and generated lineshapes of m_A = 300 GeV, m_H = 130 GeV for Γ_A/m_A = 5% (left), Γ_A/m_A = 10% (middle), and Γ_A/m_A = 20% (right).

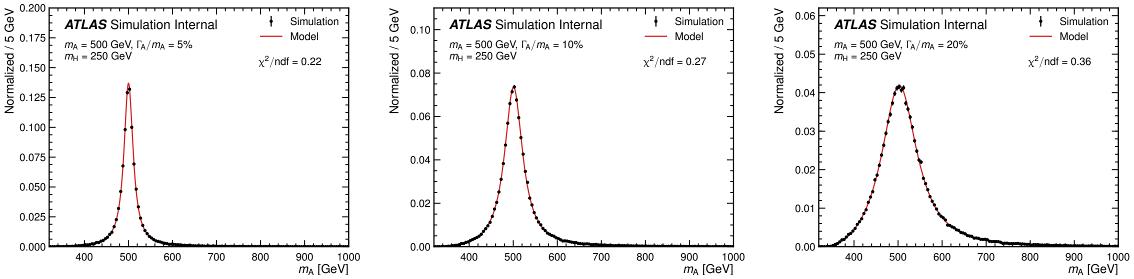

(a) Linear plots

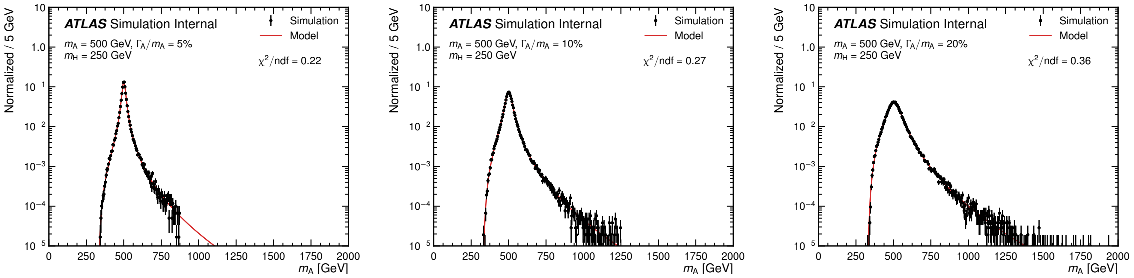

(b) Semi-logarithmic plots

Figure 6.16: Comparisons between the parameterized and generated lineshapes of m_A = 500 GeV, m_H = 250 GeV for Γ_A/m_A = 5% (left), Γ_A/m_A = 10% (middle), and Γ_A/m_A = 20% (right).

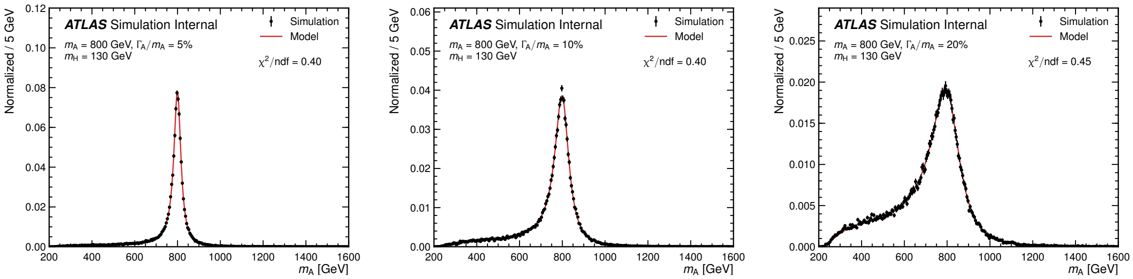

(a) Linear plots

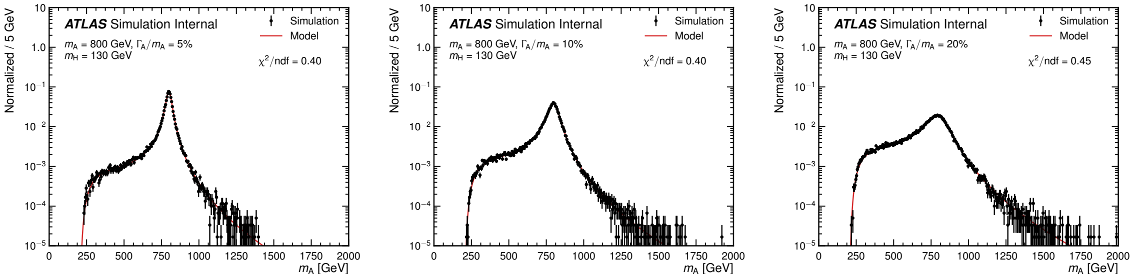

(b) Semi-logarithmic plots

Figure 6.17: Comparisons between the parameterized and generated lineshapes of $m_{\mathrm{A}} = 800$ GeV, $m_{\mathrm{H}} = 130$ GeV for $\Gamma_A/m_{\mathrm{A}} = 5\%$ (left), $\Gamma_A/m_{\mathrm{A}} = 10\%$ (middle), and $\Gamma_A/m_{\mathrm{A}} = 20\%$ (right).

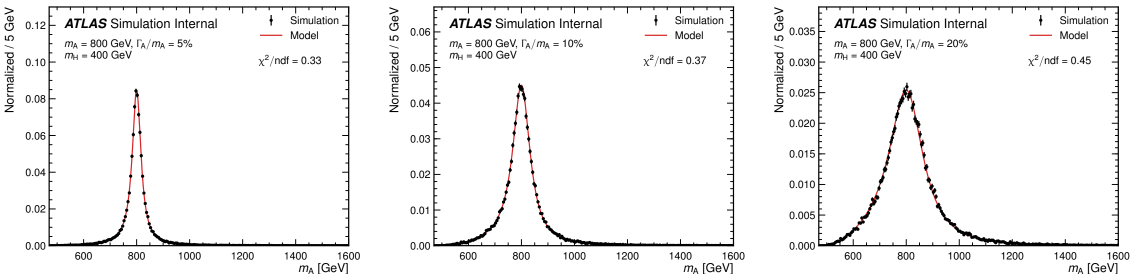

(a) Linear plots

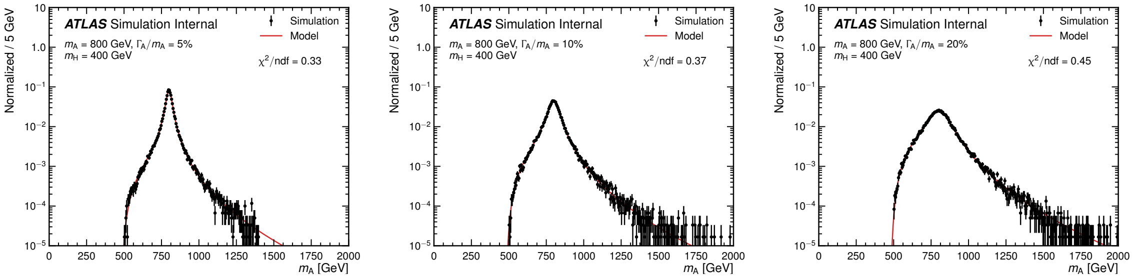

(b) Semi-logarithmic plots

Figure 6.18: Comparisons between the parameterized and generated lineshapes of $m_{\mathrm{A}} = 800$ GeV, $m_{\mathrm{H}} = 400$ GeV for $\Gamma_A/m_{\mathrm{A}} = 5\%$ (left), $\Gamma_A/m_{\mathrm{A}} = 10\%$ (middle), and $\Gamma_A/m_{\mathrm{A}} = 20\%$ (right).

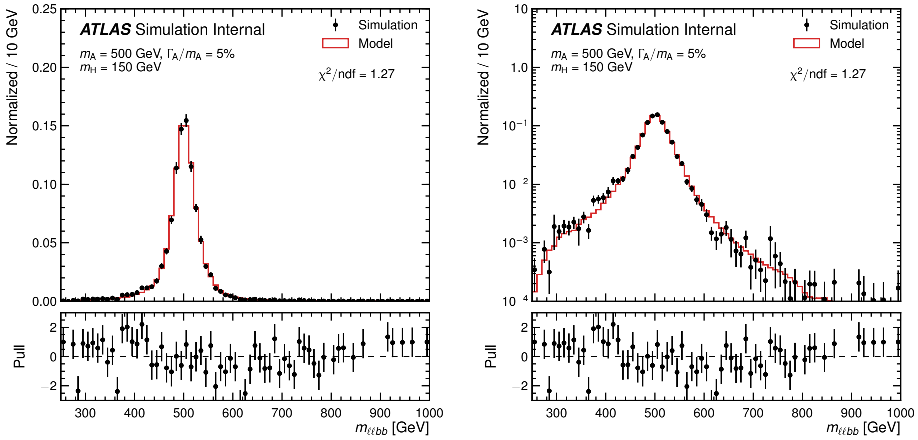

(a) $\Gamma_\mathrm{A}/m_\mathrm{A} = 5\%$

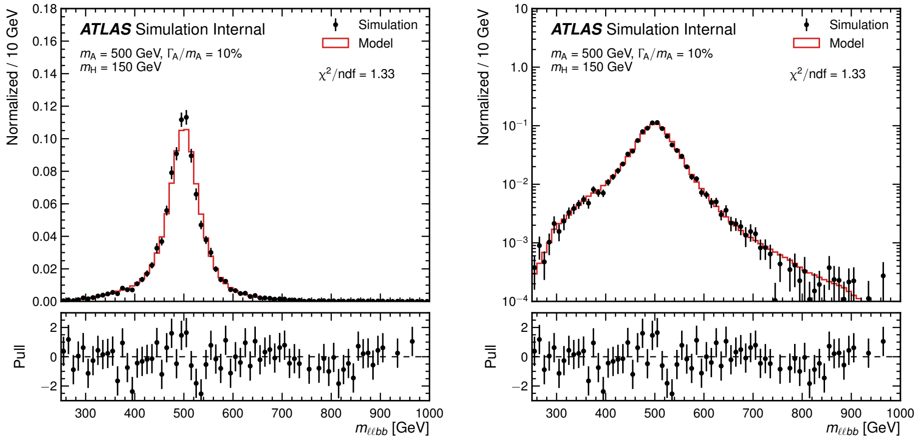

(b) $\Gamma_\mathrm{A}/m_\mathrm{A} = 10\%$

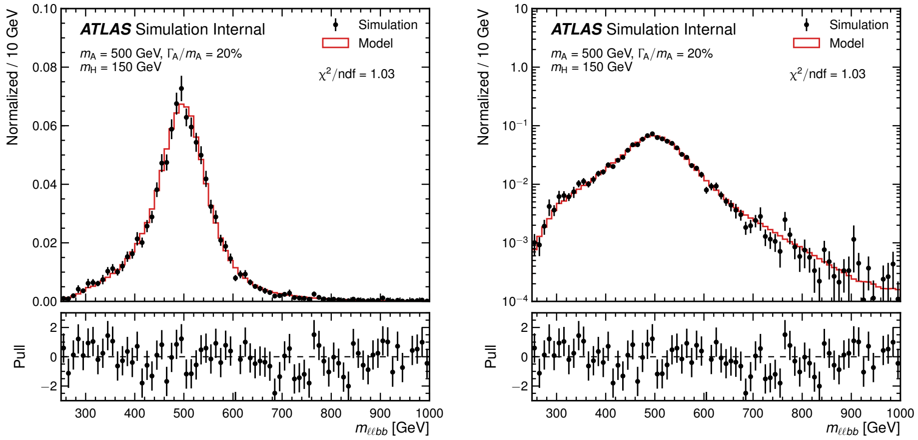

(c) $\Gamma_\mathrm{A}/m_\mathrm{A} = 20\%$

Figure 6.19: Comparisons of the invariant mass spectra of the $\ell\ell bb$ four-body system for $m_\mathrm{A} = 500$ GeV, $m_\mathrm{H} = 150$ GeV for different A boson widths. The dots correspond to the shape from simulation and the red histogram represents the model template based on the method described by Equation (6.6).

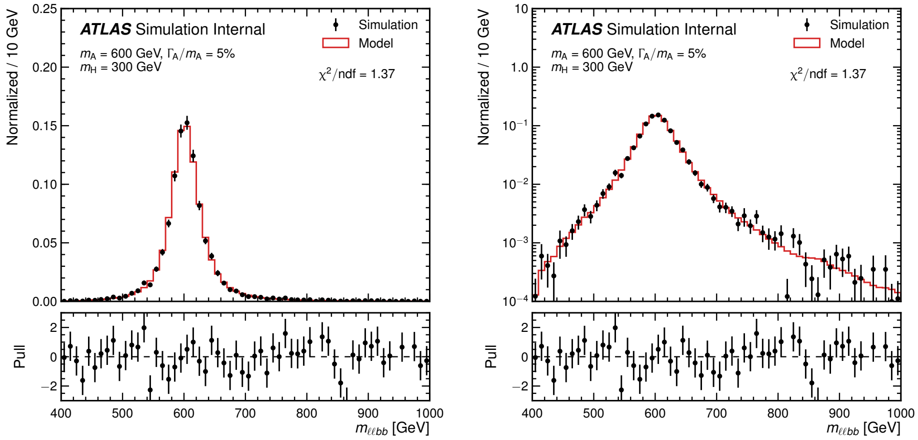

(a) $\Gamma_{\mathrm{A}}/m_{\mathrm{A}} = 5\%$

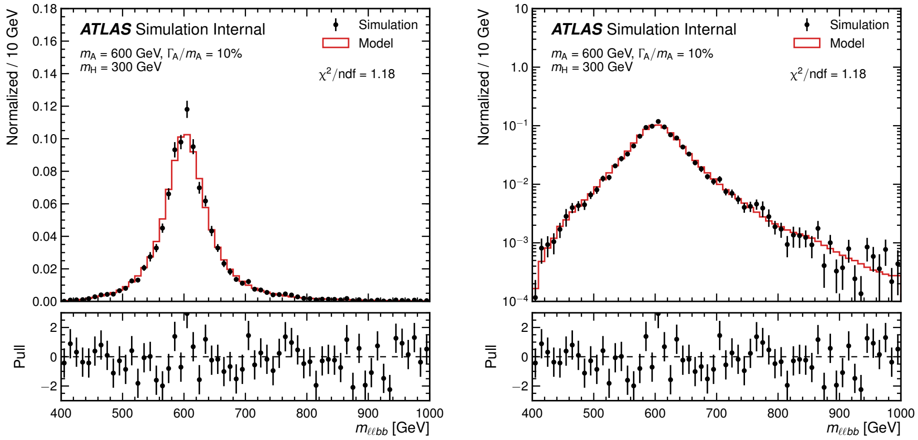

(b) $\Gamma_{\mathrm{A}}/m_{\mathrm{A}} = 10\%$

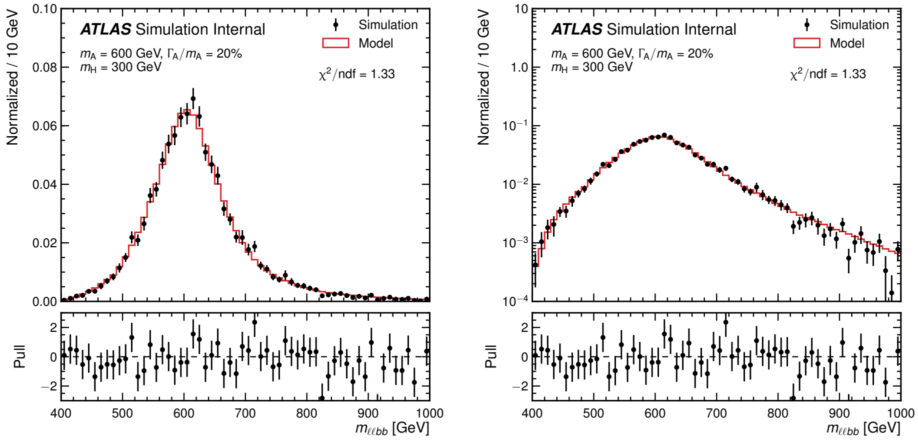

(c) $\Gamma_{\mathrm{A}}/m_{\mathrm{A}} = 20\%$

Figure 6.20: Comparisons of the invariant mass spectra of the $\ell\ell bb$ four-body system for $m_{\mathrm{A}} = 600$ GeV, $m_{\mathrm{H}} = 300$ GeV for different A boson widths. The dots correspond to the shape from simulation and the red histogram represents the model template based on the method described by Equation (6.6).

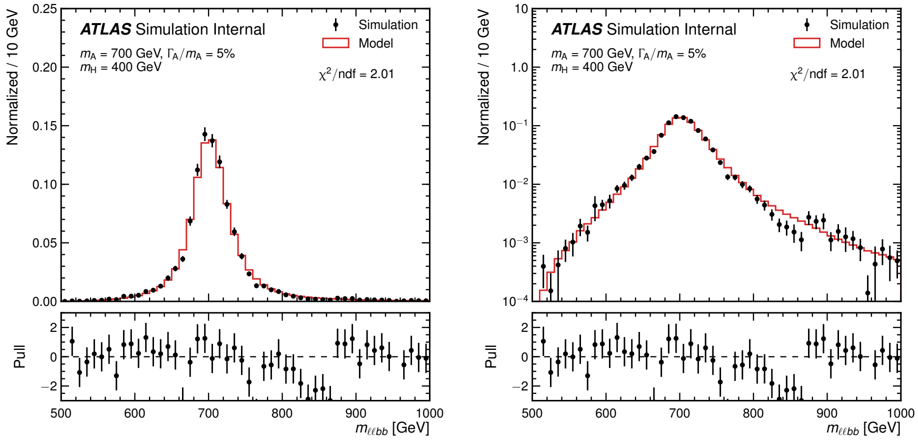

(a) $\Gamma_{\mathrm{A}}/m_{\mathrm{A}} = 5\%$

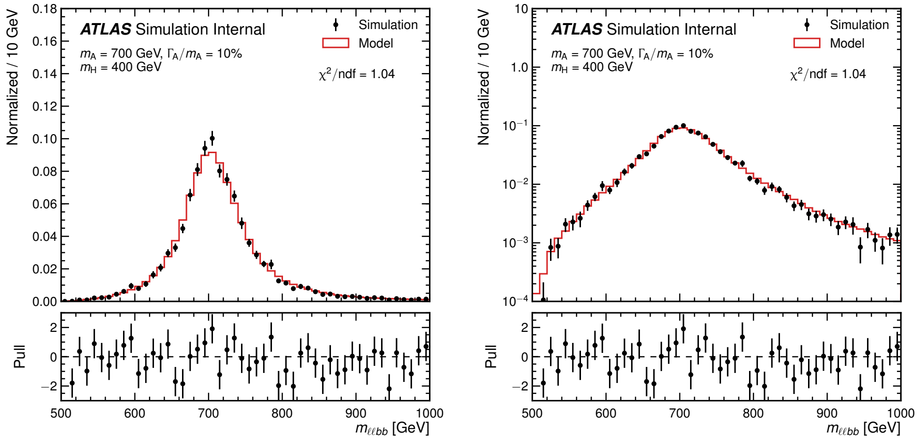

(b) $\Gamma_{\mathrm{A}}/m_{\mathrm{A}} = 10\%$

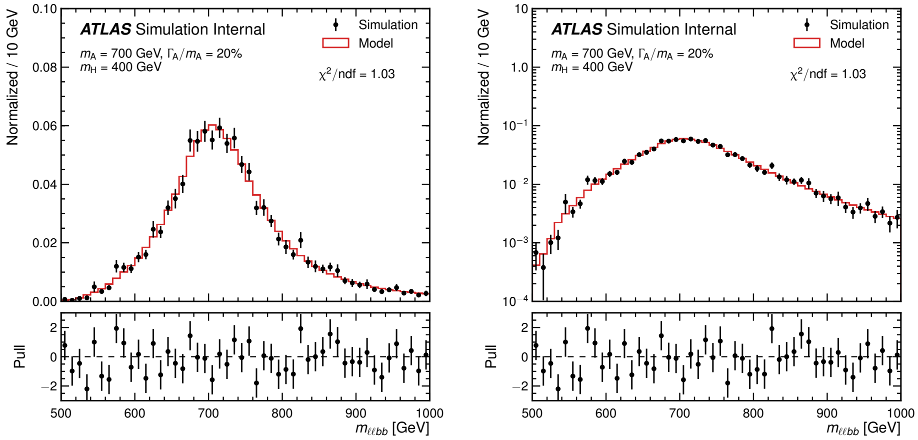

(c) $\Gamma_{\mathrm{A}}/m_{\mathrm{A}} = 20\%$

Figure 6.21: Comparisons of the invariant mass spectra of the $\ell\ell bb$ four-body system for $m_{\mathrm{A}} = 700$ GeV, $m_{\mathrm{H}} = 400$ GeV for different A boson widths. The dots correspond to the shape from simulation and the red histogram represents the model template based on the method described by Equation (6.6).

Validation of the method

Only a few MC simulations with different widths are generated for purposes of validating the above method. $m_{\ell\ell bb}$ distributions obtained using the method based on Equation (6.6) are compared to the simulated distributions with all the relevant selection criteria in Section 6.3 applied. The full comparisons are shown in Figures 6.19–6.21, which suggest that the $m_{\ell\ell bb}$ templates are able to describe the simulated $m_{\ell\ell bb}$ spectra reasonably well. The $A \times \epsilon$ of the large-width signals is estimated using the same methodology, after replacing the EGE or DSCB function with the TPS interpolation of $A \times \epsilon$ for the narrow-width signals.

An example of the parameterized signal distributions with different widths is shown in Figure 6.22.

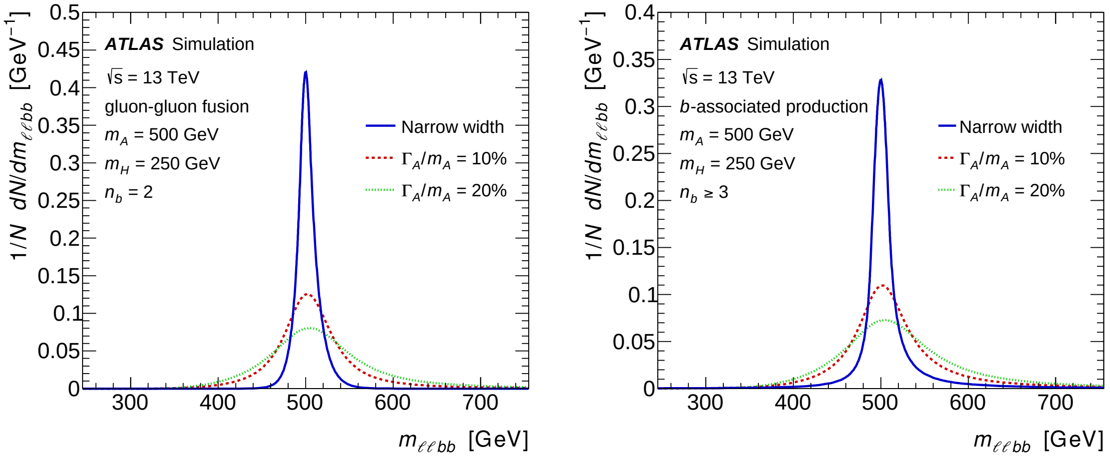

(a) (b)

Figure 6.22: The interpolated $m_{\ell\ell bb}$ distribution assuming $m_{\mathrm{A}} = 500\,\mathrm{GeV}$ and $m_{\mathrm{H}} = 250\,\mathrm{GeV}$ with various A boson widths for: (a) gluon-gluon fusion in the $n_b = 2$ category and (b) b-associated production in the $n_b \geq 3$ category [109].

6.5 Systematic Uncertainties

The experimental systematic uncertainties associated with the physics objects used in this analysis are identical to those of the $X \rightarrow ZV \rightarrow \ell\ell qq$ analysis (Section 5.4.1).

For modeling of the Z+jets background, the most important sources of uncertainty are associated with the shapes of the transverse momentum of the Z boson and the di-jet invariant mass. The modeling uncertainties are estimated using a data-driven approach. Events after all the selection criteria but the m_{bb} selection are enriched with the Z+jets background and any potential signal processes will be diluted. Since this region is dominated by the Z+jets process, the disagreement between data and the total background prediction can be attributed to the modeling uncertainties associated with the Z+jets process. The shape uncertainties are then evaluated by taking the ratio of data, after the subtraction of the total MC estimation, to Z+jets MC estimation, as represented by the solid dots in Figure 6.23 for $p_{\mathrm{T}}(Z)$ and Figure 6.24 for m_{bb}. Analytical functional forms are subsequently used to parametrize the shape differences as functions of $p_{\mathrm{T}}(Z)$ and m_{bb} separately. Parameterizations of the shape differences are denoted by the red curves in Figure 6.23 and Figure 6.24. These parametrized uncertainties are then propagated to the final signal regions in the likelihood function.

The determination of the modeling uncertainties of the $t\bar{t}$ background adheres to the same philosophy. The top-enriched control region is utilized to measure and parameterize the shape differences in the $p_{\mathrm{T}}(Z)$ and m_{bb} distributions and the resulting data-driven estimates are extrapolated to the signal region using the same prescription for the uncertainties. Data-driven estimates of the $t\bar{t}$ modeling uncertainties are shown in Figure 6.25 and Figure 6.26.

For the other minor background processes, the relevant modeling uncertainties are obtained using a MC-based approach, by varying the factorization and renormalization scales, the amount of initial- and final-state radiation, and the choice of PDF parameterizations [109].

Signal theoretical uncertainties due to choice of PDF set, initial- and final-state radiation prescription, and factorization and renormalization scales are considered. The calculation of these uncertainties follow the same procedure as described in Section 5.4.3. In general, these uncertainties only have non-negligible effects on the acceptance of the signal. The uncertainty for PDF choice is parameterized as $(2.2 + 0.58 \cdot m_{\mathrm{A}}/100)\%$ for gluon-gluon fusion, and a flat 5% for b-associated pro-

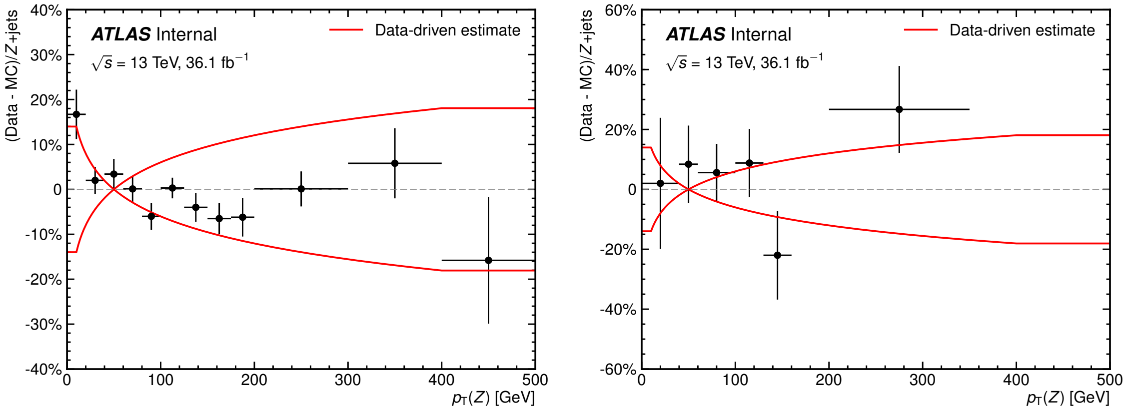

(a) $n_b = 2$ category

(b) $n_b \geq 3$ category

Figure 6.23: The ratio of $(N(\text{data}) - N(\text{MC backgrounds}))/N(Z+\text{jets})$ as a function of $p_{\text{T}}(Z)$. This ratio is taken as the modeling uncertainty associated with the $p_{\text{T}}(Z)$ of the Z+jets background in the respective categories. The red curve represents the parameterization used for the data-driven estimate.

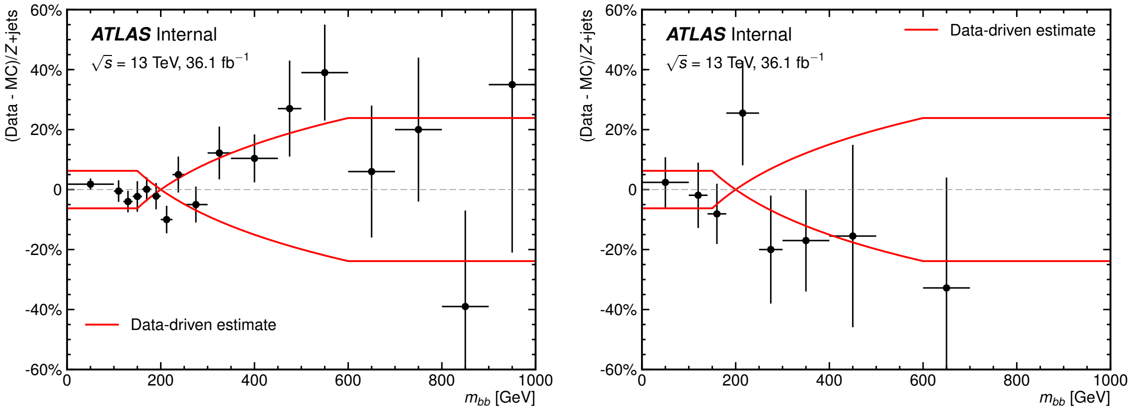

(a) $n_b = 2$ category

(b) $n_b \geq 3$ category

Figure 6.24: The ratio of $(N(\text{data}) - N(\text{MC backgrounds}))/N(Z+\text{jets})$ as a function of m_{bb}. This ratio is taken as the modeling uncertainty associated with the m_{bb} of the Z+jets background in the respective categories. The red curve represents the parameterization used for the data-driven estimate.

duction. The uncertainty associated with factorization and renormalization scales is evaluated to be 2% (1%) for gluon-gluon fusion (b-associated production). ISR/FSR uncertainties have an effect of 6% on the acceptance of gluon-gluon fusion signal and 5% on that of b-associated production.

Additional systematic uncertainties arising from the interpolation procedure are also considered. The signal interpolation procedure is performed for each experimental systematic variation, and the varying shapes and acceptances are taken as the

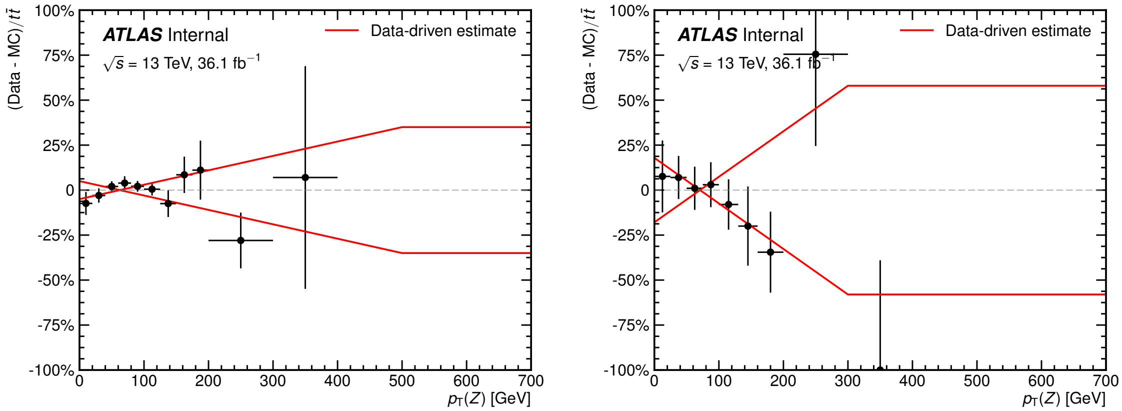

(a) $n_b = 2$ category

(b) $n_b \geq 3$ category

Figure 6.25: The ratio of $(N(\text{data}) - N(\text{MC backgrounds}))/N(t\bar{t})$ as a function of $p_\text{T}(Z)$. This ratio is taken as the modeling uncertainty associated with the $p_\text{T}(Z)$ of the $t\bar{t}$ background in the respective categories. The red curve represents the parameterization used for the data-driven estimate.

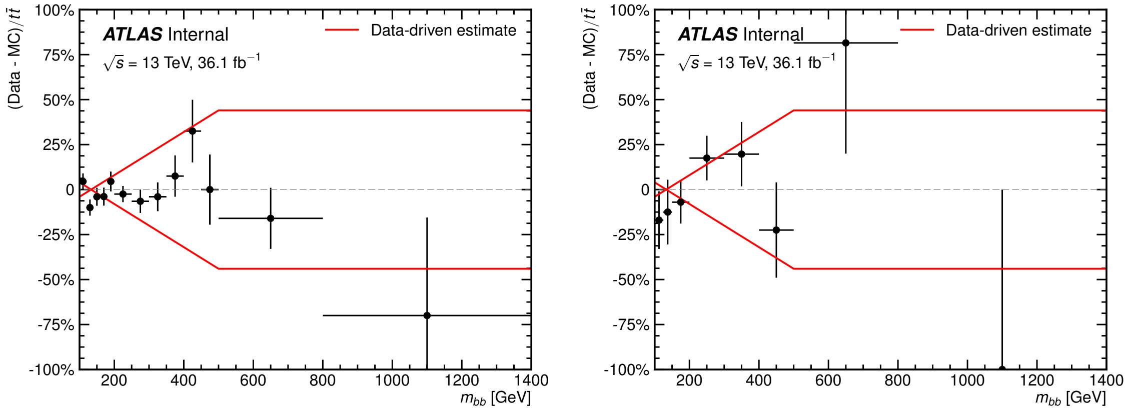

(a) $n_b = 2$ category

(b) $n_b \geq 3$ category

Figure 6.26: The ratio of $(N(\text{data})-N(\text{MC backgrounds}))/N(t\bar{t})$ as a function of m_{bb}. This ratio is taken as the modeling uncertainty associated with the m_{bb} of the $t\bar{t}$ background in the respective categories. The red curve represents the parameterization used for the data-driven estimate.

systematic variations associated with the experimental uncertainties for the signal Monte Carlo. A flat 5% (10%) variation is applied to the σ of the signal parameterization of gluon-gluon fusion (b-associated production). A 5.5% uncertainty on the signal acceptance due to the thin plate spline interpolation is applied to cover the differences between the nominal and interpolated acceptances in the bulk of the parameter space.

6.6 Statistical Analysis

The statistical analysis is conducted based on the aforementioned statistical framework as described in Section 5.5. Although this analysis probes a two-dimensional parameter space, the likelihood models constructed only depend on m_{A} due to the fact that the mass of the A boson is scanned for one m_{H} hypothesis at a time. To put it mathematically, the likelihood function considered in this analysis can be expressed as:

$$\mathcal{L}_{\mathrm{tot}}(m_{\mathrm{A}}, m_{\mathrm{H}}) \to \mathcal{L}^{i}_{\mathrm{tot}}(\mu, m_{\mathrm{A}}, m_{\mathrm{H}}, \theta|\mathcal{D}, \mathcal{G})\Big|_{m^{i}_{\mathrm{H}}}, \tag{6.8}$$

where μ is the signal strength parameter, $\mathcal{D}$ represents the collection of the observed events, and $\mathcal{G}$ corresponds to the set of the observed values of the nuisance parameters (Section 5.5.1). In Equation (6.8), the likelihood function in the $(m_{\mathrm{A}}, m_{\mathrm{H}})$ plane is transformed into a series of conditional likelihood functions evaluated at $m_{\mathrm{H}} = m^{i}_{\mathrm{H}}$ for the i-th function.

Table 6.4: Summary of the inputs entering the likelihood function. "N_{evt}" indicates that the number of events is used as the discriminant without any shape information and α refers to scale factors applied to the major background processes.

Fit inputs for each m_{H} hypothesis		
Input region	Discriminant	Scale factor
$n_b = 2$ category		
Signal region	$m_{\ell\ell bb}$ spectrum	$\alpha^{n_b=2}_{Z+\mathrm{jets}}$, $\alpha^{n_b=2}_{t\bar{t}}$
Z+jets control region	N_{evt}	$\alpha^{n_b=2}_{Z+\mathrm{jets}}$
Top control region	N_{evt}	$\alpha^{n_b=2}_{t\bar{t}}$
$n_b \geq 3$ category		
Signal region	$m_{\ell\ell bb}$ spectrum	$\alpha^{n_b\geq 3}_{Z+\mathrm{jets}}$, $\alpha^{n_b\geq 3}_{t\bar{t}}$
Z+jets control region	N_{evt}	$\alpha^{n_b\geq 3}_{Z+\mathrm{jets}}$
Top control region	N_{evt}	$\alpha^{n_b\geq 3}_{t\bar{t}}$

For each category, two free parameters governing the normalizations of the Z+jets and $t\bar{t}$ background processes are included in the likelihood function. They are determined simultaneously by the singal region and the respective control regions. Signal and the other minor background processes are normalized based on the theoretical cross sections and selection efficiencies. Typical values of scale factors are close to unity. Taking $(m_{\mathrm{A}}, m_{\mathrm{H}}) = (700, 200)\,\mathrm{GeV}$ as an example, the Z+jets scale factor is 1.12 ± 0.09 for the $n_b = 2$ category and 1.1 ± 0.2 for the $n_b \geq 3$ category. Similarly, the $t\bar{t}$ scale factors are 0.96 ± 0.06 and 1.2 ± 0.2 for the two corresponding categories [109]. Systematic uncertainties are incorporated in the likelihood model as nuisance parameters with either Gaussian or log-normal constraint terms, as described in Section 5.5. The fit inputs that enter the likelihood function of the analysis are summarized in Table 6.4.

6.7 Results

In each m_{bb} mass window considered, the $m_{\ell\ell bb}$ spectrum is scanned for potential excesses beyond the background prediction in the observed data. This procedure is performed for the narrow-width A bosons of both gluon-gluon fusion and b-associated productions. p-values are calculated from the test statistic q_0 in Section 5.5 and the results are shown in Figure 6.27. The alternative hypothesis in each p_0 calculation assumes the production of a specific $(m_\mathrm{A}, m_\mathrm{H})$ point under the narrow-width assumption. Both $n_b = 2$ and $n_b \geq 3$ categories are taken into account in the b-associated production, whereas gluon-gluon fusion only considers the $n_b = 2$ category.

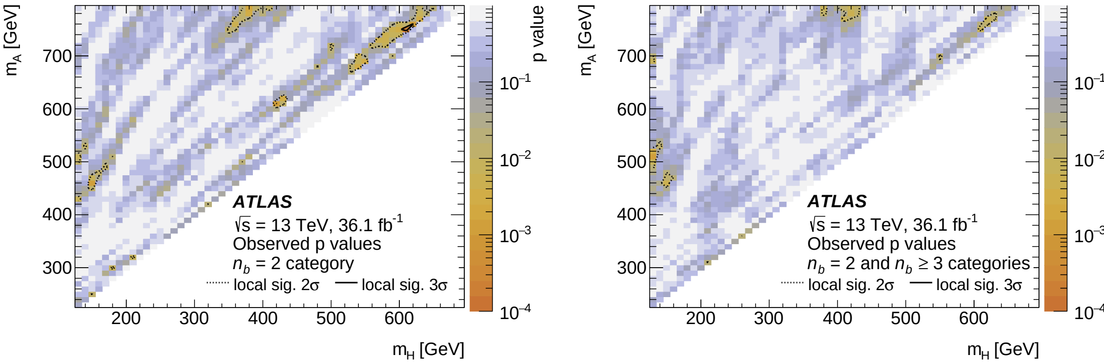

(a)

(b)

Figure 6.27: Scan of the p-values from the q_0 test statistic for (a) the gluon-gluon fusion and (b) the b-associated production signal assumption.

In all cases, the observed data are consistent with the null (background-only) hypothesis to a reasonable degree as no statistically significant excess is found. The most significant excess for gluon-gluon fusion is $3.5\,\sigma$ at $(m_\mathrm{A}, m_\mathrm{H}) = (750, 610)$ GeV, and $2.0\,\sigma$ after taking into account the look-elsewhere effect. The global significance is calculated based on a procedure for estimating the significance of a signal in a multi-dimensional search [124]. For b-associated production, the largest deviation occurs at $(m_\mathrm{A}, m_\mathrm{H}) = (510, 130)$ GeV with a local (global) significance of 3.0 (1.2) σ. The observed and expected mass spectra corresponding to the $m_\mathrm{H} = 610$ GeV and the $m_\mathrm{H} = 130$ GeV hypotheses are shown in Figure 6.28 and Figure 6.29, respectively. A few other representative mass distributions are shown in Figures 6.30-6.32 for various m_H hypotheses. The SM background estimates in these plots are obtained from background-only fits (Section 5.6.1).

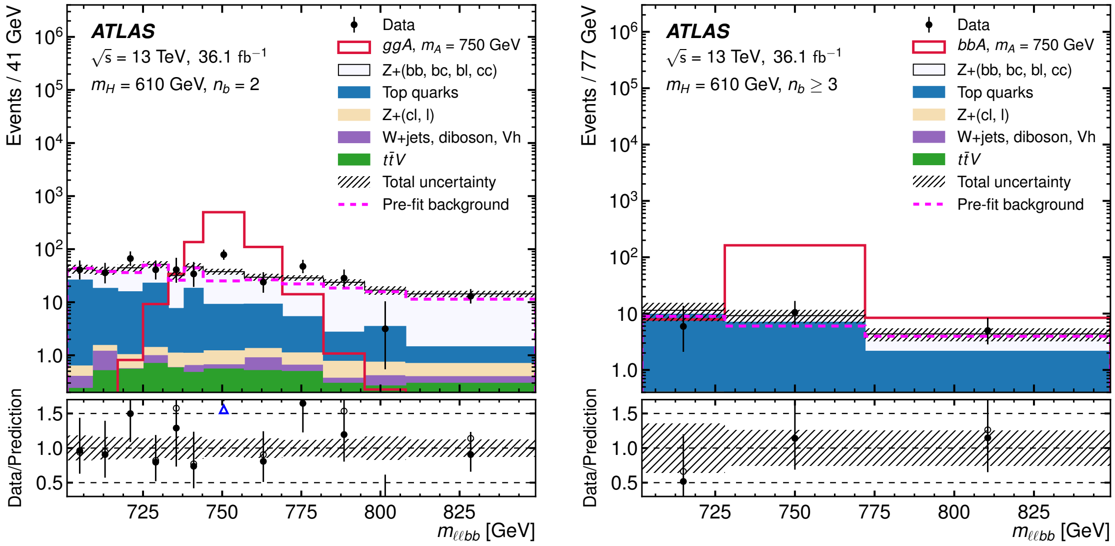

(a) (b)

Figure 6.28: Distributions of the $m_{\ell\ell bb}$ spectrum for the $m_{\mathrm{H}} = 610\,\mathrm{GeV}$ hypothesis in the (a) $n_b = 2$ category and (b) the $n_b \geq 3$ category. The solid dots in the lower panels represent the ratio of the data to the background prediction obtained from the conditional MLE with $\mu = 0$, while the open circles correspond to the ratio of the data to the pre-fit background prediction. The signal distributions shown in these plots assume that $\sigma \times \mathcal{B}(A \to ZH) \times \mathcal{B}(H \to bb) = 1\,\mathrm{pb}$.

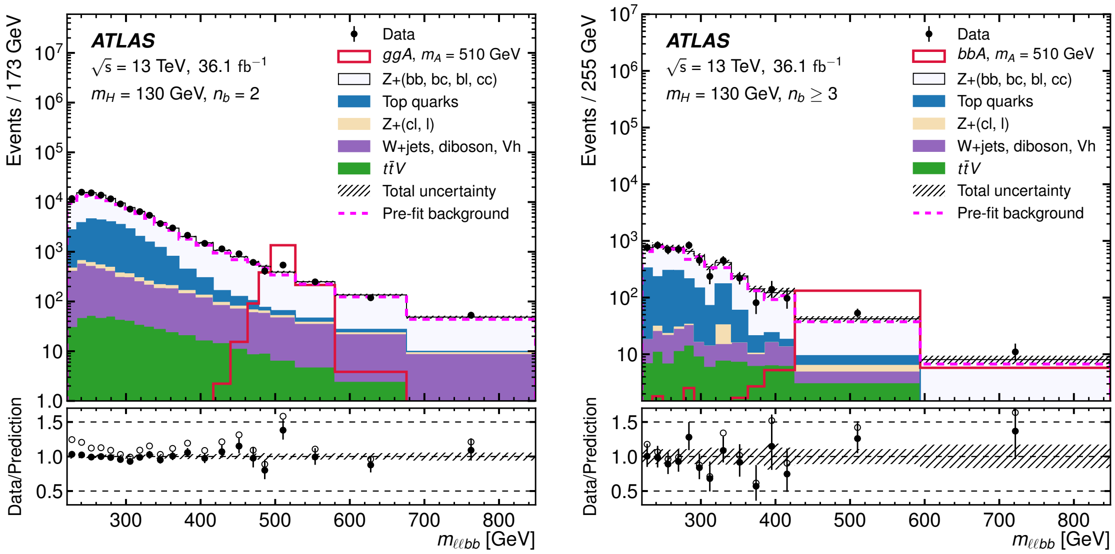

(a) (b)

Figure 6.29: Distributions of the $m_{\ell\ell bb}$ spectrum for the $m_{\mathrm{H}} = 130\,\mathrm{GeV}$ hypothesis in the (a) $n_b = 2$ category and (b) the $n_b \geq 3$ category. See Figure 6.28 for more explanations for the background and signal distributions.

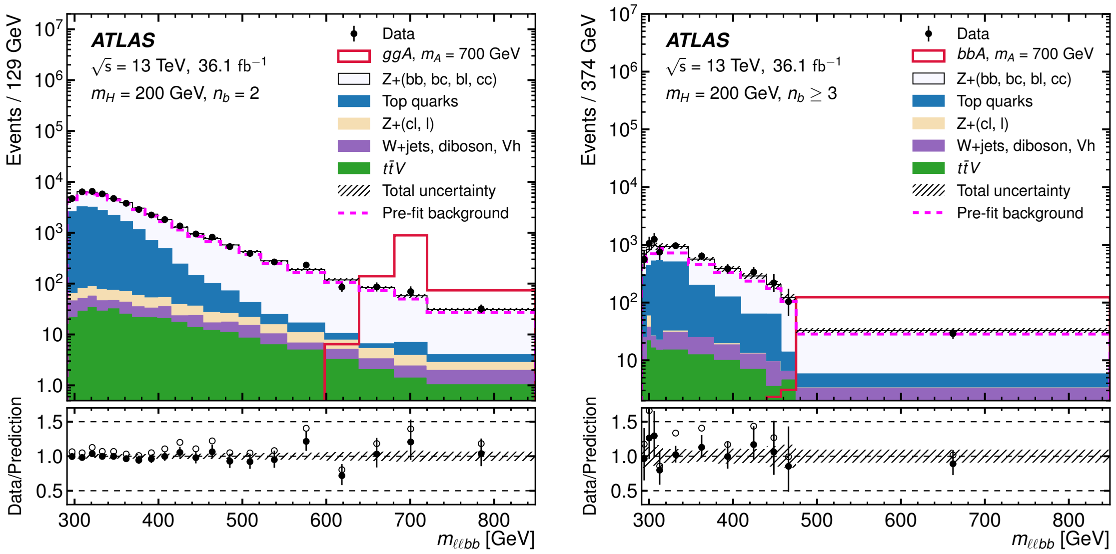

(a) (b)

Figure 6.30: Distributions of the $m_{\ell\ell bb}$ spectrum for the $m_{\mathrm{H}} = 200\,\mathrm{GeV}$ hypothesis in the (a) $n_b = 2$ category and (b) the $n_b \geq 3$ category. See Figure 6.28 for more explanations for the background and signal distributions.

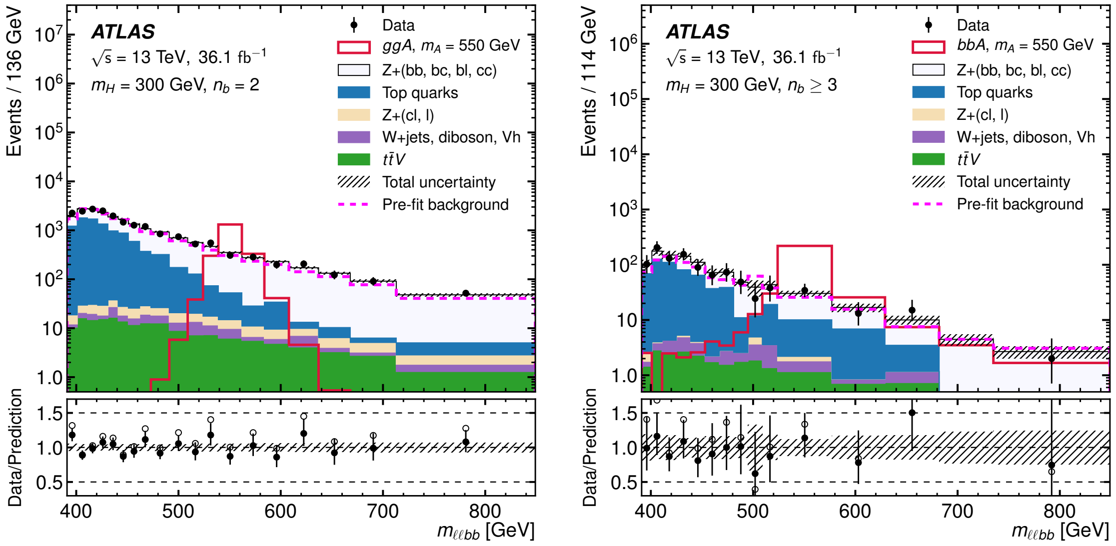

(a) (b)

Figure 6.31: Distributions of the $m_{\ell\ell bb}$ spectrum for the $m_{\mathrm{H}} = 300\,\mathrm{GeV}$ hypothesis in the (a) $n_b = 2$ category and (b) the $n_b \geq 3$ category. See Figure 6.28 for more explanations for the background and signal distributions.

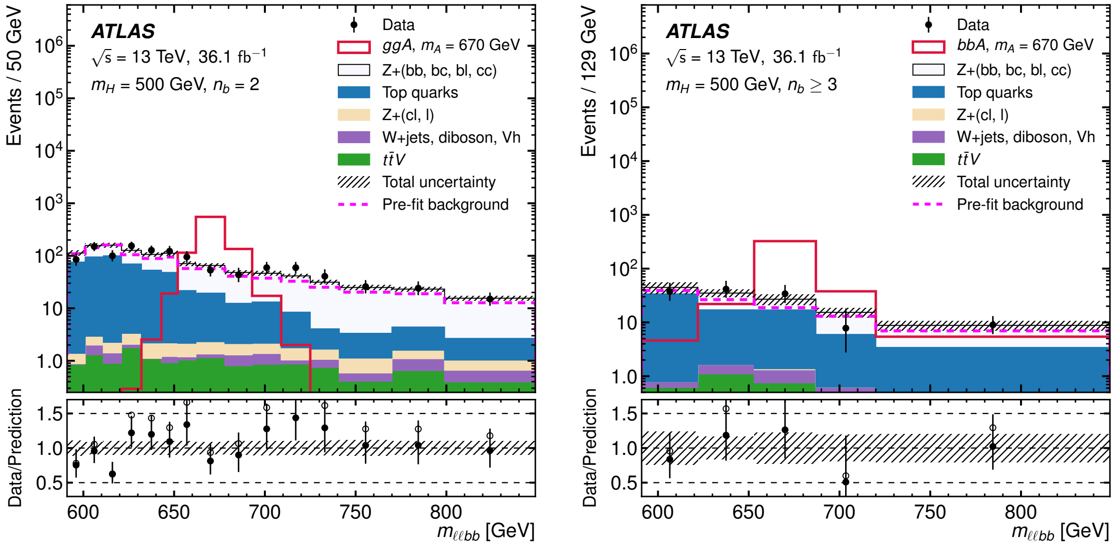

(a) (b)

Figure 6.32: Distributions of the $m_{\ell\ell bb}$ spectrum for the $m_{\mathrm{H}} = 500\,\mathrm{GeV}$ hypothesis in the (a) $n_b = 2$ category and (b) the $n_b \geq 3$ category. See Figure 6.28 for more explanations for the background and signal distributions.

Using the CL$_s$ method, upper limits are derived asymptotically at 95% CL on the production of a narrow-width A boson with the subsequent $A \to ZH$ and $H \to bb$ decays. The upper limits on $\sigma \times \mathcal{B}(A \to ZH) \times \mathcal{B}(H \to bb)$ are shown in Figure 6.33 for gluon-gluon fusion production and Figure 6.34 for b-associated production.

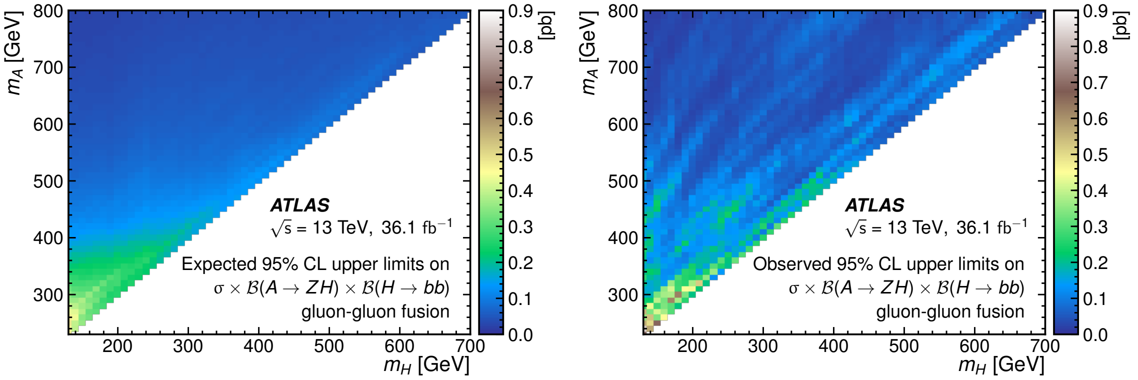

(a) (b)

Figure 6.33: The (a) expected and (b) observed upper limits at 95% CL on $\sigma \times \mathcal{B}(A \to ZH) \times \mathcal{B}(H \to bb)$ for gluon-gluon fusion production.

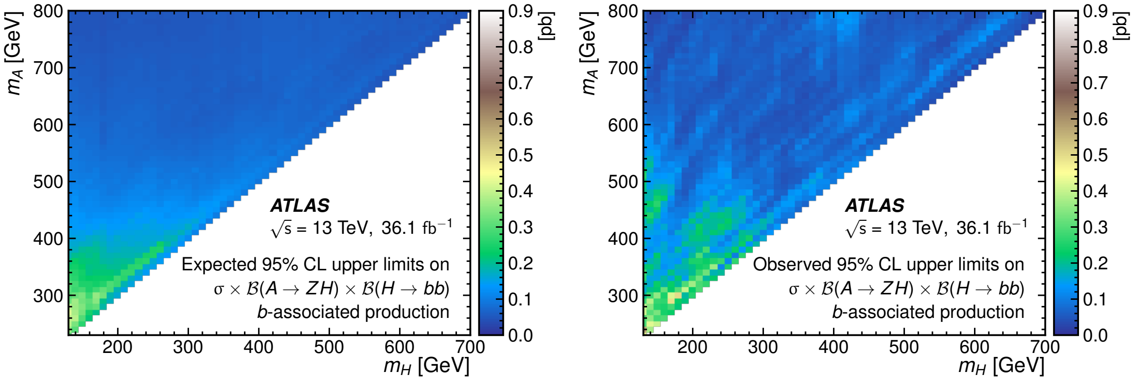

(a) (b)

Figure 6.34: The (a) expected and (b) observed upper limits at 95% CL on $\sigma \times \mathcal{B}(A \to ZH) \times \mathcal{B}(H \to bb)$ for *b*-associated production.

The observed data events are also interpreted in the context of 2HDMs. The number of free parameters in a 2HDM are first reduced by making some explicit assumptions. The 2HDM is required to comply with the SM alignment limit by setting $\cos(\beta - \alpha) = 0$. The lightest Higgs boson in the model, h, will then have properties similar to those of the recently discovered Higgs boson at the LHC. The m_{12}^2 parameter is fixed to $m_{\mathrm{A}}^2 \tan\beta/(1+\tan^2\beta)$. The widths of the A bosons are taken from the predictions of the 2HDM and the corresponding parameterizations of the large-width signals are used. The cross sections of the A boson production are calculated with up to NNLO corrections in the 2HDM [125–127]. Figure 6.35 shows the observed and expected limits for the Type I, Type II, "lepton specific" and "flipped" 2HDMs for various $\tan\beta$ values in the $(m_{\mathrm{A}}, m_{\mathrm{H}})$ plane. An exclusion up to $m_{\mathrm{H}} = 350\,\mathrm{GeV}$ is observed for $\tan\beta = 1$. The $H \to \tau\tau$ is preferred in the lepton specific scenario for $\tan\beta > 1$, leading to a much lower sensitivity compared to Type I. For higher values of $\tan\beta$, the coupling of the H boson to down-type quarks is enhanced in Type II and flipped 2HDMs but suppressed in the other two scenarios. Therefore, Type II and flipped 2HDMs have greater exclusion powers in the high $\tan\beta$ region.

The effects of the leading sources of systematic uncertainty are also studied following the same approach described in Section 5.6.3, as shown in Table 6.5 for two representative signal points of both gluon-gluon fusion and *b*-associated production of a narrow-width A boson. In all cases, the amount of the Monte Carlo statistics is the leading source of systematic uncertainty. The effect of the total systematic uncertainty is comparable to that of the dataset size, with the latter being larger at high mass. The leading sources of systematic uncertainty and their impacts are similar for the other signal points studied and for large-width assumptions of the A boson as well.

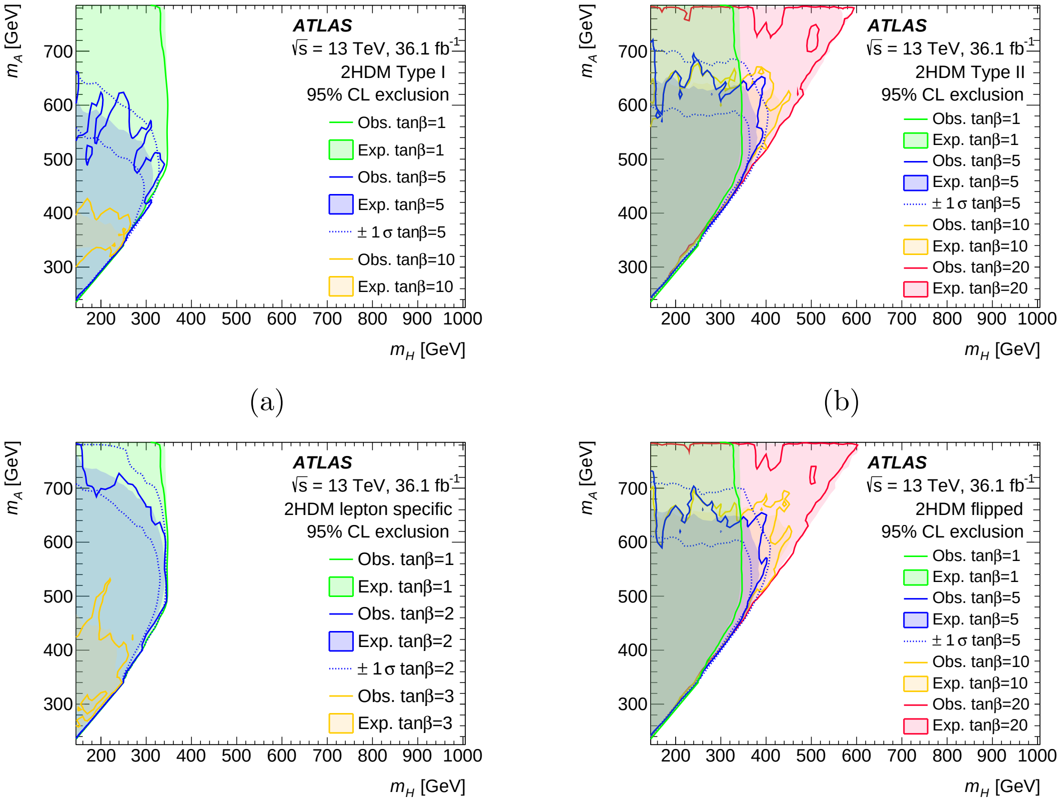

(a)

(b)

(c)

(d)

Figure 6.35: Observed and expected 95% CL exclusion regions in the $(m_\mathrm{A}, m_\mathrm{H})$ plane for various $\tan\beta$ values for (a) Type I, (b) Type II, (c) lepton specific and (d) flipped 2HDMs.

Table 6.5: The effects of the most important sources of uncertainty on the strength parameter (μ) at two example mass points of $(m_{\mathrm{A}}, m_{\mathrm{H}}) = (230, 130)$ GeV and $(m_{\mathrm{A}}, m_{\mathrm{H}}) = (700, 200)$ GeV for both the gluon–gluon fusion and b-associated production of a narrow-width A boson. The signal cross-sections are taken to be the expected median upper limits as shown in Figure 6.33 and Figure 6.34. JES and JER stand for jet energy scale and jet energy resolution, 'Sim. stat.' for simulation statistics, and "Bkg. model." for the background modelling.

Gluon–gluon fusion production				b-associated production			
(230, 130) GeV		(700, 200) GeV		(230, 130) GeV		(700, 200) GeV	
Source	$\Delta\mu/\mu$ [%]	Source	$\Delta\mu/\mu$ [%]	Source	$\Delta\mu/\mu$ [%]	Source	$\Delta\mu/\mu$ [%]
Data stat.	32	Data stat.	49	Data stat.	35	Data stat.	46
Total syst.	36	Total syst.	22	Total syst.	38	Total syst.	26
Sim. stat.	22	Sim. stat.	10	Sim. stat.	26	Sim. stat.	12
Bkg. model.	16	Bkg. model.	10	b-tagging	14	Bkg. model.	11
JES/JER	12	Theory	9.1	JES/JER	11	b-tagging	10
b-tagging	9.9	b-tagging	8.5	Bkg. model.	9.8	Theory	6.8
Theory	7.5	Leptons	4.2	Theory	7.0	JES/JER	6.2

CHAPTER 7

Conclusion

In this dissertation, searches for heavy resonances decaying into ZZ, ZW or ZH are presented, using $36.1\,\mathrm{fb}^{-1}$ of proton-proton collision data at a center-of-mass energy of $\sqrt{s} = 13\,\mathrm{TeV}$ and recorded in 2015 and 2016 by the ATLAS detector at the LHC. The observed data are found to be compatible with the SM prediction, with no significant excesses observed.

The searches for ZZ and ZW resonances explore the final state in which a Z boson decays into a pair of charged leptons, and the other boson decays into a pair of quarks. These searches are performed in the mass range from 300 GeV to 5000 GeV of the new resonance. The two quarks are identified as either one large-radius jet or two separate small-radius jets depending on the transverse momentum of the hadronically decaying boson. Boson tagging algorithms are employed to identify large-radius jets with masses and substructures compatible with the hadronic decays of high-momentum W or Z bosons. Moreover, the searches are performed in two event categories aiming at both VBF production and ggF or DY production of the resonances.

Upper limits on the production cross section times branching ratio, $\sigma \times \mathcal{B}(X \to ZV)$, as a function of the resonance mass are derived at 95% CL. In the case of a heavy neutral Higgs boson, upper limits on $\sigma \times \mathcal{B}(H \to ZZ)$ vary from 1.7 (0.42) pb at $m_{\mathrm{H}} = 300\,\mathrm{GeV}$ to 1.4 (1.1) fb at $m_{\mathrm{H}} = 3\,\mathrm{TeV}$ for the ggF (VBF) production process. In the context of the phenomenological heavy-vector-triplet (HVT) benchmark model A (model B) with the coupling constant $g_V = 1$ ($g_V = 3$), exclusions up to 2.9 (3.2) TeV are derived for a spin-1 vector triplet W' produced via the Drell-Yan process. Upper limits on $\sigma \times \mathcal{B}(W' \to ZW)$ are also set for the HVT VBF model, which range from 0.98 pb at $m_{W'} = 300\,\mathrm{GeV}$ to 2.8 fb at $m_{W'} = 4\,\mathrm{TeV}$. A spin-2 Kaluza-Klein graviton produced via the gluon-gluon fusion process is excluded for masses below 1.3 TeV and 1.0 TeV for the bulk Randall-Sundrum model with $k/\overline{M}_{\mathrm{Pl}} = 1$ and $k/\overline{M}_{\mathrm{Pl}} = 0.5$, respectively.

The search for a heavy Higgs boson, A, decaying into a Z boson and another heavy Higgs boson, H, with $m_{\mathrm{H}} > 125\,\mathrm{GeV}$ is performed in the $\ell\ell bb$ final state. Both the gluon-gluon fusion production and the b-associated production of the A boson are considered; consequently, a $n_b = 2$ category and a $n_b \geq 3$ category are utilized to classify events according to the number of b-jets.

With no significant deviation from the SM background prediction observed, upper limits are set on the product $\sigma \times \mathcal{B}(A \rightarrow ZH) \times \mathcal{B}(H \rightarrow bb)$. The upper limits range from 14 fb to 830 fb and from 26 fb to 570 fb for the gluon-gluon fusion production and the b-associated production of a narrow-width A boson, respectively. The search also tightens the constraints on different types of two-Higgs double models (2HDMs) in the part of the parameter space with a large mass splitting between m_{A} and m_{H}. These constraints are established for Type I, Type II, lepton-specific and flipped 2HDMs in the $(m_{\mathrm{A}}, m_{\mathrm{H}})$ plane assuming different $\tan\beta$ values.

As the LHC physics program continues, the diboson channel remains a vital probe of new physics beyond the SM. The ATLAS detector recorded $46.9\,\mathrm{fb}^{-1}$ of proton-proton collision data in 2017 and will accumulate a total integrated luminosity of more than $100\,\mathrm{fb}^{-1}$ by the end of Run-II. The Run-III operation of the LHC is on the horizon, with a goal of delivering around $300\,\mathrm{fb}^{-1}$ of data at a center-of-mass energy of 14 TeV. Further down the road, the High Luminosity LHC program envisages an instantaneous luminosity of approximately five times the current nominal LHC peak luminosity ($10^{34}\,\mathrm{cm}^{-2}\mathrm{s}^{-1}$) and a total integrated luminosity of about $3000\,\mathrm{fb}^{-1}$ in around 10–12 years. All of these will further extend the discovery potential at the LHC and lend increased sensitivities to rare and elusive processes in the quest for a more complete picture of the elementary particles.

BIBLIOGRAPHY

BIBLIOGRAPHY

[1] D. Griffiths, *Introduction to Elementary Particles*, Wiley, 2008.

[2] M. Srednicki, *Quantum Field Theory*, Cambridge University Press, 2007.

[3] M. Peskin and D. Schroeder, *An Introduction To Quantum Field Theory*, Frontiers in Physics, Avalon Publishing, 1995.

[4] G. Aad et al., *Observation of a new particle in the search for the Standard Model Higgs boson with the ATLAS detector at the LHC*, Phys. Lett. **B716** (2012) 1, arXiv: `1207.7214 [hep-ex]`.

[5] S. Chatrchyan et al., *Observation of a new boson at a mass of 125 GeV with the CMS experiment at the LHC*, Phys. Lett. **B716** (2012) 30, arXiv: `1207.7235 [hep-ex]`.

[6] The ATLAS Collaboration, *The ATLAS Experiment at the CERN Large Hadron Collider*, J. Instrum **3** (2008) S08003, URL: `http://stacks.iop.org/1748-0221/3/i=08/a=S08003`.

[7] The CMS Collaboration, *The CMS experiment at the CERN LHC*, J. Instrum **3** (2008) S08004, URL: `http://stacks.iop.org/1748-0221/3/i=08/a=S08004`.

[8] L. Evans and P. Bryant, *LHC Machine*, J. Instrum **3** (2008) S08001, URL: `http://stacks.iop.org/1748-0221/3/i=08/a=S08001`.

[9] F. Englert and R. Brout, *Broken Symmetry and the Mass of Gauge Vector Mesons*, Phys. Rev. Lett. **13** (9 1964) 321.

[10] P. W. Higgs, *Broken symmetries, massless particles and gauge fields*, Phys. Lett. **12** (1964) 132.

[11] P. W. Higgs, *Broken Symmetries and the Masses of Gauge Bosons*, Phys. Rev. Lett. **13** (1964) 508.

[12] G. S. Guralnik, C. R. Hagen, and T. W. B. Kibble, *Global Conservation Laws and Massless Particles*, Phys. Rev. Lett. **13** (1964) 585.

[13] P. W. Higgs, *Spontaneous Symmetry Breakdown without Massless Bosons*, Phys. Rev. **145** (1966) 1156.

[14] T. W. B. Kibble, *Symmetry breaking in nonAbelian gauge theories*, Phys. Rev. **155** (1967) 1554.

[15] E. Noether, *Invariant variation problems*, Transport Theor. Stat. Phys. **1** (1971) 186, arXiv: `physics/0503066`.

[16] T. D. Lee, *A Theory of Spontaneous T Violation*, Phys. Rev. **D8** (1973) 1226.

[17] G. C. Branco et al., *Theory and phenomenology of two-Higgs-doublet models*, Phys. Rept. **516** (2012) 1, arXiv: `1106.0034 [hep-ph]`.

[18] G. C. Dorsch et al., *Echoes of the Electroweak Phase Transition: Discovering a Second Higgs Doublet through $A_0 \to ZH_0$*, Phys. Rev. Lett. **113** (21 2014) 211802, arXiv: `1405.5537`.

[19] J. de Blas, J. M. Lizana, and M. Prez-Victoria, *Combining searches of Z' and W' bosons*, JHEP **2013** (2013) 166.

[20] D. Pappadopulo et al., *Heavy vector triplets: bridging theory and data*, JHEP **2014** (2014) 60.

[21] L. Randall and R. Sundrum, *Large Mass Hierarchy from a Small Extra Dimension*, Phys. Rev. Lett. **83** (17 1999) 3370.

[22] K. Agashe et al., *Warped gravitons at the CERN LHC and beyond*, Phys. Rev. D **76** (3 2007) 036006.

[23] L. Fitzpatrick et al., *Searching for the Kaluza-Klein graviton in bulk RS models*, JHEP **2007** (2007) 013.

[24] D. E. Morrissey and M. J. Ramsey-Musolf, *Electroweak baryogenesis*, New J. Phys **14** (2012) 125003, arXiv: `1206.2942`.

[25] G. C. Dorsch, S. J. Huber, and J. M. No, *A strong electroweak phase transition in the 2HDM after LHC8*, Journal of High Energy Physics **2013** (2013) 29, arXiv: `1305.6610 [hep-ph]`.

[26] R. D. Ball et al., *Parton distributions with LHC data*, Nucl. Phys. B **867** (2013) 244, arXiv: `1207.1303 [hep-ph]`.

[27] O. S. Brning et al., *LHC Design Report*, CERN Yellow Reports: Monographs, CERN, 2004, URL: `https://cds.cern.ch/record/782076`.

[28] O. S. Brning et al., *LHC Design Report*, CERN Yellow Reports: Monographs, CERN, 2004, URL: `http://cds.cern.ch/record/815187`.

[29] M. Benedikt et al., *LHC Design Report*, CERN Yellow Reports: Monographs, CERN, 2004, URL: `http://cds.cern.ch/record/823808`.

[30] LHCb Collaboration, *The LHCb Detector at the LHC*, J. Instrum **3** (2008) S08005, URL: `http://stacks.iop.org/1748-0221/3/i=08/a=S08005`.

[31] ALICE Collaboration, *The ALICE experiment at the CERN LHC*, J. Instrum **3** (2008) S08002, URL: `http://stacks.iop.org/1748-0221/3/i=08/a=S08002`.

[32] O. S. Brning et al., *LHC Design Report*, CERN Yellow Reports: Monographs, CERN, 2004, URL: `https://cds.cern.ch/record/782076`.

[33] ATLAS Collaboration, *ATLAS inner detector: Technical Design Report, 1*, Technical Design Report ATLAS, CERN, 1997, URL: `https://cds.cern.ch/record/331063`.

[34] ATLAS Collaboration, *ATLAS inner detector: Technical Design Report, 2*, Technical Design Report ATLAS, CERN, 1997, URL: `https://cds.cern.ch/record/331064`.

[35] M. Capeans et al., "ATLAS Insertable B-Layer Technical Design Report", tech. rep., 2010, URL: `https://cds.cern.ch/record/1291633`.

[36] ATLAS Collaboration, "The Expected Performance of the ATLAS Inner Detector", tech. rep., 2008, URL: `https://cds.cern.ch/record/1118445`.

[37] ATLAS Collaboration, *ATLAS liquid-argon calorimeter: Technical Design Report*, Technical Design Report ATLAS, CERN, 1996, URL: `https://cds.cern.ch/record/331061`.

[38] ATLAS Collaboration, *ATLAS tile calorimeter: Technical Design Report*, Technical Design Report ATLAS, CERN, 1996, URL: `https://cds.cern.ch/record/331062`.

[39] ATLAS Collaboration, *ATLAS muon spectrometer: Technical Design Report*, Technical Design Report ATLAS, CERN, 1997, URL: `https://cds.cern.ch/record/331068`.

[40] ATLAS Collaboration, *The evolution of the Trigger and Data Acquisition System in the ATLAS experiment*, J. Phys. Conf. Ser. **523** (2014) 012019.

[41] G. Duckeck et al., *ATLAS computing: Technical design report*, (2005).

[42] W. Lampl et al., "Calorimeter Clustering Algorithms: Description and Performance", tech. rep., 2008, URL: `https://cds.cern.ch/record/1099735`.

[43] ATLAS Collaboration, "Electron efficiency measurements with the ATLAS detector using the 2015 LHC proton-proton collision data", tech. rep., 2016, URL: `http://cds.cern.ch/record/2157687`.

[44] ATLAS Collaboration, "Improved electron reconstruction in ATLAS using the Gaussian Sum Filter-based model for bremsstrahlung", tech. rep., 2012, URL: `https://cds.cern.ch/record/1449796`.

[45] ATLAS Collaboration, "Electron efficiency measurements with the ATLAS detector using the 2012 LHC proton-proton collision data", tech. rep., 2014, URL: `https://cds.cern.ch/record/1706245`.

[46] G. Aad et al., *Muon reconstruction performance of the ATLAS detector in proton–proton collision data at* $\sqrt{s} = 13$ *TeV*, Eur. Phys. J. C **76** (2016) 292.

[47] M. Cacciari, G. P. Salam, and G. Soyez, *The anti-*k_t *jet clustering algorithm*, JHEP **2008** (2008) 063.

[48] ATLAS Collaboration, *Topological cell clustering in the ATLAS calorimeters and its performance in LHC Run 1*, Eur. Phys. J. C **77** (2017) 490.

[49] M. Cacciari, G. P. Salam, and G. Soyez, *The catchment area of jets*, JHEP **2008** (2008) 005, arXiv: `0802.1188`, URL: `http://stacks.iop.org/1126-6708/2008/i=04/a=005`.

[50] M. Cacciari, G. P. Salam, and G. Soyez, *FastJet user manual*, Eur. Phys. J. C **72** (2012) 1896.

[51] ATLAS Collaboration, *Jet energy scale measurements and their systematic uncertainties in proton-proton collisions at* $\sqrt{s} = 13$ *TeV with the ATLAS detector*, Phys. Rev. D **96** (7 2017) 072002.

[52] ATLAS Collaboration, *Performance of b-jet identification in the ATLAS experiment*, J. Instrum **11** (2016) P04008.

[53] ATLAS Collaboration, "Optimisation of the ATLAS *b*-tagging performance for the 2016 LHC Run", tech. rep., 2016, URL: `https://cds.cern.ch/record/2160731`.

[54] ATLAS Collaboration, *Performance of jet substructure techniques for large-R jets in proton-proton collisions at* $\sqrt{s} = 13$ *TeV using the ATLAS detector*, JHEP **2013** (2013) 76.

[55] ATLAS Collaboration, "Jet mass reconstruction with the ATLAS Detector in early Run 2 data", tech. rep., 2016, URL: `http://cds.cern.ch/record/2200211`.

[56] A. J. Larkoski, I. Moult, and D. Neill, *Power counting to better jet observables*, JHEP **2014** (2014) 9.

[57] A. J. Larkoski, I. Moult, and D. Neill, *Analytic boosted boson discrimination*, JHEP **2016** (2016) 117.

[58] ATLAS Collaboration, "Identification of boosted, hadronically-decaying W and Z bosons in $\sqrt{s} = 13$ TeV Monte Carlo Simulations for ATLAS", tech. rep., 2015, URL: `http://cds.cern.ch/record/2041461`.

[59] B. Brunt et al., "Performance of missing transverse momentum reconstruction with the ATLAS detector using proton-proton collisions at $\sqrt{s} = 13$ TeV", tech. rep., 2016, URL: `https://cds.cern.ch/record/2149445`.

[60] ATLAS Collaboration, *Searches for heavy ZZ and ZW resonances in the $\ell\ell qq$ and $\nu\nu qq$ final states in pp collisions at $\sqrt{s} = 13$ TeV with the ATLAS detector*, JHEP **2018** (2018) 9.

[61] V. Barger et al., *CERN LHC phenomenology of an extended standard model with a real scalar singlet*, Phys. Rev. D **77** (3 2008) 035005.

[62] J. Shelton, *TASI Lectures on Jet Substructure*, ArXiv e-prints (2013), arXiv: `1302.0260 [hep-ph]`.

[63] ATLAS Collaboration, *Measurement of the Inelastic Proton-Proton Cross Section at $\sqrt{s} = 13$ TeV with the ATLAS Detector at the LHC*, Phys. Rev. Lett. **117** (2016) 182002, arXiv: `1606.02625 [hep-ex]`.

[64] S. Agostinelli et al., *GEANT4: A simulation toolkit*, Nucl. Instrum. Meth. A **506** (2003) 250.

[65] ATLAS Collaboration, *The ATLAS Simulation Infrastructure*, Eur. Phys. J. C **70** (2010) 823.

[66] T. Gleisberg et al., *Event generation with SHERPA 1.1*, JHEP **2009** (2009) 007.

[67] T. Gleisberg and S. Hche, *Comix, a new matrix element generator*, JHEP **2008** (2008) 039.

[68] F. Cascioli, P. Maierhfer, and S. Pozzorini, *Scattering Amplitudes with Open Loops*, Phys. Rev. Lett. **108** (11 2012) 111601.

[69] H.-L. Lai et al., *New parton distributions for collider physics*, Phys. Rev. D **82** (7 2010) 074024.

[70] S. Alioli et al., *Erratum: NLO single-top production matched with shower in POWHEG: s- and t-channel contributions*, JHEP **2010** (2010) 11.

[71] R. Frederix, E. Re, and P. Torrielli, *Single-top t-channel hadroproduction in the four-flavour scheme with POWHEG and aMC@NLO*, JHEP **2012** (2012) 130.

[72] E. Re, *Single-top Wt-channel production matched with parton showers using the POWHEG method*, Eur. Phys. J. C **71** (2011) 1547.

[73] S. Frixione, G. Ridolfi, and P. Nason, *A positive-weight next-to-leading-order Monte Carlo for heavy flavour hadroproduction*, JHEP **2007** (2007) 126.

[74] T. Sjstrand, S. Mrenna, and P. Skands, *PYTHIA 6.4 physics and manual*, JHEP **2006** (2006) 026.

[75] J. Pumplin et al., *New Generation of Parton Distributions with Uncertainties from Global QCD Analysis*, JHEP **2002** (2002) 012.

[76] P. Z. Skands, *Tuning Monte Carlo generators: The Perugia tunes*, Phys. Rev. D **82** (7 2010) 074018.

[77] D. J. Lange, *The EvtGen particle decay simulation package*, Nucl. Instrum. Meth. A **462** (2001) 152.

[78] C. Anastasiou et al., *High-precision QCD at hadron colliders: Electroweak gauge boson rapidity distributions at next-to-next-to leading order*, Phys. Rev. D **69** (9 2004) 094008.

[79] S. Hche et al., *NLO matrix elements and truncated showers*, JHEP **2011** (2011) 123.

[80] M. Czakon, P. Fiedler, and A. Mitov, *Total Top-Quark Pair-Production Cross Section at Hadron Colliders Through* $\mathcal{O}(\alpha_S^4)$, Phys. Rev. Lett. **110** (25 2013) 252004.

[81] M. Czakon and A. Mitov, *Top++: A program for the calculation of the top-pair cross-section at hadron colliders*, Comput. Phys. Commun **185** (2014) 2930.

[82] N. Kidonakis, *Next-to-next-to-leading logarithm resummation for s-channel single top quark production*, Phys. Rev. D **81** (5 2010) 054028.

[83] N. Kidonakis, *Two-loop soft anomalous dimensions for single top quark associated production with a* W^- *or* H^-, Phys. Rev. D **82** (5 2010) 054018.

[84] J. Alwall et al., *The automated computation of tree-level and next-to-leading order differential cross sections, and their matching to parton shower simulations*, JHEP **2014** (2014) 79.

[85] T. Sjstrand, S. Mrenna, and P. Skands, *A brief introduction to PYTHIA 8.1*, Comput. Phys. Commun **178** (2008) 852.

[86] ATLAS Collaboration, "ATLAS Run 1 Pythia8 tunes", tech. rep., 2014, URL: `https://cds.cern.ch/record/1966419`.

[87] ATLAS Collaboration, *Measurement of the Z/γ^* boson transverse momentum distribution in pp collisions at $\sqrt{s} = 7$ TeV with the ATLAS detector*, JHEP **2014** (2014) 145.

[88] ATLAS Collaboration, "Electron and photon energy calibration with the ATLAS detector using data collected in 2015 at $\sqrt{s} = 13$ TeV", tech. rep., 2016, URL: `https://cds.cern.ch/record/2203514`.

[89] ATLAS Collaboration, "Tagging and suppression of pileup jets with the ATLAS detector", tech. rep., 2014, URL: `https://cds.cern.ch/record/1700870`.

[90] ATLAS Collaboration, "In-situ measurements of the ATLAS large-radius jet response in 13 TeV pp collisions", tech. rep., 2017, URL: `https://cds.cern.ch/record/2275655`.

[91] A. Ruiz-Martinez et al., "Electron and photon trigger efficiency plots using the full 2016 dataset", tech. rep., 2017, URL: `https://cds.cern.ch/record/2254973`.

[92] L. Dell'Asta, M. Morgenstern, and M. Owen, "Muon trigger efficiency plots for RRB", tech. rep., 2017, URL: `https://cds.cern.ch/record/2288150`.

[93] ATLAS Collaboration, "Selection of jets produced in 13TeV proton-proton collisions with the ATLAS detector", tech. rep., 2015, URL: `https://cds.cern.ch/record/2037702`.

[94] C. Patrignani et al., *Review of Particle Physics*, Chin. Phys. **C40** (2016) 100001.

[95] K. Olive and P. D. Group, *Review of Particle Physics*, Chin. Phys. C **38** (2014) 090001.

[96] M. E. Nelson et al., "The Derivation and Performance of the Combined Jet Mass in the ATLAS Experiment", tech. rep., 2016, URL: `https://cds.cern.ch/record/2231534`.

[97] ATLAS Collaboration, "Expected performance of missing transverse momentum reconstruction for the ATLAS detector at $\sqrt{s} = 13$ TeV", tech. rep., 2015, URL: `https://cds.cern.ch/record/2037700`.

[98] ATLAS Collaboration, *Measurement of the Inelastic Proton-Proton Cross Section at* $\sqrt{s} = 13$ *TeV with the ATLAS Detector at the LHC*, Phys. Rev. Lett. **117** (18 2016) 182002.

[99] ATLAS Collaboration, "Simulation of top quark production for the ATLAS experiment at sqrt(s) = 13 TeV", tech. rep., 2016, URL: `https://cds.cern.ch/record/2120417`.

[100] L. A. Harland-Lang et al., *Parton distributions in the LHC era: MMHT 2014 PDFs*, Eur. Phys. J. C **75** (2015) 204.

[101] S. Dulat et al., *New parton distribution functions from a global analysis of quantum chromodynamics*, Phys. Rev. D **93** (3 2016) 033006.

[102] M. Botje et al., *The PDF4LHC Working Group Interim Recommendations*, ArXiv e-prints (2011), arXiv: `1101.0538 [hep-ph]`.

[103] G. Aad et al., *Combined search for the Standard Model Higgs boson in pp collisions at* $\sqrt{s}$=7 TeV *with the ATLAS detector*, Phys. Rev. D **86** (3 2012) 032003.

[104] G. Cowan et al., *Asymptotic formulae for likelihood-based tests of new physics*, Eur. Phys. J. C **71** (2011) 1554.

[105] J. S. Conway, *Incorporating Nuisance Parameters in Likelihoods for Multisource Spectra*, ArXiv e-prints (2011), arXiv: `1103.0354 [physics.data-an]`.

[106] E. Gross and O. Vitells, *Trial factors for the look elsewhere effect in high energy physics*, Eur. Phys. J. C **70** (2010) 525.

[107] ATLAS Collaboration, *Evidence for the* $H \to b\bar{b}$ *decay with the ATLAS detector*, JHEP **2017** (2017) 24.

[108] ATLAS Collaboration, *Search for heavy resonances decaying into a W or Z boson and a Higgs boson in final states with leptons and b-jets in 36* fb^{-1} *of* $\sqrt{s} = 13$ *TeV pp collisions with the ATLAS detector*, JHEP **03** (2018) 174, arXiv: `1712.06518 [hep-ex]`.

[109] ATLAS Collaboration, *Search for a heavy Higgs boson decaying into a Z boson and another heavy Higgs boson in the $\ell\ell bb$ final state in pp collisions at $\sqrt{s} = 13$ TeV with the ATLAS detector*, ArXiv e-prints (2018), arXiv: `1804.01126 [hep-ex]`.

[110] J. Alwall et al., *MadGraph 5: going beyond*, JHEP **06** (2011) 128, arXiv: `1106.0522 [hep-ph]`.

[111] S. Frixione, P. Nason, and C. Oleari, *Matching NLO QCD computations with Parton Shower simulations: the POWHEG method*, JHEP **11** (2007) 070, arXiv: `0709.2092 [hep-ph]`.

[112] M. Wiesemann et al., *Higgs production in association with bottom quarks*, JHEP **02** (2015) 132, arXiv: `1409.5301 [hep-ph]`.

[113] D. de Florian et al., *Handbook of LHC Higgs Cross Sections: 4. Deciphering the Nature of the Higgs Sector*, (2016), arXiv: `1610.07922 [hep-ph]`.

[114] T. Gehrmann et al., *W^+W^- Production at hadron colliders in next to next to leading order QCD*, Phys. Rev. Lett. **113** (2014) 212001, arXiv: `1408.5243 [hep-ph]`.

[115] M. Grazzini et al., *$W^{\pm}Z$ production at hadron colliders in NNLO QCD*, Phys. Lett. B **761** (2016) 179, arXiv: `1604.08576 [hep-ph]`.

[116] M. Grazzini, S. Kallweit, and D. Rathlev, *ZZ production at the LHC: fiducial cross sections and distributions in NNLO QCD*, Phys. Lett. B **750** (2015) 407, arXiv: `1507.06257 [hep-ph]`.

[117] F. Cascioli et al., *ZZ production at hadron colliders in NNLO QCD*, Phys. Lett. B **735** (2014) 311, arXiv: `1405.2219 [hep-ph]`.

[118] N. Kidonakis, *NNLL resummation for s-channel single top quark production*, Phys. Rev. D **81** (2010) 054028, arXiv: `1001.5034 [hep-ph]`.

[119] N. Kidonakis, *Next-to-next-to-leading-order collinear and soft gluon corrections for t-channel single top quark production*, Phys. Rev. D **83** (2011) 091503, arXiv: `1103.2792 [hep-ph]`.

[120] N. Kidonakis, *Two-loop soft anomalous dimensions for single top quark associated production with a W- or H-*, Phys. Rev. D **82** (2010) 054018, arXiv: `1005.4451 [hep-ph]`.

[121] S. Das, *A simple alternative to the Crystal Ball function*, ArXiv e-prints (2016), arXiv: `1603.08591 [hep-ex]`.

[122] M. Oreglia, *A Study of the Reactions $\psi' \to \gamma\gamma\psi$*, SLAC-R-0236 (1980).

[123] J. Duchon, *Interpolation des fonctions de deux variables suivant le principe de la flexion des plaques minces*, fre, ESAIM: Mathematical Modelling and Numerical Analysis - Modlisation Mathmatique et Analyse Numrique **10** (1976) 5, URL: `https://eudml.org/doc/193284`.

[124] E. Gross and O. Vitells, *Estimating the significance of a signal in a multi-dimensional search*, Astropart. Phys. **35** (2011) 230, arXiv: `1105.4355 [physics.data-an]`.

[125] R. V. Harlander and W. B. Kilgore, *Higgs boson production in bottom quark fusion at next-to-next-to leading order*, Phys. Rev. D **68** (2003) 013001, arXiv: `hep-ph/0304035`.

[126] R. Harlander and P. Kant, *Higgs production and decay: Analytic results at next-to-leading order QCD*, JHEP **12** (2005) 015, arXiv: `hep-ph/0509189`.

[127] R. V. Harlander and W. B. Kilgore, *Next-to-next-to-leading order Higgs production at hadron colliders*, Phys. Rev. Lett. **88** (2002) 201801, arXiv: `hep-ph/0201206`.